Vibrations of Carbon Nanotubes by a nonlocal shell model

Eduardo Henrique Lopes Marinho Gonçalves

Supervisor: Prof. Dr. Pedro Leal Ribeiro

A Dissertation submitted for the degree of
Master of Science in Mechanical Engineering
to Faculdade de Engenharia, Universidade do Porto

Porto, June 2020

This research was carried out in the framework of project Nº 030348, POCI-01-0145-FEDER-030348, ”Laminated composite panels reinforced with carbon nanotubes and curvilinear carbon fibres for enhanced vibration and flutter characteristics”, funded by FEDER, through Programa Operacional Competitividade e Internacionalização – COMPETE 2020, and by National Funds (PIDDAC), through FCT/MCTES.

Cofinanciado por:

COMPETE 2020

PORTUGAL 2020

UNIÃO EUROPEIA
Fundo Europeu
de Desenvolvimento Regional

Title: Vibrations of carbon nanotubes by a nonlocal shell model

Abstract

The knowledge and insight on the behaviour of carbon nanotubes is strongly tied to the study of their dynamic response for many of the applications they are employed on. From early on, particular physical properties were identified, after their successful synthesis, leading to the application of CNT onto several fields such as sensors, oscillators, field emission devices, charge detectors, mass detection NEMS devices and other biological usages, setting room for potential devices in the fields of power electronics and heat exchangers.

The carbon nanotubes vibrational response reveals itself a crutial topic of research, as not only the cited applications involve direct dependency on modes of vibration (and respective shifts on the natural frequency and mode shapes), but also different measurement processes that focus on the study of mechanical properties, and production of the nanotubes and derived composite materials which include CNTs are linked to this response. Thus, the research of the overall dynamic behaviour as the natural frequency and mode shapes for different parameters and boundary conditions of the CNTs is of great relevance in this field of nanotechnology.

In this dissertation, the linear undamped free vibration of single-walled carbon nanotubes and double-walled carbon nanotubes is studied. For the order of magnitude of the present study, the nanometers, the relatively low size of the considered shells may yield results which are distant from the expected ones. Thus, as the nonlocal small-size effect is relevant, a nonlocal parameter is considered and is the focus of a meticulous approach. Two equivalent continuum models are then formulated using the Sanders-Koiter shell theory, accounting for the Eringen's nonlocal elasticity theory, one for SWCNTs, and another for DWCNTs, where for the latter the van der Waals pressure is also included. For both, the p-version finite element method is applied to discretize the displacements and obtain the equations of motion and equivalent matrices featuring the Galerkin method.

The results for the natural frequencies of both models for different parameters and boundary conditions are then presented and compared to several results from available literature. Later, the mode shapes associated with the already stated natural frequency values are also illustrated, with some being validated by referenced data. The local and nonlocal models are therefore validated, yielding satisfactory results.

A study on the influence of the nonlocal parameter is then conducted, focusing on the calibration of this parameter for different order natural frequencies of CNTs and investigating onto the different effects for each. Critical values of length for which the nonlocal theory remains relevant are proposed for determined parameters and boundary conditions. The influence on the frequency ratio and the circumferential mode number effect on the natural frequency order is also studied, as well as the nonlocal parameter influence effect on the mode shapes of the carbon nanotubes.

Lastly, a model for a SWCNT and DWCNT with an attached mass is developed and implemented using the p-version finite element method. The validation is performed by comparison to results from literature, and the influence of the nonlocal parameter is studied, as a calibration is performed, and the dynamic behaviour of a bridged CNT with an concentrated mass is characterized.

Keywords: Single-walled carbon nanotubes (SWCNT); Double-walled carbon nanotubes (DWCNT); Sanders-Koiter shell theory; p-version Finite Element Method; Linear vibration; Natural frequency; Mode shape; Nonlocal theory; Nonlocal effects; Mass detection; Attached concentrated mass.

Título: Vibrações de nanotubos de carbono por um modelo de cascas não local

Resumo

O conhecimento e compreensão do comportamento de nanotubos de carbono está fortemente ligado ao estudo da resposta dinâmica de diversos aparelhos nos quais estes são utilizados. Desde a sua descoberta e síntese, as propriedades físicas dos nanotubos de carbono foram identificadas, tendo levado à aplicação destes nanotubos em vários setores como sensores, osciladores, dispositivos de emissão por campo, detetores de carga elétrica, dispositivos de deteção de massa e outras aplicações biológicas, abrindo espaço para potenciais aplicações na área da potência eletrónica e permutadores de calor.

A resposta vibratória dos nanotubos de carbono revela-se, portanto, um tópico de investigação crucial, uma vez que as suas aplicações envolvem diretamente descrição dos respetivos modos de vibração (e respetivas variações nos valores de frequências e formas naturais), bem como determinados processos de medição que permitem estudar propriedades mecânicas e ainda processos de produção de nanotubos e materiais que os incorporam. Assim, o estudo da resposta dinâmica sob a forma dos modos de vibração para diferentes parâmetros e condições de fronteira do nanotubo é de grande interesse para este ramo da nanotecnologia.

Na presente dissertação, o estudo é focado em vibração de nanotubos de camada singular e de dupla camada em regime livre e não-amortecido. Para a ordem de grandeza deste estudo, na ordem de nanómetros, o tamanho relativamente reduzido das cascas consideradas podem produzir resultados distantes dos esperados se se usar uma teoria clássica de cascas. Como tal, os efeitos de escala tornam-se relevantes, pelo que uma teoria que englobe os efeitos não locais deve ser considerada, tornando-se o foco deste trabalho. Deste modo, dois modelos equivalentes contínuos são enunciados, com base na teoria de Sanders-Koiter para cascas finas, incluíndo os efeitos não locais pela teoria não local de Eringen, tanto para nanotubos de camada singular como de camada dupla, sendo que para o último as forças intercamada de van der Waals são consideradas. Posteriormente, para ambos, a versão p do método dos elementos finitos é utilizada para discretizar os deslocamentos e obter as equações de movimento e matrizes equivalentes recorrendo ao método de Galerkin.

Os resultados relativamente a frequências naturais para ambos os modelos tendo em conta diferentes parâmetros e condições de fronteira são posteriormente apresentados, realizando-se uma comparação com resultados de bibliografia disponível. As formas naturais associadas a estas frequências são também ilustradas e validadas com recurso a trabalho de outros autores. Por fim, o modelo local e não local dá-se por validado, produzindo valores satisfatórios.

De seguida, é conduzido um estudo relativo à influência do parâmetro não local, focando-se primeiramente na calibração deste parâmetro para frequências naturais de diferente ordem, e investigando-se o respetivo efeito em cada. Relativamente a determinados parâmetros e condições de fronteira, são também propostos valores críticos de comprimento do nanotubo, para os quais a teoria não local passa a ter relevância desprezável. A razão de frequências entre teoria não local e local é também estudada, a par com a influência do número de ondas em direção circunferencial nos valores e ordem das frequências naturais, sendo que o estudo é concluído investigando a influência do parâmetro não local nas formas de vibração dos nanotubos de carbono.

Finalmente, é desenvolvido um modelo para um nanotubo de carbono de camada singular e dupla com uma massa concentrada e implementado com a versão p do método dos elementos finitos. Este é validado com recurso a resultados da literatura existente, sendo posteriormente investigada a influência do parâmetro não local, executada uma calibração deste parâmetro, e caracterizado o comportamento dinâmico de um nanotubo de carbono encastrado com uma massa concentrada na zona central da superfície.

Palavras-chave: Nanotubos de carbono de camada singular; Nanotubos de carbono de camada dupla; Teoria de cascas Sanders-Koiter; Versão *p* do Método dos Elementos Finitos; Vibração linear; Frequência Natural; Forma natural de vibração; Teoria não local; Efeitos não locais; Deteção de massas; Massa concentrada.

Acknowledgements

The present work comes as a result of acquired knowledge and experience over the past five years, as this academic stage culminates in this very dissertation.

First, I would like to thank the institution which welcomed me in my development as a future engineer, Faculdade de Engenharia da Universidade do Porto, and all the people that influenced and taught me something new, contributing for my academic and personal growth over the last years.

I would like to thank Prof. Dr. Pedro Leal Ribeiro, my supervisor, for his guidance, support, and invaluable knowledge shared with me specially during the course of this work, on a topic I cherish very much - vibrations and dynamics -, without which this dissertation would not have been possible.

I would like to thank my family, who have made everything in their way to make sure I would miss nothing, specially during these worldwide troubled times, for their unconditional love and support not only for and during this work, but also for all my academic course and degree, and most importantly, my education, improvement and growth as a person.

Finally, to all the special people in this journey, my girlfriend, my close friends, my black cloak companions, my course colleagues, who all have made a difference in my life their own way, a big thank you.

Contents

List of Figures

List of Tables

List of Symbols

Roman and Greek Symbols/Mathematical Operators

a	internal characteristic carbon bond-length;
$\tilde{a}$	inter-atomic spacing of the carbon atoms;
c_{ij}	van der Waals coefficient;
d	diameter;
$\bar{d}$	distance between the interacting atoms;
$\bar{d}_0$	distance between the interacting atoms prior to deformation;
e_0	empirical material nonlocal constant;
E	equivalent Young's modulus;
E_0	effective Young's modulus;
$F(\bar{d})$	van der Waals force;
f_l	generic applied force;
h	equivalent thickness;
h_0	effective thickness;
f_r	transverse shape functions for x;
g_r	internal membrane shape functions for x;
$i\theta$	auxiliary variable;
$i\xi$	auxiliary variable;
$j\theta$	auxiliary variable;
$j\xi$	auxiliary variable;
K	kinetic energy;
k_x	curvature in the x direction;
$k_{x\theta}$	shear curvature;
k_θ	curvature in the θ direction;
k	number of complete longitudinal waves in x;
l	length of the nanotube;
M_{conc}	attached concentrated mass;
M_{xx}	moment in x direction;
$M_{x\theta}$	shear moment;
$M_{\theta\theta}$	moment in θ direction;
n	circumferential mode number (for θ);
N_{xx}	normal force in the x direction;
$N_{x\theta}$	shear normal force;
$N_{\theta\theta}$	normal force in the θ direction;
$\overline{p}_{ij}$	initial uniform van der Waals pressure;
p_{vdW}	van der Waals pressure;
p_x	external force per surface area in the axial direction;
p_y	external force per surface area in the circumferential direction;
pgu	number of shape functions employed to displacement u^0 in the x coordinate;

pgv	number of shape functions employed to displacement v^0 in the x coordinate;
ptu	number of shape functions employed to displacement u^0 in the θ coordinate;
ptv	number of shape functions employed to displacement v^0 in the θ coordinate;
ptw	number of shape functions employed to displacement w^0 in the θ coordinate;
pw	number of shape functions employed to displacement w^0 in the x coordinate;
q	external force per surface area in the radial direction;
$q_{ij}^u(t)$	generalized displacements for u_0;
$q_{ij}^v(t)$	generalized displacements for v_0;
$q_{ij}^w(t)$	generalized displacements for w_0;
$\ddot{q}_{ij}^u(t)$	generalized accelerations for u_0;
$\ddot{q}_{ij}^v(t)$	generalized accelerations for v_0;
$\ddot{q}_{ij}^w(t)$	generalized accelerations for w_0;
$\overline{q}_{rs}^u$	generalized displacements coefficients for u_0, independent of time;
$\overline{q}_{rs}^v$	generalized displacements coefficients for v_0, independent of time;
$\overline{q}_{rs}^w$	generalized displacements coefficients for w_0, independent of time;
R	radius of a single-walled carbon nanotube;
R_1	inner radius of a double-walled carbon nanotube;
R_2	outer radius of a double-walled carbon nanotube;
t	time variable;
t_{kl}	stress tensor;
t_1	initial time condition;
t_2	final time condition;
tu_n	axial shape functions for θ;
tv_n	circumferential shape functions for θ;
tw_n	transverse shape functions for θ;
U	potential energy;
u	axial displacement;
u_0	middle surface axial displacement;
$\dot{u}$	axial velocity;
$\dot{u}^0$	middle surface axial velocity;
$\ddot{u}^0$	middle surface axial acceleration;
$\ddot{u}_l$	generic acceleration;
V	generic volume;
V_{IJ}	Lennard-Jones pair potential;
v	circumferential displacement;
v_0	middle surface circumferential displacement;
$\dot{v}$	circumferential velocity;
$\dot{v}^0$	middle surface circumferential velocity;
$\ddot{v}^0$	middle surface circumferential acceleration;
w	transverse displacement;
w_0	middle surface transverse displacement;
$\dot{w}$	transverse velocity;
$\dot{w}^0$	middle surface transverse velocity;
$\ddot{w}^0$	middle surface transverse acceleration;
W	external forces;

$\alpha\left(\|x'\text{-}x\|,\tau\right)$	nonlocal kernel function;
$\gamma_{x\theta}$	shear membrane strain;
$\gamma_{x\theta,0}$	shear membrane strain component on the middle surface;
γ_{xz}	transverse shear strain;
γ_{yz}	transverse shear strain;
$\gamma_{\theta z}$	transverse shear strain;
$\Delta p_i(x,\theta)$	pressure increment after DWCNT deformation;
Δp_{ij}	contribution of the pressure increment on the ith layer from the jth layer;
δ	Dirac delta;
δK	variation of the kinetic energy;
δU	variation of the potential energy;
δW	virtual work of the external forces;
ε	depth of the potential;
$\varepsilon_{x,0}$	normal strain component in x direction on the middle surface;
ε_{xx}	normal strain in x direction;
$\varepsilon_{\theta,0}$	normal strain component in θ direction on the middle surface;
$\varepsilon_{\theta\theta}$	normal strain in θ direction;
ε_{zz}	normal strain in z direction;
ν	equivalent Poisson's ratio;
ν_0	effective Poisson's ration;
ξ	natural coordinate in the x direction;
ξ^p	point of application of the concentrated mass;
ρ	equivalent mass density;
σ	surface density of graphite;
$\sigma_{kl}(x')$	local stress tensor at x';
σ_{vdW}	equilibrium distance parameter;
σ_{xx}	normal stress in the x direction;
$\sigma_{\theta\theta}$	normal stress in the θ direction;
σ_{xz}	transverse shear stress;
σ_{yz}	transverse shear stress;
$\sigma_{\theta z}$	transverse shear stress;
$\tau_{x\theta}$	shear membrane stress;
χ	aspect ratio;
Ω	surface area of the shell;

∇^2	laplacian operator;
$\mathcal{L}$	linear differential operator;
$\mathcal{L}_u$	expansion of the equation of motion for the axial component;
$\mathcal{L}_v$	expansion of the equation of motion for the circumferential component;
$\mathcal{L}_w$	expansion of the equation of motion for the radial component.

Vectors and Matrices

$\vec{C}_h$	chiral vector;
$\{de^0\}$	vector of middle surface displacements;
$\{F_i\}$	external forces;
$[K_{ij}]$	generic stiffness submatrix for the equation of motion in i component and displacement j;
$[M_{ij}]$	generic mass submatrix for the equation of motion in i component and displacement j;
$[M_{ij}^{\mu}]$	generic nonlocal mass submatrix for the equation of motion in i component and displacement j;
$[N]$	shape function matrix;
$\{q\}$	generalized displacements vector;
$\{q^u\}$	generalized displacements vector for the axial component;
$\{q^v\}$	generalized displacements vector for the circumferential component;
$\{q^w\}$	generalized displacements vector for the radial component;
$\{\ddot{q}^u\}$	generalized accelerations vector for the axial component;
$\{\ddot{q}^v\}$	generalized accelerations vector for the circumferential component;
$\{\ddot{q}^w\}$	generalized accelerations vector for the radial component;
$\{r_i\}$	position vector of particle i;
$\{v_i\}$	velocity vector of particle i.

Acronyms

AFM	atomic force microscopes;
CC	clamped-clamped boundary conditions;
CF	clamped-free boundary conditions;
CNT	carbon nanotube;
CVD	chemical vapor deposition;
DFT	density functional theory;
DWCNT	double-walled carbon nanotube;
FE	finite element;
FEA	finite element analysis;
FEM	finite element method;
FF	free-free boundary conditions;
MD	molecular dynamics;
MEMS	micro-eletro-mechanical systems;
MWCNT	multi-walled carbon nanotube;
NEMS	nano-eletro-mechanical systems;
PECVD	plasma-enhanced chemical vapor deposition;
RBM	radial breathing mode;
RRS	Raman spectroscopy;
SERS	surface-enhanced Raman spectroscopy;
SS	simply supported-simply supported boundary conditions;
SWCNT	single-walled carbon nanotube.

Chapter 1

Introduction

1.1 General Overview and Motivation

The most recent advances in nanoscience and nanotechnology have made them earn a proper spot in the areas of engineering, materials science, medicine, biology, electronics and energy production. Ever since the Carbon nanotubes (CNTs) were discovered in 1991 by Iijima [1], who pioneered the analysis of the synthesis of molecular carbon structures in the form of fullerenes and then reported the processing of a needle-like tubes of finite carbon structure, the helical tubules of graphene sheets, the carbon nanotubes, the ongoing research and consequent number of publications on the topic have taken an important part of the scientific community.

Due to their great mechanical and physical properties, along with small dimensions, carbon nanotubes are used as ultrahigh frequency nanomechanical resonators in a wide range of nanoeletromechanical resonators (as their reduced size and high stiffness amplify the resonant frequency and reduce its energy consumption, improving its sensivitity), such as sensors, oscillators, charge detectors, field emission devices [2], NEMS devices linked to mass detection and biological applications [3], as well as making them renowned candidates for applications of power electronics, eletric motors, generators and heat exchangers [4].

These applications are strongly connected to the study of vibration characteristics of CNTs, as different boundary conditions along with different vibrational responses - linear and nonlinear - occur, not only in the direct application but also as part of nondestructive measuring procedures as Raman spectroscopy (which allows for the estimation of mechanical properties) [5], or dispersion of carbon nanotubes along the production of homogeneous composites which include them as reinforcement [2]. Thus, the modal analysis of carbon nanotubes reveals its extreme importance as it allows for the prediction of vibrational response associated with resonant frequencies and mode shapes, which influences the mechanical and electronic properties of nanotube resonators, having been a significant branch of the focus of the investigation regarding nanotechnology in the past years, despite the numerous challenges it presents.

Several approaches have employed molecular dynamics simulations onto the investigation of vibrations of CNTs [6–9], composing a reliable method which yields results close to experimental studies. Different approaches regarding continuum models using beam or shell theories have also been published [10–13]. These studies include efforts to characterize linear, nonlocal and nonlinear theories onto the CNTs, considering both single-walled and multi-walled carbon nanotubes, as both encapsulate different applications and distinct vibrational behaviour.

In this dissertation, the linear and nonlocal free vibrations of single-walled and double-walled carbon nanotubes are studied by employing the Sanders-Koiter theory and using the p-version finite element method to aid with the discretization and implementation, while using molecular dynamics and different continuum models results to validate the model, and later investigating the influence of the nonlocal parameter on the modal response of the nanotubes.

1.2 Literature Review

1.2.1 Morphology and characteristics of carbon nanotubes

Carbon nanotubes can be described as a thin sheet of graphene folded into a tube. graphene is formed as a 2-D sheet of carbon atoms, displayed in an hexagonal array, so that when rolled into cylinders, carbon nanotubes are formed, opening various possibilities in terms of atomic orientation. Nanotubes properties depend on this orientation, the tube diameter and length, and the nano structure. CNTs can exist as single-walled carbon nanotubes (SWCNTs) and as multi-walled carbon nanotubes (MWCNTs), being the latest an aggregation of concentric single-walled carbon nanotubes, where each one of these can express different chiralities, and are held to each other by van der Waals bonding. In terms of fundamental investigations of CNTs, single-walled are the most desired as the intra-tube interactions increse the analysis complexity. It is important to note that SWCNTs and MWCNTs present different properties, as stated later on this dissertation.

The structure of the nanotube at the atomic level is mainly described through its chirality, defined by the chiral vector, $\vec{C}_h$ and the chiral angle, θ. The chiral vector can be described by the following equation:

$$\vec{C}_h = n\vec{a}_1 + m\vec{a}_2 \tag{1.1}$$

where the group of integers (n, m) - also noted (r, s) on further chapters of this dissertation - are the multipliers of the zig-zag carbon bonds of hexagonal lattice, while $\vec{a}_1$ and $\vec{a}_2$ are the vectors of the same lattice. The chiral angle represents the slope of the vector relative to a original position, the zig-zag. This way, there are three main distinct types of the main lattice orientation, being the default zig-zag (0°), armchair (30°) and the intermediate one, chiral, with a different angle from the previous two. The limiting cases - zig-zag and armchair - are based on the geometry of the carbon bonds, so that the chiral vector can be defined, for a zig-zag nanotube, as (n,0), and for the armchair as (m,m), as illustrated on Figures 1.1 and 1.2. This vector also defines the tube's diameter by the following expression [14]:

$$d = \frac{\tilde{a}}{\pi}\sqrt{n^2 + nm + m^2} \tag{1.2}$$

where $\tilde{a}$ is the inter-atomic spacing of the carbon atoms [14], being $\tilde{a} = 0.246$ nm for graphene sheets and consequently carbon nanotubes.

It is known that the chirality of the nanotube has significant influence on the material properties, in particular, on the electronic properties of CNTs [15]. Graphene is characterized as a semi-metal, although it it has been proven that it can assume metallic or semiconducting behaviours, depending on the tube chirality [16]. Wei et al. [17] demonstrated that MWCNTs display high current carrying capacity, which generated considerable interest in its utilization in nanoelectronics. The electromechanical behaviour

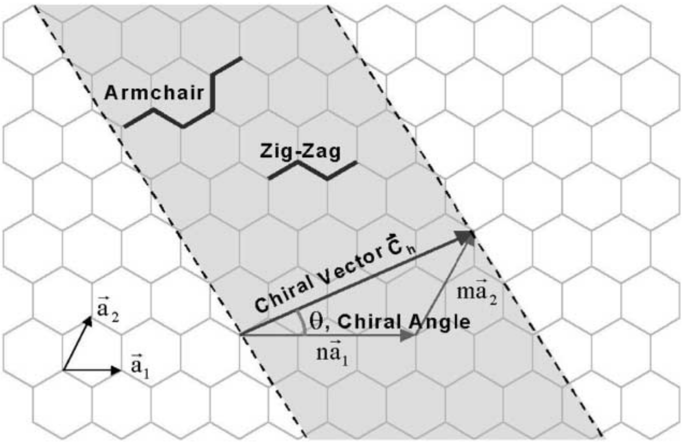

Figure 1.1: Schematic representation of a hexagonal graphene sheet rolled into a carbon nanotube. Reprinted from [15] with permission from Elsevier

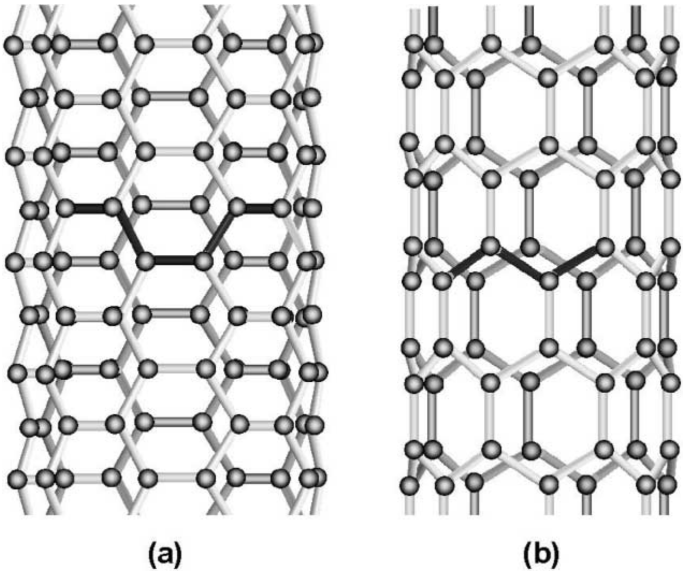

Figure 1.2: Representation of the atomic structure of (a) an armchair and (b) a zig-zag carbon nanotube. Reprinted from [15] with permission from Elsevier

of nanotubes has also been reported, as the injection of charge induced mechanical deformation [18]. On the other side, it was concluded that bending deformation altered the band structure of the nanotube, and depending on nanotube chirality, eletrical properties may be altered. On the same note, Li and Chou electrically charged singe-walled carbon nanotubes by subjecting them to a electric field (electromechanical coupling effect), registering quantitatively the local deformations that arise. They have shown that the large radial strain was localized in a small region near the nanotube ends, while the rest of the tube length between the ends had uniform radial strain. The main conclusion was that for open-ended SWCNTs, the radial deformation in the ends was much higher than for close-ended SWCNTs. For the latest, the distribution of radial strain was different and the transition more gradual [19]. Again, in the same study, similar conclusions were taken regarding the behaviour of charge-induced behaviour in armchair and zigzag nanotubes (comparing to [18]), as well as revealing that the bond breaking occurred differently for open and close-ended nanotubes.

Closely related to electromechanical coupling of CNTs is the nanotubes pull-in. When the resultant current applied in a nanotube from a determined voltage exceeds the maximum allowable value given by the elastostatic force, the CNT electrically breaks down and deforms in the direction of the ground plane (electrode). Thus, the study of this nanotubes' characteristic is crucial for nanodevices in which CNTs are included [20].

As can be inferred from the applicability of CNTs in nanotechnology, the nanodevices produced may be subjected to coupled actions of an electric field and mechanical loading. This leads to an emerging need of understanding the coupled effect on the failure of nanotubes. Guo and Guo have developed studies on the topic involving SWCNTs, and concluded that nanotube strengh under electric field is subject to more significant decay than under mechanical loading alone [21].

Early studies on the mechanical properties of CNTs have also had remarkable conclusions, reason why the research and application of carbon nanotubes have been a relevant subject of study for the past three decades. It was shown that CNTs are very resilient and suitable to extreme strain with no relevant signs of plasticity and brittleness, while also having an unstable response beyond linear motion, and demonstrating a high elastic modulus along with fracture strain sustaining capability [15, 22].

Static and dynamic measurements have been, since early research, a trustworthy method to characterize mechanical properties of CNTs, as both mechanical test methods have been used to study their elastic moduli, for example [2]. In a particular study, loaded nanobeams composed of SWCNTs were used to estimate the elastic moduli, determined to be on the order of 1 TPa, while the shear modulus was calculated to be about 1 GPa [23]. These values were confirmed later, while also stating a decrease of the elastic moduli with the diameter of a MWCNT, which was associated with rippling on the compression side of the larger diameter nanotubes with larger amplitude motions (leading to the possible relevance of the nonlinear behaviour). Later, this dependence was disproved and constant values usage was established. Along with this study, Ru [24] discovered an actual value for the bending stiffness of SWCNTs much lower than the one given by the elastic-continuum shell model, with the common value of thickness used. Thus, it was proposed an effective nanotube bending stiffness value, not related to the actual thickness, leading the computational results to be more on pair with molecular dynamics simulations. Later on, an effective value for thickness, for example, was also put in use, as will also be used further in this dissertation, regarding the model validation. On a last note regarding the vibrational analysis importance, Barnard [25] very recently concluded about and documented the weakly chaotic mechanical breather emergence (specially in the Brownian limit), meaning that the concentrating energy in the low-frequency modes disperses into the higher-frequency modes, returning to the first ones. Along with the coupling of vibrational modes, this study also comes in support to the study of nonlinear modes approach in numerical models. Moreover, evidence about the strong influence of the Brownian limit (system driven by thermal fluctuations) is discussed regarding nanotube resonators, a common application of CNTs.

A widely used technique involving the excitation of a sample with intense monochromatic light followed by observations of the scattering of the radiation, specially in the area of materials science, is Raman Spectroscopy [5]. As the radiation scatters, its frequencies correspond to the vibrational modes of the molecules in the sample (Raman Spectrum), being different from the frequency of the incident radiation. The CNTs dimensions are of the same order of magnitude as the molecules analysed by Raman spectroscopy, which reveals CNTs as excellent targets for this method. In fact, Raman spectra analysis has been set as a unique characterization tool for SWCNTs [26]. One of the main features made possible is the information gathering of vibration symmetries of vibrational modes, directly obtained from polarized Raman spectra, using different polarization configurations (parallel or perpendicular), as the effects of polarization are usually observed in low-dimensional materials - as SWCNTs. This technique led to the characterization of two main vibrational modes in carbon nanotubes: radial breathing mode (RBM) and G-band mode [27]. It is also important to note that Raman scattering has been extensively used to study the dependence of SWCNT breathing mode resonances on the nanotube diameter [28]. Raman spectroscopy had great relevance during the first and second decades of study of CNTs, while still being relevant nowadays in model validation, as will be seen further in this dissertation. The study on CNTs using this method has produced many publications, and for the comprehensibility of this section, it is kept short. Lastly, for the study of MWCNTs this technique was usually followed by another method, the Surface-Enhanced Raman Spectroscopy (SERS), also vastly used in the nanooptical scale [2].

On another note, there has been used field emission to observe resonance frequencies of MWCNTs in the MHz range [29]. Later studies show that these values can go up to the order of THz [30].

Microwave excitation related experiments have been conducted in carbon nanotubes, yielding several conclusions regarding the heating of CNTs. It was found that with microwave irradiation, HiPco SWCNTs rapidly increased their temperature to about 1850°C, releasing hydrogen, steam and carbon derivates [31]. Microwave response properties on composites was also studied [32], revealing that the maximum absorption was noted as the concentration of CNTs increased. Microwaves in the range of 2.45GHz were also observed to cause ignition, burning and reconstruction of unpurified SWCNTs. These properties have important effects on the processing of nanotube-inforced polymer composites (as discussed in subsection "Applications"), as microwave radiation is often used for curing the polymer matrix and because CNTs can be grown my using microwave-enhanced CVD process [2].

Storage of gases and fluids inside CNTs has also been subject of study and controversy. Studies revealed that a fluid flowing through the CNT tends to straighten it as it flexes, as well as excite the longitudinal vibration modes of the same CNT [33, 34]. It was also concluded that the resonant frequencies of the CNT differ based on the fluid flow velocity, while these characteristics disappear when the CNTs are embedded in a matrix material composite.

When it comes to mechanical properties on a macro level, CNTs show promising and unique properties that facilitate their usage, and are directly linked to the type of application they are associated to, which will be discussed later in this chapter.

1.2.2 Production

Ever since CNTs were discovered, a wide variery of techniques for production were developed. The first observed nanotubes were synthesized from the electric-arc discharge technique [1], resulting in the first MWCNTs ever processed. Later, the first SWCNTs were processed by a very similar process, also connected to arc-discharge [35]. With the development of research, new processes were created, displaying a wide range of options besides the arc-discharge [36], as laser ablation [37], gas-phase catalystic growth from carbon monoxide [38] and chemical vapor deposition (CVD) from hydrocarbons [39–41].

When produced for industrial applications, more specifically in composites, large quantities of CNTs are allocated, which by definition reveals preference for certain methods. On the other hand, during CNTs production, a considerable amount of impurities - catalyst particles, amorphous carbon and non-tubular fullerenes - are also synthesised, requiring further purification. As the gas-phase processes produce fewer impurities and are more suitable for large-scale processing, it is stated that these techniques, such as CVD, are the most valuable for large-scale production usually needed as a supplement to composites [15].

The electric-arc discharge technique usually involves the use of high-purity graphene rods as the anode and cathode. Both are merged in a helium atmosphere, with voltage applied, forming a stable arc. As the anode is consumed, the material is deposited on the cathode, building an outside shell of fused material and a softer fibrous core - nanotubes. SWCNTs are synthesised doping the electrodes with a small amount of metallic catalyst particles [36].

Laser ablation was firstly used to produce fullerenes, and has been later improved to produce SWCNTs [37]. Here, a laser is used to vaporize a graphite object located in controlled atmospheres at temperatures near 1200°C. To produce SWCNTs instead of MWCNTs, the graphite object was supplemented with cobalt and nickel catalyst. Later, it is collected the condensed product on a water-cooled target.

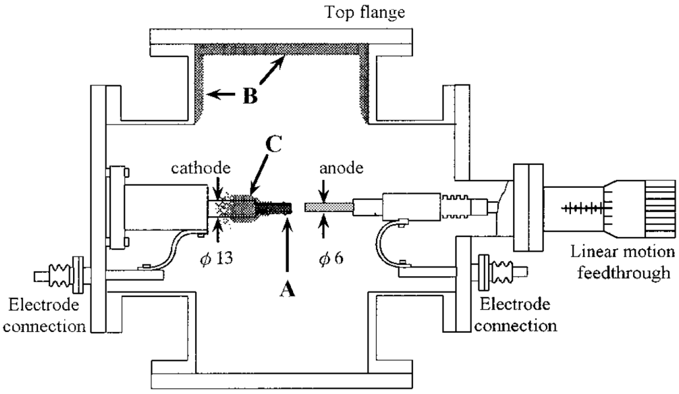

Figure 1.3: Schematic representation of the electric-arc discharge method. Reprinted from [42] with permission of AIP Publishing

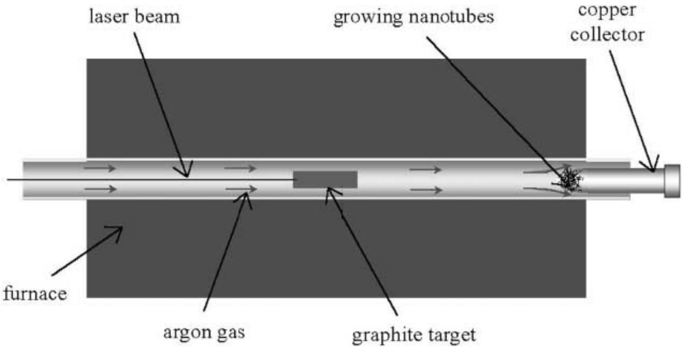

Figure 1.4: Schematic representation of the laser ablation discharge method. Reprinted from [15] with permission from Elsevier

The arc-discharge and the laser ablation technique are both limited to the amount of CNTs that can be produced, in relation to the mass of the carbon source. In other words, the process cannot be continuous, and has to be periodically stopped to replace the source of material. Furthermore, these processes required extensive purification steps to claim the nanotubes from by-products, revealing these processes as not ideal for industrial level [15]. This way, gas-phase techniques were developed - CVD, for example -, forming CNTs by decomposition of carbon-containing gas. Not only this process conducts to high-purity results, requiring few steps for purification, but also allows for a continuous process, systematically replacing the carbon source along the process with flowing gas, and allowing for collecting the product during its synthesis.

One of the first and renowned gas-phase techniques is called the HiPco process [38], as it can produce high-purity SWCNTs in large quantities with carbon monoxide as the carbon source, in a high pressure environment. Other gas-phase techniques involve hydrocarbon gases as the carbon source for production of both SWCNTs and MWCNTs, named CVD. Here, the working temperature is very low compared to the HiPco process, diminishing the purity in the product, but also allowing the growth of nanotubes on a wide variety of substrates [43]. CVD techniques may involve a substrate coated with nickel catalyst, with ammonia as the catalytic gas and acetylene as the carbon source [39, 40]. Furthermore, a DC power may generate the plasma that enhances the reaction [41], while the nanotube length, diameter and graphitization are controlled by changing the growth time and temperature. Here, the synthesis of well-aligned, straight carbon nanotubes on a variety of substrates is accomplished by the use of the plasma, giving name to the plasma-enhanced chemical vapor deposition technique (PECVD).

In fact, highly aligned arrays of carbon nanotubes with great control over its properties can be achieved by PECVD, at a larger cost and fewer quantity, while a larger quantity associated with a cheaper price may be achieved by CVD techniques, with less control over the product properties uniformity [15].

1.2.3 Applications

The emergence of nanotechnology has been enabling the development of devices working at the nanoscale, projected for particular goals as actuation, sensing and detection. The areas of micro-electro-mechanical systems (MEMS) and more specifically, the nano-electro-mechanical systems (NEMS) are one of the main targets of CNTs research, aiming at its further palpable application. In general, a reasonable way to manufacture NEMS is to scale down conventional MEMS, but CNT-based NEMS have several advantages over the previous devices, mainly related to their dynamic behaviour. Enlightening examples are nanometer-sized silicon-based systems that are unprovided with high-Q mechanical resonances due to dominant surface effects, while CNT-based NEMS have higher strength, damping, stiffness, and thermal and electrical conductivity [44]. Still, MEMS and more importantly NEMS devices have introduced new opportunities when it comes to sensitive detection of physical quantities as spin, molecular mass, quantum state, thermal fluctuation, coupled resonance and biochemical reactions [45]. A general highlight of a NEMS device, a nanomechanical resonator, is its unprecedented dynamic behaviour, registering frequencies in the magnitude of GHz and THz. In fact, the resonant frequencies of the device are related to the CNTs length, which adds to the fact that the sensitivity of the device increases the higher the frequencies are, which may be verified in Chapter 5. This fact itself qualifies nanodevices as a great candidate for small physical quantities detection [46]. In addition to the measurement of other already listed properties, nanomechanical resonators show openings for a development of lab toolkits capable of a wide range of functions.

As an illustration of the NEMS resonators potential, it was proven that nanoscale mass spectometers are able to measure the molecular weight of determined molecules. This itself implies that NEMS are a potential alternative to conventional mass spectrometry, while not being limited to low value molecular masses [3]. Unlike molecular recognition, which uses labeling, these devices have fast and reliable detection of molecules that can be associated with determined diseases, implying interest in diagnosis gadgets [47].

This characteristic has different embranchments when it comes to biological detection, more specifically, cell detection. For example, a NEMS resonant cantilever was employed do detect *E.Coli* cells in different environments, having its surface chemically modified with antibodies that detect these specific organisms [48]. Additionally, the number of colected cells by the cantilever was directly linked to the resonant frequency shift, implying the importance of the vibrational research. On the same note, virus detection was also possible using the same technique of mass detection through resonant frequency shift [49], as well as protein detection [50], with the addition of the nanocantilever bending deflection motion measurement. This last method is also used in specific DNA sequences detection [51], while enzymatic activity was able to be detected by the cantilever mass reduction, and consequent resonant frequency increase [52]. The comparison between the utilization or not of CNTs in the NEMS was also studied [53], as chemical sensors based on SWCNTs revealed faster responses and higher sensitivities than existing solid-state sensors. Other applications as membrane chemical and pH sensors have also been documented [54].

All these biologic detection areas have employed considerable effort in further research, as from all the above mentioned, DNA and enzymatic activity detection are reported to be the least developed areas in terms of NEMS application, with great potential stored [45]. It is important to note that these applications of NEMS resonators composed of CNTs as the primary component for its designed function lay on different principles of mass detection, such as flexural deflection, resonance motion, and lastly, nonlinear oscillations, with less established experimental work [55]. Nonlinear vibrational behaviour exists due to geometric nonlinearity, increasing the resonant frequency and stiffening the structure [45]. As the topic of nonlinearity is matter of current and increasing investigation, great hints from the above mentioned applications come that highlight the importance of such matter.

CNTs also reveal applicability in reinforcing the conventional atomic force microscopes (AFM), increasing sensitivity and resolution due to their large aspect ratio, while being resistant to damage from tip crashes (where they are placed), resulting in a better image of surface topography [56].

A particular and interesting application of CNTs are nanotweezers. Already developed before the implantation of CNTs in their core (more specifically, at the end of the substrate), nanotweezers are electrically stimulated, and allow for grabbing and manipulation of submicron cluster and nanowires. Given the conductive properties of the carbon nanotubes, the nanotweezers were also used for testing of electrical properties of of silicon carbide nanoclusters and gallium arsenide nanowires [57].

Research related to the behaviour of layered Nafion/SWCNTs polymer composite nanodevices took place and revealed a large mechanical response at low voltages without the use of an electrolyte. This nanoactuator allowed the authors to conclude about the significance of the area of the nanotubes, playing a crucial role enhancing actuation response, along with a separate influence just from the nanotubes themself [58]. Regarding the nanotubes alignment in the matrix, it was concluded on a different study that certain specific angles of alignment were ideal for a maximum value of electrical conductivity, desired in certain types of actuators [59]. One of the major setbacks faced during processing of carbon nanotube-reinforced or nanoparticle-reinforced polymer composites is the apparent inability to achieve a uniform dispersion of the nanotubes in the polymer. CNTs tend to agglomerate due to physical entanglements of the tubes, as well as van der Waals forces between tube's surfaces. Different methods to achieve uniform dispersion were studied - sonication, for example -, but will not be discussed in this dissertation [2]. Thermal conductivity also plays a significant role in the application of the nanotubes in their polymeric nanocomposites, as recent research established CNTs as promising candidates for advanced applications as power electronics, electric motors, generators, and heat exchangers [4].

CNTs have their developing place in the ceramic and metal-matrix composites, along with the already discussed polymer composites. Although ceramics have high stiffness, high thermal stability and low density, their brittleness disables them for use as a structural material. Study related to the application of carbon nanotubes to different ceramics, highlighting the CNTs property of excellent resilience, may have great results. Not only the resulting composites would potentially have high-temperature stability, but the toughness and creep resistance of the final product would also be of great value [15].

1.2.4 CNT Modelling

CNT behavioural research and description is greatly enhanced by experimental studying, as already described in the ”Applications” section. In fact, the primary reason of research on the carbon nanotubes topic is clearly related to the necessity of correct and accurate models that allow for CNT mechanical and electrical properties description, leading to a reliable prediction of results close to experiment ones, enabling for a correct investments onto CNT-including devices.

Experimental studies are not only complex to conduct, but are also expensive at the nano-scale, requiring the use of high-resolution transmission electron microscopes, while also not allowing for the natural frequencies of different vibration modes within the frequency spectrum to be separated and identified easily (partially due to being of close values). Thus, three distinct types of approaches are labelled for modelling nanostructures: atomistic modelling; hybrid atomistic-continuum modelling; continuum modelling. The first, atomistic modelling, includes methods such as molecular dynamics (MD) and density functional theory (DFT) [60]. in this dissertation, numerical results and the developed model will be tested and validated mostly by molecular dynamics results from bibliography, as MD simulations provide good predictions of the mechanical behaviour of CNTs with results close to experiments [13]. Due to this, a single section will be dedicated to this method, still in the current chapter. Hybrid atomistic-continuum modelling is a blend method between the first and third ones, and serves as an intermediate position allowing to introduce interatomic potentials into the continuum analysis, by incorporationg the molecular potential energy of a nanostructured device onto the mechanical strain energy of the limited volume element of the continuum model [61]. In the cited study, the authors were able to determine the bending rigidity of a graphene sheet, transitioning to a multi-scale level approach. Lastly, continuum modelling includes classical (local) beam, plate and shell theories that allow for an analysis of nanostructures approaching them as large-scale systems. The main advantages of continuum modelling are linked to the mostly easier formulation and to the fact that the implementation and execution comes with a computationally more appealing price [10]. Thus, specific phenomena simulation and research in nanotubes such as buckling, wave propagation, free vibration, nonlinear vibration and energy exchange is backed up by a continuum model [60, 62]. The continuum mechanics theory is based on the continuous assumption along the model, and necessarily implies a verification of results from molecular dynamics/experimental studies to validate the model.

As already discussed, it is key knowledge to understand the mechanical properties of the CNTs, more so when their applications require specific properties such has natural frequencies and mode shapes. The goal of the models discussed in this section is to obtain reliable and exact results regarding the stated properties, for a wide range of SWCNTs or MWCNTs, with varying lentgh, diameter and chirality, etc. The continuum models treat the CNTs composed of covalent carbon atoms bonds as continuous and homogeneous macrostructures, ignoring the lattice spacing between individual carbon atoms. Thus, the stress at any given point is function of the strain at that point, as dictated by the local model. For this reason, and even though several studies have taken part applying local models, their pertinence at small scales is not ideal [63]. Thus, their limited applicability, coming from the fact that at small size the lattice spacing between individual atoms becomes more important and the approximation of homogeneity to a continuum model is not exact, size effects must be taken into account. In fact, the carbon tubes' properties on a nano-scale are size dependent, and the small scale effect/parameter needs to be included for a better model of the materials behaviour. Here, Eringen's nonlocal theory [64] is mostly used, which essentially indicates that the stress state at a given reference point is a function of the strain field at every point of the defined volume, hence including information about the CNT length and diameter - scale effect - along with the long range forces between atoms of the said body.

Due to large elastic deformation, nonlinear vibration in microeletromecanical systems (MEMS) and nanoelectromechanical systems (NEMS) appear in the practical engineering and occupy a relevant role in the design and analysis of these systems [65]. A wide range of studies have been incorporating geometric nonlinearity in order to model what is proven to be a common behaviour of CNTs deformation in nature [66]. One of the most characteristic phenomenons of nonlinear vibration coming from the expected higher amplitudes of vibration is the increase of the natural frequencies. This effect has been linked not only to the stiffening of the material (coming from a large amplitude), but also to interlayer molecular forces - van der Waals force - nonlinearity, more specifically in MWCNTs [67]. Nonlinearity is still a fresh topic that has been studied in the past decade, and accounts for many of the current efforts of research and modelling of carbon nanotubes, along with the local and nonlocal models, for a better representation and characterization of CNTs properties.

Over the past two decades several studies have been conducted regarding the modelling of CNTs. More specifically related to vibrations, the next paragraphs focus on the most relevant papers that contextualize and lead to the work presented in this dissertation.

When developing continuum models for CNTs, the first theories that come to mind are beam and shell theories. Regarding the first, beam theories were firstly used to describe flexural vibrations of carbon nanotubes. Both Euler-Bernoulli and Timoshenko theories were applied (the first for thin beams without rotary inertia and shear effects, and the second for thick, short length, higher modes with rotary inertia and through thickness shear deformation). The limitations of these theories are evident, as they are modelling a nanoshell, even though they are often employed to describe shells due to their simplicity compared to shell theories, despite the latter yielding better results. Hybrid theories accounting for van der Waals interactions between nanotubes layers in MWCNTs were also presented, complementing beam theories, but were deemed incomplete [2, 68]. Thus, various shell theories were developed, for example Wang [69] applied the Flugge elastic shell theory [70] in order to complement the flexural vibrational modes study with radial breathing modes (RBM). On the same study, van der Waals forces were also considered for MWCNTs, illustrating its significant effect on the RBMs, from all of the flexural, torsional and axial modes. The same author developed simplified elastic shell models for buckling and free vibration based on Flugge and Donnell theories.

Finite Element techniques have been employed to perform vibrational analysis of CNTs [63], based on beam elements. 3D models were developed with elastic beams and point masses, taking into account the covalent bonds of the carbon atoms in the hexagonal lattice of the nanotubes. Both FE and MD techniques have revealed inefficient due to the computational effort, concretely regarding the representation of the nonlinear behaviour in MWCNTs that incorporate a large number of atoms.

Silvestre et al. [71] compared the Donnell shallow shell and Sanders-Koiter thin shell theories regarding axial buckling of SWCNTs. It was demonstrated that the Sanders-Koiter theory produced better and accurate results reproducing buckling strains and mode shapes of axially compressed nanotubes. Silvestre also proved that Sanders-Koiter theory is more suitable regarding buckling under torsion - specifically the angle of twist - leading to more accurate results than the Donnell theory [72].

It is important to note that the shell theories discussed in this dissertation consider the nanotube model an isotropic and homogenous material, and the tube as a thin shell. In fact, different studies study and cite the anisotropy of the graphene and in CNTs [73], still, the difference between an anisotropic and isotropic models is almost neglectable (as is the case for plates [74]), and thus an isotropic model is assumed. For this reason, different equivalent mechanical and geometrical parameters have been proposed to fulfill the properties descriptions necessity, allowing for a transposition between atomistic modelling and continuum modelling. Yakobson et al. [22] performed research on the instabilities beyond linear response of CNTs with large amplitudes. On this study, the equivalent parameters Poisson's ratio, Young's modulus and wall thickness were documented, being the same parameter used in this dissertation.

Regarding the nonlocal theory modelling research, diverse studies have taken place: Wang et al. [75] accurately applied the nonlocal theory to a Flugge theory model, predicting the wave propagation behaviour in CNTs with different properties (length, aspect ratio, chirality), and estimated the range of the scale parameter employing said theory; Duan et al. [7] presented a calibration of the small-scale parameter using a Timoshenko theory to model CNTs, allowing for further developments in research; Ansari et al. [76] applied Eringen's nonlocal elasticity theory onto a classical beam theory to study CNTs free vibrational characteristics, concluding that the type of nonlocal beam theory, along with the boundary conditions of the CNTs significantly influence the appropriate value of the nonlocal parameter. This study is greatly complemented by Hu [30] in terms of chirality dependent wave dispersion both for SWCNTs and DWCNTs. Avramov [10], besides focusing on the nonlinearity of the model, performed analysis on the nonlocal parameter when comparing to MD simulation of CNTs vibration modes. In fact, several other research papers have been published on the matter of nonlocal elasticity theory; still, room for further investigation is left for this dissertation, as will be enlightened in the Objectives section.

Nonlinear vibrational behaviour has been growing in research publications through the last decade. Amabili [77] published a book covering the majority of the relevant theories and approaches to nonlinearity both in shells and plates, with significant detail and foundation. Strozzi et al. conducted many different studies with opportunity for publication regarding nonlinearity, starting with a introductory study on linear vibrations from a local shell theory (Sanders-Koiter), also developing a reduced model, while studying and confirming the inadequacy of reduced Donnell's theory when covering CNTs vibrational characteristics [11]. The same authors performed a study on circunferential flexural modes of vibration, based on the previous paper, considering the influence of diverse CNTs properties as aspect ratio and chirality, along with different boundary conditions, and focusing on the stability of vibration modes [13]. This study served as framework for the next study, which enlightened the energy exchange along SWCNTs axis in nonlinear field in RBMs, presenting evidence on the influence of initial excitation [62]. Different studies focused on complememtary issues, such as the forced vibration of fluid-conveying CNTs, establishing a critical value of external force amplitude that disables resonant vibration on the nanotube [65], free vibration of a curved MWCNTs embedded in elastic medium, accounting for geometric and van der Waals force nonlinearity, and studying the effect of boundary conditions on the variation on natural frequencies and characteristic expression in nonlinear behaviour [66].

Most of the discussed papers in this section show different approaches and theories regarding the carbon nanotubes dynamic behaviour description. From beam to shell theories, nonlocal theories and presence of nonlinear behaviour significant enough to not be neglected, a model will be developed and described in further sections.

1.2.5 Molecular Dynamics

Atomistic approaches to the analysis of CNT vibrations include mostly Molecular Dynamics. This section briefly introduces the concept and method of molecular dynamics simulations - MD - as they are used in this dissertation as a bibliographical reference to validate the continuum model results, even though none are performed as a thesis objective.

Molecular dynamics emerged as one of the first simulation methods from the pioneering applications in dynamics of liquids. As computational efficiency and algorithmic research improved, several other areas of interest have embodied this technique, such as chemistry and biochemistry, mostly since the 1970s, from the study of structure and dynamics of macromolecules [78].

From MD methods two main ramifications stand out as to the model chosen to represent the physical system. The first, classical molecular dynamic simulations, treats molecules as classical objects, as atoms correspond to masses and bonds correspond to stiffness, being defined by general classical mechanics laws. The second, quantum molecular dynamic simulations, explicitly take into account the quantum nature of the chemical bond, applying the electron density function for the valence electrons that determine bonding, and classical dynamics to the ions [2, 78, 79].

A classical MD simulation is essentially a particle method with the objective to solve governing equations of particle dynamics based on Newton's second law [79]. First, the simulation starts by defining the base conditions of the particles, in order to determine the potential function of the system at each atoms position, $U(\boldsymbol{r}_1, ..., \boldsymbol{r}_n)$. This potential represents the potential energy of N interacting atoms as a function of their positions $\{r_i\} = (x_i, y_i, z_i)$. The acting force on each ith atom is given by:

$$\{F_i\} = -\nabla_{\boldsymbol{r}_i} U(\boldsymbol{r}_1, ..., \boldsymbol{r}_n) = -\left(\frac{\partial U}{\partial x}, \frac{\partial U}{\partial y}, \frac{\partial U}{\partial z}\right) \tag{1.3}$$

As can be observed, the initial position $\boldsymbol{r}_i$ of each atom is a necessary input. Along with this, is is also needed the initial velocity of each atom $\boldsymbol{v}_i$. It is noted that all the forces among the atoms of the system can be derived from this potential. Moreover, the potential energy U can be divided onto the respective potential energy from bonded or non-bonded atoms. Bonded atoms potential energy includes stretching, bending, dihedral angle torsion and out of plane torsion, while non-bonded atoms mainly express potential energy through van der Waals forces. These are expressed in Figure 1.5.

It is important to understand that the concept of atom is not accurate in the light of the quantum mechanics theory. As electrons may be shared by different nuclei, decentralized electronic clouds appear and influence chemical bonding. This way, it is crucial to introduce the concept of potential energy surface into the dynamics of the nuclei, in order to not study each electron individually. Thus, transitional characteristics of the electronic cloud are neglected and an average field is considered, which allows to represent the electronic cloud effect on nuclei by the potential function - a deterministic approach instead of probabilistic -, leading to the following equations that, considering Newton's second law, solve the dynamic system [78]:

$$\{F_i\} = m_i \frac{\partial^2 \{r_i(t)\}}{\partial t^2} \tag{1.4}$$

The solution of the system of equations are the position $\boldsymbol{r}_i$ and velocity $\boldsymbol{v}_i$ for each atom. These values are often calculated by the Verlet algorithm or derivations, within a atomic

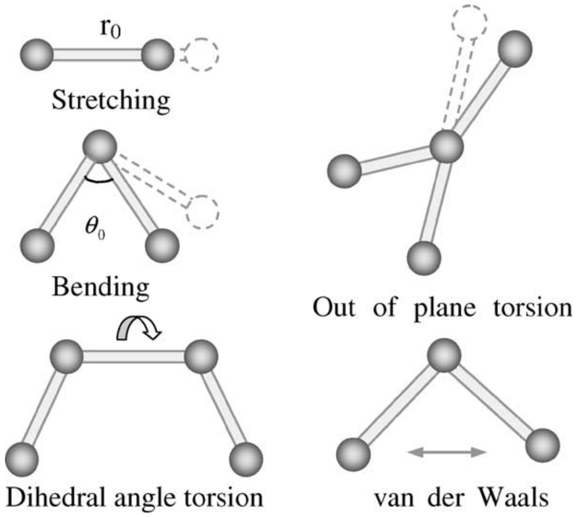

Figure 1.5: Interatomic interactions in the molecular structural mechanics approach. Reprinted by permission from [80]

discretization followed by numerical integration of the differential equations iteratively. The main Verlet algorithm is given by the following equation:

$$\{r_i(t+\Delta t)\} \approx 2\{r_i(t)\} - \{r_i(t-\Delta t)\} + \frac{\{F_i(t)\}}{m_i}\Delta t^2 \tag{1.5}$$

It is important to understand that due to the complexity and range of the discretization needed in molecular dynamics simulations, the method is extremely costly in terms of computation. Besides this disadvantage, usual MD techniques such as classical, which do not take into account quantum effects, has its Schrödinger equations replaced by Newtonistic motion equation, a relatively simplistic theory. When the inter-particle distance is small and/or the inter-layer forces become significant (MWCNTs case), the classical models show inaccuracies comparing to quantum models. Here, quantum corrections may be introduced to the classical MD model. A different problem regarding MD simulations is time-scale, being in some cases in the magnitude of femtoseconds. This brings computational balances as large systems are not able to be studied by MD, requiring a continuum model [78].

In-depth studies have been presented regarding MD simulations. In fact, even though the number of publications is not astounding, there are a few resources well received by the community which served as groundwork for many research on continuum modelling. Regarding the present dissertation, it is important to note the crucial work of Duan et al. [7], where the authors investigate the natural frequencies of CNTs on different chiralities, aspect-ratios and boundary conditions. The amount of documented data from MD simulations is, in fact, of great aid in the present thesis, as will be seen in further chapters. Nonlocal studying as also taken place by Ansari et al. regarding the free vibrations of SWCNTs and DWCNTs, investigating size effects on classical models comparing to MD simulations of different CNT chiralities [12]. Lastly, torsional vibration modes have been proposed by Khademolhosseini et al., completing the available research of RBM and axial vibrational modes associated with the nonlocal Eringen's theory, producing MD simulations that provide validation and calibration, opening room for wave propagation study in the specific conditions of the study [6].

1.3 Continuum Model

In this dissertation a continuum model will be developed based on Kirchhoff-Love assumptions, which mainly yields the hypothesis that the transverse shear stresses and transverse normal stress may be neglected, as the thickness of the shell is very small compared to other dimensions. Thus, a thin shell theory is adequate for the present model. Among different shell theories as Donnell's, Flugge's or Sanders-Koiter's, for example, the results from the linear field study are very similar [10]. With the aim to establish the groundwork and open the possibilities of future development for nonlinear field, Sanders-Koiter theory is selected.

Regarding the study of structures in the order of magnitude of the nanometers, as is the case of the carbon nanotubes, the original continuum model reveals itself insufficient to characterize the dynamic behaviour, as the small-scale effect resultant from the inter-atomic interaction is not taken into account. For this reason, a nonlocal elasticity theory is employed, as for an atomic scale structure the Hooke's elasticity law is incapable of describing the stress tensor at an arbitrary reference point [30], and thus the hypothesis that the stress tensor at said reference point is dependent on the strains of the complete structure is assumed. Therefore, the Eringen's nonlocal elasticity theory [64] is applied and implemented on the shell model.

Firstly, a generalized model is developed for a single-walled carbon nanotube, which is then adapted onto a model for a double-walled carbon nanotube. The last requires further incorporation of the interlayer forces between the different shells on the same nanotube, also known as van der Waals forces, developed from the Lennard-Jones pair potential [81]. These van der Waals forces take into account the effect of each atom of a layer on each atom of the other layer, resulting in the coefficients that describe the van der Waals pressure on each of the layers, describing the rigidity coupling between them.

For both models, the implementation is held through the p-version finite element method, which after discretization of the displacement components, is aided by the Galerkin method to formulate the rigidity and mass matrices necessary to solve the linear dynamic problem that processes the natural frequency and mode shape results.

One last model is developed, based on the SWCNT one, with the addition of a concentrated mass. This mass is characterized for having a defined value and being applied in defined coordinates on the surface of the CNT. The implementation follows the same principles, utilizing the p-version finite element method for the discretization of displacement components, featuring the Galerkin method to deduce the finite element matrices.

1.4 Objectives

The main goal of the present work is to study the linear vibration modes of single-walled and double-walled carbon nanotubes, using the thin shell Sanders-Koiter theory and discretizing the model by the p-version finite element method, with the application of the Galerkin method to obtain the weak formulation and matrices that characterize the modal vibration problem. The influence of the nonlocal parameter on the natural frequencies and mode shapes should also be investigated, and thus intermediate tasks are defined to be completed along the study developed on this dissertation:

- Development of a generalized equivalent continuum model based on the thin shell Sanders-Koiter theory, based on Kirchhoff-Love assumptions, for a single-walled carbon nanotube;

- Adaptation of the continuum model onto a double-walled carbon nanotube, including the interlayer forces defined by van der Waals coefficients;

- Inclusion of the small scale parameter by incorporation of Eringen's nonlocal theory onto the stress components and consequently onto the equations of motion;
- Development of an equivalent continuum model that allows for inclusion of a concentrated mass on a variable and defined point on the surface of the nanotube;
- Implementation of the models by the p-version finite element method, aided by the Galerkin method to obtain the weak formulation and deduce the finite element matrices, by application of the Rodrigues' form of Legendre's orthogonal polynomials;
- Convergence and validation of the model by comparison to distinct studies and molecular dynamics simulations;
- Validation and illustration of the mode shapes associated with different parameters, boundary conditions and wave numbers;
- Calibration of the nonlocal parameter onto clamped-clamped boundary conditions case and study of its influence on different order natural frequencies;
- Study on the influence of the nonlocal parameter on the frequency ratio, mode shapes and relevance of the circumferential mode number;
- Investigation onto the dynamic behaviour of a carbon nanotube with a concentrated attached mass and prediction of natural frequency/ concentrated mass values, studying the sensitivity of the system and respective nonlocal effects;
- Study on the influence of the nonlocal parameter on the natural frequencies given for a model accounting for a concentrated mass; proposal of a calibration of the nonlocal parameter for different mass values and investigation onto a singular nonlocal parameter global influence;

1.5 Layout

This dissertation is structured in six chapters, with the first being the present introductory one, where the main objectives and motivations for the execution of the work are expressed. Regarding the following chapters, they are described as:

- **Chapter 2, Mathematical Formulation** - On this chapter, the mathematical formulation of the single-walled and double-walled carbon nanotubes continuum model is presented, based on the p-version finite element method. The establishment process of the equations of motion is detailed, stating with the Kirchhoff-Love assumptions for thin shells, and application of the Hamilton's principle to obtain the equations of motion with respect to stresses after selection of Sanders-Koiter theory. Eringen's nonlocal theory is presented and implemented. The p-version finite element method is finally used to discretize the domain and obtain the matricial formulation needed to solve the modal linear problem, resorting to the Galerkin method.
- **Chapter 3, Linear Model Validation** - Here, the developed and implemented model on *Maple* is convergence tested, by comparison to results from bibliography, in terms of different characteristic parameters and boundary conditions - clamped, free, simply-supported. The natural frequency values are, therefore, evaluated, as well as the respective mode shapes, which are also validated by comparison to referenced data. Different types of mode shapes are also presented, illustrating the versatility of the model implemented using the p-version FEM.

- **Chapter 4, Study of the nonlocal parameter influence** - On this chapter, the already validated results of the thin shell model are used to perform a study on the influence of the nonlocal parameter, adjusting the results of the developed model to MD simulations results, by proposing a nonlocal parameter calibrated value. It is then possible to conclude on the influence of this parameter for different order natural frequencies. The effect of the nonlocal parameter for different chiralities and aspect ratios is also established by studying the frequency ratio for each case, while the weight of the circumferential mode number and phenomena created on shells is discussed. Finally, the influence of the nonlocal parameter on the mode shapes is also illustrated and studied.

- **Chapter 5, Study of a CNT with an attached mass** - On this chapter, a model for a SWCNT and DWCNT with an attached concentrated mass for a defined point in the surface of the CNT is developed. With the inclusion of the Eringen's nonlocal elasticity theory, the model is implemented via p-version finite element method, discretizing the displacement components and generating the finite element matrices using the Galerkin method. The model is then tested for validation using available literature data, after which a study focusing on the dynamic behaviour of a CNT with an attached mass, regarding the relation between the natural frequencies and the mass value is performed, also investigating into the nonlocal parameter influence for nanotubes of distinct characteristics;

- **Chapter 6, Conclusions** - Finally, the main conclusions drawn from the current dissertation are presented in this final chapter. These include the main ideas from the validation, implementation and study of the nonlocal linear developed model. Lastly, the future work possibilities are also discussed, as this work leaves room for further work based on the conclusions of the dissertation and on the current research state of vibrations of carbon nanotubes, possible to be done on a wider duration of study.

Chapter 2

Mathematical Formulation

2.1 Introduction and outline

In this chapter the formulation of a continuum model for both a single-walled and double-walled carbon nanotube will be presented. The carbon nanotubes, as already discussed, are essentially a folded graphene sheet, meaning their thickness is that of the carbon atoms of the said sheet. It is therefore correct to assume a thin shell theory to describe a CNT, being single-walled or multi-walled (in the latter case, van der Waals forces between each tube will be considered and formulated).

A thin shell is defined as a three-dimensional body bounded by two closely spaced curved surfaces, the distance between the surfaces being small in comparison with the other dimensions (length and diameter). The group of points lying midway between the two surfaces is called the middle surface of the shell. The distance between the surfaces measured in the radial direction - normal to the middle surface - is called thickness of the shell at a given point. The thickness value may not be considered constant in the formulation, but a constant value yields governing equations simpler to solve, and, in the case of CNTs, it is an approximation that does not induct significant errors, as the value is related to the diameter of the atom (even though it is an estimation obtained along with the Young's modulus value) and initial deformation in the curvature is neglected.

Shells may be regarded as a generalization of a flat plate, as inversely a flat plate may be a case of a shell with no curvature. Many theories approach shells exactly as the first situation, as shells present a very large radius - or a very small curvature - reason why they are designated shallow shells. Considerations such as a linear elasticity with isotropic and homogeneous materials are assumed (having been identified for both plates [74] and shells [73], revealing a relatively small significance compared to anisotropic models, even though the latter case was deemed relevant for certain cases, for example CNTs under tension-twisting [82, 83]) along with small displacements - for linear behaviour. Nonlinear behaviour may come from considerable displacements that revoke the linearly elastic material assumption, as well as from geometrical basis [10]. Shear deformation and rotary inertia effects are also neglected, along with initial stress and deformation [84].

Among different thin shell theories, a specific one is analysed and chosen for the present dissertation, specially regarding its documented behaviour in nonlinear dynamic domain, as for linear motions the difference between theories as Flügge's, Donnell's or Sanders-Koiter, for example, is not significant. Regarding the neglect of the thickness in early stages of the formulation, more precisely in the stress equations, Sanders-Koiter's thin shell theory is applied.

A p-version finite element model will be formulated for SWCNT and DWCNT in the present chapter. Logically organized regarding the order of development, it is necessary to enunciate the Kirchhoff-Love's principles, before presenting the general displacement field and strain field. Then, the equations of motion are calculated along with the stress equations, with the aid of the Hamilton's Principle. The next section presents the foundation of the nonlocal Eringen's theory of elasticity, introducing the small-scale parameters into the equations of motion. Then, the p-version method is presented, followed by the the application of the Galerkin method, transforming the differential equations of motion into their weak formulation, respectively in two distinct and consecutive sections for a SWCNT and DWCNT case.

2.2 Kirchhoff-Love assumptions

Before heading to the main theory applied in CNTs in the present dissertation, it is important to describe its core assumptions and ideas behind a thin shell theory.

The Kirchhoff's hypothesis are defined for plate bending, stating that normals to the undeformed middle surface remain straight and normal to the deformed middle surface and suffer no extension. This principle is parallel to the one applied in Euler-Bernoulli's thin beam theory, which is only valid for thin beams where the thickness is very small compared to the length (raises problems for thicker beams, in which Timoshenko's theory is necessary). Thus, the thin plates yield the following hypothesis [85]:

$$\begin{cases} \gamma_{xz} = 0 \\ \gamma_{yz} = 0 \\ \varepsilon_{zz} = 0 \end{cases} \tag{2.1}$$

and therefore, from the Hooke's law, transverse shear stresses come as:

$$\sigma_{xz} = \sigma_{yz} = 0 \tag{2.2}$$

Later, Love adapted the hypothesis described in Equation (2.1) onto thin shells [85], defined as the Kirchhoff-Love hypothesis, yielding in cylindrical coordinates:

$$\begin{cases} \gamma_{xz} = 0 \\ \gamma_{\theta z} = 0 \\ \varepsilon_{zz} = 0 \end{cases} \tag{2.3}$$

and therefore transverse shear stresses come as:

$$\sigma_{xz} = \sigma_{\theta z} = 0 \tag{2.4}$$

Love's assumptions come specifically for the classical theory of small displacements of thin shells [84]:

1. "The thickness of the shell is small compared with the other dimensions, for example, the smallest radius of curvature of the middle surface of the shell."

2. "Strains and displacements are sufficiently small so that the quantities of second and higher-order magnitude in the strain-displacement relations may be neglected in comparison with the first-order terms."
3. "The transverse normal stress is small compared with the other normal stress components and may be neglected."

These three assumptions along with the Kirchhoff-Love assumption, also named the fourth assumption of Love, give rise to what Love called his "first approximation" shell theory. It is important to understand that these approximations allow for the formulation of the linear field model, given the nonlinear behaviour requires extra steps [84].

The first assumption defines what the name "thin shells" resembles, setting stage for the whole theory. Denoting the thickness of the shell by h and the radius of curvature by R, it will be convenient at numerous instances in the subsequent derivation of the shell theory to neglect higher powers of z/R or h/R in comparison with unity. The second assumption allows one to refer all calculations to the original configuration of the shell and ensures that the differential equations come as linear. The third assumption and the Kirchhoff's hypothesis deal with the constitutive equations of thin elastic shells, assuming a special type of orthotropy when isotropy is still not considered, so that $E_z = G_{xz} = G_{\theta z} = \infty$ and $\nu_{xz} = \nu_{\theta z} = 0$ [84].

2.3 Sanders-Koiter thin shell theory

Following Sanders procedure [77, 86] in order to apply the theory to a cylindrical shell, and considering the Cylindrical coordinates (x,θ,z), comes the displacement field as:

$$u(x,\theta,z,t) = u^0(x,\theta,t) - z\frac{\partial w^0(x,\theta,t)}{\partial x} \tag{2.5a}$$

$$v(x,\theta,z,t) = v^0(x,\theta,t) - \frac{z}{R}\frac{\partial w^0(x,\theta,t)}{\partial \theta} \tag{2.5b}$$

$$w(x,\theta,z,t) = w^0(x,\theta,t) \tag{2.5c}$$

where $u^0(x,\theta,t)$, $v^0(x,\theta,t)$ and $w^0(x,\theta,t)$ refer to the displacement components in the middle surface, Ω, as is represented in Figure 2.1.

And thus, according to Amabili [77], the strain field from Sanders-Koiter shell theory comes expressed as the middle surface strains and displacement projections as follows:

$$\varepsilon_{x,0} = \frac{\partial u^0}{\partial x} \tag{2.6a}$$

$$\varepsilon_{\theta,0} = \frac{1}{R}\frac{\partial v^0}{\partial \theta} + \frac{w^0}{R} \tag{2.6b}$$

$$\gamma_{x\theta,0} = \frac{1}{R}\frac{\partial u^0}{\partial \theta} + \frac{\partial v^0}{\partial x} \tag{2.6c}$$

$$k_x = -\frac{\partial^2 w^0}{\partial x^2} \tag{2.6d}$$

$$k_\theta = \frac{1}{R^2}\frac{\partial v^0}{\partial \theta} - \frac{1}{R^2}\frac{\partial^2 w^0}{\partial \theta^2} \tag{2.6e}$$

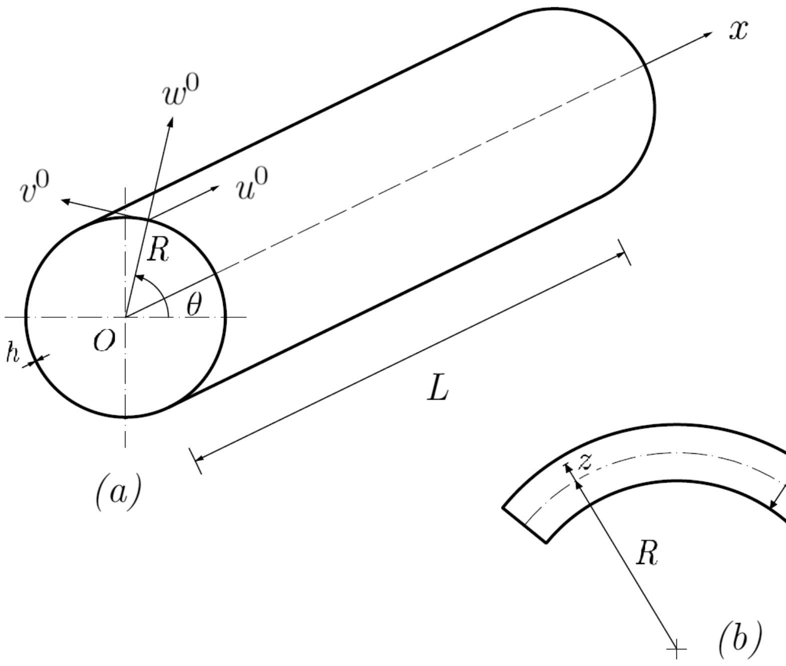

Figure 2.1: Geometry of the circular cylindrical shell: (a) complete view and (b) cross-section view

$$k_{x\theta} = -2\frac{1}{R}\frac{\partial^2 w^0}{\partial x \partial\theta} + \frac{1}{2R}\left(3\frac{\partial v^0}{\partial x} - \frac{1}{R}\frac{\partial u^0}{\partial\theta}\right) \tag{2.6f}$$

being the strains ε_{xx}, $\varepsilon_{\theta\theta}$, $\gamma_{x\theta}$ of the point at z distance from the middle surface given by:

$$\varepsilon_{xx} = \varepsilon_{x,0} + zk_x \tag{2.7a}$$

$$\varepsilon_{\theta\theta} = \varepsilon_{\theta,0} + zk_\theta \tag{2.7b}$$

$$\gamma_{x\theta} = \gamma_{x\theta,0} + zk_{x\theta} \tag{2.7c}$$

As already explained and stated in (2.3) the transverse shear strains are null and are not taken into account for the next step: calculating the equations of motion.

Invoking Hamilton's Principle, the total variation of the mechanical energy over a period of time is null:

$$\int_{t_1}^{t_2} (\delta K - \delta U + \delta W)\, dt = 0 \tag{2.8}$$

being δK the variation of kinetic energy, δU the variation of potential energy, and δW the virtual work of forces that either do not have a potential function (non-conservative forces) or whose potential function is not included in U. For the sake of simplicity, these forces are labelled *non-conservative*.

The variation of potential energy δU is given by:

$$\begin{aligned}
\delta U &= \int_\Omega \int_{-\frac{h}{2}}^{\frac{h}{2}} \sigma_{xx}\delta\varepsilon_{xx} + \sigma_{\theta\theta}\delta\varepsilon_{\theta\theta} + \tau_{x\theta}\delta\gamma_{x\theta}\ dz\ d\Omega \\
&= \int_\Omega \int_{-\frac{h}{2}}^{\frac{h}{2}} \sigma_{xx}(\delta\varepsilon_{x,0} + z\delta k_x) + \sigma_{\theta\theta}(\delta\varepsilon_{\theta\theta} + z\delta k_\theta) + \tau_{x\theta}(\delta\gamma_{x\theta,0} + z\delta k_{x\theta})\ dz\ d\Omega
\end{aligned} \tag{2.9}$$

Given the internal membrane forces and moments (also known as stress resultants) dependencies on the general stress field, they can be expressed as:

$$\{N_{xx}, N_{\theta\theta}, N_{x\theta}, M_{xx}, M_{\theta\theta}, M_{x\theta}\} = \int_{-\frac{h}{2}}^{\frac{h}{2}} \left(1 - \frac{z}{R}\right)\{\sigma_{xx}, \sigma_{\theta\theta}, \tau_{x\theta}, z\sigma_{xx}, z\sigma_{\theta\theta}, z\tau_{x\theta}\}\ dz \tag{2.10}$$

Thus, performing the substitution of Equation (2.10) into Equation (2.9), while neglecting the term $1 - z/R$ by approximating $1 - z/R \approx 1$ and integrating along the shell, yields the following form of the variation of the potential energy:

$$\delta U = \underbrace{\int_0^{2\pi}\int_0^l}_{\int_\Omega} (N_{xx}\delta\varepsilon_{x,0} + N_{\theta\theta}\delta\varepsilon_{\theta\theta} + N_{x\theta}\delta\gamma_{x\theta,0} + M_{xx}\delta k_x + M_{\theta\theta}\delta k_\theta + M_{x\theta}\delta k_{x\theta})\ \underbrace{R\ \mathrm{d}x\ \mathrm{d}\theta}_{d\Omega} \tag{2.11}$$

Heading now to the variation of the kinetic energy, it comes that:

$$\begin{aligned}
\delta K &= \int_0^{2\pi}\int_0^l\int_{-\frac{h}{2}}^{\frac{h}{2}} \rho(\dot{u}\delta\dot{u} + \dot{v}\delta\dot{v} + \dot{w}\delta\dot{w})\ dz\ R\ \mathrm{d}x\ \mathrm{d}\theta \\
&= \int_0^{2\pi}\int_0^l\int_{-\frac{h}{2}}^{\frac{h}{2}} \rho\Bigg[\left(\dot{u}^0 - z\frac{\partial\dot{w}^0}{\partial x}\right)\left(\delta\dot{u}^0 - z\frac{\partial\delta\dot{w}^0}{\partial x}\right) + \left(\dot{v}^0 - \frac{z}{R}\frac{\partial\dot{w}^0}{\partial\theta}\right)\left(\delta\dot{v}^0 - \frac{z}{R}\frac{\partial\delta\dot{w}^0}{\partial\theta}\right) \\
&\qquad + \dot{w}^0\delta\dot{w}^0\Bigg]\ R\ \mathrm{d}x\ \mathrm{d}\theta \\
&= \int_0^{2\pi}\int_0^l \rho\left[h\,\dot{u}^0\delta\dot{u}^0 + \frac{h^3}{12}\frac{\partial\dot{w}^0}{\partial x}\frac{\partial}{\partial x}(\delta\dot{w}^0) + h\,\dot{v}^0\delta\dot{v}^0 + \frac{h^3}{12}\frac{1}{R^2}\frac{\partial\dot{w}^0}{\partial\theta}\frac{\partial}{\partial\theta}(\delta\dot{w}^0) + h\,\dot{w}^0\delta\dot{w}^0\right]\ R\ \mathrm{d}x\ \mathrm{d}\theta \\
&= \int_0^{2\pi}\int_0^l \rho h\left[\dot{u}^0\delta\dot{u}^0 + \dot{v}^0\delta\dot{v}^0 + \dot{w}^0\delta\dot{w}^0\right] + \frac{\rho h^3}{12}\left[\frac{\partial\dot{w}^0}{\partial x}\frac{\partial}{\partial x}(\delta\dot{w}^0) + \frac{1}{R^2}\frac{\partial\dot{w}^0}{\partial\theta}\frac{\partial}{\partial\theta}(\delta\dot{w}^0)\right]\ R\ \mathrm{d}x\ \mathrm{d}\theta
\end{aligned} \tag{2.12}$$

where $\dot{u}^0$, $\dot{v}^0$ and $\dot{w}^0$ indicates the velocity in the respective direction, in an arbitrary point, according to Figure 2.1, as $\delta\dot{u}^0$, $\delta\dot{v}^0$ and $\delta\dot{w}^0$ represent their respective variation.

Lastly, defining the variation of the work of the external forces which will be the only non-conservative forces per surface area considered in this derivation, comes:

$$\delta W = \int_0^{2\pi}\int_0^l (p_x\delta u^0 + p_y\delta v^0 + q\delta w^0)\ R\ \mathrm{d}x\ \mathrm{d}\theta \tag{2.13}$$

Before substituting the respective equations of variation of potential energy, kinetic energy, and work of external forces, it is illustrated in the following equations the procedure of integration by parts and consequent isolation of the variational of displacement (removing the derivatives associated with it), by substituting only the first term of each variation of energy in the Hamilton's principle, as an example, comes:

$$\int_{t_1}^{t_2} \underbrace{\int_\Omega \rho h \dot{u}^0 \delta \dot{u}^0 \, d\Omega}_{(1)} - \underbrace{\int_\Omega N_{xx} \delta\left(\frac{\partial u^0}{\partial x}\right) d\Omega}_{(2)} + \int_\Omega p_x \delta u^0 \, d\Omega \; dt \tag{2.14}$$

$$\begin{aligned}
(1):\; \int_{t_1}^{t_2}\int_\Omega \rho h\, \dot{u}^0 \delta \dot{u}^0 \, d\Omega &= \int_{t_1}^{t_2}\int_\Omega \rho h\, \dot{u}^0 \frac{d}{dt}(\delta u^0)\, d\Omega \\
&= \underbrace{\int_\Omega \rho h\, \dot{u}^0\, \delta \dot{u}^0 \, d\Omega \bigg|_{t_1}^{t_2}}_{=0,\, as\, \delta u^0(t_2)=\delta u^0(t_1)=0} - \int_{t_1}^{t_2}\int_\Omega \rho h\, \ddot{u}^0\, \delta u^0 \, d\Omega \, dt \\
&= -\int_{t_1}^{t_2}\int_\Omega \rho h\, \ddot{u}^0\, \delta u^0 d\Omega \, dt
\end{aligned} \tag{2.15a}$$

$$\begin{aligned}
(2):\; -\int_{t_1}^{t_2}\int_\Omega N_{xx} \delta\left(\frac{\partial u^0}{\partial x}\right) d\Omega &= -\int_{t_1}^{t_2}\int_\Omega N_{xx} \frac{\partial}{\partial x}\delta u^0 \, d\Omega \\
&= \underbrace{-\int_\Omega N_{xx} \delta u^0 \, d\Omega \bigg|_{t_1}^{t_2}}_{=0,\, as\, \delta u^0(t_2)=\delta u^0(t_1)=0} + \int_{t_1}^{t_2}\int_\Omega \frac{\partial N_{xx}}{\partial x}\delta u^0 \, d\Omega \, dt \\
&= \int_{t_1}^{t_2}\int_\Omega \frac{\partial N_{xx}}{\partial x}\delta u^0 \, d\Omega \, dt
\end{aligned} \tag{2.15b}$$

where $\ddot{u}^0$, $\ddot{v}^0$ and $\ddot{w}^0$ indicate the acceleration components in their respective direction, according to Figure 2.1.

Introducing Equations (2.11), (2.12) and (2.13) into the Hamilton's Principle equation (2.8), and substituting equations (2.6) into the respective strains from the variation of potential energy, the following expression is found:

$$\begin{aligned}
0 &= \int_{t_1}^{t_2} (\delta K - \delta U + \delta W) \; dt \\
&= \int_{t_1}^{t_2} \Bigg[\int_\Omega \rho h \big[\dot{u}^0 \delta \dot{u}^0 + \dot{v}^0 \delta \dot{v}^0 + \dot{w}^0 \delta \dot{w}^0 \big] + \frac{\rho h^3}{12} \left[\frac{\partial \dot{w}^0}{\partial x} \frac{\partial}{\partial x} (\delta \dot{w}^0) + \frac{1}{R^2} \frac{\partial \dot{w}^0}{\partial \theta} \frac{\partial}{\partial \theta} (\delta \dot{w}^0) \right] d\Omega \\
&\quad - \int_\Omega \Bigg[N_{xx}\, \delta\left(\frac{\partial u^0}{\partial x}\right) + N_{\theta\theta}\, \delta\left(\frac{1}{R}\frac{\partial v^0}{\partial \theta} + \frac{w^0}{R}\right) + N_{x\theta}\, \delta\left(\frac{1}{R}\frac{\partial u^0}{\partial \theta} + \frac{\partial v^0}{\partial x}\right) + M_{xx}\, \delta\left(-\frac{\partial^2 w^0}{\partial x^2}\right) \\
&\qquad + M_{\theta\theta}\, \delta\left(\frac{1}{R^2}\frac{\partial v^0}{\partial \theta} - \frac{1}{R^2}\frac{\partial^2 w^0}{\partial \theta^2}\right) + M_{x\theta}\, \delta\left(-2\frac{1}{R}\frac{\partial^2 w^0}{\partial x \partial \theta} + \frac{1}{2R}\left(3\frac{\partial v^0}{\partial x} - \frac{1}{R}\frac{\partial u^0}{\partial \theta}\right)\right) \Bigg] d\Omega \\
&\qquad\qquad + \int_\Omega \left[p_x \delta u^0 + p_y \delta v^0 + q \delta w^0 \right] d\Omega \Bigg] \, dt
\end{aligned} \tag{2.16}$$

Developing the last equation, integrating by parts and performing the permutation of the variational in the terms of the variation of kinetic and potential energy, following the procedure of (2.15), comes:

$$
\begin{aligned}
\int_{t_1}^{t_2} \Bigg[&- \int_{\Omega} \rho h[\ddot{u}^0 \delta u^0 + \ddot{v}^0 \delta v^0 + \ddot{w}^0 \delta w^0] + \frac{\rho h^3}{12}\left[\frac{\partial^2 \ddot{w}^0}{\partial x^2}\,\delta w^0 + \frac{1}{R^2}\frac{\partial^2 \ddot{w}^0}{\partial \theta^2}\,\delta w^0\right] d\Omega \\
&+ \int_{\Omega} \Bigg[\frac{\partial N_{xx}}{\partial x}\delta u_0 + \frac{1}{R}\frac{\partial N_{\theta\theta}}{\partial \theta}\delta v_0 - \frac{N_{\theta\theta}}{R}\delta w_0 + \frac{1}{R}\frac{\partial N_{x\theta}}{\partial \theta}\delta u_0 + \frac{\partial N_{x\theta}}{\partial x}\delta v_0 + \frac{\partial^2 M_{xx}}{\partial x^2}\delta w_0 \\
&+ \frac{1}{R^2}\frac{\partial M_{\theta\theta}}{\partial \theta}\delta v_0 + \frac{1}{R^2}\frac{\partial M_{\theta\theta}}{\partial \theta}\delta w_0 + \frac{2}{R}\frac{\partial^2 M_{x\theta}}{\partial x \partial \theta}\delta w_0 + \frac{3}{2R}\frac{\partial M_{x\theta}}{\partial x}\delta v_0 - \frac{1}{2R^2}\frac{\partial M_{x\theta}}{\partial \theta}\delta u_0 \Bigg] d\Omega \\
&+ \int_{\Omega} \left[p_x \delta u^0 + p_y \delta v^0 + q \delta w^0\right] d\Omega \Bigg] dt = 0
\end{aligned}
\tag{2.17}
$$

Selecting the terms affected by $\delta\dot{u}^0$, $\delta\dot{v}^0$ and $\delta\dot{w}^0$ for each equation, and considering that along the domain $[t_1, t_2]$, as $\delta\dot{u}^0$, $\delta\dot{v}^0$ and $\delta\dot{w}^0$ can be replaced by any arbitrary value inside the domain, they are set to zero, and the equations of motion come as:

$$
-\rho h \ddot{u}^0 + \frac{\partial N_{xx}}{\partial x} + \frac{1}{R}\frac{\partial N_{x\theta}}{\partial \theta} - \frac{1}{2R^2}\frac{\partial M_{x\theta}}{\partial \theta} + p_x = 0 \tag{2.18}
$$

$$
-\rho h \ddot{v}^0 + \frac{1}{R}\frac{\partial N_{\theta\theta}}{\partial \theta} + \frac{\partial N_{x\theta}}{\partial x} + \frac{1}{R^2}\frac{\partial M_{\theta\theta}}{\partial \theta} + \frac{3}{2R}\frac{\partial M_{x\theta}}{\partial x} + p_y = 0 \tag{2.19}
$$

$$
-\rho h \ddot{w}^0 + \underbrace{\frac{\rho h^3}{12}\left[\frac{\partial^2 \ddot{w}^0}{\partial x^2} + \frac{1}{R^2}\frac{\partial^2 \ddot{w}^0}{\partial \theta^2}\right]}_{rotary\ inertia} - \frac{N_{\theta\theta}}{R} + \frac{\partial^2 M_{xx}}{\partial x^2} + \frac{1}{R^2}\frac{\partial M_{\theta\theta}}{\partial \theta} + \frac{2}{R}\frac{\partial^2 M_{x\theta}}{\partial x \partial \theta} + q = 0 \tag{2.20}
$$

Neglecting the rotary inertia from Equation (2.20) as these terms only affect higher frequencies and have little influence on the CNTs vibration, while also setting the external forces per surface area in the u, v, w axial, circumferential and radial directions respectively equal to zero, as only free vibrations will be studied, and lastly, swapping the signals in the equations, in order to later arrive at a positive definite mass matrix and positive semidefinite stiffness matrix, maintaining mechanical coherence, come the final equations of motion with dependence on the forces and moments:

$$
\rho h \ddot{u}^0 - \frac{\partial N_{xx}}{\partial x} - \frac{1}{R}\frac{\partial N_{x\theta}}{\partial \theta} + \frac{1}{2R^2}\frac{\partial M_{x\theta}}{\partial \theta} = 0 \tag{2.21}
$$

$$
\rho h \ddot{v}^0 - \frac{1}{R}\frac{\partial N_{\theta\theta}}{\partial \theta} - \frac{\partial N_{x\theta}}{\partial x} - \frac{1}{R^2}\frac{\partial M_{\theta\theta}}{\partial \theta} - \frac{3}{2R}\frac{\partial M_{x\theta}}{\partial x} = 0 \tag{2.22}
$$

$$
\rho h \ddot{w}^0 + \frac{N_{\theta\theta}}{R} - \frac{\partial^2 M_{xx}}{\partial x^2} - \frac{1}{R^2}\frac{\partial M_{\theta\theta}}{\partial \theta} - \frac{2}{R}\frac{\partial^2 M_{x\theta}}{\partial x \partial \theta} = 0 \tag{2.23}
$$

Regarding the dependence of the forces and moments on the influence of displacements (and related partial derivatives) coming from the theory of elasticity, it is important to define these relations based on classical elasticity. Thus, based on Equation (2.10), and considering an isotropic material, as already stated, comes:

$$\sigma_{xx} = \frac{E}{1-\nu^2}\left(\varepsilon_{xx} + \nu\varepsilon_{\theta\theta}\right) \tag{2.24a}$$

$$\sigma_{\theta\theta} = \frac{E}{1-\nu^2}\left(\varepsilon_{\theta\theta} + \nu\varepsilon_{xx}\right) \tag{2.24b}$$

$$\tau_{x\theta} = \frac{E}{2(1+\nu)}\,\gamma_{x\theta} \tag{2.24c}$$

And consequently, integrating along the thickness comes:

$$\begin{aligned} N_{xx} &= \int_{-\frac{h}{2}}^{\frac{h}{2}} \sigma_{xx}\,dz = \int_{-\frac{h}{2}}^{\frac{h}{2}} \frac{E}{1-\nu^2}\left(\varepsilon_{xx} + \nu\varepsilon_{\theta\theta}\right)dz \\ &= \int_{-\frac{h}{2}}^{\frac{h}{2}} \frac{E}{1-\nu^2}\left(\frac{\partial u^0}{\partial x} - z\frac{\partial^2 w^0}{\partial x^2} + \nu\left[\frac{1}{R}\frac{\partial v^0}{\partial \theta} + \frac{w^0}{R} + z\left(\frac{1}{R^2}\frac{\partial v^0}{\partial \theta} - \frac{1}{R^2}\frac{\partial^2 w^0}{\partial \theta^2}\right)\right]\right)dz \\ &= \frac{Eh}{1-\nu^2}\left[\varepsilon_{x,0} + \nu\,\varepsilon_{\theta,0}\right] \\ &= \frac{Eh}{1-\nu^2}\left[\frac{\partial u^0}{\partial x} + \nu\left(\frac{1}{R}\frac{\partial v^0}{\partial \theta} + \frac{w^0}{R}\right)\right] \end{aligned} \tag{2.25a}$$

$$N_{\theta\theta} = \int_{-\frac{h}{2}}^{\frac{h}{2}} \sigma_{\theta\theta}\,dz = \int_{-\frac{h}{2}}^{\frac{h}{2}} \frac{E}{1-\nu^2}\left(\varepsilon_{\theta\theta} + \nu\varepsilon_{xx}\right)dz = \frac{Eh}{1-\nu^2}\left(\frac{1}{R}\frac{\partial v^0}{\partial \theta} + \frac{w^0}{R} + \nu\frac{\partial u^0}{\partial x}\right) \tag{2.25b}$$

$$N_{x\theta} = \int_{-\frac{h}{2}}^{\frac{h}{2}} \tau_{x\theta}\,dz = \int_{-\frac{h}{2}}^{\frac{h}{2}} \frac{E}{2(1+\nu)}\,\gamma_{x\theta}dz = \frac{Eh}{2(1+\nu)}\left(\frac{1}{R}\frac{\partial u^0}{\partial \theta} + \frac{\partial v^0}{\partial x}\right) \tag{2.25c}$$

$$\begin{aligned} M_{xx} &= \int_{-\frac{h}{2}}^{\frac{h}{2}} \sigma_{xx} z\,dz = \int_{-\frac{h}{2}}^{\frac{h}{2}} \frac{E}{1-\nu^2}\left(\varepsilon_{xx} + \nu\varepsilon_{\theta\theta}\right) z\,dz = \\ &= \frac{Eh^3}{12(1-\nu^2)}\left(-\frac{\partial^2 w^0}{\partial x^2} + \nu\,\frac{1}{R^2}\frac{\partial v^0}{\partial \theta} - \nu\,\frac{1}{R^2}\frac{\partial^2 w^0}{\partial \theta^2}\right) \end{aligned} \tag{2.25d}$$

$$\begin{aligned} M_{\theta\theta} &= \int_{-\frac{h}{2}}^{\frac{h}{2}} \sigma_{\theta\theta} z\,dz = \int_{-\frac{h}{2}}^{\frac{h}{2}} \frac{E}{1-\nu^2}\left(\varepsilon_{\theta\theta} + \nu\varepsilon_{xx}\right) z\,dz = \\ &= \frac{Eh^3}{12(1-\nu^2)}\left(\frac{1}{R^2}\frac{\partial v^0}{\partial \theta} - \frac{1}{R^2}\frac{\partial^2 w^0}{\partial \theta^2} - \nu\,\frac{\partial^2 w^0}{\partial x^2}\right) \end{aligned} \tag{2.25e}$$

$$\begin{aligned} M_{x\theta} &= \int_{-\frac{h}{2}}^{\frac{h}{2}} \tau_{x\theta} z\,dz = \int_{-\frac{h}{2}}^{\frac{h}{2}} \frac{E}{2(1+\nu)}\,\gamma_{x\theta}\,z\,dz = \\ &= \frac{Eh^3}{24(1+\nu)}\left(-\frac{2}{R}\frac{\partial^2 w^0}{\partial x\partial \theta} + \frac{3}{2R}\frac{\partial v^0}{\partial x} - \frac{1}{2R^2}\frac{\partial u^0}{\partial \theta}\right) \end{aligned} \tag{2.25f}$$

2.4 Eringen's Nonlocal elasticity theory

Eringen developed a nonlocal elasticity theory [64], including the small scale effect and whole body-range atomic interactions relevant in carbon nanotubes, as previously discussed. In fact, this theory generally leads to a continuum model that is able converge closer to molecular dynamics simulations, as it considers that the stress at a reference point x in the body depends not only on the strains at x but also on strains at all the other points of the body, which is in agreement with phonon dispersion experimental observations [64]. When the effects of strains at other points other than x are neglected, the classical theory of elasticity is obtained. Thus, the linear theory is expressed as:

$$t_{kl,k} + \rho\,(f_l - \ddot{u}_l) = 0 \tag{2.26}$$

as $t_{kl,k}$ indicates the stress tensor, ρ indicates the mass density, f_l indicates the body force density and $\ddot{u}_l$ designates the displacement vector at a reference point x in the body, at a time t. The stress tensor $t_{kl,k}$ can be expanded and defined as:

$$t_{kl,k} = \int_V \alpha\,(|x' - x|, \tau)\sigma_{kl}(x')\,dv\,(x') \tag{2.27}$$

as $\alpha(|x'-x|,\tau)$ designates the nonlocal kernel function, dependent on $\tau = e_0 a/l$, with a being an internal characteristic length (lattice parameter or granular distance, for example), l an external characteristic length and e_0 a constant appropriate to each material.$\sigma_{kl}(x')$ designates the macroscopic/classical/local stress tensor at x', which is related to the linear strain tensor at any point x', $e_{kl}(x')$. It is important to note that this nonlocal elasticity theory has great relevance at small scales, as it is size-dependent and for large dimensions ($\tau \rightarrow 0$) the influence of the nonlocal parameter is expected to fade and be negligible.

Further on it is necessary to solve the Equation (2.27), which is a hard process, specially for three-dimensional problems. Thus, it was found that assuming that the nonlocal kernel function was dependent on a Green's function of a linear differential operator, still unknown, as seen in Equation (2.28), lead to a prompt solution of the imposed problem:

$$\mathcal{L}\,\alpha\,(|x' - x|, \tau) = \delta(|x' - x|) \tag{2.28}$$

This equation can be simplified into:

$$\mathcal{L}\,t_{kl} = \sigma_{kl} \tag{2.29}$$

Imposing the previous equation in Equation (2.26) and assuming the differential operator $\mathcal{L}$ has constant coefficients comes the following:

$$\sigma_{kl,k} + \mathcal{L}\,\rho\,(f_l - \ddot{u}_l) = 0 \tag{2.30}$$

And finally, by equating the lattice models with the phonon dispersion curves, while proving the accuracy of the proposed differential operator by an approximation of atomic dispersion relations, the following is taken as definition:

$$\mathcal{L} = 1 - (e_0 a)^2 \nabla^2 \tag{2.31}$$

As can also be expressed by substituting in Equation (2.29) [64]:

$$\left[\,1-(e_0a)^2\nabla^2\,\right]t_{kl}=\sigma_{kl} \tag{2.32}$$

Necessarily implying that the nonlocal parameter is affected onto the classical stress tensor, dependent on the Young's modulus and strain tensor. It is important to note that a specific value for e_0 was given by Eringen [64] ($e_0 = 0.39$), although no experiments have revealed a constant and transversal value for CNTs. As the a parameter is assumed to be independent of the length, diameter and chirality of CNTs, a value is proposed in [30], $a = 0.142\,\mathrm{nm}$, with e_0 suffering calibration by comparison to MD simulations, according to each case, as discussed further on this dissertation. With the nonlocal theory in consideration, more specifically Equation (2.32), it is applied to the components of forces and moments equations (2.25), and for homogeneous and isotropic solids, come the following equations:

$$N_{xx}-(e_0a)^2\,\nabla^2N_{xx}=\frac{Eh}{1-\nu^2}\left[\frac{\partial u^0}{\partial x}+\nu\left(\frac{1}{R}\frac{\partial v^0}{\partial\theta}+\frac{w^0}{R}\right)\right] \tag{2.33a}$$

$$N_{\theta\theta}-(e_0a)^2\,\nabla^2N_{\theta\theta}=\frac{Eh}{1-\nu^2}\left(\frac{1}{R}\frac{\partial v^0}{\partial\theta}+\frac{w^0}{R}+\nu\frac{\partial u^0}{\partial x}\right) \tag{2.33b}$$

$$N_{x\theta}-(e_0a)^2\,\nabla^2N_{x\theta}=\frac{Eh}{2(1+\nu)}\left(\frac{1}{R}\frac{\partial u^0}{\partial\theta}+\frac{\partial v^0}{\partial x}\right) \tag{2.33c}$$

$$M_{xx}-(e_0a)^2\,\nabla^2M_{xx}=\frac{Eh^3}{12(1-\nu^2)}\left(-\frac{\partial^2w^0}{\partial x^2}+\nu\,\frac{1}{R^2}\frac{\partial v^0}{\partial\theta}-\nu\,\frac{1}{R^2}\frac{\partial^2w^0}{\partial\theta^2}\right) \tag{2.33d}$$

$$M_{\theta\theta}-(e_0a)^2\,\nabla^2M_{\theta\theta}=\frac{Eh^3}{12(1-\nu^2)}\left(\frac{1}{R^2}\frac{\partial v^0}{\partial\theta}-\frac{1}{R^2}\frac{\partial^2w^0}{\partial\theta^2}-\nu\,\frac{\partial^2w^0}{\partial x^2}\right) \tag{2.33e}$$

$$M_{x\theta}-(e_0a)^2\,\nabla^2M_{x\theta}=\frac{Eh^3}{24(1+\nu)}\left(-\frac{2}{R}\frac{\partial^2w^0}{\partial x\partial\theta}+\frac{3}{2R}\frac{\partial v^0}{\partial x}-\frac{1}{2R^2}\frac{\partial u^0}{\partial\theta}\right) \tag{2.33f}$$

where in the case of a cylindrical shell comes:

$$\nabla^2=\frac{\partial^2}{\partial x^2}+\frac{1}{R^2}\frac{\partial^2}{\partial\theta^2} \tag{2.34}$$

Thus, applying the linear differential operator $\mathcal{L}$ onto Equations (2.21), (2.22) and (2.23), taking into account the already established components of forces and moments affected by the nonlocal elasticity theory, expressed in the equations (2.33), comes:

$$\begin{aligned}\rho h\left(1-(e_0a)^2\nabla^2\right)\ddot{u}^0-\frac{Eh}{1-\nu^2}\left[\frac{\partial^2u^0}{\partial x^2}+\frac{1-\nu}{2}\frac{1}{R^2}\frac{\partial^2u^0}{\partial\theta^2}+\nu\,\frac{1}{R}\frac{\partial w^0}{\partial x}+\frac{1+\nu}{2}\frac{1}{R}\frac{\partial^2v^0}{\partial x\partial\theta}\right]&\\ -\frac{Eh^3}{24(1+\nu)R^3}\left[\frac{\partial^3w^0}{\partial x\partial\theta^2}-\frac{3}{4}\frac{\partial^2v^0}{\partial x\partial\theta}+\frac{1}{4R}\frac{\partial^2u^0}{\partial\theta^2}\right]&=0\end{aligned} \tag{2.35}$$

$$
\begin{aligned}
\rho h\left(1-(e_0a)^2\nabla^2\right)\ddot{v}^0 &- \frac{Eh}{1-\nu^2}\left[\frac{1}{R^2}\frac{\partial^2 v^0}{\partial\theta^2}+\frac{1}{R^2}\frac{\partial w^0}{\partial\theta}+\frac{1+\nu}{2}\frac{1}{R}\frac{\partial^2 u^0}{\partial x\partial\theta}+\frac{1-\nu}{2}\frac{\partial^2 v^0}{\partial x^2}\right]\\
&- \frac{Eh^3}{12(1-\nu^2)}\left[\frac{1}{R^4}\frac{\partial^2 v^0}{\partial\theta^2}-\frac{1}{R^4}\frac{\partial^3 w^0}{\partial\theta^3}-\frac{3-\nu}{2}\frac{1}{R^2}\frac{\partial^3 w^0}{\partial x^2\partial\theta}\right.\\
&\qquad\left.+\frac{9(1-\nu)}{8R^2}\frac{\partial^2 v^0}{\partial x^2}-\frac{3(1-\nu)}{8R^3}\frac{\partial^2 u^0}{\partial x\partial\theta}\right]=0
\end{aligned}
\tag{2.36}
$$

$$
\begin{aligned}
\rho h\left(1-(e_0a)^2\nabla^2\right)\ddot{w}^0 &+ \frac{Eh}{1-\nu^2}\left[\frac{1}{R^2}\frac{\partial v^0}{\partial\theta}+\frac{w^0}{R^2}+\nu\frac{1}{R}\frac{\partial u^0}{\partial x}\right]+\frac{Eh^3}{12(1-\nu^2)}\left[\frac{\partial^4 w^0}{\partial x^4}\right.\\
&\left.-\frac{3-\nu}{2R^2}\frac{\partial^3 v^0}{\partial x^2\partial\theta}+\frac{2}{R^2}\frac{\partial^4 w^0}{\partial x^2\partial\theta^2}-\frac{1}{R^4}\frac{\partial^3 v^0}{\partial\theta^3}+\frac{1}{R^4}\frac{\partial^4 w^0}{\partial\theta^4}+\frac{1-\nu}{2}\frac{1}{R^3}\frac{\partial^3 u^0}{\partial x\partial\theta^2}\right]=0
\end{aligned}
\tag{2.37}
$$

These equations are denominated equations of motion (in respect to displacements), and are the three main equations that describe the thin shell. In order to apply them and extract a weak formulation, further work is presented on the next sections.

2.5 Single-walled carbon nanotube

2.5.1 The *p*-version Finite Element Method

Discretization of displacement components

Two main finite element method version are used to analyze a structure and refine its solution convergence. The first and most common is the h-version finite element method, which principle sets on varying the number of elements of an object, increasing them (refining the mesh) to improve the results accuracy. Here, the displacement and strain field of a single element is not the target of variation, as the size of the elements decreases with the increase of number of elements. The other viable method is the p-version finite element method, that typically uses a small number of elements, while relying on a higher number of shape functions (increasing the order of the polynomials, if the shape functions are, in fact, polynomials, which is often the case) and generalized coordinates to improve the accuracy of the results. Here, the displacement field is variable and refined by using more shape functions, and the number/size of elements usually remains constant. The previously used functions are also kept in improved approximations, which is why the method is designated as hierarchical by some authors. It is also stated [87] that the p-version FEM has several advantages over the traditional h-version FEM, as it requires a smaller number of elements and a smaller number of degrees-of-freedom, while keeping the versatility of the h-version FEM, to output better results. The p-version also allows the modelling of simple structures with only one element, as it is the case of the present study, reducing the computational effort and illustrating a higher convergence ratio.

For the p-version FEM, a set of shape functions has to be selected. For the present model, Rodrigues' form of Legendre's orthogonal polynomials are chosen for the x coordinate [88–90].

Thus, for internal membrane displacements, the set of shape functions is given by:

$$
g_r(\xi)=\sum_{n=0}^{Int(r/2)}\frac{(-1)^n(2r-2n-5)!!}{2^n n!(r-2n-1)!}\xi^{r-2n-1}, r>2 \tag{2.38}
$$

While for transverse displacements the particular set of functions is selected:

$$f_r(\xi) = \sum_{n=0}^{Int(r/2)} \frac{(-1)^n(2r-2n-7)!!}{2^n n!(r-2n-1)!}\xi^{r-2n-1}, r > 4 \tag{2.39}$$

noting that $r!! = r(r-2)...(2 \text{ or } 1), 0!! = (-1)!! = 1$, that $Int(r/2)$ denotes the integer part of $r/2$ and that terms respecting the condition $(r-2n-1)! < 0$ are ignored.

The main difference between the internal membrane shape functions and the out-of-plane/transverse shape functions lays on the fact that the first ones, $g_r(\xi)$, have null value for $\xi = -1$ and $\xi = 1$, while the second ones, $f_r(\xi)$ have both null value and slope for $\xi = -1$ and $\xi = 1$.

The first two functions of $g_r(\xi)$ and the first four functions of $f_r(\xi)$ may be adjusted depending on the boundary conditions. Typically, $g_1^{BC}(\xi)$ and $g_2^{BC}(\xi)$ allow for displacements in each one of the extremities while the other one is fixed, while $f_1^{BC}(\xi)$ and $f_3^{BC}(\xi)$ allow for the same displacement behaviour with no slope, and $f_2^{BC}(\xi)$ and $f_4^{BC}(\xi)$ allow for no displacements, but enable rotation (slope) in each one of the extremities respectively. These properties allow for proper adjustments depending on the studied case, selecting the right functions that fit the boundary conditions. It is important to note that the set of two and four functions of $g_r(\xi)$ and $f_r(\xi)$ are not deduced from the Equations (2.38) and (2.39), and thus are defined as comes, with the index BC to be distinguished from the expressions deduced by the referred equations:

$$g_1^{BC}(\xi) = \frac{1}{2} - \frac{1}{2}\xi \tag{2.40a}$$

$$g_2^{BC}(\xi) = \frac{1}{2} + \frac{1}{2}\xi \tag{2.40b}$$

$$f_1^{BC}(\xi) = \frac{1}{2} - \frac{3}{4}\xi + \frac{1}{4}\xi^3 \tag{2.40c}$$

$$f_2^{BC}(\xi) = \frac{1}{4} - \frac{1}{4}\xi - \frac{1}{4}\xi^2 + \frac{1}{4}\xi^3 \tag{2.40d}$$

$$f_3^{BC}(\xi) = \frac{1}{2} + \frac{3}{4}\xi - \frac{1}{4}\xi^3 \tag{2.40e}$$

$$f_4^{BC}(\xi) = -\frac{1}{4} - \frac{1}{4}\xi + \frac{1}{4}\xi^2 + \frac{1}{4}\xi^3 \tag{2.40f}$$

For example, for clamped-clamped cases, none of the above described functions are used, while for free-free cases all the above functions are selected. It is important to register that the number notation of the functions used for free-free boundary conditions cause the described functions to occupy such positions $r = 1, 2, 3, 4$, as the ones produced by the summations (2.38) and (2.39) occupy the following positions $r = 5, 6...$, with the same order, while for clamped-clamped, the right order and indexes that come from said equations remain intact.

It is also possible to make the distinction between odd and even functions, as the appropriate set may require symmetric shape functions - odd ones - or assymmetric shape functions - even ones -, relative to the point $\xi = 0$.

Regarding the θ coordinate, a different set of functions is selected, based on [11]. It is a set of trigonometric harmonic functions, widely used when describing the dynamic behaviour along the cylindrical coordinate θ.

Thus, for u^0 displacement, comes:

$$tu_n(\theta) = cos(n\,\theta) \tag{2.41}$$

For v^0 displacement, comes:

$$tv_n(\theta) = sin(n\,\theta) \tag{2.42}$$

And finally for w^0 displacement, comes:

$$tw_n(\theta) = cos(n\,\theta) \tag{2.43}$$

As these shape functions purpose is to describe the conduct in the θ coordinate, for each one of the displacement u^0, v^0 and w^0, they can also be adjusted to better fit specific variations of boundary conditions of the shell model. For example, to study beam-like modes of vibration, one must calibrate the value of n to be $n = 1$, allowing for a better representation of such modes. For radial breathing modes, one must calibrate the value of n to be $n = 0$, and for the inextensional modes of vibration or Rayleigh, Love or Koga [91], greater values of n are employed.

As will be seen further on this dissertation, different boundary conditions may imply a variation of the shape functions use, as out-of-plane/tranverse functions may be used to describe the internal membrane dynamic behaviour of v^0 in very specific cases. For this reason, a uniform nomenclature for the functions with respect to u^0, v^0 and w^0 is used, so that $f^u_{r/s}(x)$ is the shape function attributed to the displacement u^0 in the coordinate x, $f^u_{r/s}(\theta)$ is the shape function attributed to the displacement u^0 in the coordinate θ, and so on following this logic, giving place to $f^v_{r/s}(x)$, $f^v_{r/s}(\theta)$, $f^w_{r/s}(x)$, $f^w_{r/s}(\theta)$. It is important to note that the index r/s is used as the application of the Galerkin method requires a combination of the functions that two indexes justify. For the sake of reading easiness, the nomenclature is simplified so that $f^u_{r/s}(x)$ becomes $f^u_{r/s\,x}$.

The middle surface displacements can be described as the product of a shape function combination matrix and the vector of generalized displacements, as follows:

$$\begin{aligned} \{de^0\} &= \begin{Bmatrix} u^0 \\ v^0 \\ w^0 \end{Bmatrix} = [N]\{q\} \\ &= \begin{bmatrix} \{\delta_1\}^T & 0 & 0 \\ 0 & \{\delta_2\}^T & 0 \\ 0 & 0 & \{\delta_3\}^T \end{bmatrix} \{q\} \end{aligned} \tag{2.44}$$

where:

$$\{\delta_1\}^T = \{f^u_{1x} f^u_{1\theta}, f^u_{1x} f^u_{2\theta}, \ldots, f^u_{pgu\,x}, f^u_{ptu\,\theta}\}$$

$$\{\delta_2\}^T = \{f^v_{1x} f^v_{1\theta}, f^v_{1x} f^v_{2\theta}, \ldots, f^v_{pgv\,x}, f^v_{ptv\,\theta}\}$$

$$\{\delta_3\}^T = \{f^w_{1x} f^w_{1\theta}, f^w_{1x} f^w_{2\theta}, \ldots, f^w_{pw\,x}, f^w_{ptw\,\theta}\}$$

And $\{q\}^T$ is defined as:

$$\{q\}^T = \{q^u_{11}; q^u_{12}; \dots ; q^u_{pgu-ptu} \quad q^v_{11}; q^v_{12}; \dots ; q^v_{pgv-ptv} \quad q^w_{11}; q^w_{12}; \dots ; q^w_{pw-ptw}\} \tag{2.45}$$

where pgu, pgv and pw define the number of shape functions allocated to the displacement components of u^0, v^0 and w^0 in the coordinate of x, respectively, and ptu, ptv and ptw define the number of shape functions allocated to the displacements of u^0, v^0 and w^0 in the coordinate of θ, respectively.

Lastly, the displacements in Equation (2.44) can be displayed as follows:

$$\{de^0(x,\theta,t)\} = \begin{Bmatrix} u^0(x,\theta,t) \\ v^0(x,\theta,t) \\ w^0(x,\theta,t) \end{Bmatrix} = \begin{cases} \sum_{r=1}^{pgu} \sum_{s=1}^{ptu} f^u_{rx}(x) f^u_{s\theta}(\theta)\, q^u_{rs}(t) \\ \sum_{r=1}^{pgv} \sum_{s=1}^{ptv} f^v_{rx}(x) f^v_{s\theta}(\theta)\, q^v_{rs}(t) \\ \sum_{r=1}^{pw} \sum_{s=1}^{ptw} f^w_{rx}(x) f^w_{s\theta}(\theta)\, q^w_{rs}(t) \end{cases} \tag{2.46}$$

Finite element matrices

To arrive at the p-version finite element method matrices corresponding to the described discretization, comes the option to obtain a weak formulation of Equations (2.35), (2.36) and (2.37) (from integration by parts). Thus, Galerkin method is applied, discretizing the continuous partial differential equations onto algebraic equations [92], as comes from the following equations:

$$\int_0^{2\pi} \int_0^l f^u_r(x)\, f^u_s(\theta)\, \mathcal{L}_u(x,\theta,t)\, \mathrm{d}x\, R\, \mathrm{d}\theta \tag{2.47}$$

$$\int_0^{2\pi} \int_0^l f^v_r(x)\, f^v_s(\theta)\, \mathcal{L}_v(x,\theta,t)\, \mathrm{d}x\, R\, \mathrm{d}\theta \tag{2.48}$$

$$\int_0^{2\pi} \int_0^l f^w_r(x)\, f^w_s(\theta)\, \mathcal{L}_w(x,\theta,t)\, \mathrm{d}x\, R\, \mathrm{d}\theta \tag{2.49}$$

where $\mathcal{L}_u(x,\theta,t)$, $\mathcal{L}_v(x,\theta,t)$ and $\mathcal{L}_w(x,\theta,t)$ are (2.35), (2.36) and (2.37), respectively.

Moreover, the x coordinate will be permuted to the natural coordinate ξ in the domain $[-1,1]$, in order to apply correctly the selected shape functions dependent on the natural coordinate ξ. In order to perform the transformation, the following relation must be defined:

$$\mathrm{d}x = \frac{l}{2}\,\mathrm{d}\xi \tag{2.50}$$

The computational implementation can only be made possible by considering all the combinations of products between shape functions. Thus, auxiliary variables are created, where N designates the number of respective shape functions of a considering displacement and coordinate, taking the values of either pgu, pgv, pw, ptu, ptv and ptw. Note that i and j designate, respectively, the column and row numbers of the resultant matrices. The new variable indexes will replace the lower index in the current nomenclature (note that both for the shape functions f and the generalized nodal displacements $q(t)$, highlighting the index variation that comes with the implementation, so that it is expressed as:

$$\begin{aligned} i\xi &= Int\left(\tfrac{i-1}{N}\right)+1 \qquad & j\xi &= Int\left(\tfrac{j-1}{N}\right)+1 \\ i\theta &= i-(i\xi-1)\,N \qquad & j\theta &= j-(j\xi-1)\,N \end{aligned} \tag{2.51}$$

The following procedure consists of the application of the Galerkin method for each one of the three equations of motion, $\mathcal{L}_u(x,\theta,t)$, $\mathcal{L}_v(x,\theta,t)$ and $\mathcal{L}_w(x,\theta,t)$.

The equations of motion come with the differential operator ∇ expanded, and with each differential term associated with the respective sum term resultant from the Galerkin method application, designated from $ter(1)$ to $ter(34)$, and resulting in the linear model algebraic terms.

For the equation of motion in u^0 comes:

$$\begin{aligned} \mathcal{L}_u(x,\theta,t) = \rho h \Bigg[\underbrace{\frac{\partial^2 u^0}{\partial t^2}}_{ter(1)} - (e_0\,a)^2 \Bigg[\underbrace{\frac{\partial^2}{\partial x^2}\left(\frac{\partial^2 u^0}{\partial t^2}\right)}_{ter(2)} + \underbrace{\frac{1}{R^2}\frac{\partial^2}{\partial \theta^2}\left(\frac{\partial^2 u^0}{\partial t^2}\right)}_{ter(3)} \Bigg] \Bigg] \\ - \frac{Eh}{1-\nu^2}\Bigg[\underbrace{\frac{\partial^2 u^0}{\partial x^2}}_{ter(4)} + \underbrace{\frac{1-\nu}{2}\frac{1}{R^2}\frac{\partial^2 u^0}{\partial \theta^2}}_{ter(5)} + \nu\underbrace{\frac{1}{R}\frac{\partial w^0}{\partial x}}_{ter(6)} + \underbrace{\frac{1+\nu}{2}\frac{1}{R}\frac{\partial^2 v^0}{\partial x \partial \theta}}_{ter(7)} \Bigg] \\ - \frac{Eh^3}{24(1+\nu)R^3}\Bigg[\underbrace{\frac{\partial^3 w^0}{\partial x \partial \theta^2}}_{ter(8)} - \underbrace{\frac{3}{4}\frac{\partial^2 v^0}{\partial x \partial \theta}}_{ter(9)} + \underbrace{\frac{1}{4R}\frac{\partial^2 u^0}{\partial \theta^2}}_{ter(10)} \Bigg] = 0 \end{aligned} \tag{2.52}$$

For the equation of motion in v^0 comes:

$$\begin{aligned} \mathcal{L}_v(x,\theta,t) = \rho h \Bigg[\underbrace{\frac{\partial^2 v^0}{\partial t^2}}_{ter(11)} - (e_0\,a)^2 \Bigg[\underbrace{\frac{\partial^2}{\partial x^2}\left(\frac{\partial^2 v^0}{\partial t^2}\right)}_{ter(12)} + \underbrace{\frac{1}{R^2}\frac{\partial^2}{\partial \theta^2}\left(\frac{\partial^2 v^0}{\partial t^2}\right)}_{ter(13)} \Bigg] \Bigg] \\ - \frac{Eh}{1-\nu^2}\Bigg[\underbrace{\frac{1}{R^2}\frac{\partial^2 v^0}{\partial \theta^2}}_{ter(14)} + \underbrace{\frac{1}{R^2}\frac{\partial w^0}{\partial \theta}}_{ter(15)} + \underbrace{\frac{1+\nu}{2}\frac{1}{R}\frac{\partial^2 u^0}{\partial x \partial \theta}}_{ter(16)} + \underbrace{\frac{1-\nu}{2}\frac{\partial^2 v^0}{\partial x^2}}_{ter(17)} \Bigg] \\ - \frac{Eh^3}{12(1-\nu^2)}\Bigg[\underbrace{\frac{1}{R^4}\frac{\partial^2 v^0}{\partial \theta^2}}_{ter(18)} - \underbrace{\frac{1}{R^4}\frac{\partial^3 w^0}{\partial \theta^3}}_{ter(19)} - \underbrace{\frac{3-\nu}{2}\frac{1}{R^2}\frac{\partial^3 w^0}{\partial x^2 \partial \theta}}_{ter(20)} \\ + \underbrace{\frac{9(1-\nu)}{8R^2}\frac{\partial^2 v^0}{\partial x^2}}_{ter(21)} - \underbrace{\frac{3(1-\nu)}{8R^3}\frac{\partial^2 u^0}{\partial x \partial \theta}}_{ter(22)} \Bigg] = 0 \end{aligned} \tag{2.53}$$

And finally, for the equation of motion in w^0 comes:

$$\begin{aligned}\mathcal{L}_w(x,\theta,t) = \rho h \Bigg[\underbrace{\frac{\partial^2 w^0}{\partial t^2}}_{ter(23)} -(e_0\,a)^2 \Bigg[\underbrace{\frac{\partial^2}{\partial x^2}\left(\frac{\partial^2 w^0}{\partial t^2}\right)}_{ter(24)} + \underbrace{\frac{1}{R^2}\frac{\partial^2}{\partial \theta^2}\left(\frac{\partial^2 w^0}{\partial t^2}\right)}_{ter(25)} \Bigg] \Bigg] \\ + \frac{Eh}{1-\nu^2}\Bigg[\underbrace{\frac{1}{R^2}\frac{\partial v^0}{\partial \theta}}_{ter(26)} + \underbrace{\frac{w^0}{R^2}}_{ter(27)} + \nu \underbrace{\frac{1}{R}\frac{\partial u^0}{\partial x}}_{ter(28)} \Bigg] + \frac{Eh^3}{12(1-\nu^2)}\Bigg[\underbrace{\frac{\partial^4 w^0}{\partial x^4}}_{ter(29)} - \underbrace{\frac{3-\nu}{2R^2}\frac{\partial^3 v^0}{\partial x^2 \partial \theta}}_{ter(30)} + \underbrace{\frac{2}{R^2}\frac{\partial^4 w^0}{\partial x^2 \partial \theta^2}}_{ter(31)} \\ - \underbrace{\frac{1}{R^4}\frac{\partial^3 v^0}{\partial \theta^3}}_{ter(32)} + \underbrace{\frac{1}{R^4}\frac{\partial^4 w^0}{\partial \theta^4}}_{ter(33)} + \underbrace{\frac{1-\nu}{2}\frac{1}{R^3}\frac{\partial^3 u^0}{\partial x \partial \theta^2}}_{ter(34)} \Bigg] = 0\end{aligned} \tag{2.54}$$

Expanding the terms of Equations (2.47), (2.48) and (2.49), comes:

$$\begin{aligned} ter(1) : \rho\, h \int_0^{2\pi}\int_0^l f^u_{ix}\, f^u_{i\theta} \cdot (f^u_{jx}\, f^u_{j\theta})\, \mathrm{d}x\, R\, \mathrm{d}\theta\ \ddot{q}^u_{ij}(t) \\ = \rho\, h\, R\, \frac{l}{2} \int_0^{2\pi} f^u_{i\theta}\, f^u_{j\theta}\, \mathrm{d}\theta \int_{-1}^{1} f^u_{i\xi}\, f^u_{j\xi} \mathrm{d}\xi\ \ddot{q}^u_{ij}(t) \end{aligned} \tag{2.55}$$

$$\begin{aligned} ter(2) : -\rho\, h\, (e_0\, a)^2 \int_0^{2\pi}\int_0^l f^u_{ix}\, f^u_{i\theta} \cdot \frac{\partial^2}{\partial x^2}\big(f^u_{jx}\, f^u_{j\theta}\big)\, \mathrm{d}x\, R\, \mathrm{d}\theta\ \ddot{q}^u_{ij}(t) \\ = \rho\, h\, (e_0\, a)^2\, R\, \frac{2}{l} \int_0^{2\pi} f^u_{i\theta}\, f^u_{j\theta}\, \mathrm{d}\theta \int_{-1}^{1} \frac{\mathrm{d}f^u_{i\xi}}{\mathrm{d}\xi}\, \frac{\mathrm{d}f^u_{j\xi}}{\mathrm{d}\xi} \mathrm{d}\xi\ \ddot{q}^u_{ij}(t) \end{aligned} \tag{2.56}$$

$$\begin{aligned} ter(3) : -\rho\, h\, (e_0\, a)^2 \frac{1}{R^2} \int_0^{2\pi}\int_0^l f^u_{ix}\, f^u_{i\theta} \cdot \frac{\partial^2}{\partial \theta^2}\big(f^u_{jx}\, f^u_{j\theta}\big)\, \mathrm{d}x\, R\, \mathrm{d}\theta\ \ddot{q}^u_{ij}(t) \\ = \rho\, h\, (e_0\, a)^2\, \frac{1}{R}\, \frac{l}{2} \int_0^{2\pi} \frac{\mathrm{d}f^u_{i\theta}}{\mathrm{d}\theta}\, \frac{\mathrm{d}f^u_{j\theta}}{\mathrm{d}\theta}\, \mathrm{d}\theta \int_{-1}^{1} f^u_{i\xi}\, f^u_{j\xi} \mathrm{d}\xi\ \ddot{q}^u_{ij}(t) \end{aligned} \tag{2.57}$$

$$\begin{aligned} ter(4) : -\frac{Eh}{1-\nu^2} \int_0^{2\pi}\int_0^l f^u_{ix}\, f^u_{i\theta} \cdot \frac{\partial^2}{\partial x^2}\big(f^u_{jx}\, f^u_{j\theta}\big)\, \mathrm{d}x\, R\, \mathrm{d}\theta\ q^u_{ij}(t) \\ = \frac{2}{l}\, \frac{EhR}{1-\nu^2} \int_0^{2\pi} f^u_{i\theta}\, f^u_{j\theta}\, \mathrm{d}\theta \int_{-1}^{1} \frac{\mathrm{d}f^u_{i\xi}}{\mathrm{d}\xi}\, \frac{\mathrm{d}f^u_{j\xi}}{\mathrm{d}\xi} \mathrm{d}\xi\ q^u_{ij}(t) \end{aligned} \tag{2.58}$$

$$\begin{aligned} ter(5) : -\frac{Eh}{1-\nu^2}\, \frac{1-\nu}{2R^2} \int_0^{2\pi}\int_0^l f^u_{ix}\, f^u_{i\theta} \cdot \frac{\partial^2}{\partial \theta^2}\big(f^u_{jx}\, f^u_{j\theta}\big)\, \mathrm{d}x\, R\, \mathrm{d}\theta\ q^u_{ij}(t) \\ = \frac{Ehl\,(1-\nu)}{4(1-\nu^2)R} \int_0^{2\pi} \frac{\mathrm{d}f^u_{i\theta}}{\mathrm{d}\theta}\, \frac{\mathrm{d}f^u_{i\theta}}{\mathrm{d}\theta}\, \mathrm{d}\theta \int_{-1}^{1} f^u_{i\xi}\, f^u_{j\xi} \mathrm{d}\xi\ q^u_{ij}(t) \end{aligned} \tag{2.59}$$

$$\begin{aligned} ter(6) : -\frac{Eh\,\nu}{(1-\nu^2)R} \int_0^{2\pi}\int_0^l f^u_{ix}\, f^u_{i\theta} \cdot \frac{\partial}{\partial x}\big(f^w_{jx}\, f^w_{j\theta}\big)\, \mathrm{d}x\, R\, \mathrm{d}\theta\ q^w_{ij}(t) \\ = -\frac{Eh\nu}{1-\nu^2} \int_0^{2\pi} f^u_{i\theta}\, f^w_{j\theta}\, \mathrm{d}\theta \int_{-1}^{1} f^u_{i\xi}\, \frac{\mathrm{d}f^w_{j\xi}}{\mathrm{d}\xi} \mathrm{d}\xi\ q^w_{ij}(t) \end{aligned} \tag{2.60}$$

$$\begin{aligned} ter(7) :& -\frac{Eh}{1-\nu^2}\frac{1+\nu}{2R}\int_0^{2\pi}\int_0^l f_{ix}^u\, f_{i\theta}^u \cdot \frac{\partial^2}{\partial x \partial \theta}\big(f_{jx}^v\, f_{j\theta}^v\big)\,\mathrm{d}x\, R\,\mathrm{d}\theta\;\, q_{ij}^v(t) \\ &= -\frac{Eh}{1-\nu^2}\frac{1+\nu}{2}\int_0^{2\pi} f_{i\theta}^u\,\frac{\mathrm{d}f_{j\theta}^v}{\mathrm{d}\theta}\,\mathrm{d}\theta\,\int_{-1}^1 f_{i\xi}^u\,\frac{\mathrm{d}f_{j\xi}^v}{\mathrm{d}\xi}\mathrm{d}\xi\;\, q_{ij}^v(t) \end{aligned} \tag{2.61}$$

$$\begin{aligned} ter(8) :& -\frac{Eh^3}{24(1+\nu)R^3}\int_0^{2\pi}\int_0^l f_{ix}^u\, f_{i\theta}^u \cdot \frac{\partial^3}{\partial x \partial \theta^2}\big(f_{jx}^w\, f_{j\theta}^w\big)\,\mathrm{d}x\, R\,\mathrm{d}\theta\;\, q_{ij}^w(t) \\ &= \frac{Eh^3}{24(1+\nu)R^2}\int_0^{2\pi} \frac{\mathrm{d}f_{i\theta}^u}{\mathrm{d}\theta}\,\frac{\mathrm{d}f_{j\theta}^w}{\mathrm{d}\theta}\,\mathrm{d}\theta\,\int_{-1}^1 f_{i\xi}^u\,\frac{\mathrm{d}f_{j\xi}^w}{\mathrm{d}\xi}\mathrm{d}\xi\;\, q_{ij}^w(t) \end{aligned} \tag{2.62}$$

$$\begin{aligned} ter(9) :& \ \frac{3}{4}\frac{Eh^3}{24(1+\nu)R^3}\int_0^{2\pi}\int_0^l f_{ix}^u\, f_{i\theta}^u \cdot \frac{\partial^2}{\partial x \partial \theta}\big(f_{jx}^v\, f_{j\theta}^v\big)\,\mathrm{d}x\, R\,\mathrm{d}\theta\;\, q_{ij}^v(t) \\ &= \frac{Eh^3}{32(1+\nu)R^2}\int_0^{2\pi} f_{i\theta}^u\,\frac{\mathrm{d}f_{j\theta}^v}{\mathrm{d}\theta}\,\mathrm{d}\theta\,\int_{-1}^1 f_{i\xi}^u\,\frac{\mathrm{d}f_{j\xi}^v}{\mathrm{d}\xi}\mathrm{d}\xi\;\, q_{ij}^v(t) \end{aligned} \tag{2.63}$$

$$\begin{aligned} ter(10) :& -\frac{Eh^3}{24(1+\nu)R^3}\frac{1}{4R}\int_0^{2\pi}\int_0^l f_{ix}^u\, f_{i\theta}^u \cdot \frac{\partial^2}{\partial \theta^2}\big(f_{jx}^u\, f_{j\theta}^u\big)\,\mathrm{d}x\, R\,\mathrm{d}\theta\;\, q_{ij}^u(t) \\ &= \frac{Eh^3 l}{192(1+\nu)R^3}\int_0^{2\pi} \frac{\mathrm{d}f_{i\theta}^u}{\mathrm{d}\theta}\,\frac{\mathrm{d}f_{j\theta}^u}{\mathrm{d}\theta}\,\mathrm{d}\theta\,\int_{-1}^1 f_{i\xi}^u\, f_{j\xi}^u\mathrm{d}\xi\;\, q_{ij}^u(t) \end{aligned} \tag{2.64}$$

$$\begin{aligned} ter(11) :& \ \rho\, h\int_0^{2\pi}\int_0^l f_{ix}^v\, f_{i\theta}^v \cdot \big(f_{jx}^v\, f_{j\theta}^v\big)\,\mathrm{d}x\, R\,\mathrm{d}\theta\;\, \ddot{q}_{ij}^v(t) \\ &= \rho\, h\, R\,\frac{l}{2}\int_0^{2\pi} f_{i\theta}^v\, f_{j\theta}^v\,\mathrm{d}\theta\,\int_{-1}^1 f_{i\xi}^v\, f_{j\xi}^v\mathrm{d}\xi\;\, \ddot{q}_{ij}^v(t) \end{aligned} \tag{2.65}$$

$$\begin{aligned} ter(12) :& -\rho\, h\,(e_0\, a)^2\int_0^{2\pi}\int_0^l f_{ix}^v\, f_{i\theta}^v \cdot \frac{\partial^2}{\partial x^2}\big(f_{jx}^v\, f_{j\theta}^v\big)\,\mathrm{d}x\, R\,\mathrm{d}\theta\;\, \ddot{q}_{ij}^v(t) \\ &= \rho\, h\,(e_0\, a)^2\, R\,\frac{2}{l}\int_0^{2\pi} f_{i\theta}^v\, f_{j\theta}^v\,\mathrm{d}\theta\,\int_{-1}^1 \frac{\mathrm{d}f_{i\xi}^v}{\mathrm{d}\xi}\,\frac{\mathrm{d}f_{j\xi}^v}{\mathrm{d}\xi}\mathrm{d}\xi\;\, \ddot{q}_{ij}^v(t) \end{aligned} \tag{2.66}$$

$$\begin{aligned} ter(13) :& -\rho\, h\,(e_0\, a)^2\frac{1}{R^2}\int_0^{2\pi}\int_0^l f_{ix}^v\, f_{i\theta}^v \cdot \frac{\partial^2}{\partial \theta^2}\big(f_{jx}^v\, f_{j\theta}^v\big)\,\mathrm{d}x\, R\,\mathrm{d}\theta\;\, \ddot{q}_{ij}^v(t) \\ &= \rho\, h\,(e_0\, a)^2\,\frac{1}{R}\,\frac{l}{2}\int_0^{2\pi} \frac{\mathrm{d}f_{i\theta}^v}{\mathrm{d}\theta}\,\frac{\mathrm{d}f_{j\theta}^v}{\mathrm{d}\theta}\,\mathrm{d}\theta\,\int_{-1}^1 f_{i\xi}^v\, f_{j\xi}^v\mathrm{d}\xi\;\, \ddot{q}_{ij}^v(t) \end{aligned} \tag{2.67}$$

$$\begin{aligned} ter(14) :& -\frac{Eh}{1-\nu^2}\frac{1}{R^2}\int_0^{2\pi}\int_0^l f_{ix}^v\, f_{i\theta}^v \cdot \frac{\partial^2}{\partial \theta^2}\big(f_{jx}^v\, f_{j\theta}^v\big)\,\mathrm{d}x\, R\,\mathrm{d}\theta\;\, q_{ij}^v(t) \\ &= \frac{Ehl}{(1-\nu^2)2R}\int_0^{2\pi} \frac{\mathrm{d}f_{i\theta}^v}{\mathrm{d}\theta}\,\frac{\mathrm{d}f_{j\theta}^v}{\mathrm{d}\theta}\,\mathrm{d}\theta\,\int_{-1}^1 f_{i\xi}^v\, f_{j\xi}^v\mathrm{d}\xi\;\, q_{ij}^v(t) \end{aligned} \tag{2.68}$$

$$\begin{aligned} ter(15) : &-\frac{Eh}{1-\nu^2}\frac{1}{R^2}\int_0^{2\pi}\int_0^l f^v_{ix}\, f^v_{i\theta}\cdot\frac{\partial}{\partial\theta}\big(f^w_{jx}\, f^w_{j\theta}\big)\,\mathrm{d}x\, R\,\mathrm{d}\theta\;\, q^w_{ij}(t) \\ &= -\frac{Ehl}{(1-\nu^2)2R}\int_0^{2\pi} f^v_{i\theta}\,\frac{\mathrm{d}f^w_{j\theta}}{\mathrm{d}\theta}\,\mathrm{d}\theta\int_{-1}^1 f^v_{i\xi}\, f^w_{j\xi}\mathrm{d}\xi\;\, q^w_{ij}(t) \end{aligned} \tag{2.69}$$

$$\begin{aligned} ter(16) : &-\frac{Eh}{1-\nu^2}\frac{1+\nu}{2}\frac{1}{R}\int_0^{2\pi}\int_0^l f^v_{ix}\, f^v_{i\theta}\cdot\frac{\partial^2}{\partial x\partial\theta}\big(f^u_{jx}\, f^u_{j\theta}\big)\,\mathrm{d}x\, R\,\mathrm{d}\theta\;\, q^u_{ij}(t) \\ &= -\frac{Eh}{1-\nu^2}\frac{1+\nu}{2}\int_0^{2\pi} f^v_{i\theta}\,\frac{\mathrm{d}f^u_{j\theta}}{\mathrm{d}\theta}\,\mathrm{d}\theta\int_{-1}^1 f^v_{i\xi}\,\frac{\mathrm{d}f^u_{j\xi}}{\mathrm{d}\xi}\mathrm{d}\xi\;\, q^u_{ij}(t) \end{aligned} \tag{2.70}$$

$$\begin{aligned} ter(17) : &-\frac{Eh}{1-\nu^2}\frac{1-\nu}{2}\int_0^{2\pi}\int_0^l f^v_{ix}\, f^v_{i\theta}\cdot\frac{\partial^2}{\partial x^2}\big(f^v_{jx}\, f^v_{j\theta}\big)\,\mathrm{d}x\, R\,\mathrm{d}\theta\;\, q^v_{ij}(t) \\ &= \frac{Eh(1-\nu)R}{(1-\nu^2)\, l}\int_0^{2\pi} f^v_{i\theta}\, f^v_{j\theta}\,\mathrm{d}\theta\int_{-1}^1 \frac{\mathrm{d}f^v_{i\xi}}{\mathrm{d}\xi}\,\frac{\mathrm{d}f^v_{j\xi}}{\mathrm{d}\xi}\mathrm{d}\xi\;\, q^v_{ij}(t) \end{aligned} \tag{2.71}$$

$$\begin{aligned} ter(18) : &-\frac{Eh^3}{12(1-\nu^2)}\frac{1}{R^4}\int_0^{2\pi}\int_0^l f^v_{ix}\, f^v_{i\theta}\cdot\frac{\partial^2}{\partial\theta^2}\big(f^v_{jx}\, f^v_{j\theta}\big)\,\mathrm{d}x\, R\,\mathrm{d}\theta\;\, q^v_{ij}(t) \\ &= \frac{Eh^3 l}{24(1-\nu^2)R^3}\int_0^{2\pi} \frac{\mathrm{d}f^v_{i\theta}}{\mathrm{d}\theta}\,\frac{\mathrm{d}f^v_{j\theta}}{\mathrm{d}\theta}\,\mathrm{d}\theta\int_{-1}^1 f^v_{i\xi}\, f^v_{j\xi}\mathrm{d}\xi\;\, q^v_{ij}(t) \end{aligned} \tag{2.72}$$

$$\begin{aligned} ter(19) : &\frac{Eh^3}{12(1-\nu^2)}\frac{1}{R^4}\int_0^{2\pi}\int_0^l f^v_{ix}\, f^v_{i\theta}\cdot\frac{\partial^3}{\partial\theta^3}\big(f^w_{jx}\, f^w_{j\theta}\big)\,\mathrm{d}x\, R\,\mathrm{d}\theta\;\, q^w_{ij}(t) \\ &= -\frac{Eh^3 l}{24(1-\nu^2)R^3}\int_0^{2\pi} \frac{\mathrm{d}f^v_{i\theta}}{\mathrm{d}\theta}\,\frac{\mathrm{d}^2 f^w_{j\theta}}{\mathrm{d}\theta^2}\,\mathrm{d}\theta\int_{-1}^1 f^v_{i\xi}\, f^w_{j\xi}\mathrm{d}\xi\;\, q^w_{ij}(t) \end{aligned} \tag{2.73}$$

$$\begin{aligned} ter(20) : &\frac{Eh^3(3-\nu)}{24(1-\nu^2)R^2}\int_0^{2\pi}\int_0^l f^v_{ix}\, f^v_{i\theta}\cdot\frac{\partial^3}{\partial x^2\partial\theta}\big(f^w_{jx}\, f^w_{j\theta}\big)\,\mathrm{d}x\, R\,\mathrm{d}\theta\;\, q^w_{ij}(t) \\ &= -\frac{Eh^3(3-\nu)}{12(1-\nu^2)\, lR}\int_0^{2\pi} f^v_{i\theta}\,\frac{\mathrm{d}f^w_{j\theta}}{\mathrm{d}\theta}\,\mathrm{d}\theta\int_{-1}^1 \frac{\mathrm{d}f^v_{i\xi}}{\mathrm{d}\xi}\,\frac{\mathrm{d}f^w_{j\xi}}{\mathrm{d}\xi}\mathrm{d}\xi\;\, q^w_{ij}(t) \end{aligned} \tag{2.74}$$

$$\begin{aligned} ter(21) : &-\frac{Eh^3}{12(1-\nu^2)}\frac{9(1-\nu)}{8R^2}\int_0^{2\pi}\int_0^l f^v_{ix}\, f^v_{i\theta}\cdot\frac{\partial^2}{\partial x^2}\big(f^v_{jx}\, f^v_{j\theta}\big)\,\mathrm{d}x\, R\,\mathrm{d}\theta\;\, q^v_{ij}(t) \\ &= \frac{9Eh^3(1-\nu)}{48(1-\nu^2)lR}\int_0^{2\pi} f^v_{i\theta}\, f^v_{j\theta}\,\mathrm{d}\theta\int_{-1}^1 \frac{\mathrm{d}f^v_{i\xi}}{\mathrm{d}\xi}\,\frac{\mathrm{d}f^v_{j\xi}}{\mathrm{d}\xi}\mathrm{d}\xi\;\, q^v_{ij}(t) \end{aligned} \tag{2.75}$$

$$\begin{aligned} ter(22) : &\frac{Eh^3}{12(1-\nu^2}\frac{3(1-\nu}{8R^3}\int_0^{2\pi}\int_0^l f^v_{ix}\, f^v_{i\theta}\cdot\frac{\partial^2}{\partial x\partial\theta}\big(f^u_{jx}\, f^u_{j\theta}\big)\,\mathrm{d}x\, R\,\mathrm{d}\theta\;\, q^u_{ij}(t) \\ &= \frac{Eh^3(1-\nu)}{32(1-\nu^2)R^2}\int_0^{2\pi} f^v_{i\theta}\,\frac{\mathrm{d}f^u_{j\theta}}{\mathrm{d}\theta}\,\mathrm{d}\theta\int_{-1}^1 f^v_{i\xi}\,\frac{\mathrm{d}f^u_{j\xi}}{\mathrm{d}\xi}\mathrm{d}\xi\;\, q^u_{ij}(t) \end{aligned} \tag{2.76}$$

$$\begin{aligned} ter(23) : &\,\rho\, h\int_0^{2\pi}\int_0^l f^w_{ix}\, f^w_{i\theta}\cdot\big(f^w_{jx}\, f^w_{j\theta}\big)\,\mathrm{d}x\, R\,\mathrm{d}\theta\;\, \ddot{q}^w_{ij}(t) \\ &= \rho\, h\, R\,\frac{l}{2}\int_0^{2\pi} f^w_{i\theta}\, f^w_{j\theta}\,\mathrm{d}\theta\int_{-1}^1 f^w_{i\xi}\, f^w_{j\xi}\mathrm{d}\xi\;\, \ddot{q}^w_{ij}(t) \end{aligned} \tag{2.77}$$

$$\begin{aligned} ter(24): &-\rho\, h\, (e_0\, a)^2 \int_0^{2\pi}\int_0^l f_{ix}^w\, f_{i\theta}^w \cdot \frac{\partial^2}{\partial x^2}\big(f_{jx}^w\, f_{j\theta}^w\big)\, \mathrm{d}x\, R\, \mathrm{d}\theta\;\, \ddot{q}_{ij}^w(t) \\ &= \rho\, h\, (e_0\, a)^2\, R\, \frac{2}{l} \int_0^{2\pi} f_{i\theta}^w\, f_{j\theta}^w\, \mathrm{d}\theta \int_{-1}^1 \frac{\mathrm{d}f_{i\xi}^w}{\mathrm{d}\xi}\, \frac{\mathrm{d}f_{j\xi}^w}{\mathrm{d}\xi} \mathrm{d}\xi\;\, \ddot{q}_{ij}^w(t) \end{aligned} \tag{2.78}$$

$$\begin{aligned} ter(25): &-\rho\, h\, (e_0\, a)^2 \frac{1}{R^2} \int_0^{2\pi}\int_0^l f_{ix}^w\, f_{i\theta}^w \cdot \frac{\partial^2}{\partial \theta^2}\big(f_{jx}^w\, f_{j\theta}^w\big)\, \mathrm{d}x\, R\, \mathrm{d}\theta\;\, \ddot{q}_{ij}^w(t) \\ &= \rho\, h\, (e_0\, a)^2\, \frac{1}{R}\, \frac{l}{2} \int_0^{2\pi} \frac{\mathrm{d}f_{i\theta}^w}{\mathrm{d}\theta}\, \frac{\mathrm{d}f_{j\theta}^w}{\mathrm{d}\theta}\, \mathrm{d}\theta \int_{-1}^1 f_{i\xi}^w\, f_{j\xi}^w \mathrm{d}\xi\;\, \ddot{q}_{ij}^w(t) \end{aligned} \tag{2.79}$$

$$\begin{aligned} ter(26): &\frac{Eh}{1-\nu^2}\, \frac{1}{R^2} \int_0^{2\pi}\int_0^l f_{ix}^w\, f_{i\theta}^w \cdot \frac{\partial}{\partial \theta}\big(f_{jx}^v\, f_{j\theta}^v\big)\, \mathrm{d}x\, R\, \mathrm{d}\theta\;\, q_{ij}^v(t) \\ &= \frac{Ehl}{(1-\nu^2)2R} \int_0^{2\pi} f_{i\theta}^w\, \frac{\mathrm{d}f_{j\theta}^v}{\mathrm{d}\theta}\, \mathrm{d}\theta \int_{-1}^1 f_{i\xi}^w\, f_{j\xi}^v \mathrm{d}\xi\;\, q_{ij}^v(t) \end{aligned} \tag{2.80}$$

$$\begin{aligned} ter(27): &\frac{Eh}{1-\nu^2}\, \frac{1}{R^2} \int_0^{2\pi}\int_0^l f_{ix}^w\, f_{i\theta}^w \cdot \big(f_{jx}^w\, f_{j\theta}^w\big)\, \mathrm{d}x\, R\, \mathrm{d}\theta\;\, q_{ij}^w(t) \\ &= \frac{Eh}{1-\nu^2}\, \frac{1}{R}\, \frac{l}{2} \int_0^{2\pi} f_{i\theta}^w\, f_{j\theta}^w\, \mathrm{d}\theta \int_{-1}^1 f_{i\xi}^w\, f_{j\xi}^w \mathrm{d}\xi\;\, q_{ij}^w(t) \end{aligned} \tag{2.81}$$

$$\begin{aligned} ter(28): &\frac{Eh\,\nu}{(1-\nu^2)R} \int_0^{2\pi}\int_0^l f_{ix}^w\, f_{i\theta}^w \cdot \frac{\partial}{\partial x}\big(f_{jx}^u\, f_{j\theta}^u\big)\, \mathrm{d}x\, R\, \mathrm{d}\theta\;\, q_{ij}^u(t) \\ &= \frac{Eh\nu}{1-\nu^2} \int_0^{2\pi} f_{i\theta}^w\, f_{j\theta}^u\, \mathrm{d}\theta \int_{-1}^1 f_{i\xi}^w\, \frac{\mathrm{d}f_{j\xi}^u}{\mathrm{d}\xi} \mathrm{d}\xi\;\, q_{ij}^u(t) \end{aligned} \tag{2.82}$$

$$\begin{aligned} ter(29): &\frac{Eh^3}{12(1-\nu^2} \int_0^{2\pi}\int_0^l f_{ix}^w\, f_{i\theta}^w \cdot \frac{\partial^4}{\partial x^4}\big(f_{jx}^w\, f_{j\theta}^w\big)\, \mathrm{d}x\, R\, \mathrm{d}\theta\;\, q_{ij}^w(t) \\ &= \frac{2Eh^3R}{3(1-\nu^2)l^3} \int_0^{2\pi} f_{i\theta}^w\, f_{j\theta}^w\, \mathrm{d}\theta \int_{-1}^1 \frac{\mathrm{d}^2 f_{i\xi}^w}{\mathrm{d}\xi^2}\, \frac{\mathrm{d}^2 f_{j\xi}^w}{\mathrm{d}\xi^2} \mathrm{d}\xi\;\, q_{ij}^w(t) \end{aligned} \tag{2.83}$$

$$\begin{aligned} ter(30): &-\frac{Eh^3(3-\nu)}{24(1-\nu^2)R^2} \int_0^{2\pi}\int_0^l f_{ix}^w\, f_{i\theta}^w \cdot \frac{\partial^3}{\partial x^2 \partial \theta}\big(f_{jx}^v\, f_{j\theta}^v\big)\, \mathrm{d}x\, R\, \mathrm{d}\theta\;\, q_{ij}^v(t) \\ &= \frac{Eh^3(3-\nu)}{12(1-\nu^2)\, lR} \int_0^{2\pi} f_{i\theta}^w\, \frac{\mathrm{d}f_{j\theta}^v}{\mathrm{d}\theta}\, \mathrm{d}\theta \int_{-1}^1 \frac{\mathrm{d}f_{i\xi}^w}{\mathrm{d}\xi}\, \frac{\mathrm{d}f_{j\xi}^v}{\mathrm{d}\xi} \mathrm{d}\xi\;\, q_{ij}^v(t) \end{aligned} \tag{2.84}$$

$$\begin{aligned} ter(31): &\frac{Eh^3}{12(1-\nu^2)}\, \frac{2}{R^2} \int_0^{2\pi}\int_0^l f_{ix}^w\, f_{i\theta}^w \cdot \frac{\partial^4}{\partial x^2 \partial \theta^2}\big(f_{jx}^w\, f_{j\theta}^w\big)\, \mathrm{d}x\, R\, \mathrm{d}\theta\;\, q_{ij}^w(t) \\ &= \frac{Eh^3}{3(1-\nu^2)\, l\, R} \int_0^{2\pi} \frac{\mathrm{d}f_{i\theta}^w}{\mathrm{d}\theta}\, \frac{\mathrm{d}f_{j\theta}^w}{\mathrm{d}\theta}\, \mathrm{d}\theta \int_{-1}^1 \frac{\mathrm{d}f_{i\xi}^w}{\mathrm{d}\xi}\, \frac{\mathrm{d}f_{j\xi}^w}{\mathrm{d}\xi} \mathrm{d}\xi\;\, q_{ij}^w(t) \end{aligned} \tag{2.85}$$

$$\begin{aligned} ter(32): &-\frac{Eh^3}{12(1-\nu^2)}\, \frac{1}{R^4} \int_0^{2\pi}\int_0^l f_{ix}^w\, f_{i\theta}^w \cdot \frac{\partial^3}{\partial \theta^3}\big(f_{jx}^v\, f_{j\theta}^v\big)\, \mathrm{d}x\, R\, \mathrm{d}\theta\;\, q_{ij}^v(t) \\ &= \frac{Eh^3 l}{24(1-\nu^2)R^3} \int_0^{2\pi} \frac{\mathrm{d}f_{i\theta}^w}{\mathrm{d}\theta}\, \frac{\mathrm{d}^2 f_{j\theta}^v}{\mathrm{d}\theta^2}\, \mathrm{d}\theta \int_{-1}^1 f_{i\xi}^w\, f_{j\xi}^v \mathrm{d}\xi\;\, q_{ij}^v(t) \end{aligned} \tag{2.86}$$

$$\begin{aligned} ter(33) : & \frac{Eh^3}{12(1-\nu^2}\frac{1}{R^4}\int_0^{2\pi}\int_0^l f_{ix}^w\, f_{i\theta}^w \cdot \frac{\partial^4}{\partial\theta^4}\big(f_{jx}^w\, f_{j\theta}^w\big)\,\mathrm{d}x\,R\,\mathrm{d}\theta\;q_{ij}^w(t) \\ &= \frac{Eh^3 l}{24(1-\nu^2)R^3}\int_0^{2\pi}\frac{\mathrm{d}^2 f_{i\theta}^w}{\mathrm{d}\theta^2}\,\frac{\mathrm{d}^2 f_{j\theta}^w}{\mathrm{d}\theta^2}\,\mathrm{d}\theta\int_{-1}^{1} f_{i\xi}^w\, f_{j\xi}^w \mathrm{d}\xi\;q_{ij}^w(t) \end{aligned} \tag{2.87}$$

$$\begin{aligned} ter(34) : & \frac{Eh^3}{12(1-\nu^2)}\frac{1-\nu}{2R^3}\int_0^{2\pi}\int_0^l f_{ix}^w\, f_{i\theta}^w \cdot \frac{\partial^3}{\partial x\partial\theta^2}\big(f_{jx}^u\, f_{j\theta}^u\big)\,\mathrm{d}x\,R\,\mathrm{d}\theta\;q_{ij}^u(t) \\ &= -\frac{Eh^3}{24(1+\nu)R^2}\int_0^{2\pi}\frac{\mathrm{d} f_{i\theta}^w}{\mathrm{d}\theta}\,\frac{\mathrm{d} f_{j\theta}^u}{\mathrm{d}\theta}\,\mathrm{d}\theta\int_{-1}^{1} f_{i\xi}^w\, \frac{\mathrm{d} f_{j\xi}^u}{\mathrm{d}\xi}\mathrm{d}\xi\;q_{ij}^u(t) \end{aligned} \tag{2.88}$$

Expressing the complete model in the matrix form, as the generalized nodal displacements still depend on the time variable, the dynamic problem may be expressed as:

$$\begin{aligned} & \left(\begin{bmatrix} [M_{uu}] & 0 & 0 \\ 0 & [M_{vv}] & 0 \\ 0 & 0 & [M_{ww}] \end{bmatrix} + \begin{bmatrix} [M_{uu}^\mu] & 0 & 0 \\ 0 & [M_{vv}^\mu] & 0 \\ 0 & 0 & [M_{ww}^\mu] \end{bmatrix}\right)\begin{Bmatrix} \{\ddot{q}^u(t)\} \\ \{\ddot{q}^v(t)\} \\ \{\ddot{q}^w(t)\} \end{Bmatrix} \\ & \qquad + \begin{bmatrix} [K_{uu}] & [K_{uv}] & [K_{uw}] \\ [K_{vu}] & [K_{vv}] & [K_{vw}] \\ [K_{wu}] & [K_{wv}] & [K_{ww}] \end{bmatrix}\begin{Bmatrix} \{q^u(t)\} \\ \{q^v(t)\} \\ \{q^w(t)\} \end{Bmatrix} = \begin{Bmatrix} 0 \\ 0 \\ 0 \end{Bmatrix} \end{aligned} \tag{2.89}$$

where each one of the submatrixes are defined as:

- $[M_{uu}] \leftarrow ter(1)$
- $[M_{vv}] \leftarrow ter(11)$
- $[M_{ww}] \leftarrow ter(23)$
- $[M_{uu}^\mu] \leftarrow ter(2) + ter(3)$
- $[M_{vv}^\mu] \leftarrow ter(12) + ter(13)$
- $[M_{ww}^\mu] \leftarrow ter(24) + ter(25)$
- $[K_{uu}] \leftarrow ter(4) + ter(5) + ter(10)$
- $[K_{uv}] \leftarrow ter(7) + ter(9)$
- $[K_{uw}] \leftarrow ter(6) + ter(8)$
- $[K_{vu}] \leftarrow ter(16) + ter(22)$
- $[K_{vv}] \leftarrow ter(14) + ter(17) + ter(18) + ter(21)$
- $[K_{vw}] \leftarrow ter(15) + ter(19) + ter(20)$
- $[K_{wu}] \leftarrow ter(28) + ter(34)$
- $[K_{wv}] \leftarrow ter(26) + ter(30) + ter(32)$
- $[K_{ww}] \leftarrow ter(27) + ter(29) + ter(31) + ter(33)$

As the linear problem is implemented to be solved and the modes of vibration extracted, one last decomposition must be considered regarding the time dependence: the generalized displacements are assumed to be dependent on an harmonic function, as done for linear vibrations of a conservative system, coming as expressed below:

$$q^u_{rs}(t) = \overline{q}^u_{rs}\, cos\,\omega t \tag{2.90a}$$

$$q^v_{rs}(t) = \overline{q}^v_{rs}\, cos\,\omega t \tag{2.90b}$$

$$q^w_{rs}(t) = \overline{q}^w_{rs}\, cos\,\omega t \tag{2.90c}$$

Hence, regarding the generalized accelerations comes as:

$$\ddot{q}^u_{rs}(t) = -\omega^2\, \overline{q}^u_{rs}\, cos\,\omega t \tag{2.91a}$$

$$\ddot{q}^v_{rs}(t) = -\omega^2\, \overline{q}^v_{rs}\, cos\,\omega t \tag{2.91b}$$

$$\ddot{q}^w_{rs}(t) = -\omega^2\, \overline{q}^w_{rs}\, cos\,\omega t \tag{2.91c}$$

This process allows to drop the harmonic function from every term, resulting in time-independent equations. This simplification may be assumed as the model is studied in the linear field, where the displacements amplitudes are relatively small.

2.6 Double-walled carbon nanotube

In the present section, the modelling for a double-walled carbon nanotube is developed, following the same procedure described for a single-walled carbon nanotube (or generalized single shell) in the current chapter. For this formulation, the Sanders-Koiter theory is applied to both shells.

First of all, it is necessary to introduce the nomenclature of the new displacements and consequent generalized displacements, for each of the carbon nanotubes in the considered structure: For the inner tube, the displacement components in the middle plane, following the same principle of Figure 2.1, are u^0_1, v^0_1 and w^0_1, while for the outer tube the displacement components are designated u^0_2, v^0_2 and w^0_2.

Following the same procedure applied to obtain Equations (2.18)-(2.20), the governing equations of a double-walled CNT, after neglecting the rotary inertia and considering the effect of the van der Waals pressure on the transverse direction in the place of the initial formulation for non-conservative forces, as its effect on the axial and circumferential direction is negligible [93], come as:

$$\rho h \ddot{u}^0 - \frac{\partial N_{xx}}{\partial x} - \frac{1}{R}\frac{\partial N_{x\theta}}{\partial \theta} + \frac{1}{2R^2}\frac{\partial M_{x\theta}}{\partial \theta} = 0 \tag{2.92}$$

$$\rho h \ddot{v}^0 - \frac{1}{R}\frac{\partial N_{\theta\theta}}{\partial \theta} - \frac{\partial N_{x\theta}}{\partial x} - \frac{1}{R^2}\frac{\partial M_{\theta\theta}}{\partial \theta} - \frac{3}{2R}\frac{\partial M_{x\theta}}{\partial x} = 0 \tag{2.93}$$

$$\rho h \ddot{w}^0 + \frac{N_{\theta\theta}}{R} - \frac{\partial^2 M_{xx}}{\partial x^2} - \frac{1}{R^2}\frac{\partial M_{\theta\theta}}{\partial \theta} - \frac{2}{R}\frac{\partial^2 M_{x\theta}}{\partial x \partial \theta} - p_{vdW} = 0 \tag{2.94}$$

where p_{vdW} is the van der Waals pressure exerted on a shell.

2.6.1 Van der Waals interlayer pressure

According to Timoshenko et al. [94], the van der Waals pressure for a multi-walled shell may be expressed as:

$$p_{vdW} = p_i(x,\theta) = -\sum_{j=1}^{i-1} \overline{p}_{ij} + \sum_{j=i+1}^{Nl} \overline{p}_{ij} + \Delta p_i(x,\theta) = 0 \tag{2.95}$$

where $\overline{p}_{ij}$ is the initial uniform van der Waals pressure contribution to the ith layer from the jth layer before deformation, Nl is the total number of layers of a multi-walled CNT, and $\Delta p_i(x,\theta)$ is the pressure increment after deformation of the CNT. It should be noted that the outward pressure is assumed to be positive, leading to the attractive pressure being positive and the repulsive pressure being negative for the inner tube, with the reverse being true for the outer tube. Considering only the infinitesimal pressure increment, $\Delta p_i(x,\theta)$ is considered to be linearly proportional to the deflection between two layers, resulting in the following expression:

$$\Delta p_i = \sum_{j=1}^{Nl} \Delta p_{ij} = \sum_{j=1}^{Nl} c_{ij}(w_i - w_j) = w_i \sum_{j=1}^{Nl} c_{ij} - \sum_{j=1}^{Nl} c_{ij} w_j \tag{2.96}$$

where Δp_{ij} is the contribution of the pressure increment Δp_i exerted on the ith layer from the jth layer, and c_{ij} is the van der Waals interaction coefficient. Finally, for a double-walled carbon nanotube, the pressure increment comes as:

$$\Delta p_i = w_i \sum_{j=1}^{2} c_{ij} - \sum_{j=1}^{2} c_{ij} w_j \tag{2.97}$$

To determine the coefficient c_{ij}, the van der Waals interaction model between two layers, the Lennard-Jones pair potential V_{IJ} is adopted as [81, 95]:

$$V_{IJ}(\bar{d}) = 4\,\varepsilon \left[\left(\frac{\sigma_{vdW}}{\bar{d}} \right)^{12} - \left(\frac{\sigma_{vdW}}{\bar{d}} \right)^{6} \right] \tag{2.98}$$

where $\bar{d}$ represents the distance between the interacting atoms, ε indicates the depth of the potential, and σ_{vdW} is the parameter determined by the equilibrium distance, adequate to carbon atoms included in a graphene sheet. The van der Waals force F is obtained from taking the derivative of the Lennard-Jones pair potential, as comes:

$$F(\bar{d}) = \frac{\mathrm{d}V_{IJ}(\bar{d})}{\mathrm{d}\bar{d}} = \frac{24\,\varepsilon}{\sigma_{vdW}} \left[2\left(\frac{\sigma_{vdW}}{\bar{d}} \right)^{13} - \left(\frac{\sigma_{vdW}}{\bar{d}} \right)^{7} \right] \tag{2.99}$$

As only the infinitesimal deflection of the CNT is of interest, the van der Waals force may be estimated by the Taylor expansion to the first order around the equilibrium position prior to deflection, as comes:

$$\begin{aligned} F(\bar{d}) &= F(\bar{d}_0) + \frac{\mathrm{d}F(\bar{d}_0)}{\mathrm{d}\bar{d}} \\ &= \frac{24\,\varepsilon}{\sigma_{vdW}} \left[2\left(\frac{\sigma_{vdW}}{\bar{d}_0} \right)^{13} - \left(\frac{\sigma_{vdW}}{\bar{d}_0} \right)^{7} \right] + \frac{24\,\varepsilon}{\sigma_{vdW}^2} \left[26\left(\frac{\sigma_{vdW}}{\bar{d}_0} \right)^{14} - 7\left(\frac{\sigma_{vdW}}{\bar{d}_0} \right)^{8} \right] (\bar{d} - \bar{d}_0) \end{aligned} \tag{2.100}$$

where $\bar{d}_0 = \Big(\big(R_j \cos\theta - R_i\big)^2 + R_j^2 \sin^2\theta + x^2\Big)^{1/2}$ is the initial distance between atoms of different tubes prior to deflection.

Then, the van der Waals force exerted on any atom of the tube may be estimated by summing all forces between a given atom and the atoms of the other tube. Taking into consideration the assumption of the nanotube as a continuum cylindrical shell, as well as the area of each carbon atom to be of $9a^2/4\sqrt{3}$ [96], Equation (2.100) is integrated along the entire nanotube resulting in the analytical representation of the pressure contribution p_i caused by van der Waals interaction as follows:

$$\begin{aligned} p_i &= \left(\frac{4\sqrt{3}}{9a^2}\right)^2 \frac{24\,\varepsilon}{\sigma_{vdW}} \int_{-\pi}^{\pi} \int_{-L/2}^{L/2} \left[2\left(\frac{\sigma_{vdW}}{\bar{d}_0}\right)^{13} - \left(\frac{\sigma_{vdW}}{\bar{d}_0}\right)^{7}\right] R_j \,\mathrm{d}x\,\mathrm{d}\theta \\ &= \left[\frac{2048\varepsilon\sigma_{vdW}^{12}}{9a^4} \sum_{k=0}^{5} \frac{(-1)^k}{2k+1} \binom{5}{k} E_{ij}^{12} - \frac{1024\varepsilon\sigma_{vdW}^{6}}{9a^4} \sum_{k=0}^{2} \frac{(-1)^k}{2k+1} \binom{2}{k} E_{ij}^{6}\right] R_j \end{aligned} \tag{2.101}$$

Finally, the pressure increment comes:

$$\begin{aligned} \Delta p_i &= -\left(\frac{4\sqrt{3}}{9a^2}\right)^2 \frac{24\,\varepsilon}{\sigma_{vdW}} \int_{-\pi}^{\pi} \int_{-L/2}^{L/2} \left[26\left(\frac{\sigma_{vdW}}{\bar{d}_0}\right)^{14} - 7\left(\frac{\sigma_{vdW}}{\bar{d}_0}\right)^{8}\right] \big(\bar{d} - \bar{d}_0\big) R_j \,\mathrm{d}x\,\mathrm{d}\theta \\ &= -\left[\frac{1001\pi\varepsilon\sigma_{vdW}^{12}}{3a^4} E_{ij}^{13} - \frac{1120\pi\varepsilon\sigma_{vdW}^{6}}{9a^4} E_{ij}^{7}\right] R_j (w_i - w_j) \end{aligned} \tag{2.102}$$

where a is the C-C bond length, already defined in this dissertation, R_j is the radius of the jth layer, the subscripts i and j denote the ith and jth layers respectively, and E_{ij}^6, E_{ij}^7, E_{ij}^{12} and E_{ij}^{13} denote the elliptic integrals defined as:

$$E_{ij}^{m} = (R_j + R_i)^{-m} \int_0^{\pi/2} \frac{1}{\big[1 - K_{ij}\cos^2\theta\big]^{m/2}} \tag{2.103}$$

where m is an integer and

$$K_{ij} = \frac{4R_j R_i}{\big(R_j + R_i\big)^2} \tag{2.104}$$

Lastly, comparing Equations (2.102) and (2.97), the van der Waals interaction coefficients may be expressed as:

$$c_{ij} = -\left[\frac{1001\pi\varepsilon\sigma_{vdW}^{12}}{3a^4} E_{ij}^{13} - \frac{1120\pi\varepsilon\sigma_{vdW}^{6}}{9a^4} E_{ij}^{7}\right] R_j \tag{2.105}$$

2.6.2 Application of Eringen's nonlocal elasticity theory

After the development and application of the Lennard-Jones potential in the van der Waals pressure, the equations of motion for each nanotube may be developed as the previously described Eringen's nonlocal theory is incorporated into the stress components, in Equations (2.33) and further substituted in Equations (2.92)-(2.94). Thus, the generalized equations of motions for a nanotube i come as:

$$\begin{aligned}\rho h\left(1-(e_0a)^2\nabla^2\right)\ddot{u}_i^0 - \frac{Eh}{1-\nu^2}\left[\frac{\partial^2 u_i^0}{\partial x^2} + \frac{1-\nu}{2}\frac{1}{R_i^2}\frac{\partial^2 u_i^0}{\partial \theta^2} + \nu\frac{1}{R_i}\frac{\partial w_i^0}{\partial x} + \frac{1+\nu}{2}\frac{1}{R_i}\frac{\partial^2 v_i^0}{\partial x\partial\theta}\right]\\ - \frac{Eh^3}{24(1+\nu)R_i^3}\left[\frac{\partial^3 w_i^0}{\partial x\partial\theta^2} - \frac{3}{4}\frac{\partial^2 v_i^0}{\partial x\partial\theta} + \frac{1}{4R_i}\frac{\partial^2 u_i^0}{\partial\theta^2}\right] = 0\end{aligned} \tag{2.106}$$

$$\begin{aligned}\rho h\left(1-(e_0a)^2\nabla^2\right)\ddot{v}_i^0 - \frac{Eh}{1-\nu^2}\left[\frac{1}{R_i^2}\frac{\partial^2 v_i^0}{\partial\theta^2} + \frac{1}{R_i^2}\frac{\partial w_i^0}{\partial\theta} + \frac{1+\nu}{2}\frac{1}{R_i}\frac{\partial^2 u_i^0}{\partial x\partial\theta} + \frac{1-\nu}{2}\frac{\partial^2 v_i^0}{\partial x^2}\right]\\ - \frac{Eh^3}{12(1-\nu^2)}\left[\frac{1}{R_i^4}\frac{\partial^2 v_i^0}{\partial\theta^2} - \frac{1}{R_i^4}\frac{\partial^3 w_i^0}{\partial\theta^3} - \frac{3-\nu}{2}\frac{1}{R_i^2}\frac{\partial^3 w_i^0}{\partial x^2\partial\theta}\right.\\ \left. + \frac{9(1-\nu)}{8R_i^2}\frac{\partial^2 v_i^0}{\partial x^2} - \frac{3(1-\nu)}{8R_i^3}\frac{\partial^2 u_i^0}{\partial x\partial\theta}\right] = 0\end{aligned} \tag{2.107}$$

$$\begin{aligned}\rho h\left(1-(e_0a)^2\nabla^2\right)\ddot{w}_i^0 + \frac{Eh}{1-\nu^2}\left[\frac{1}{R_i^2}\frac{\partial v_i^0}{\partial\theta} + \frac{w_i^0}{R_i^2} + \nu\frac{1}{R_i}\frac{\partial u_i^0}{\partial x}\right] + \frac{Eh^3}{12(1-\nu^2)}\left[\frac{\partial^4 w_i^0}{\partial x^4}\right.\\ \left. - \frac{3-\nu}{2R_i^2}\frac{\partial^3 v_i^0}{\partial x^2\partial\theta} + \frac{2}{R_i^2}\frac{\partial^4 w_i^0}{\partial x^2\partial\theta^2} - \frac{1}{R_i^4}\frac{\partial^3 v_i^0}{\partial\theta^3} + \frac{1}{R_i^4}\frac{\partial^4 w_i^0}{\partial\theta^4} + \frac{1-\nu}{2}\frac{1}{R_i^3}\frac{\partial^3 u_i^0}{\partial x\partial\theta^2}\right]\\ - \left(1-(e_0a)^2\nabla^2\right)\left[w_i^0\sum_{j=1}^{2}c_{ij} - \sum_{j=1}^{2}c_{ij}w_j^0\right] = 0\end{aligned} \tag{2.108}$$

where $i = 1, 2$ for the inner and the outer tube, respectively.

2.6.3 The *p*-version Finite Element Method

Discretization of displacement components

Regarding the discretization of displacement components, a similar process to the one described for SWCNT is applied. The chosen shape functions are the same than those described on the SWCNT section, and thus the are not mentioned again on this subsection.

Analogously, the middle surface displacements can be described as the product of a shape function combination matrix and the vector of generalized nodal displacements, as follows:

$$\{de^0\} = \begin{Bmatrix} u_1^0 \\ v_1^0 \\ w_1^0 \\ u_2^0 \\ v_2^0 \\ w_2^0 \end{Bmatrix} = [N]\{q\} = \begin{bmatrix} \{\delta_1\}^T & 0 & 0 & 0 & 0 & 0 \\ 0 & \{\delta_2\}^T & 0 & 0 & 0 & 0 \\ 0 & 0 & \{\delta_3\}^T & 0 & 0 & 0 \\ 0 & 0 & 0 & \{\delta_4\}^T & 0 & 0 \\ 0 & 0 & 0 & 0 & \{\delta_5\}^T & 0 \\ 0 & 0 & 0 & 0 & 0 & \{\delta_6\}^T \end{bmatrix}\{q\} \tag{2.109}$$

where:

$$\{\delta_1\}^T = \{f^{u_1}_{1x} f^{u_1}_{1\theta}, f^{u_1}_{1x} f^{u_1}_{2\theta}, \dots, f^{u_1}_{pgu\,x} f^{u_1}_{ptu\,\theta}\}$$

$$\{\delta_2\}^T = \{f^{v_1}_{1x} f^{v_1}_{1\theta}, f^{v_1}_{1x} f^{v_1}_{2\theta}, \dots, f^{v_1}_{pgv\,x} f^{v_1}_{ptv\,\theta}\}$$

$$\{\delta_3\}^T = \{f^{w_1}_{1x} f^{w_1}_{1\theta}, f^{w_1}_{1x} f^{w_1}_{2\theta}, \dots, f^{w_1}_{pw\,x} f^{w_1}_{ptw\,\theta}\}$$

$$\{\delta_4\}^T = \{f^{u_2}_{1x} f^{u_2}_{1\theta}, f^{u_2}_{1x} f^{u_2}_{2\theta}, \dots, f^{u_2}_{pgu\,x} f^{u_2}_{ptu\,\theta}\}$$

$$\{\delta_5\}^T = \{f^{v_2}_{1x} f^{v_2}_{1\theta}, f^{v_2}_{1x} f^{v_2}_{2\theta}, \dots, f^{v_2}_{pgv\,x} f^{v_2}_{ptv\,\theta}\}$$

$$\{\delta_6\}^T = \{f^{w_2}_{1x} f^{w_2}_{1\theta}, f^{w_2}_{1x} f^{w_2}_{2\theta}, \dots, f^{w_2}_{pw\,x} f^{w_2}_{ptw\,\theta}\}$$

And $\{q\}$ is defined as:

$$\{q\} = \begin{Bmatrix} q^{u_1}_{11}; q^{u_1}_{12}; \cdots ; q^{u_1}_{pgu-ptu} \\ q^{v_1}_{11}; q^{v_1}_{12}; \cdots ; q^{v_1}_{pgv-ptv} \\ q^{w_1}_{11}; q^{w_1}_{12}; \cdots ; q^{w_1}_{pw-ptw} \\ q^{u_2}_{11}; q^{u_2}_{12}; \cdots ; q^{u_2}_{pgu-ptu} \\ q^{v_2}_{11}; q^{v_2}_{12}; \cdots ; q^{v_2}_{pgv-ptv} \\ q^{w_2}_{11}; q^{w_2}_{12}; \cdots ; q^{w_2}_{pw-ptw} \end{Bmatrix} \tag{2.110}$$

where pgu, pgv and pw define the number of shape functions allocated to the displacements of u_i^0, v_i^0 and w_i^0 $(i = 1, 2)$ in the coordinate of x, respectively, and ptu, ptv and ptw define the number of shape functions allocated to the displacements of u_i^0, v_i^0 and w_i^0 $(i = 1, 2)$ in the coordinate of θ, respectively.

Lastly, the displacements in Equation (2.109) can be displayed in the compact matrix form, as follows:

$$\{de^0(x,\theta,t)\} = \begin{Bmatrix} u_1^0(x,\theta,t) \\ v_1^0(x,\theta,t) \\ w_1^0(x,\theta,t) \\ u_2^0(x,\theta,t) \\ v_2^0(x,\theta,t) \\ w_2^0(x,\theta,t) \end{Bmatrix} = \begin{Bmatrix} \sum\limits_{r=1}^{pgu} \sum\limits_{s=1}^{ptu} f^{u_1}_{rx}(x) f^{u_1}_{s\theta}(\theta)\, q^{u_1}_{rs}(t) \\ \sum\limits_{r=1}^{pgv} \sum\limits_{s=1}^{ptv} f^{v_1}_{rx}(x) f^{v_1}_{s\theta}(\theta)\, q^{v_1}_{rs}(t) \\ \sum\limits_{r=1}^{pw} \sum\limits_{s=1}^{ptw} f^{w_1}_{rx}(x) f^{w_1}_{s\theta}(\theta)\, q^{w_1}_{rs}(t) \\ \sum\limits_{r=1}^{pgu} \sum\limits_{s=1}^{ptu} f^{u_2}_{rx}(x) f^{u_2}_{s\theta}(\theta)\, q^{u_2}_{rs}(t) \\ \sum\limits_{r=1}^{pgv} \sum\limits_{s=1}^{ptv} f^{v_2}_{rx}(x) f^{v_2}_{s\theta}(\theta)\, q^{v_2}_{rs}(t) \\ \sum\limits_{r=1}^{pw} \sum\limits_{s=1}^{ptw} f^{w_2}_{rx}(x) f^{w_2}_{s\theta}(\theta)\, q^{w_2}_{rs}(t) \end{Bmatrix} \tag{2.111}$$

Finite Element Matrices

Following a procedure analogous to the one for a single-walled nanotube in the present chapter, the Galerkin method is applied in order to obtain the weak formulation. The following equations are presented:

$$\int_0^{2\pi} \int_0^l f_r^{u_1}(x)\, f_s^{u_1}(\theta)\, \mathcal{L}_{u_1}(x,\theta,t)\, \mathrm{d}x\, R_1\, \mathrm{d}\theta \tag{2.112}$$

$$\int_0^{2\pi} \int_0^l f_r^{v_1}(x)\, f_s^{v_1}(\theta)\, \mathcal{L}_{v_1}(x,\theta,t)\, \mathrm{d}x\, R_1\, \mathrm{d}\theta \tag{2.113}$$

$$\int_0^{2\pi}\int_0^{l} f_r^{w_1}(x)\, f_s^{w_1}(\theta)\, \mathcal{L}_{w_1}(x,\theta,t)\, \mathrm{d}x\, R_1\, \mathrm{d}\theta \tag{2.114}$$

$$\int_0^{2\pi}\int_0^{l} f_r^{u_2}(x)\, f_s^{u_2}(\theta)\, \mathcal{L}_{u_2}(x,\theta,t)\, \mathrm{d}x\, R_2\, \mathrm{d}\theta \tag{2.115}$$

$$\int_0^{2\pi}\int_0^{l} f_r^{v_2}(x)\, f_s^{v_2}(\theta)\, \mathcal{L}_{v_2}(x,\theta,t)\, \mathrm{d}x\, R_2\, \mathrm{d}\theta \tag{2.116}$$

$$\int_0^{2\pi}\int_0^{l} f_r^{w_2}(x)\, f_s^{w_2}(\theta)\, \mathcal{L}_{w_2}(x,\theta,t)\, \mathrm{d}x\, R_2\, \mathrm{d}\theta \tag{2.117}$$

where $\mathcal{L}_{u_1}(x,\theta,t)$ and $\mathcal{L}_{u_2}(x,\theta,t)$ come from Equation (2.106), $\mathcal{L}_{v_1}(x,\theta,t)$ and $\mathcal{L}_{v_1}(x,\theta,t)$ come from Equation (2.107), and finally $\mathcal{L}_{w_1}(x,\theta,t)$ and $\mathcal{L}_{w_2}(x,\theta,t)$ come from Equation (2.108) after substitution of the value of i.

It is important to note that the employed formulation allows for the usage of different shape functions for the inner and the outer tube. Therefore, hypothetically, the boundary conditions of the inner and outer tubes may be different and a study on that matter may be performed. Furthermore, these equations are then presented with the differential operator ∇ expanded, and with each differential term associated with the respective sum term resultant from the Galerkin method application, designated from $ter(35)$ to , resulting again in the linear model algebraic terms.

Thus, for the equation of motion in u_1^0 comes:

$$\begin{aligned}
\mathcal{L}_{u_1}(x,\theta,t) = \rho h & \left[\underbrace{\frac{\partial^2 u_1^0}{\partial t^2}}_{ter(35)} - (e_0\, a)^2 \left[\underbrace{\frac{\partial^2}{\partial x^2}\left(\frac{\partial^2 u_1^0}{\partial t^2}\right)}_{ter(36)} + \underbrace{\frac{1}{R_1^2}\frac{\partial^2}{\partial \theta^2}\left(\frac{\partial^2 u_1^0}{\partial t^2}\right)}_{ter(37)} \right] \right] \\
& - \frac{Eh}{1-\nu^2}\left[\underbrace{\frac{\partial^2 u_1^0}{\partial x^2}}_{ter(38)} + \underbrace{\frac{1-\nu}{2}\frac{1}{R_1^2}\frac{\partial^2 u_1^0}{\partial \theta^2}}_{ter(39)} + \nu \underbrace{\frac{1}{R_1}\frac{\partial w_1^0}{\partial x}}_{ter(40)} + \underbrace{\frac{1+\nu}{2}\frac{1}{R_1}\frac{\partial^2 v_1^0}{\partial x \partial \theta}}_{ter(41)} \right] \\
& \qquad - \frac{Eh^3}{24(1+\nu)R_1^3}\left[\underbrace{\frac{\partial^3 w_1^0}{\partial x \partial \theta^2}}_{ter(42)} - \underbrace{\frac{3}{4}\frac{\partial^2 v_1^0}{\partial x \partial \theta}}_{ter(43)} + \underbrace{\frac{1}{4R_1}\frac{\partial^2 u_1^0}{\partial \theta^2}}_{ter(44)} \right] = 0
\end{aligned} \tag{2.118}$$

For the equation of motion in v_1^0 comes:

$$\begin{aligned}
\mathcal{L}_{v_1}(x,\theta,t) = \rho h & \left[\underbrace{\frac{\partial^2 v_1^0}{\partial t^2}}_{ter(45)} - (e_0\, a)^2 \left[\underbrace{\frac{\partial^2}{\partial x^2}\left(\frac{\partial^2 v_1^0}{\partial t^2}\right)}_{ter(46)} + \underbrace{\frac{1}{R_1^2}\frac{\partial^2}{\partial \theta^2}\left(\frac{\partial^2 v_1^0}{\partial t^2}\right)}_{ter(47)} \right] \right] \\
& - \frac{Eh}{1-\nu^2}\left[\underbrace{\frac{1}{R_1^2}\frac{\partial^2 v_1^0}{\partial \theta^2}}_{ter(48)} + \underbrace{\frac{1}{R_1^2}\frac{\partial w_1^0}{\partial \theta}}_{ter(49)} + \underbrace{\frac{1+\nu}{2}\frac{1}{R_1}\frac{\partial^2 u_1^0}{\partial x \partial \theta}}_{ter(50)} + \underbrace{\frac{1-\nu}{2}\frac{\partial^2 v_1^0}{\partial x^2}}_{ter(51)} \right] \\
& - \frac{Eh^3}{12(1-\nu^2)}\left[\underbrace{\frac{1}{R_1^4}\frac{\partial^2 v_1^0}{\partial \theta^2}}_{ter(52)} - \underbrace{\frac{1}{R_1^4}\frac{\partial^3 w_1^0}{\partial \theta^3}}_{ter(53)} - \underbrace{\frac{3-\nu}{2}\frac{1}{R_1^2}\frac{\partial^3 w_1^0}{\partial x^2 \partial \theta}}_{ter(54)} \right. \\
& \qquad \left. + \underbrace{\frac{9(1-\nu)}{8R_1^2}\frac{\partial^2 v_1^0}{\partial x^2}}_{ter(55)} - \underbrace{\frac{3(1-\nu)}{8R_1^3}\frac{\partial^2 u_1^0}{\partial x \partial \theta}}_{ter(56)} \right] = 0
\end{aligned} \tag{2.119}$$

For the equation of motion in w_1^0 comes:

$$\begin{aligned}\mathcal{L}_{w_1}(x,\theta,t) = \rho h &\left[\underbrace{\frac{\partial^2 w_1^0}{\partial t^2}}_{ter(57)} - (e_0\, a)^2 \left[\underbrace{\frac{\partial^2}{\partial x^2}\left(\frac{\partial^2 w_1^0}{\partial t^2}\right)}_{ter(58)} + \underbrace{\frac{1}{R_1^2}\frac{\partial^2}{\partial \theta^2}\left(\frac{\partial^2 w_1^0}{\partial t^2}\right)}_{ter(59)} \right] \right] \\
+ \frac{Eh}{1-\nu^2} &\left[\underbrace{\frac{1}{R_1^2}\frac{\partial v_1^0}{\partial \theta}}_{ter(60)} + \underbrace{\frac{w_1^0}{R_1^2}}_{ter(61)} + \nu \underbrace{\frac{1}{R_1}\frac{\partial u_1^0}{\partial x}}_{ter(62)} \right] + \frac{Eh^3}{12(1-\nu^2)} \left[\underbrace{\frac{\partial^4 w_1^0}{\partial x^4}}_{ter(63)} - \underbrace{\frac{3-\nu}{2R_1^2}\frac{\partial^3 v_1^0}{\partial x^2 \partial \theta}}_{ter(64)} + \underbrace{\frac{2}{R_1^2}\frac{\partial^4 w_1^0}{\partial x^2 \partial \theta^2}}_{ter(65)} \right. \\
&\left. - \underbrace{\frac{1}{R_1^4}\frac{\partial^3 v_1^0}{\partial \theta^3}}_{ter(66)} + \underbrace{\frac{1}{R_1^4}\frac{\partial^4 w_1^0}{\partial \theta^4}}_{ter(67)} + \underbrace{\frac{1-\nu}{2}\frac{1}{R_1^3}\frac{\partial^3 u_1^0}{\partial x \partial \theta^2}}_{ter(68)} \right] \\
&+ c_{12} \left[\underbrace{w_2^0}_{ter(69)} - \underbrace{w_1^0}_{ter(70)} + (e_0 a)^2 \left(\underbrace{\frac{\partial^2 w_1^0}{\partial x^2}}_{ter(71)} + \underbrace{\frac{1}{R_1^2}\frac{\partial^2 w_1^0}{\partial \theta^2}}_{ter(72)} - \underbrace{\frac{\partial^2 w_2^0}{\partial x^2}}_{ter(73)} - \underbrace{\frac{1}{R_1^2}\frac{\partial^2 w_2^0}{\partial \theta^2}}_{ter(74)} \right) \right] = 0
\end{aligned} \tag{2.120}$$

For the equation of motion in u_2^0 comes:

$$\begin{aligned}\mathcal{L}_{u_2}(x,\theta,t) = \rho h &\left[\underbrace{\frac{\partial^2 u_2^0}{\partial t^2}}_{ter(75)} - (e_0\, a)^2 \left[\underbrace{\frac{\partial^2}{\partial x^2}\left(\frac{\partial^2 u_2^0}{\partial t^2}\right)}_{ter(76)} + \underbrace{\frac{1}{R_2^2}\frac{\partial^2}{\partial \theta^2}\left(\frac{\partial^2 u_2^0}{\partial t^2}\right)}_{ter(77)} \right] \right] \\
- \frac{Eh}{1-\nu^2} &\left[\underbrace{\frac{\partial^2 u_2^0}{\partial x^2}}_{ter(78)} + \underbrace{\frac{1-\nu}{2}\frac{1}{R_2^2}\frac{\partial^2 u_2^0}{\partial \theta^2}}_{ter(79)} + \nu \underbrace{\frac{1}{R_2}\frac{\partial w_2^0}{\partial x}}_{ter(80)} + \underbrace{\frac{1+\nu}{2}\frac{1}{R_2}\frac{\partial^2 v_2^0}{\partial x \partial \theta}}_{ter(81)} \right] \\
&- \frac{Eh^3}{24(1+\nu)R_2^3} \left[\underbrace{\frac{\partial^3 w_2^0}{\partial x \partial \theta^2}}_{ter(82)} - \underbrace{\frac{3}{4}\frac{\partial^2 v_2^0}{\partial x \partial \theta}}_{ter(83)} + \underbrace{\frac{1}{4R_2}\frac{\partial^2 u_2^0}{\partial \theta^2}}_{ter(84)} \right] = 0
\end{aligned} \tag{2.121}$$

For the equation of motion in v_2^0 comes:

$$\begin{aligned}\mathcal{L}_{v_2}(x,\theta,t) = \rho h &\left[\underbrace{\frac{\partial^2 v_2^0}{\partial t^2}}_{ter(85)} - (e_0\, a)^2 \left[\underbrace{\frac{\partial^2}{\partial x^2}\left(\frac{\partial^2 v_2^0}{\partial t^2}\right)}_{ter(86)} + \underbrace{\frac{1}{R_2^2}\frac{\partial^2}{\partial \theta^2}\left(\frac{\partial^2 v_2^0}{\partial t^2}\right)}_{ter(87)} \right] \right] \\
- \frac{Eh}{1-\nu^2} &\left[\underbrace{\frac{1}{R_2^2}\frac{\partial^2 v_2^0}{\partial \theta^2}}_{ter(88)} + \underbrace{\frac{1}{R_2^2}\frac{\partial w_2^0}{\partial \theta}}_{ter(89)} + \underbrace{\frac{1+\nu}{2}\frac{1}{R_2}\frac{\partial^2 u_2^0}{\partial x \partial \theta}}_{ter(90)} + \underbrace{\frac{1-\nu}{2}\frac{\partial^2 v_2^0}{\partial x^2}}_{ter(91)} \right] \\
- \frac{Eh^3}{12(1-\nu^2)} &\left[\underbrace{\frac{1}{R_2^4}\frac{\partial^2 v_2^0}{\partial \theta^2}}_{ter(92)} - \underbrace{\frac{1}{R_2^4}\frac{\partial^3 w_2^0}{\partial \theta^3}}_{ter(93)} - \underbrace{\frac{3-\nu}{2}\frac{1}{R_2^2}\frac{\partial^3 w_2^0}{\partial x^2 \partial \theta}}_{ter(94)} \right. \\
&\left. + \underbrace{\frac{9(1-\nu)}{8R_2^2}\frac{\partial^2 v_2^0}{\partial x^2}}_{ter(95)} - \underbrace{\frac{3(1-\nu)}{8R_2^3}\frac{\partial^2 u_2^0}{\partial x \partial \theta}}_{ter(96)} \right] = 0
\end{aligned} \tag{2.122}$$

For the equation of motion in w_2^0 comes:

$$\begin{aligned}
\mathcal{L}_{w_2}(x,\theta,t) = \rho h \Bigg[& \underbrace{\frac{\partial^2 w_2^0}{\partial t^2}}_{ter(97)} - (e_0\, a)^2 \Bigg[\underbrace{\frac{\partial^2}{\partial x^2}\left(\frac{\partial^2 w_2^0}{\partial t^2}\right)}_{ter(98)} + \underbrace{\frac{1}{R_2^2}\frac{\partial^2}{\partial \theta^2}\left(\frac{\partial^2 w_2^0}{\partial t^2}\right)}_{ter(99)} \Bigg] \Bigg] \\
+ \frac{Eh}{1-\nu^2} \Bigg[& \underbrace{\frac{1}{R_2^2}\frac{\partial v_2^0}{\partial \theta}}_{ter(100)} + \underbrace{\frac{w_2^0}{R_2^2}}_{ter(101)} + \nu \underbrace{\frac{1}{R_2}\frac{\partial u_2^0}{\partial x}}_{ter(102)} \Bigg] + \frac{Eh^3}{12(1-\nu^2)} \Bigg[\underbrace{\frac{\partial^4 w_2^0}{\partial x^4}}_{ter(103)} - \underbrace{\frac{3-\nu}{2R_2^2}\frac{\partial^3 v_2^0}{\partial x^2 \partial \theta}}_{ter(104)} + \underbrace{\frac{2}{R_2^2}\frac{\partial^4 w_2^0}{\partial x^2 \partial \theta^2}}_{ter(105)} \\
& - \underbrace{\frac{1}{R_2^4}\frac{\partial^3 v_2^0}{\partial \theta^3}}_{ter(106)} + \underbrace{\frac{1}{R_2^4}\frac{\partial^4 w_2^0}{\partial \theta^4}}_{ter(107)} + \underbrace{\frac{1-\nu}{2}\frac{1}{R_2^3}\frac{\partial^3 u_2^0}{\partial x \partial \theta^2}}_{ter(108)} \Bigg] \\
+ c_{21} \Bigg[& \underbrace{w_1^0}_{ter(109)} - \underbrace{w_2^0}_{ter(110)} + (e_0 a)^2 \left(\underbrace{\frac{\partial^2 w_2^0}{\partial x^2}}_{ter(111)} + \underbrace{\frac{1}{R_2^2}\frac{\partial^2 w_2^0}{\partial \theta^2}}_{ter(112)} - \underbrace{\frac{\partial^2 w_1^0}{\partial x^2}}_{ter(113)} - \underbrace{\frac{1}{R_2^2}\frac{\partial^2 w_1^0}{\partial \theta^2}}_{ter(114)} \right) \Bigg] = 0
\end{aligned} \tag{2.123}$$

As may be concluded comparison to the single shell model, the terms $ter(35) - ter(68)$ for the inner tube, and $ter(75) - ter(108)$ for the outer tube from the present model are analogous to the terms $ter(1) - ter(34)$, which were already expanded in the previous section. It is, therefore, redundant to expand the terms associated with the singular shell model for each layer, as the main difference in formulation is the radius and the associated generalized coordinate. Thus, only the terms with respect to the van der Waals force are expanded, from Equations (2.114) and (2.117):

$$\begin{aligned}
ter(69):\ & c_{12} \int_0^{2\pi} \int_0^l f_{ix}^{w_1}\, f_{i\theta}^{w_1} \cdot (f_{jx}^{w_2}\, f_{j\theta}^{w_2})\, \mathrm{d}x\, R_1\, \mathrm{d}\theta\ q_{ij}^{w_2}(t) \\
& = c_{12}\, R_1\, \frac{l}{2} \int_0^{2\pi} f_{i\theta}^{w_1}\, f_{j\theta}^{w_2}\, \mathrm{d}\theta \int_{-1}^{1} f_{i\xi}^{w_1}\, f_{j\xi}^{w_2} \mathrm{d}\xi\ q_{ij}^{w_2}(t)
\end{aligned} \tag{2.124}$$

$$\begin{aligned}
ter(70):\ & -c_{12} \int_0^{2\pi} \int_0^l f_{ix}^{w_1}\, f_{i\theta}^{w_1} \cdot (f_{jx}^{w_1}\, f_{j\theta}^{w_1})\, \mathrm{d}x\, R_1\, \mathrm{d}\theta\ q_{ij}^{w_1}(t) \\
& = -c_{12}\, R_1\, \frac{l}{2} \int_0^{2\pi} f_{i\theta}^{w_1}\, f_{j\theta}^{w_1}\, \mathrm{d}\theta \int_{-1}^{1} f_{i\xi}^{w_1}\, f_{j\xi}^{w_1} \mathrm{d}\xi\ q_{ij}^{w_1}(t)
\end{aligned} \tag{2.125}$$

$$\begin{aligned}
ter(71):\ & c_{12}\, (e_0\, a)^2 \int_0^{2\pi} \int_0^l f_{ix}^{w_1}\, f_{i\theta}^{w_1} \cdot \frac{\partial^2}{\partial x^2} \big(f_{jx}^{w_1}\, f_{j\theta}^{w_1}\big)\, \mathrm{d}x\, R_1\, \mathrm{d}\theta\ q_{ij}^{w_1}(t) \\
& = -c_{12}\, (e_0\, a)^2\, R_1\, \frac{2}{l} \int_0^{2\pi} f_{i\theta}^{w_1}\, f_{j\theta}^{w_1}\, \mathrm{d}\theta \int_{-1}^{1} \frac{\mathrm{d}f_{i\xi}^{w_1}}{\mathrm{d}\xi}\, \frac{\mathrm{d}f_{j\xi}^{w_1}}{\mathrm{d}\xi} \mathrm{d}\xi\ q_{ij}^{w_1}(t)
\end{aligned} \tag{2.126}$$

$$\begin{aligned}
ter(72):\ & c_{12}\, (e_0\, a)^2 \frac{1}{R_1^2} \int_0^{2\pi} \int_0^l f_{ix}^{w_1}\, f_{i\theta}^{w_1} \cdot \frac{\partial^2}{\partial \theta^2} \big(f_{jx}^{w_1}\, f_{j\theta}^{w_1}\big)\, \mathrm{d}x\, R_1\, \mathrm{d}\theta\ q_{ij}^{w_1}(t) \\
& = -c_{12}\, (e_0\, a)^2\, \frac{1}{R_1}\, \frac{l}{2} \int_0^{2\pi} \frac{\mathrm{d}f_{i\theta}^{w_1}}{\mathrm{d}\theta}\, \frac{\mathrm{d}f_{j\theta}^{w_1}}{\mathrm{d}\theta}\, \mathrm{d}\theta \int_{-1}^{1} f_{i\xi}^{w_1}\, f_{j\xi}^{w_1} \mathrm{d}\xi\ q_{ij}^{w_1}(t)
\end{aligned} \tag{2.127}$$

$$\begin{aligned}
ter(73):\ & -c_{12}\,(e_0\,a)^2 \int_0^{2\pi}\int_0^l f_{ix}^{w_1}\,f_{i\theta}^{w_1}\cdot\frac{\partial^2}{\partial x^2}\big(f_{jx}^{w_2}\,f_{j\theta}^{w_2}\big)\,\mathrm{d}x\,R_1\,\mathrm{d}\theta\;q_{ij}^{w_2}(t)\\
&= c_{12}\,(e_0\,a)^2\,R_1\,\frac{2}{l}\int_0^{2\pi} f_{i\theta}^{w_1}\,f_{j\theta}^{w_2}\,\mathrm{d}\theta\int_{-1}^{1}\frac{\mathrm{d}f_{i\xi}^{w_1}}{\mathrm{d}\xi}\,\frac{\mathrm{d}f_{j\xi}^{w_2}}{\mathrm{d}\xi}\mathrm{d}\xi\;q_{ij}^{w_2}(t)
\end{aligned} \tag{2.128}$$

$$\begin{aligned}
ter(74):\ & -c_{12}\,(e_0\,a)^2\frac{1}{R_1^2}\int_0^{2\pi}\int_0^l f_{ix}^{w_1}\,f_{i\theta}^{w_1}\cdot\frac{\partial^2}{\partial \theta^2}\big(f_{jx}^{w_2}\,f_{j\theta}^{w_2}\big)\,\mathrm{d}x\,R_1\,\mathrm{d}\theta\;q_{ij}^{w_2}(t)\\
&= c_{12}\,(e_0\,a)^2\,\frac{1}{R_1}\,\frac{l}{2}\int_0^{2\pi}\frac{\mathrm{d}f_{i\theta}^{w_1}}{\mathrm{d}\theta}\,\frac{\mathrm{d}f_{j\theta}^{w_2}}{\mathrm{d}\theta}\,\mathrm{d}\theta\int_{-1}^{1} f_{i\xi}^{w_1}\,f_{j\xi}^{w_2}\mathrm{d}\xi\;q_{ij}^{w_2}(t)
\end{aligned} \tag{2.129}$$

$$\begin{aligned}
ter(109):\ & c_{21}\int_0^{2\pi}\int_0^l f_{ix}^{w_2}\,f_{i\theta}^{w_2}\cdot\big(f_{jx}^{w_1}\,f_{j\theta}^{w_1}\big)\,\mathrm{d}x\,R_2\,\mathrm{d}\theta\;q_{ij}^{w_1}(t)\\
&= c_{21}\,R_2\,\frac{l}{2}\int_0^{2\pi} f_{i\theta}^{w_2}\,f_{j\theta}^{w_1}\,\mathrm{d}\theta\int_{-1}^{1} f_{i\xi}^{w_2}\,f_{j\xi}^{w_1}\mathrm{d}\xi\;q_{ij}^{w_1}(t)
\end{aligned} \tag{2.130}$$

$$\begin{aligned}
ter(110):\ & -c_{21}\int_0^{2\pi}\int_0^l f_{ix}^{w_2}\,f_{i\theta}^{w_2}\cdot\big(f_{jx}^{w_2}\,f_{j\theta}^{w_2}\big)\,\mathrm{d}x\,R_2\,\mathrm{d}\theta\;q_{ij}^{w_2}(t)\\
&= -c_{21}\,R_2\,\frac{l}{2}\int_0^{2\pi} f_{i\theta}^{w_2}\,f_{j\theta}^{w_2}\,\mathrm{d}\theta\int_{-1}^{1} f_{i\xi}^{w_2}\,f_{j\xi}^{w_2}\mathrm{d}\xi\;q_{ij}^{w_2}(t)
\end{aligned} \tag{2.131}$$

$$\begin{aligned}
ter(111):\ & c_{21}\,(e_0\,a)^2 \int_0^{2\pi}\int_0^l f_{ix}^{w_2}\,f_{i\theta}^{w_2}\cdot\frac{\partial^2}{\partial x^2}\big(f_{jx}^{w_2}\,f_{j\theta}^{w_2}\big)\,\mathrm{d}x\,R_2\,\mathrm{d}\theta\;q_{ij}^{w_2}(t)\\
&= -c_{21}\,(e_0\,a)^2\,R_2\,\frac{2}{l}\int_0^{2\pi} f_{i\theta}^{w_2}\,f_{j\theta}^{w_2}\,\mathrm{d}\theta\int_{-1}^{1}\frac{\mathrm{d}f_{i\xi}^{w_2}}{\mathrm{d}\xi}\,\frac{\mathrm{d}f_{j\xi}^{w_2}}{\mathrm{d}\xi}\mathrm{d}\xi\;q_{ij}^{w_2}(t)
\end{aligned} \tag{2.132}$$

$$\begin{aligned}
ter(112):\ & c_{21}\,(e_0\,a)^2\frac{1}{R_2^2}\int_0^{2\pi}\int_0^l f_{ix}^{w_2}\,f_{i\theta}^{w_2}\cdot\frac{\partial^2}{\partial \theta^2}\big(f_{jx}^{w_2}\,f_{j\theta}^{w_2}\big)\,\mathrm{d}x\,R_2\,\mathrm{d}\theta\;q_{ij}^{w_2}(t)\\
&= -c_{21}\,(e_0\,a)^2\,\frac{1}{R_2}\,\frac{l}{2}\int_0^{2\pi}\frac{\mathrm{d}f_{i\theta}^{w_2}}{\mathrm{d}\theta}\,\frac{\mathrm{d}f_{j\theta}^{w_2}}{\mathrm{d}\theta}\,\mathrm{d}\theta\int_{-1}^{1} f_{i\xi}^{w_2}\,f_{j\xi}^{w_2}\mathrm{d}\xi\;q_{ij}^{w_2}(t)
\end{aligned} \tag{2.133}$$

$$\begin{aligned}
ter(113):\ & -c_{21}\,(e_0\,a)^2 \int_0^{2\pi}\int_0^l f_{ix}^{w_2}\,f_{i\theta}^{w_2}\cdot\frac{\partial^2}{\partial x^2}\big(f_{jx}^{w_1}\,f_{j\theta}^{w_1}\big)\,\mathrm{d}x\,R_2\,\mathrm{d}\theta\;q_{ij}^{w_1}(t)\\
&= c_{21}\,(e_0\,a)^2\,R_2\,\frac{2}{l}\int_0^{2\pi} f_{i\theta}^{w_2}\,f_{j\theta}^{w_1}\,\mathrm{d}\theta\int_{-1}^{1}\frac{\mathrm{d}f_{i\xi}^{w_2}}{\mathrm{d}\xi}\,\frac{\mathrm{d}f_{j\xi}^{w_1}}{\mathrm{d}\xi}\mathrm{d}\xi\;q_{ij}^{w_1}(t)
\end{aligned} \tag{2.134}$$

$$\begin{aligned}
ter(114):\ & -c_{21}\,(e_0\,a)^2\frac{1}{R_2^2}\int_0^{2\pi}\int_0^l f_{ix}^{w_2}\,f_{i\theta}^{w_2}\cdot\frac{\partial^2}{\partial \theta^2}\big(f_{jx}^{w_1}\,f_{j\theta}^{w_1}\big)\,\mathrm{d}x\,R_2\,\mathrm{d}\theta\;q_{ij}^{w_1}(t)\\
&= c_{21}\,(e_0\,a)^2\,\frac{1}{R_2}\,\frac{l}{2}\int_0^{2\pi}\frac{\mathrm{d}f_{i\theta}^{w_2}}{\mathrm{d}\theta}\,\frac{\mathrm{d}f_{j\theta}^{w_1}}{\mathrm{d}\theta}\,\mathrm{d}\theta\int_{-1}^{1} f_{i\xi}^{w_2}\,f_{j\xi}^{w_1}\mathrm{d}\xi\;q_{ij}^{w_1}(t)
\end{aligned} \tag{2.135}$$

Expressing the model in the matrix form, the dynamic problem comes as:

$$\left(\begin{bmatrix} [M_{u_1u_1}] & 0 & 0 & 0 & 0 & 0 \\ 0 & [M_{v_1v_1}] & 0 & 0 & 0 & 0 \\ 0 & 0 & [M_{w_1w_1}] & 0 & 0 & 0 \\ 0 & 0 & 0 & [M_{u_2u_2}] & 0 & 0 \\ 0 & 0 & 0 & 0 & [M_{v_2v_2}] & 0 \\ 0 & 0 & 0 & 0 & 0 & [M_{w_2w_2}] \end{bmatrix} + \right.$$

$$\left. \begin{bmatrix} [M^{\mu}_{u_1u_1}] & 0 & 0 & 0 & 0 & 0 \\ 0 & [M^{\mu}_{v_1v_1}] & 0 & 0 & 0 & 0 \\ 0 & 0 & [M^{\mu}_{w_1w_1}] & 0 & 0 & 0 \\ 0 & 0 & 0 & [M^{\mu}_{u_2u_2}] & 0 & 0 \\ 0 & 0 & 0 & 0 & [M^{\mu}_{v_2v_2}] & 0 \\ 0 & 0 & 0 & 0 & 0 & [M^{\mu}_{w_2w_2}] \end{bmatrix}\right) \begin{Bmatrix} \{\ddot{q}^{u_1}(t)\} \\ \{\ddot{q}^{v_1}(t)\} \\ \{\ddot{q}^{w_1}(t)\} \\ \{\ddot{q}^{u_2}(t)\} \\ \{\ddot{q}^{v_2}(t)\} \\ \{\ddot{q}^{w_2}(t)\} \end{Bmatrix}$$

$$+ \begin{bmatrix} [K_{u_1u_1}] & [K_{u_1v_1}] & [K_{u_1w_1}] & 0 & 0 & 0 \\ [K_{v_1u_1}] & [K_{v_1v_1}] & [K_{v_1w_1}] & 0 & 0 & 0 \\ [K_{w_1u_1}] & [K_{w_1v_1}] & [K_{w_1w_1}] & 0 & 0 & [K_{w_1w_2}] \\ 0 & 0 & 0 & [K_{u_2u_2}] & [K_{u_2v_2}] & [K_{u_2w_2}] \\ 0 & 0 & 0 & [K_{v_2u_2}] & [K_{v_2v_2}] & [K_{v_2w_2}] \\ 0 & 0 & [K_{w_2w_1}] & [K_{w_2u_2}] & [K_{w_2v_2}] & [K_{w_2w_2}] \end{bmatrix} \begin{Bmatrix} \{q^{u_1}(t)\} \\ \{q^{v_1}(t)\} \\ \{q^{w_1}(t)\} \\ \{q^{u_2}(t)\} \\ \{q^{v_2}(t)\} \\ \{q^{w_2}(t)\} \end{Bmatrix} = \begin{Bmatrix} 0 \\ 0 \\ 0 \\ 0 \\ 0 \\ 0 \end{Bmatrix} \tag{2.136}$$

where each one of the submatrixes are defined as:

- $[M_{u_1u_1}] \leftarrow ter(35)$
- $[M_{v_1v_1}] \leftarrow ter(45)$
- $[M_{w_1w_1}] \leftarrow ter(57)$
- $[M^{\mu}_{u_1u_1}] \leftarrow ter(36) + ter(37)$
- $[M^{\mu}_{v_1v_1}] \leftarrow ter(46) + ter(47)$
- $[M^{\mu}_{w_1w_1}] \leftarrow ter(58) + ter(59)$
- $[M_{u_2u_2}] \leftarrow ter(75)$
- $[M_{v_2v_2}] \leftarrow ter(85)$
- $[M_{w_2w_2}] \leftarrow ter(97)$
- $[M^{\mu}_{u_2u_2}] \leftarrow ter(76) + ter(77)$
- $[M^{\mu}_{v_2v_2}] \leftarrow ter(86) + ter(87)$
- $[M^{\mu}_{w_2w_2}] \leftarrow ter(98) + ter(99)$

- $[K_{u_1u_1}] \leftarrow ter(38) + ter(39) + ter(44)$
- $[K_{u_1v_1}] \leftarrow ter(41) + ter(43)$
- $[K_{u_1w_1}] \leftarrow ter(40) + ter(42)$
- $[K_{v_1u_1}] \leftarrow ter(50) + ter(56)$
- $[K_{v_1v_1}] \leftarrow ter(48) + ter(51) + ter(52) + ter(55)$
- $[K_{v_1w_1}] \leftarrow ter(49) + ter(53) + ter(54)$
- $[K_{w_1u_1}] \leftarrow ter(62) + ter(68)$
- $[K_{w_1v_1}] \leftarrow ter(60) + ter(64) + ter(66)$
- $[K_{w_1w_1}] \leftarrow ter(61) + ter(63) + ter(65) + ter(67) + ter(70) + ter(71) + ter(72)$
- $[K_{w_1w_2}] \leftarrow ter(69) + ter(73) + ter(74))$
- $[K_{u_2u_2}] \leftarrow ter(78) + ter(79) + ter(84)$
- $[K_{u_2v_2}] \leftarrow ter(81) + ter(83)$
- $[K_{u_2w_2}] \leftarrow ter(80) + ter(82)$
- $[K_{v_2u_2}] \leftarrow ter(90) + ter(96)$
- $[K_{v_2v_2}] \leftarrow ter(88) + ter(91) + ter(92) + ter(95)$
- $[K_{v_2w_2}] \leftarrow ter(89) + ter(93) + ter(94)$
- $[K_{w_2u_2}] \leftarrow ter(102) + ter(108)$
- $[K_{w_2v_2}] \leftarrow ter(100) + ter(104) + ter(106)$
- $[K_{w_2w_2}] \leftarrow ter(101) + ter(103) + ter(105) + ter(110) + ter(111) + ter(112)$
- $[K_{w_2w_1}] \leftarrow ter(109) + ter(113) + ter(114)$

As the linear problem is implemented and in order for the modes of vibration to be extracted, one last decomposition must be considered regarding the time dependence: the generalized displacements are assumed to be dependent on an harmonic function, as done for linear vibrations of a conservative system, an analogous procedure to the one taken for single-walled nanotubes. The consideration is expressed as follows:

$$q_{rs}^{u_1}(t) = \overline{q}_{rs}^{u_1}\, cos\,\omega t \tag{2.137a}$$

$$q_{rs}^{v_1}(t) = \overline{q}_{rs}^{v_1}\, cos\,\omega t \tag{2.137b}$$

$$q_{rs}^{w_1}(t) = \overline{q}_{rs}^{w_1}\, cos\,\omega t \tag{2.137c}$$

$$q_{rs}^{u_2}(t) = \overline{q}_{rs}^{u_2}\, cos\,\omega t \tag{2.137d}$$

$$q_{rs}^{v_2}(t) = \overline{q}_{rs}^{v_2}\, cos\,\omega t \tag{2.137e}$$

$$q_{rs}^{w_2}(t) = \overline{q}_{rs}^{w_2}\, cos\,\omega t \tag{2.137f}$$

Hence, regarding the generalized accelerations, comes:

$$\ddot{q}_{rs}^{u_1}(t) = -\omega^2\, \overline{q}_{rs}^{u_1}\, cos\,\omega t \tag{2.138a}$$

$$\ddot{q}_{rs}^{v_1}(t) = -\omega^2\, \overline{q}_{rs}^{v_1}\, cos\,\omega t \tag{2.138b}$$

$$\ddot{q}_{rs}^{w_1}(t) = -\omega^2\, \overline{q}_{rs}^{w_1}\, cos\,\omega t \tag{2.138c}$$

$$\ddot{q}_{rs}^{u_2}(t) = -\omega^2\, \overline{q}_{rs}^{u_2}\, cos\,\omega t \tag{2.138d}$$

$$\ddot{q}_{rs}^{v_2}(t) = -\omega^2\, \overline{q}_{rs}^{v_2}\, cos\,\omega t \tag{2.138e}$$

$$\ddot{q}_{rs}^{w_2}(t) = -\omega^2\, \overline{q}_{rs}^{w_2}\, cos\,\omega t \tag{2.138f}$$

This process allows to drop the harmonic function from every term, resulting in time-independent equations. This simplification is usually assumed as the model is studied in the linear field, as already explained, where the displacements amplitudes are relatively small.

2.7 Conclusions

In the present chapter, a model based on the thin shell theory of Sanders-Koiter, which lays on Kirchhoff-Love's principles is developed. The material is assumed to be homogeneous and isotropic, as commonly assumed in the reviewed bibliography. Eringen's nonlocal theory is also applied, in order to take into account the small-scale effect inherent in nanosized tubes.

First, Hamilton's principle is used to derive a set of equations of motion dependent on the shell's forces and moments. For the general displacements, the Galerkin method is applied in order to establish the discretized set of equations properly capable of representing the dynamic problem. This process is executed for both single-walled and double-walled carbon nanotubes, where the first may be interpreted as a simpler case of the second, not only for the usage of half displacement components, but also because the van der Waals pressure influence between layers is only relevant for multi-walled carbon nanotubes. The matricial formulation is finally presented with the attribution of each term resultant from the Galerkin method to the respective matrix. Lastly, the time domain of the generalized displacements is expanded due to its periodic response dependence on an harmonic function, as the latter is dropped, resulting in the characteristic vibration problem.

Chapter 3

Model Validation

3.1 Introduction

In this chapter, the previously developed model is tested and verified under different scenarios, all according to bibliographical data. The linear eigenvalue problem described as a result of the dynamic problem established in the previous chapter, used for linear vibration problems, is approached, as natural frequencies and mode shapes are calculated.

First, a convergence analysis takes place, setting a basic number of functions necessary for the solution to converge to an accurate value from the eigenvalue-type problem using different input properties, such as boundary conditions. Then, both local - SWCNT and DWCNT - and nonlocal - SWCNT - models are validated, as different nonlocal parameters are taken as input, being a crucial step for the next chapter. Lastly, a wide range of mode shapes within the local theory is documented, including different types of vibrational modes (extensional and inextensional), linked to the properties used for the model validation, illustrating the versatility of the computational implementation using the p-version FEM with less computational effort, when comparing to molecular dynamics. All the numerical values and mode shapes are produced using the software *Maple*.

3.2 Numerical results: Convergence

Before analysing the convergence of the method, it is necessary to define the boundary conditions studied in this chapter and dissertation, regarding the CNTs. Thus, clamped-clamped (CC), free-free (FF) and simply supported-simply supported (SS) boundary conditions are considered, and are defined as follows [11, 70, 97]:

- Clamped-clamped (CC)

$$u^0 = v^0 = w^0 = 0, \quad x = 0, l$$

$$\frac{\partial w^0}{\partial x} = 0, \quad x = 0, l$$

- Free-Free (FF)

$$N_{xx} = 0, \quad x = 0, l$$

$$N_{x\theta} + \frac{1}{R} M_{x\theta} = 0, \quad x = 0, l$$

$$Q_{xx} + \frac{1}{R}\frac{\partial M_{x\theta}}{\partial \theta} = 0, \quad x = 0, l$$

$$M_{xx} = 0, \quad x = 0, l$$

- Simply supported-simply supported (SS)

$$v^0 = w^0 = 0, \quad x = 0, l$$

$$N_{xx} = 0, \quad x = 0, l$$

$$M_{xx} = 0, \quad x = 0, l$$

where N indicates normal stress, M indicates moment and Q indicates transverse stress.

As can be observed, clamped-clamped conditions require geometric boundary conditions, while free-free conditions only need natural boundary conditions to describe their edges, and simply supported-simply supported state being a mix of both, as for the clamped edge it assumes the typical geometric boundary conditions and for the free edge, the natural boundary conditions described before are assumed. It should also be stated that for the problem's convergence, only the geometric boundary conditions must be respected. In fact, taking into consideration the natural boundary conditions may provide a better convergence with fewer shape functions, but they are not taken into account for the shape functions selection. Thus, for FF, all the initial four functions of f and two initial functions of g are considered, as described in the last chapter, while for CC none are considered. For SS, functions for v^0 are the same as for CC, while for u^0 both initial g functions are used, allowing for displacement in u^0, and for w^0 the $f_2^{BC}(\xi)$ and $f_4^{BC}(\xi)$ initial functions are employed, having unitary slope in each edge.

The material's and lattice properties must be defined before the computation of the problem. As stated, the material is considered homogeneous and isotropic, and thus the elastic and geometric problems arise for an equivalent model, as the one in the present dissertation. Different "effective" properties are documented, regarded as a range of values calculated from different experiments, not defining a specific set of parameters, and "equivalent" parameters, having been proposed by Yakobson et al. in [22], from the principle that the elastic-properties of a two-dimensional hexagonal structure are isotropic (assumed previously in this dissertation), and leading to the approximation that a uniform shell may be characterized by two elastic parameters: the flexural rigidity D and the resistance to membrane stretching, the in-plane stiffness C. These constants determined by semiempirical methods are used to establish the stated equivalent parameters, which are, in fact, commonly used as an approximation of the continuum model to match molecular dynamics experiments results, regarding the nanotube's behaviour under strain [22]. These parameters are stated in Table 3.1.

Table 3.1: Effective and equivalent parameters of single-walled carbon nanotubes [11, 22]

Effective thickness h_0 [nm]	0.10-0.15
Equivalent thickness h [nm]	0.066
Effective Young's modulus E_0 [TPa]	1.0-2.0
Equivalent Young's modulus E [TPa]	5.5
Effective Poisson's ratio ν_0	0.12-0.28
Equivalent Poisson's ratio ν	0.19
Surface density of graphite σ[kg/m^2]	7.718×10^{-7}
Equivalent mass density ρ[kg/m^3]	11,700

In Table 3.2 the first four linear natural frequencies of beam-like modes ($n = 1$) are presented, considering clamped-clamped boundary conditions, for a specific value of aspect ratio $\chi = \frac{l}{2R}$. Different sets of number of functions are employed, designating the number of functions of x by N applied for u^0, v^0 and w^0, being respectively pgu, pgv and pw. The results are compared to the solutions given by Strozzi et al. [11], who applied the Sanders-Koiter theory aided by the Rayleigh-Ritz method in order to implement it. It can be observed that from the value of $N = 15$ and onwards, the model converges for a difference below 0.4% consistently. As the difference values remain constant from the referred number of shape functions on, it is concluded that the natural frequencies converge. In p-version finite element method with an hierarchic set of shape functions, the eigenvalues converge to the exact solution from above, as the number of shape functions is increased [98].

Table 3.2: Convergence of local natural frequencies [THz] of beam-like modes ($n = 1$) - CC

$(r, s) = (5, 5)$	$\chi = 10.34$								
N		ω_1	Diff. (%)	ω_2	Diff. (%)	ω_3	Diff. (%)	ω_4	Diff. (%)
-	Sol. [11]	0.335	-	0.819	-	1.428	-	2.095	-
5		0.3374	0.72	0.8303	1.4	1.479	3.6	4.110	96
7		0.3357	0.21	0.8253	0.77	1.433	0.34	2.137	2.0
11		0.3346	0.13	0.8190	0.0045	1.423	0.34	2.093	0.089
15	Model	0.3344	0.17	0.8181	0.11	1.422	0.40	2.091	0.20
19		0.3344	0.17	0.8181	0.11	1.422	0.40	2.091	0.20
21		0.3344	0.18	0.8181	0.11	1.422	0.40	2.091	0.20
25		0.3344	0.18	0.8181	0.11	1.422	0.40	2.091	0.20

Another local linear model validation is described in Table 3.3 , as the first four linear and local natural frequencies of modes ($n = 2$) are calculated, for free-free boundary conditions. More sets of shape functions N are examined and compared to the model [11]. It can be observed for this case that convergence happens for a higher number of shape functions, when the difference value becomes stabilized, for $N = 24$. The discrepancy in the difference remains below 3% for all natural frequencies, also signaling the validation of the model.

Table 3.3: Convergence of local natural frequencies [THz] of modes for ($n = 2$) - FF

$(r, s) = (10, 0)$	$\chi = 12.8$								
N		ω_1	Diff. (%)	ω_2	Diff. (%)	ω_3	Diff. (%)	ω_4	Diff. (%)
-	Sol. [11]	1.174	-	1.176	-	1.195	-	1.227	-
5		1.169	0.41	1.173	0.27	1.188	0.57	1.257	2.4
7		1.169	0.41	1.173	0.28	1.187	0.66	1.221	0.50
11		1.169	0.41	1.173	0.29	1.184	0.90	1.211	1.3
15		1.169	0.41	1.172	0.34	1.179	1.3	1.198	2.4
19	Model	1.169	0.41	1.172	0.37	1.178	1.4	1.194	2.7
21		1.169	0.41	1.172	0.38	1.177	1.5	1.193	2.8
23		1.169	0.41	1.172	0.38	1.177	1.5	1.192	2.8
24		1.169	0.41	1.172	0.39	1.177	1.5	1.192	2.9
25		1.169	0.41	1.172	0.39	1.177	1.5	1.192	2.9

Lastly in the present subsection, it is important to study the convergence of the linear theory taking into account the nonlocal small-size effects. Two sets of values $e_0 = 0.3$ and $e_0 = 0.6$ are tested in Table 3.4 , as the goal is to study the convergence into the values given by Avramov [10]. As can be observed, from the value of $N = 15$ onwards, the natural frequencies converge as the value of the difference remains constant. On another note, the registered numbers come very close to the ones given by [10], hinting about the validation of the values, as the difference values are very close to 0% when comparing to a similar continuum theory.

Table 3.4: Convergence of nonlocal natural frequencies [THz] of beam-like modes ($n = 1$), for $e_0 = 0.3$ and $e_0 = 0.6$ - CC

$(r, s) = (5, 5)$		$\chi = 5.26$		$e_0 = 0.3$					
N		ω_1	Diff. (%)	ω_2	Diff. (%)	ω_3	Diff. (%)	ω_4	Diff. (%)
-	Sol. [10]	1.009	-	2.169	-	3.478	-	4.767	-
5	Model	1.014	0.50	2.190	1.00	3.524	1.3	6.116	28
7		1.010	0.088	2.174	0.23	3.481	0.090	4.810	0.91
11		1.009	0.014	2.169	0.013	3.479	0.014	4.768	0.015
15		1.009	0.013	2.169	0.012	3.479	0.013	4.767	0.012
19		1.009	0.013	2.169	0.012	3.479	0.013	4.767	0.012
21		1.009	0.013	2.169	0.012	3.479	0.013	4.767	0.012
25		1.009	0.013	2.169	0.012	3.479	0.013	4.767	0.012

$(r, s) = (5, 5)$		$\chi = 5.26$		$e_0 = 0.6$					
N		ω_1	Diff. (%)	ω_2	Diff. (%)	ω_3	Diff. (%)	ω_4	Diff. (%)
-	Sol. [10]	0.9839	-	2.103	-	3.342	-	4.522	-
5	Model	0.9888	0.50	2.124	0.98	3.385	1.3	5.795	28
7		0.9848	0.091	2.108	0.23	3.345	0.085	4.562	0.87
11		0.9841	0.018	2.103	0.017	3.342	0.015	4.523	0.019
15		0.9841	0.017	2.103	0.016	3.342	0.013	4.523	0.014
19		0.9841	0.017	2.103	0.016	3.342	0.013	4.523	0.014
21		0.9841	0.017	2.103	0.016	3.342	0.013	4.523	0.014
25		0.9841	0.017	2.103	0.016	3.342	0.013	4.523	0.014

It should be noted that as the small scale parameter increases, the natural frequencies decrease, as is possible to observe in Table 3.4. That comes from the fact that in the linear model, the nonlocal effect does not alter the stiffness, but influences the inertia of the shell model, increasing it with the increase of the parameter. This reveals to be an important factor that allows for the calibration and study of influence of the nonlocal parameter in the natural frequencies and mode shapes, as will be discussed further.

As can be observed, for different situations the natural frequencies values converge for a minimum value of N that is variable. More specifically, for different boundary conditions, the number of shape functions necessary for convergence can differ from $N = 15$ to $N = 24$. Thus, along the following sections for the calculation of natural frequencies and mode shapes, the maximum number of functions is employed, typically $N = 25$.

Although comparisons were carried out with results from other authors, allowing us to gain some confidence in the present model, the main goal of this section was to analyse the convergence properties of the latter. The data used for comparison in this section comes from models based on assumptions similar to the ones on which the present model is based; hypothetically, these models may be inadequate to represent a real carbon nanotube. Thus, the next section further validates the model with values from molecular dynamics' simulations and finite element method simulations from hybrid atomistic-continuum modelling.

3.3 Numerical Results: Validation

The present section intends to validate the values of the natural frequencies and behaviour of mode shapes obtained by the continuum model developed in this dissertation based on the Sanders-Koiter theory. The results are compared to resonant Raman Spectroscopy (RRS), Molecular Dynamics (MD), Finite Element Analysis (FEA) and lastly, to a continuum model theory, as not enough data for the specific characteristics intended to be tested were found, thus allowing for validation by comparison to a model (as done for convergence in the previous chapter), as it is an option chosen for the lack of MD or FEA results.

The first tested values are for radial breathing modes (RBM). The parameters for single-walled carbon nanotubes used are the ones already described in Table 3.1. From this paragraph on, a notation is introduced, consisting of describing the number of complete waves in the x coordinate, k, as when visualizing mode shapes it is crucial to associate them to the respective frequencies and pace (for θ the association is simpler as for the calculated values a definite value of n is employed and therefore easier to comprehend). In Table 3.5 and 3.6 different values of fundamental frequencies for RBMs are calculated and presented. For RRS, the same aspect ratio is employed as it is also constant in the source of the values, while for MD the same parameter varies.

Table 3.5: Comparison between local natural frequency [THz] for $k = 0$ of Radial Breathing Modes ($n = 0$) and Resonant Raman Spectroscopy (RRS)

(r,s)	χ	Model	RRS [99]	Diff. (%)
(10,5)	10	6.789	7.105	4.45
(11,4)	10	6.675	6.865	2.76
(9,7)	10	6.465	6.742	4.11
(10,6)	10	6.418	6.688	4.04
(14,1)	10	6.186	6.295	1.74
(18,0)	10	4.992	5.276	5.39
(17,2)	10	4.969	5.216	4.74
(16,4)	10	4.902	5.066	3.24
(15,6)	10	4.796	4.947	3.06
(11,11)	10	4.716	4.917	4.09
(14,8)	10	4.659	4.857	4.09
(19,1)	10	4.603	4.797	4.04
(18,3)	10	4.567	4.737	3.58
(13,10)	10	4.498	4.677	3.82
(17,5)	10	4.498	4.677	3.82
(16,7)	10	4.400	4.617	4.70
(12,12)	10	4.323	4.527	4.51
(15,9)	10	4.279	4.461	4.09
(21,0)	10	4.278	4.437	3.59
(20,2)	10	4.264	4.446	4.09

It is important to note that the fundamental frequencies of radial breathing modes studied for free-free edges assume a constant shape regarding the displacement in the x coordinate, so that $k = 0$, while the second natural frequency expresses a shape regarding a half wave, while for clamped-clamped CNTs, the fundamental frequency mode shape assumes a complete wave behaviour in the x coordinate. The relevancy of this fact comes from the phenomenon described for the natural frequencies of lower wave number to not be necessarily the first or less energetic natural frequency, as the mode shapes need to be

Table 3.6: Comparison between local natural frequency [THz] for $k = 0$ of Radial Breathing Modes ($n = 0$) and Molecular Dynamics (MD)

(r,s)	χ	Model	MD [100]	Diff. (%)
(12,0)	5.677	7.495	7.272	3.07
(7,7)	5.577	7.419	7.166	3.53
(9,6)	5.827	6.878	6.649	3.44
(10,5)	5.289	6.801	6.581	3.34
(8,8)	5.673	6.491	6.275	3.44
(14,0)	5.771	6.424	6.235	3.03
(11,7)	5.333	5.724	5.550	3.14
(16,0)	6.070	5.620	5.455	3.03
(10,10)	5.626	5.193	5.026	3.32
(15,4)	5.445	5.185	5.018	3.33
(18,0)	5.598	4.997	4.850	3.03
(20,0)	5.671	4.497	4.364	3.05
(12,12)	5.671	4.327	4.190	3.28
(25,0)	5.624	3.598	3.491	3.06
(15,15)	5.624	3.462	3.354	3.22
(30,0)	5.683	2.998	2.908	3.10
(18,18)	5.644	2.885	2.796	3.18
(33,0)	6.239	2.725	2.623	3.88
(20,20)	5.669	2.596	2.516	3.20
(36,0)	5.669	2.498	2.423	3.11

observed to determine the values for each table.

It should also be noted that for both comparisons the results come with a small and consistent difference value, with the maximum value to be close to 5% for RRS, and 3% for MD. For a last instance, it can be observed that for an increasing value of diameter (coming from the chiral vectors amplitude increase), the natural frequencies of $k = 0$ RBMs tend to decrease, for similar values of aspect ratio.

The following validation process describes values regarding the beam-like modes ($n = 1$) of carbon nanotubes with different values of aspect ratio, documenting the set of the first four natural frequencies under clamped-clamped boundary conditions. The natural frequency values are compared to the Molecular Dynamics calculations performed by Duan et al. [7]. These values come expressed in Table 3.7.

Analysing Table 3.7, the first conclusion that comes is that the natural frequencies tend to decrease as the aspect ratio increases, as independently from the number of the natural frequency, this behaviour is registered as already done for radial breathing modes. Generally speaking, the relative difference values also decreases for higher value aspect ratio, comparing to lower values.

For the whole range of natural frequencies, it is noted that the calculated values from the model are higher than the MD values, as expected, until a breaking point defined by a critical value of aspect ratio is attained, after which the values calculated by the local model are below the ones given by MD results. This is linked to the theory and to the parameters of the current analysis, as similar parameters were used in the analysis performed by Strozzi et al. [11] with close yielded results. Logically this fact invalidates an analysis of the effect of the nonlocal parameter for aspect ratio values superior to the critical one, which will be studied on Chapter 4.

The next analysis is carried regarding the validation of the model when comparing the values of the natural frequencies to finite element analysis results. It is important to

Table 3.7: Comparison between local natural frequencies [THz] of beam-like modes ($n = 1$) and Molecular Dynamics (MD)

	Model	MD [7]	Diff. (%)
$(r, s) = (5, 5)$, $\chi = 6.35$			
Clamped-Clamped CC			
ω_1	0.7622	0.741	2.9
ω_2	1.7027	1.654	2.9
ω_3	2.793	2.717	2.8
ω_4	3.920	3.828	2.4
$(r, s) = (5, 5)$, $\chi = 11.43$			
Clamped-Clamped CC			
ω_1	0.2792	0.282	1.0
ω_2	0.6938	0.698	0.60
ω_3	1.221	1.223	0.14
ω_4	1.813	1.811	0.12
$(r, s) = (5, 5)$, $\chi = 15.05$			
Clamped-Clamped CC			
ω_1	0.1676	0.172	2.5
ω_2	0.4319	0.440	1.8
ω_3	0.7847	0.796	1.4
ω_4	1.1967	1.210	1.1

study the effect of chirality, diameter, aspect ratio and boundary conditions of the linear model on the results, evaluating its accuracy. As seen, different chiralities and diameters are yet to be studied, and as MD simulations documentation is relatively short in number of publications, not only using FEA it is found a comparing number, but it can also be compared the p-version FEM to an h-version, as used by Sakhaee-Pour et al. [63]. Relevant results are presented in Table 3.8.

In Table 3.8, results from the validation of the model in comparison to finite element analysis are presented. It should be understood that the FEA process itself requires validation with MD results, as this is not the same source as MD, it is still relevant for the purpose of this review. Regarding the results itself, it may be concluded that a similar phenomenon takes place as the previous analysis, as for the same chirality/diameter and for different aspect ratios, not only for a higher aspect ratio the value of the natural frequency is lower independently of the boundary conditions, but the difference value is also lower. It is important to recognize a relevant detail regarding the number of significant digits presented by the authors in [63], as it may induce larger relative differences than the real ones, for example for the first natural frequency of the last two tables, only two significant digits are presented. Therefore, the number is certainly suffering an approximation (the value 0.044 may range from 0.0435 to 0.0444, considering one more digit) that given the possible range limits, may or may not represent a significant addition to the difference value.

Table 3.8: Comparison between local natural frequencies [THz] of beam-like modes ($n = 1$) and Finite Element Analysis (FEA)

	Model	FEA [63]	Diff. (%)
$(r, s) = (12, 12)$, $\chi = 6.95$			
Clamped-Clamped CC			
ω_1	0.2730	0.243	12
ω_2	0.6198	0.545	13
ω_3	1.025	0.616	66
ω_4	1.448	0.762	90
$(r, s) = (12, 12)$, $\chi = 19.65$			
Clamped-Clamped CC			
ω_1	0.04204	0.042	0.094
ω_2	0.1110	0.111	0.032
ω_3	0.2066	0.207	0.20
ω_4	0.3224	0.339	4.9
$(r, s) = (20, 0)$, $\chi = 19.60$			
Clamped-Clamped CC			
ω_1	0.04376	0.044	0.55
ω_2	0.1155	0.116	0.44
ω_3	0.2150	0.217	0.93
ω_4	0.3355	0.354	5.2

A clear conclusion may be taken from the value of difference for lower aspect ratios, as the higher the natural frequency, the higher the difference. For an aspect ratio of $\chi = 6.95$ the difference for ω_4 is very significant. The magnitude of the the difference value is, on average, on the same order for the same chirality and aspect ratio, fading higher values of difference as the aspect ratio increases and revealing satisfactory values for $\chi = 19.65$, for example.

With the effort of testing the chirality influence, the last parameter set is presented. For instance, for $(r, s) = (12, 12)$ and $\chi = 19.65$, the value of diameter and length comes as $D = 1.628\,\text{nm}$ and $l = 31.993\,\text{nm}$, while for for $(r, s) = (20, 0)$ and $\chi = 19.60$, the value of diameter and length comes as $D = 1.566\,\text{nm}$ and $l = 30.693\,\text{nm}$. These values are sufficiently close to carry out a comparison between the effects of chirality, having in mind that the developed continuum model does not account for the influence of the orientation of the lattice on the output results, as it is only able to calculate the diameter from the chiral vectors (as stated by Equation (1.2)), while FEA with discretization of the atoms as concentrated masses and bonds as rigid beams does account for that influence. Despite this fact, it can be observed that the values of the first four natural frequencies is very similar between the armchair CNT ($(r, s) = (12, 12)$) and the zig-zag CNT ($(r, s) = (20, 0)$). In fact, the magnitude of the associated differences are very similar, and the difference between the natural frequency values may be not come only from the chirality itself, but also due to the difference in the resultant diameter and the aspect ratio simulated. Nevertheless, the influence of the chirality reveals itself with few significance compared to other parameters.

Table 3.9: Comparison between local natural frequencies [THz] of modes for $n = 2$ and Free-free edges and [11]

	Model	Sol. [11]	Diff. (%)
$(r, s) = (10, 0)$, $\chi = 3.83$			
ω_1	1.164	1.188	2.0
ω_2	1.169	1.216	3.8
ω_3	1.316	1.522	14
ω_4	2.110	2.324	9.2
ω_5	3.318	3.437	3.4
ω_6	4.594	4.632	0.83
$(r, s) = (10, 0)$, $\chi = 12.8$			
ω_1	1.169	1.174	0.41
ω_2	1.172	1.176	0.39
ω_3	1.177	1.195	1.51
ω_4	1.192	1.227	2.87
ω_5	1.238	1.291	4.09
ω_6	1.333	1.399	4.73

A different validation analysis is taken regarding the free-free boundary conditions. Molecular dynamics simulations or finite element analysis were lacking for this specific boundary condition, and therefore the continuum model already used in the previous section (Strozzi et al. [11]) is again employed for this case. Results are shown in Table 3.9.

Analysing Table 3.9, the natural frequency results come in agreement with the model developed by [11]. In fact, for a smaller value of aspect ratio, the third and fourth eigenvalues of the characteristic problem come with a considerable difference associated. Despite this, for a greater number of aspect ratio, the associated difference values are considerably smaller as the natural frequency values are closer to the ones documented. The general behaviour of the values also comes as expected, as the natural frequencies are lower for a higher aspect ratio in comparison to the equivalent for a lower χ, with the exception of the first two, which are very close with a difference in the fourth significant figure, illustrating most likely a numerical malfunction. As no molecular dynamics data is used to test the accuracy of the model, no further conclusions are taken for this case.

One more validation approach is taken regarding another type of boundary conditions, namely simply supported-simply supported. The results are compared to the values given in [97], presenting results from the analytical exact natural frequency results, along with FEM results, all by the same author. The model is validated for different properties of the tubes/shells, as the material is steel and not carbon associated with larger dimensions, which come in Table 3.10.

The results of regarding the validation of the model for simply supported-simply supported edges are established in Table 3.11.

As may be further analysed from the data of Table 3.11, the results are in good agreement with the bibliography used for the present verification. In fact, the results obtained in the developed model for this dissertation are calculated with a wide range of significant digits, even though only present with four significant digits, which leads to the relative difference value seen on the fifth column, as the source only provides the digits

Table 3.10: Chosen parameters of simply supported boundary conditions result validation [97]

Equivalent thickness h [m]	0.247×10^{-3}
Equivalent Young's modulus E [Pa]	71.02×10^9
Equivalent Poisson's ratio ν	0.31
Radius [m]	0.1
Length [m]	0.2
Equivalent mass density ρ [kg/m^3]	2,796

Table 3.11: Comparison between local natural frequencies [Hz] of modes for simply supported-simply supported edges and the exact solution and Finite Element Analysis (FEA) [97]

	n	Model	Exact Sol. [97]	Diff. (%)	FEM Sol. [97]	Diff. (%)
ω_1	7	484.6	484.6	0	484.9	0.072
ω_1	8	489.6	489.6	0	490.0	0.090
ω_1	9	546.2	546.2	0	546.9	0.13
ω_1	6	553.3	553.3	0	553.7	0.066
ω_1	10	636.8	636.8	0	637.9	0.17
ω_1	5	722.1	722.1	0	722.5	0.051
ω_1	11	750.7	750.7	0	752.3	0.22
ω_1	12	882.2	882.2	0	884.6	0.27
ω_2	10	968.1	968.1	0	970.5	0.25
ω_2	11	983.4	983.4	0	985.9	0.26

exposed in the stated table, which are certainly affected by an approximation (the same consideration described regarding Table 3.8 is applied here). Regarding the comparison to the FEM solution, the results also come with a reduced relative difference, being possible to conclude that the stated boundary condition is validated for the present model.

Regarding double-walled carbon nanotubes, the validation process is conducted by comparison to the results given by Ansari et al. [101], from a molecular dynamics approach. The parameters of the CNTs are the same used in Table 3.1, and the van der Waals pressure specific parameters come in Table 3.12, as follows:

Table 3.12: Parameters regarding the van der Waals pressure [9, 93]

Bond length of carbon atoms a [nm]	0.142
Depth of the potential ε [J]	4.7483×10^{-22}
Equilibrium distance parameter σ_{vdW} [nm]	0.3407

as the bond length of the carbon atoms a was already defined before, and the respective inner and outer radius values are determined from the chirality expression stated in Equation (1.2).

The comparison of results is performed regarding different sets of boundary conditions, namely clamped-clamped and simply supported-simply supported. The results are presented in Tables 3.13 and 3.14. It is important to note that both the length of the nanotubes and the aspect ratio value are presented as the first one is stated on reference [101], and the aspect ratio is still shown to maintain coherence of the tables on this dissertation.

Analysing Tables 3.13 and 3.14, it is possible to note that generally, the fundamental frequency values given by the present model come in close agreement with the ones found in the selected bibliography. In fact, relative difference values may come above the mark

Table 3.13: Comparison between the local fundamental frequency [THz] of a DWCNT of inner tube $(r, s) = (5, 5)$ and outer tube $(r, s) = (10, 10)$, for $k = 1$ and clamped-clamped edges and Molecular Dynamics (MD)

l [nm]	χ	Model	MD [101]	Diff. (%)
2.436	1.80	1.849	2.064	10
3.680	2.71	1.137	1.086	4.8
4.914	3.62	0.7805	0.7005	11
6.156	4.54	0.5679	0.4985	14
7.360	5.43	0.4341	0.3778	15
8.602	6.34	0.3391	0.3059	11
9.815	7.24	0.2729	0.2485	9.8

Table 3.14: Comparison between the local fundamental frequency [THz] of a DWCNT of inner tube $(r, s) = (5, 5)$ and outer tube $(r, s) = (10, 10)$, for $k = 1/2$ and simply supported-simply supported edges and Molecular Dynamics (MD)

l [nm]	χ	Model	MD [101]	Diff. (%)
2.436	1.80	1.458	1.360	7.1
3.680	2.71	0.7923	0.8342	5.0
4.914	3.62	0.4931	0.5465	9.8
6.156	4.54	0.3325	0.3742	11
7.360	5.43	0.2399	0.2738	12
8.602	6.34	0.1796	0.2005	10
9.815	7.24	0.1396	0.1530	8.8

of 10%. Still, it is important to note that the aspect ratio values associated with the gathered data come in a range of values from $\chi = 1.80$ to $\chi = 7.24$, which are relatively low values of aspect ratio, as for example for different references in this dissertation this range would be defined from $\chi = 5.26$ to $\chi = 15.05$, as for the higher values of the aspect ratio range, the relative difference values would in fact be lower. As for the current case these higher aspect ratio values are not available, no conclusions may be taken. On the same topic, it can be observed that the absolute difference value, given by the subtraction of calculated and reference values, even for the apparently high relative difference values, are small and in the order of the second significant digit, tending to the third digit.

It should be noted that for clamped-clamped boundary conditions, the natural frequency values as generally higher than the ones given by MD simulations (with the exception for the first value of aspect ratio), while for simply supported-simply supported boundary conditions the opposite effect occurs, as the calculated fundamental frequency values are generally inferior to the ones given by MD simulations. This behaviour is also verified in Ansari et al. [8]. In fact, it will open the possibility of a nonlocal parameter calibration for clamped-clamped boundary conditions on the next chapter.

Lastly, a comparison between the fundamental natural frequencies of a single-walled carbon nanotube with chirality $(r, s) = (10, 10)$ and a double-walled carbon nanotube with an outer tube of chirality $(r, s) = (10, 10)$ using the present model is performed. The aim is to confirm the illustrated phenomena by Natsuki et al. [102] where for a SWCNT and DWCNT with a similar external radius, for the same length/aspect ratio, the natural frequency values of the DWCNT are lower than the ones of the SWCNT independently of the inner tube of the DWCNT. Thus, for different values of length of the nanotube, the comparison is presented on Figure 3.1.

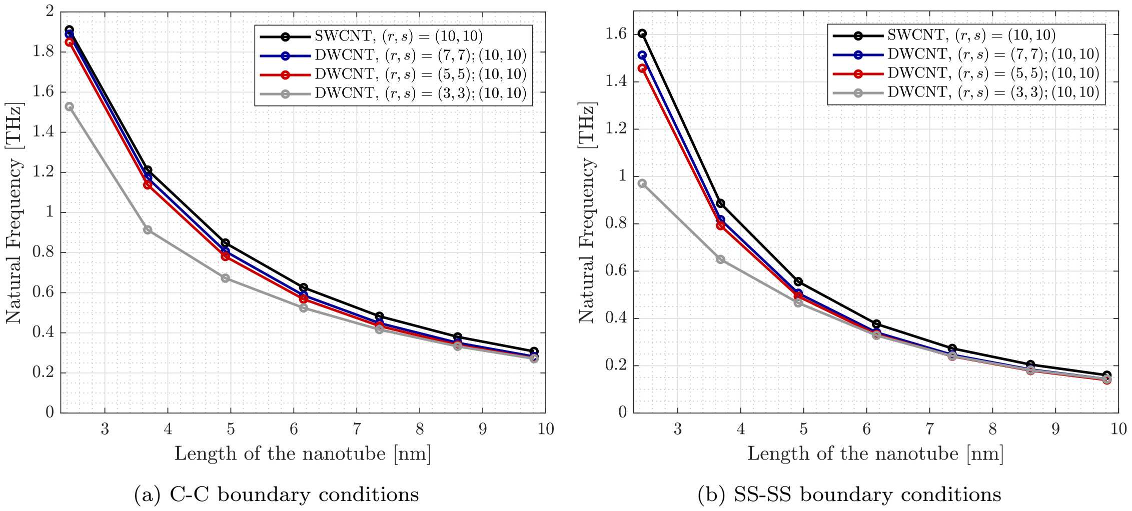

(a) C-C boundary conditions

(b) SS-SS boundary conditions

Figure 3.1: Fundamental natural frequency of different DWCNTs and SWCNT of chirality $(r, s) = (10, 10)$ for different inner tubes of the DWCNT and boundary conditions, function of the length of the nanotube

Analysing Figure 3.1, it is possible to observe that in fact, for different values of chirality of the inner tube for the DWCNT, as long as its outer tube's chirality is the same as the SWCNT (while being physically admissible), the natural frequency of the DWCNT is lower. In fact, for clamped-clamped and simply supported-simply supported boundary conditions the behaviour is verified, as well as the fact that the higher the chirality and consequently the radius of the inner tube, the closer the values of ω of the DWCNT are to the ones of de SWCNT. This allows us to conclude that for a DWCNT, for an increasing radius, the raise in the values of the stiffness is more predominant than the increase in the inertia or mass values, and thus increasing the natural frequency values. Still, comparing to a SWCNT, the addition of an inner tube inside yields a more relevant effect on the inertia than in the stiffness, and thus decreasing the values of the natural frequencies.

With the presented results along this section registered, they are now used to illustrate the mode shapes associated with each natural frequency, on the next section.

3.4 Mode Shapes

In the present section the linear mode shapes of single-walled carbon nanotubes are plotted in a three-dimensional design. As mostly values from section 3.3 are used, the equivalent parameters of SWCNTs of Table 3.1 are also employed.

In Figure 3.2 the radial breathing modes ($n = 0$) of a $(21, 0)$ carbon nanotube with $\chi = 10$ are presented, respectively for a wavenumber in x of $k = 0$, $k = 1/2$, $k = 1$ and $k = 3/2$, associated with the natural frequency presented in Table 3.5.

In Figure 3.3, the first four beam-like mode shapes ($n = 1$) of a $(5, 5)$ carbon nanotube with $\chi = 11.43$ are presented for clamped-clamped edges, as the mode shapes correspond to the natural frequencies given in the Table 3.7. The evolution of the wavenumber along the increasing values of the natural frequencies should be emphasized, behaving as expected for a beam-like mode, as confirmed by the modes presented in [63].

The mode shapes for $n = 2$ of a $(10, 0)$ carbon nanotube with $\chi = 12.8$ are presented for free-free edges, regarding the first six mode shapes associated with the natural frequencies registered in Table 3.9, in Figure 3.5. These mode shapes are compared and validated by the ones presented in [11]. It is important to note that the mode represented in Figure 3.5a, which is assigned the value $k = 0$ corresponds to Rayleigh's inextensional symmetrical mode (uniform vibration), while the mode represented in Figure 3.5b, for $k = 1/4$, corresponds to Love's inextensional asymmetrical mode. On the same Figure 3.5, on the left column symmetrical modes are represented, while on the right column asymmetrical modes are plotted. Out of curiosity, in Figure 3.4a a Rayleigh's inextensional mode shape for a wavenumber of $n = 6$ in θ coordinate is plotted, while in Figure 3.4b a Love's inextensional mode shape for a wave number of $n = 6$ in θ coordinate is illustrated. Regarding Figure 3.6, the mode shapes of simply supported-simply supported edges are plotted and illustrated, regarding modes for $n = 1$. As in Table 3.11 a wide range of values for n are selected, similar modes to the ones presented for CC boundary conditions are presented, which yields the comparison regarding the behaviour on the edges, where rotation is now allowed while displacements are not, leading the value of k for the first natural frequency, for example, to be $k = 1/2$ for SS boundary conditions while $k = 1$ for CC.

Regarding the double-walled carbon nanotubes mode shapes, the beam-like modes ($n = 1$) are presented for an inner tube of chirality $(r, s) = (5, 5)$ and outer tube of chirality $(r, s) = (10, 10)$, for an aspect ratio of $\chi = 7.24$, for clamped-clamped boundary conditions on Figure 3.7, and simply supported-simply supported boundary conditions on Figure 3.8. It is important to register that on the left column of both figures the "in-phase" mode shapes are illustrated, where the inner and outer tube display a similar behaviour in the same direction, while on the right column the "anti-phase" mode shapes are presented, where the inner and outer tube present its behaviour on an opposite direction. It is important to note that similarly to $n = 1$, for higher values of the circumferential mode number n, in-phase and anti-phase mode shapes also exist, as the axial wave number of both inner and outer nanotubes is the same for a considered mode. Thus, for the sake of illustration brevity, only beam-like modes of DWCNTs are presented in this chapter.

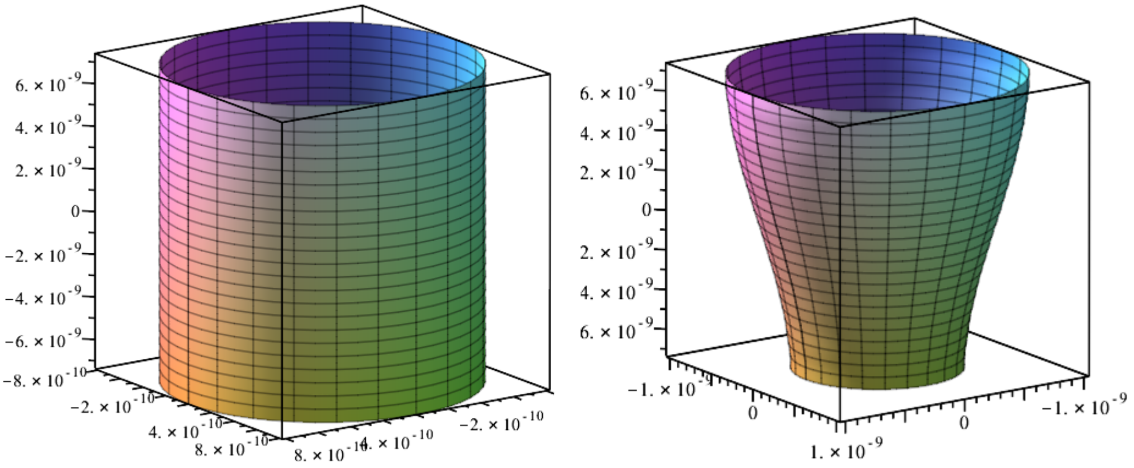

(a) $k = 0,\ \omega = 4.278$ THz

(b) $k = 1/2,\ \omega = 4.279$ THz

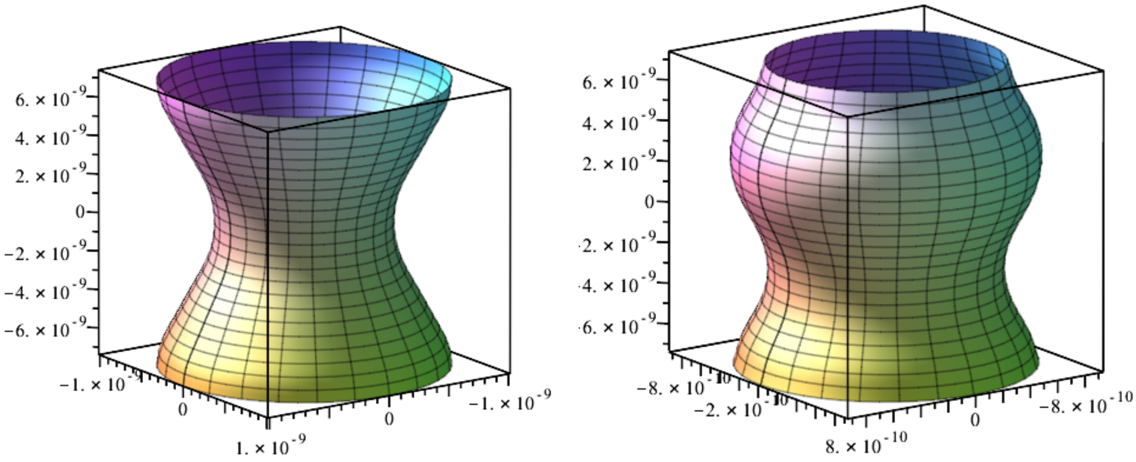

(c) $k = 1,\ \omega = 4.290$ THz

(d) $k = 3/2,\ \omega = 4.298$ THz

Figure 3.2: Mode shapes of radial breathing modes ($n = 0$), $(r, s) = (21, 0)$, $\chi = 10$, free-free edges

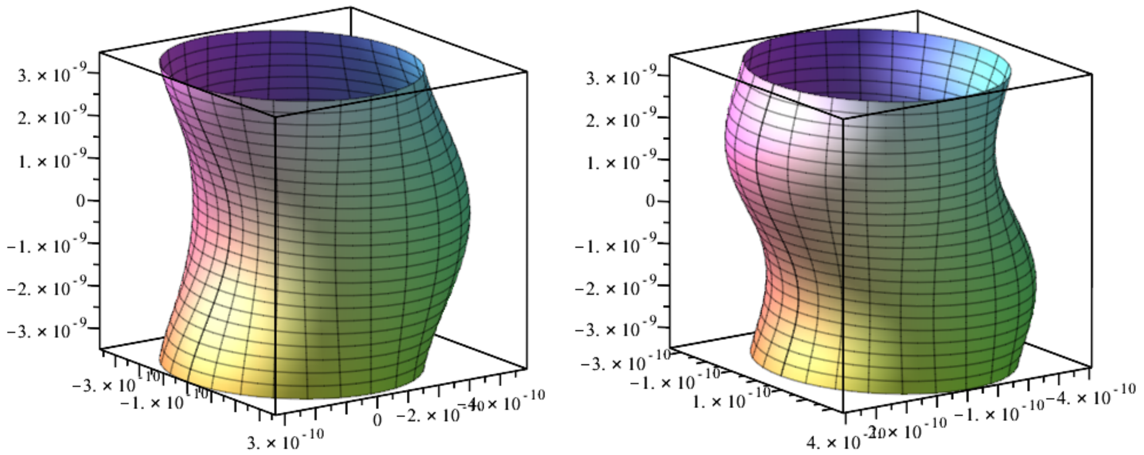

(a) $k = 1,\ \omega_1 = 0.279$ THz (b) $k = 3/2,\ \omega_2 = 0.694$ THz

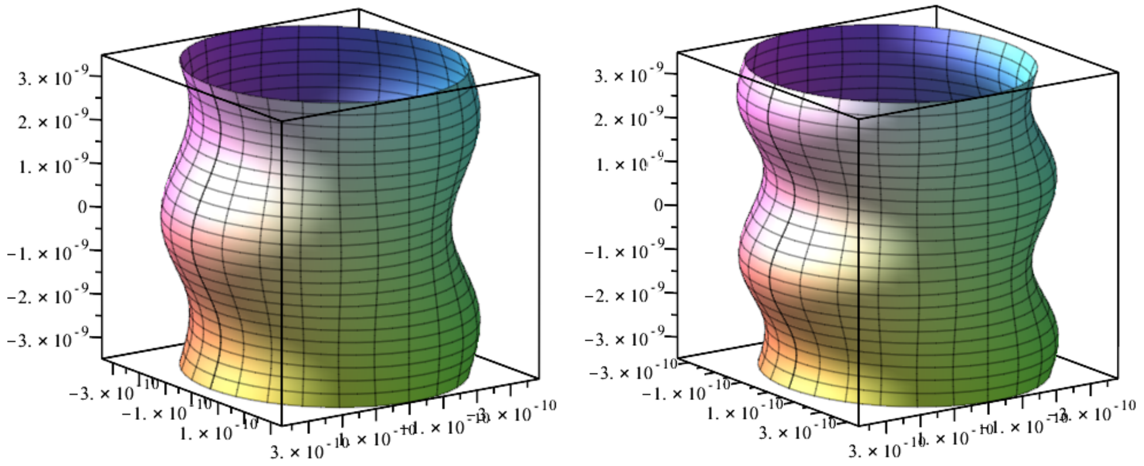

(c) $k = 2,\ \omega_3 = 1.221$ THz (d) $k = 5/2,\ \omega_4 = 1.813$ THz

Figure 3.3: Mode shapes of beam-like modes ($n = 1$), $(r, s) = (5, 5)$, $\chi = 11.43$, clamped-clamped edges

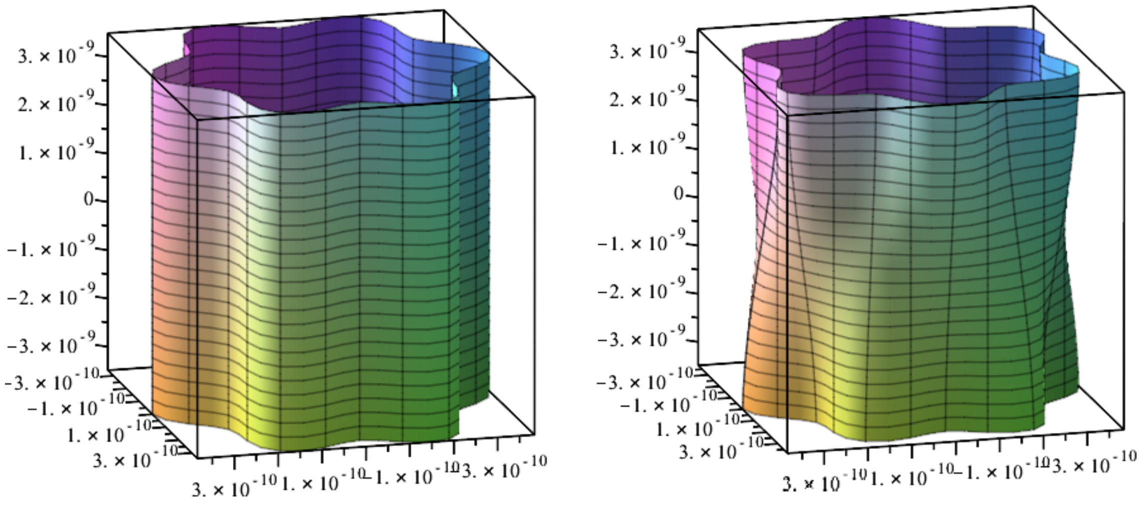

(a) $k = 0, n = 6,\ \omega = 19.985$ THz (b) $k = 1/2, n = 6,\ \omega = 19.995$ THz

Figure 3.4: Mode shapes of $n = 6$ modes , $(r, s) = (5, 5)$, $\chi = 11.43$, free-free edges

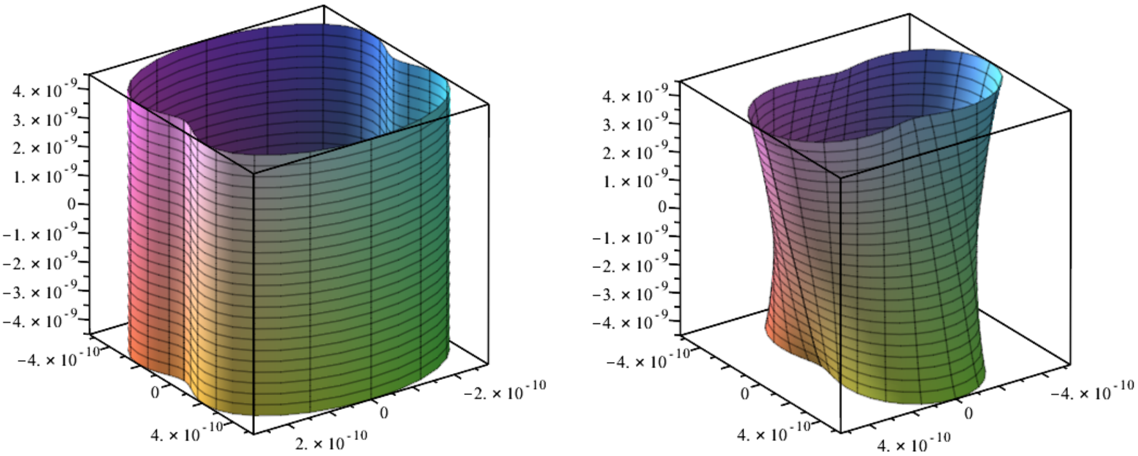

(a) $k = 0,\ \omega_1 = 1.169$ THz (b) $k = 1/4,\ \omega_2 = 1.172$ THz

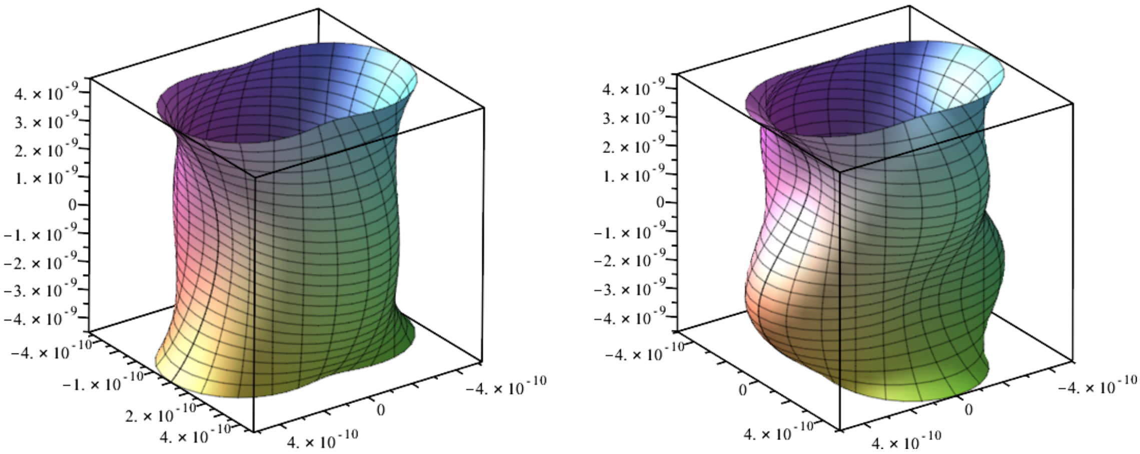

(c) $k = 1/2,\ \omega_1 = 1.177$ THz (d) $k = 3/4,\ \omega_1 = 1.192$ THz

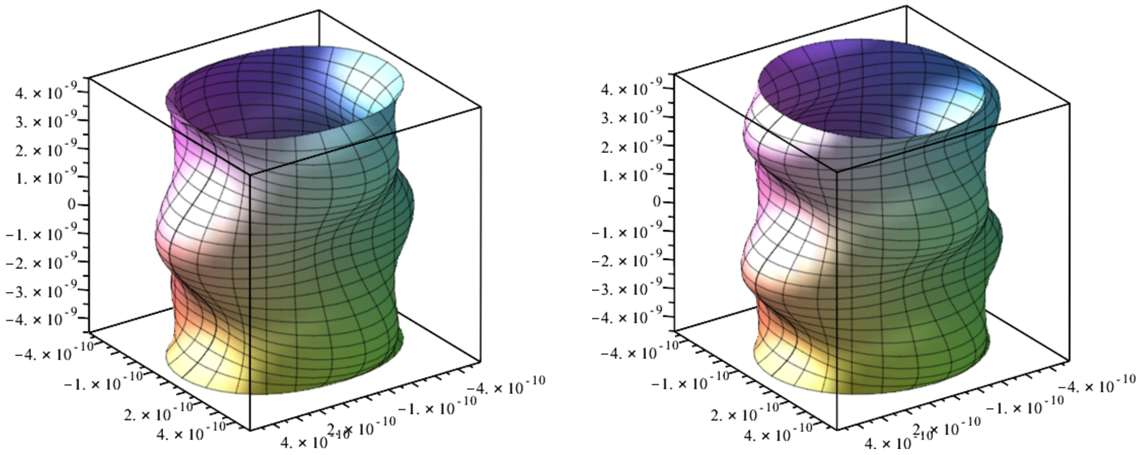

(e) $k = 1,\ \omega_1 = 1.298$ THz (f) $k = 5/4,\ \omega_1 = 1.333$ THz

Figure 3.5: Mode shapes of $n = 2$ modes , $(r, s) = (10, 0)$, $\chi = 12.8$, free-free edges

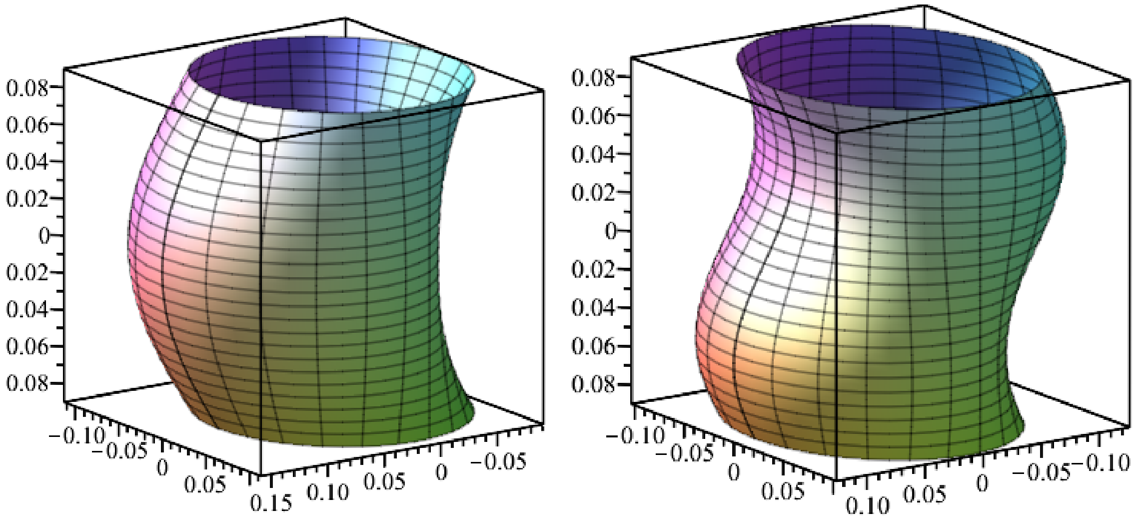

(a) $k = 1/2,\ \omega_1 = 4811$ Hz

(b) $k = 1,\ \omega_2 = 7103$ Hz

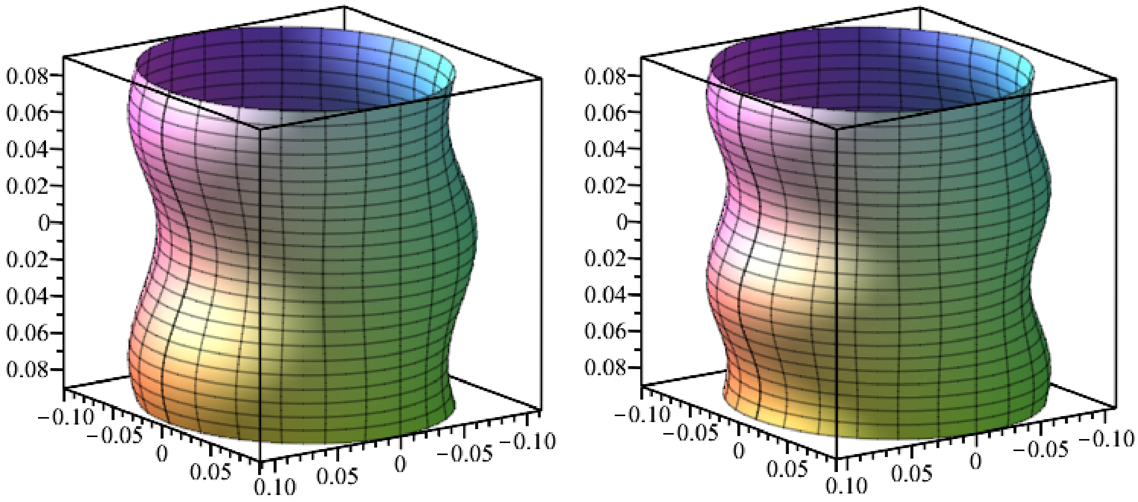

(c) $k = 3/2,\ \omega_3 = 7627$ Hz

(d) $k = 5/2,\ \omega_4 = 7806$ Hz

Figure 3.6: Mode shapes of beam-like modes ($n = 1$), simply supported-simply supported edges with parameters referring to Table 3.10

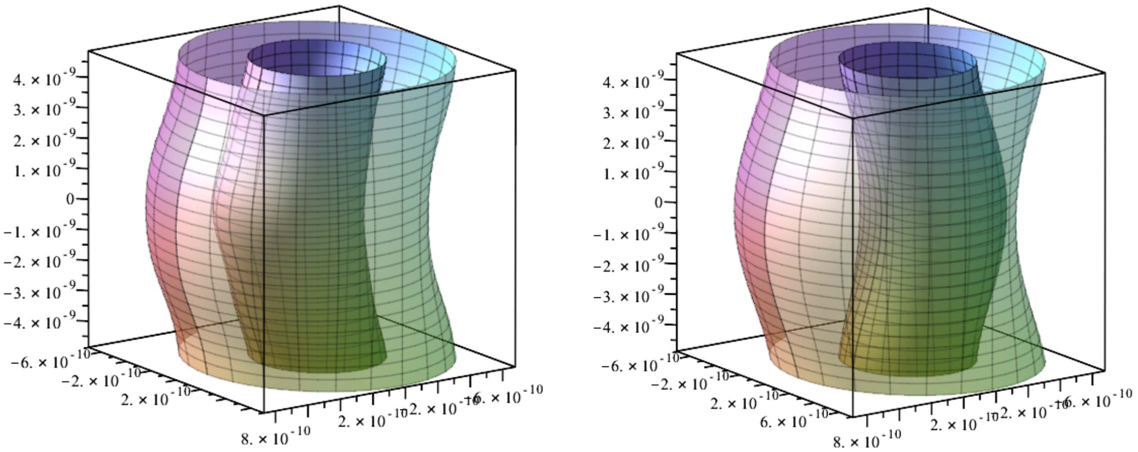

(a) $k = 1,\ \omega = 0.2729$ THz

(b) $k = 1,\ \omega = 2.003$ THz

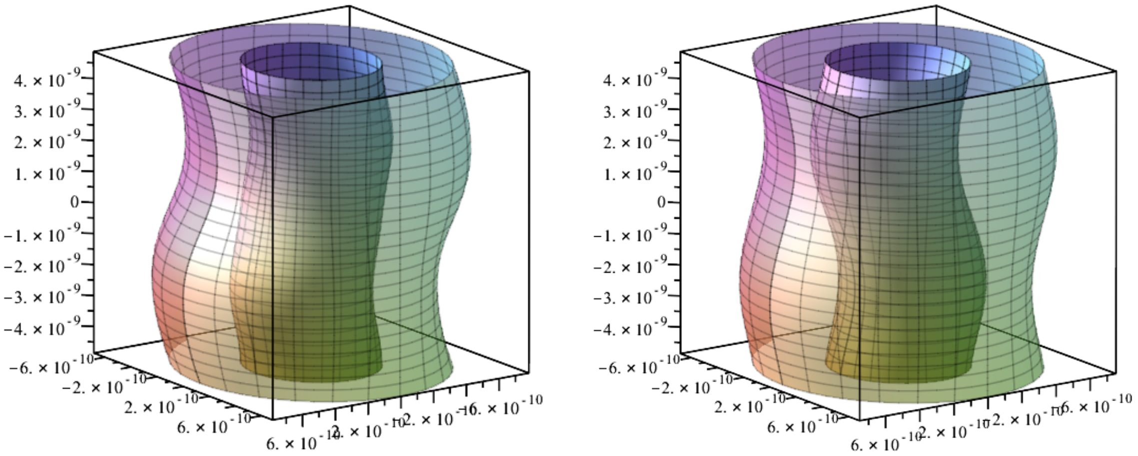

(c) $k = 3/2,\ \omega = 0.6358$ THz

(d) $k = 3/2,\ \omega = 1.927$ THz

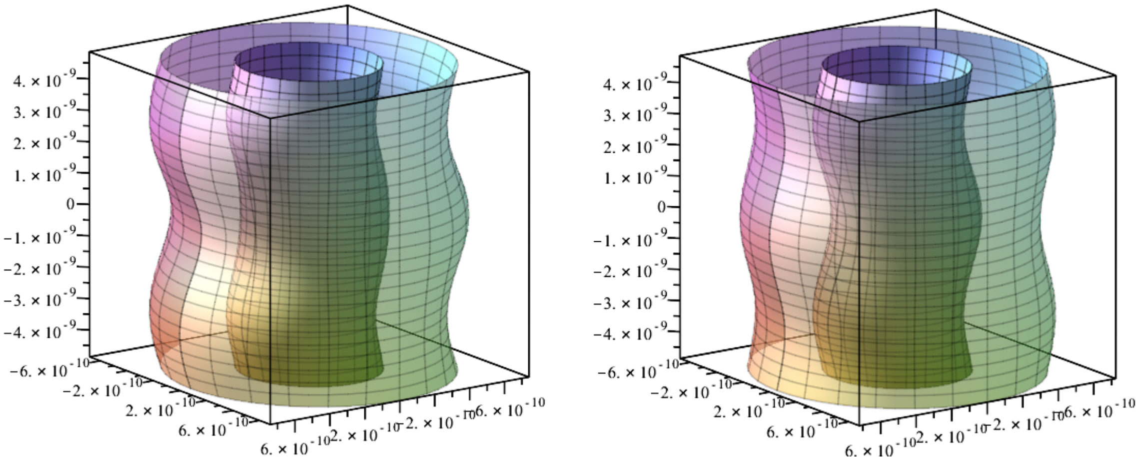

(e) $k = 2,\ \omega_1 = 1.082$ THz

(f) $k = 2,\ \omega_1 = 1.759$ THz

Figure 3.7: Mode shapes of $n = 1$ modes for a DWCNT, $(r, s) = (5, 5)$ and $(r, s) = (10, 10)$, $\chi = 7.24$, clamped-clamped edges

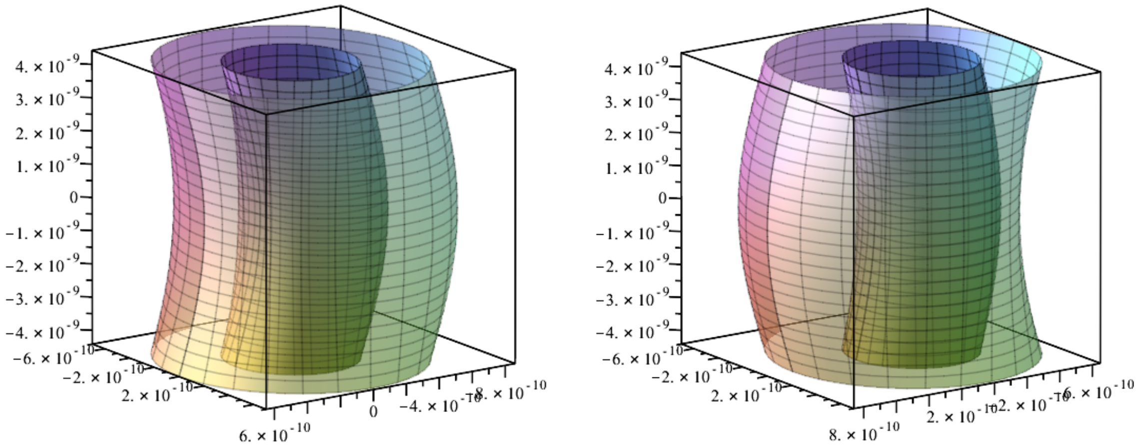

(a) $k = 1/2,\ \omega = 0.1396$ THz (b) $k = 1/2,\ \omega = 2.010$ THz

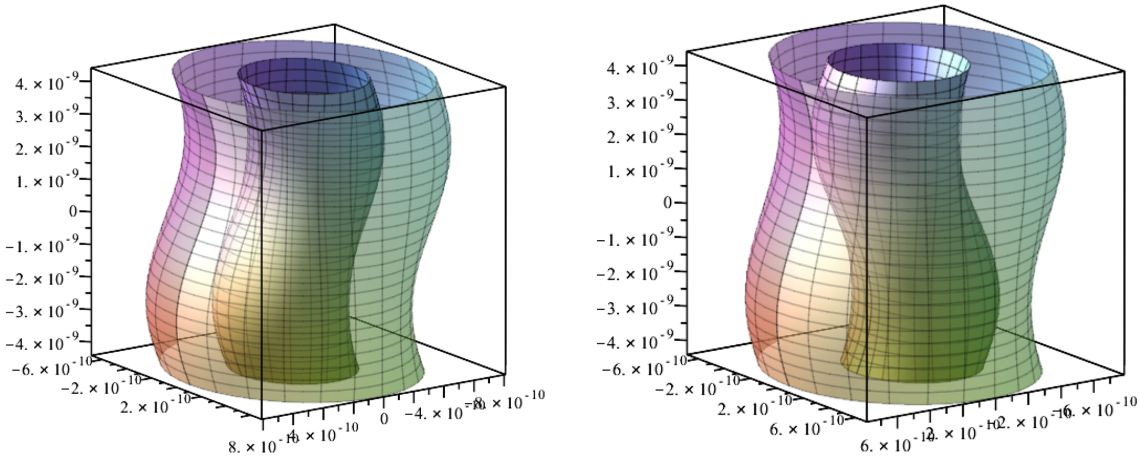

(c) $k = 1$, $\omega = 0.4945$ THz (d) $k = 1$, $\omega = 1.953$ THz

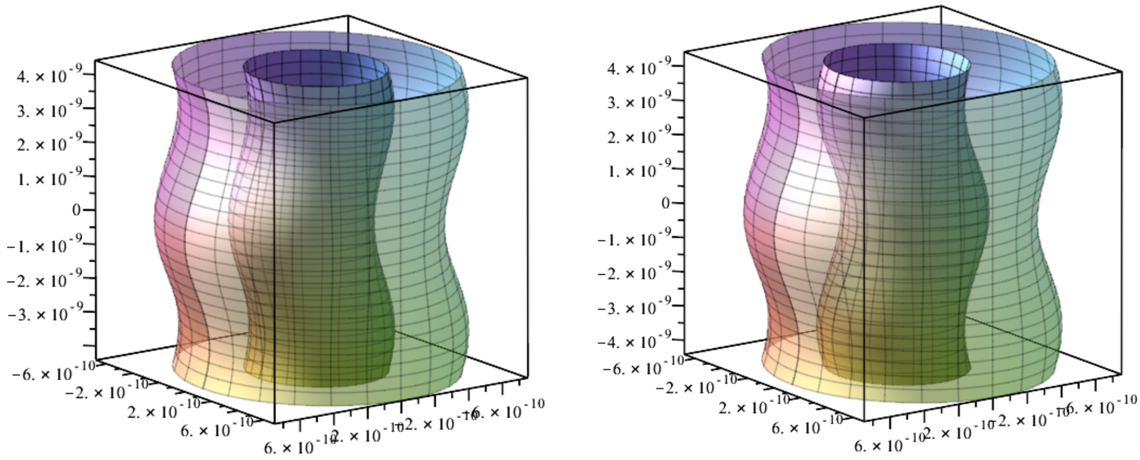

(e) $k = 3/2$, $\omega_1 = 0.9620$ THz (f) $k = 3/2$, $\omega_1 = 1.814$ THz

Figure 3.8: Mode shapes of $n = 1$ modes for a DWCNT, $(r, s) = (5, 5)$ and $(r, s) = (10, 10)$, $\chi = 7.24$, simply supported-simply supported

3.5 Conclusions

In the present chapter, convergence and validation of natural frequencies results are performed, while mode shapes of different sets of conditions and parameters are plotted.

After establishing the definition of boundary conditions and the equivalent parameters of single-walled carbon nanotubes, convergence analysis takes place. It was found that different boundary conditions imply a different set of numbers of shape functions in order for the local model to converge (in comparison to different cited published shell models), as for free-free boundary conditions the results converge for a high value of N. Thus, for the sake of accuracy, the maximum number of shape functions for the x coordinate is employed for each one of the simulations in the following sections and chapters. The convergence of the values of the nonlocal theory are compared to available bibliographical sources, as the results reveal accurate.

Regarding the validation of the local theory, the radial breathing modes were first tested. When compared to resonant Raman Spectroscopy and Molecular Dynamics simulation results, the values obtained by the developed model in the present dissertation are accurate and satisfactory. Then, beam-like modes for clamped-clamped edges were tested, revealing a high order accuracy as the dimensions of the nanotube increase, namely the diameter and specially the aspect ratio, which plays a significant factor in the magnitude of the difference. When comparing the same boundary conditions with higher diameters and lengths to FEA results, the accuracy behaviour does propagate. The free-free boundary conditions reveal accurate values as well as displaying more accurate results for higher aspect ratios, as expected. Finally, the simply supported-simply supported boundary conditions are validated by comparison to a model for a shell with different properties, while yielding results with very low relative differences, being in good agreement with the exact solution and producing better results than the FEM model proposed by the referenced author.

The natural frequencies of DWCNTs were also tested for clamped-clamped and simply supported-simply supported boundary conditions, by comparison to MD results, generating results with relatively higher difference value regarding the referenced data, while being within a reasonable range to validate the model. Then, the natural frequency values of a SWCNT of given chirality were compared to DWCNTs of the same chirality for the outer tube, with varying inner chirality parameters and consequent diameter. It was found that for lower values of inner tube diameter, the fundamental natural frequency was lower than the SWCNT one by a more significant margin, while for higher inner tube diameter values the natural frequency values would increase and tend to the SWCNT value. Therefore, it leads to believe that the stiffness increment is more preponderant than the inertia increment for an increasing value of inner tube diameter for a DWCNT, yielding higher natural frequency results, while the addition of an inner tube of a SWCNT always results in lower natural frequency values.

The mode shapes of the carbon nanotubes in the conditions described in the last paragraphs were plotted next, illustrating not only the versatility of the implemented model, but also the wide range of vibrational behaviour associated with shells. Radial breathing modes, beam-like modes and other modes for different n values were shown for different boundary conditions in SWCNT, while for DWCNT the "in-phase" and "anti-phase" beam-like modes for different boundary conditions were shown. It is important to note that although for a p-version FEM technique it is possible to adjust the input parameters to extract each one of the vibrational modes, defining the specific value of the circumferential mode number n, in real CNTs and MD/FEA the vibrational modes are extracted at once. Thus the process to identify the correspondent mode shape to each natural frequency may be lengthy, as the wavenumber of a given mode shape may not be associated with the order of the calculated natural frequencies, given the influence of the non-diagonal stiffness terms on shell dynamics, that make for apparently unpredictable behaviours of the mode shapes regarding switches in expected outputs and the actual ones. This characteristic is seen for example in modes affected by the nonlocal parameter, but specially and more widely when extracting modes for a high circumferential mode number (will be studied on the next chapter).

The study on the influence of the nonlocal parameter is not carried out in the validation process, as it is a wide and long description, and does not represent a validation, being instead a proposed calibration, according to different parameters. Thus, it is performed in the next chapter.

Chapter 4

Study on the nonlocal parameter influence

4.1 Introduction

In the present chapter the already validated thin shell model is used to perform a study on the influence of the nonlocal parameter. This parameter, e_0, is calibrated in order for the model to preview the most accurate result for each natural frequency along a set of defined values of aspect ratio. These results are compared to molecular dynamics simulations and finite element analysis, as well as continuous sets of constant nonlocal parameters.

The nonlocal parameter is lastly adjusted to inspect its influence on the frequency ratio for different aspect ratios and chiralities, along with its behaviour for different values of the circunferential mode numbers n, covering the same range of already listed characteristics. The influence on the behaviour of mode shapes is also investigated for different values of the nonlocal parameter. The results and graphics from the present study are all produced using the software *Maple* and *MATLAB*.

4.2 Calibration of e_0

4.2.1 Single-walled carbon nanotube

The calibration of the nonlocal parameter may be carried out in different terms. The first possibility is selecting a set of consecutive natural frequencies for a given chirality and aspect ratio, and adjusting the nonlocal parameter that produces the results with minimum average difference when comparing to MD or FEA results. The second option consists of calibrating a single value of e_0 for each value of natural frequency (for a given chirality and aspect ratio), for different order natural frequencies (being ω_1, ω_2, ω_3 and ω_4), minimizing the difference when comparing to the corresponding natural frequency calculated by MD or FEA. In fact, the value of the calibrated e_0 yields a similar behaviour in both analysis (a critical value of aspect ratio is identified), while the first does not provide insights about the significant behaviour differences for distinct natural frequencies - ω_i, for $i \in \mathbb{N}$. Thus, the second option is taken on this dissertation, consisting of an iterative method that ranges values of e_0 paced by 0.05 dimensionless units, selecting the minimum difference value in the end, as distinct natural frequencies are separately analysed.

Having chosen the analysis procedure, and selecting Duan et al. [7] molecular dynamics work as a reference, a comparison between the curves of the results of a clamped-clamped

CNT given by Molecular Dynamics and the values calculated by the developed model for different values of the nonlocal parameter e_0 along different values of aspect ratio $\chi = \frac{l}{2R}$ (for which the radius R is constant for each case), for a chirality of $(r, s) = (5, 5)$ is carried out and presented for the first four natural frequencies in Figure 4.1.

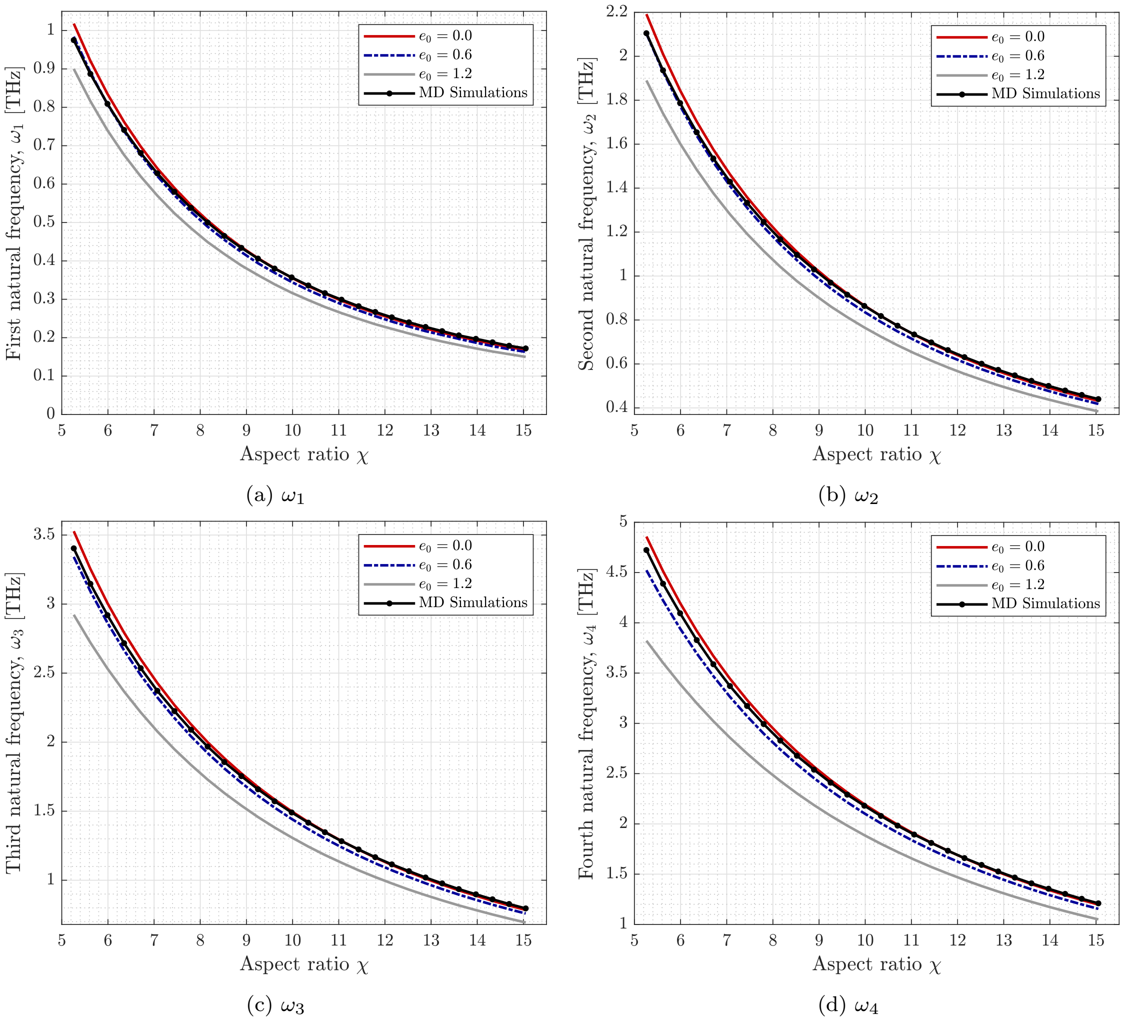

(a) ω_1 (b) ω_2

(c) ω_3 (d) ω_4

Figure 4.1: Comparison between the natural frequencies calculated by MD [7] and values from the present model for different nonlocal parameters, clamped-clamped edges CNT with $(r, s) = (5, 5)$

Investigating into Figure 4.1 results, the first noticeable characteristic is the proximity of the MD results and relatively low values of the nonlocal parameter. In fact, for the graphic of ω_1, for small values of aspect ratio, the natural frequency is in close agreement with the curve $e_0 = 0.6$, leaning onto the curve $e_0 = 0$ as the aspect ratio increases. For the following natural frequencies ω_2, ω_3 and ω_4, for lower aspect ratios the MD results tend to be closer to the $e_0 = 0$ as the natural frequency increases, with the values for higher aspect ratios keeping a tight relation to the same curve.

The concept of critical aspect ratio must also be introduced, being the value of the aspect ratio for which the nonlocal theory (and parameter) have no effect or relevance in the outcome of the natural frequency results. As already stated, with the increase of the nonlocal parameter value, the natural frequencies value tend to reduce, therefore, for an increasing aspect ratio, once the local theory yields a numerical value below the referenced one (here, MD simulations), the critical point as been achieved. From Figure 4.1, it can be concluded that for higher natural frequencies, the critical aspect ratio tends to also increase (detected on the intersection of "MD Simulations" and "$e_0 = 0$" plots).

The last point to note remains with the fact that the curves of $e_0 = 1.2$ appear to have a larger gap from the curves of $e_0 = 0$ as the order of the natural frequency increases. Even though the scale on the y-axis is different, this conclusion may be apparent, and reveals room for investigation, as will be seen further in this chapter.

Given the presented analysis, it is clear that the calibration for different numbers of natural frequencies is necessary, as its behaviour is clearly distinct. Thus, the calibration is established in Table 4.1.

Table 4.1: Calibration of the nonlocal parameter regarding natural frequencies THz clamped-clamped edges CNTs with $(r, s) = (5, 5)$ in comparison to MD results

χ	ω_{MD} [7]	e_0	ω_{Model}	Diff. (%)	ω_{MD} [7]	e_0	ω_{Model}	Diff. (%)
	First natural frequency ω_1				Second natural frequency ω_2			
5.26	0.975	0.70	0.973	0.232	2.105	0.60	2.103	0.079
5.62	0.887	0.65	0.886	0.096	1.936	0.60	1.930	0.284
5.99	0.809	0.60	0.808	0.108	1.787	0.55	1.785	0.129
6.35	0.741	0.55	0.741	0.057	1.654	0.50	1.658	0.221
6.71	0.681	0.50	0.682	0.190	1.535	0.50	1.535	0.031
7.07	0.628	0.50	0.627	0.163	1.429	0.50	1.426	0.209
7.44	0.580	0.45	0.579	0.166	1.333	0.45	1.331	0.133
7.80	0.538	0.40	0.537	0.136	1.246	0.40	1.247	0.105
8.16	0.500	0.35	0.500	0.079	1.167	0.40	1.166	0.075
8.52	0.465	0.30	0.466	0.113	1.096	0.35	1.096	0.033
8.89	0.434	0.25	0.434	0.060	1.030	0.30	1.030	0.032
9.25	0.406	0.15	0.406	0.071	0.970	0.25	0.971	0.121
9.61	0.380	0.15	0.380	0.003	0.915	0.25	0.914	0.060
9.98	0.357	0.00	0.356	0.230	0.864	0.15	0.864	0.036
10.34	0.336	0.00	0.334	0.472	0.818	0.00	0.818	0.010
10.70	0.316	0.00	0.315	0.465	0.774	0.00	0.774	0.037
11.06	0.299	0.00	0.296	0.895	0.734	0.00	0.733	0.172
11.43	0.282	0.00	0.279	1.004	0.698	0.00	0.694	0.601
11.79	0.267	0.00	0.264	1.185	0.663	0.00	0.659	0.645
12.15	0.253	0.00	0.250	1.303	0.631	0.00	0.626	0.769
12.52	0.240	0.00	0.236	1.540	0.601	0.00	0.595	0.992
12.88	0.228	0.00	0.224	1.643	0.573	0.00	0.567	1.070
13.24	0.217	0.00	0.213	1.805	0.548	0.00	0.541	1.353
13.60	0.206	0.00	0.203	1.597	0.523	0.00	0.516	1.332
13.97	0.197	0.00	0.193	2.130	0.500	0.00	0.492	1.511
14.33	0.188	0.00	0.184	2.216	0.479	0.00	0.471	1.677
14.69	0.179	0.00	0.175	1.974	0.459	0.00	0.451	1.782
15.05	0.172	0.00	0.168	2.532	0.440	0.00	0.432	1.840

χ	ω_{MD} [7]	e_0	ω_{Model}	Diff. (%)	ω_{MD} [7]	e_0	ω_{Model}	Diff. (%)
	Third natural frequency ω_3				Fourth natural frequency ω_4			
5.26	3.404	0.50	3.396	0.238	4.724	0.35	4.736	0.253
5.62	3.147	0.50	3.140	0.234	4.389	0.40	4.377	0.264
5.99	2.920	0.45	2.924	0.143	4.095	0.35	4.105	0.250
6.35	2.717	0.45	2.719	0.074	3.828	0.35	3.839	0.295
6.71	2.536	0.45	2.535	0.044	3.588	0.35	3.598	0.290
7.07	2.372	0.45	2.369	0.131	3.371	0.35	3.380	0.254
7.44	2.225	0.40	2.226	0.037	3.173	0.35	3.175	0.059
7.8	2.090	0.40	2.089	0.058	2.993	0.35	2.993	0.003
8.16	1.968	0.40	1.964	0.208	2.829	0.35	2.827	0.088
8.52	1.856	0.35	1.858	0.081	2.678	0.35	2.673	0.169
8.89	1.754	0.30	1.756	0.102	2.539	0.30	2.539	0.010
9.25	1.659	0.30	1.659	0.007	2.410	0.30	2.409	0.060
9.61	1.572	0.25	1.574	0.144	2.291	0.30	2.288	0.147
9.98	1.491	0.25	1.489	0.112	2.181	0.25	2.180	0.060
10.34	1.417	0.20	1.416	0.049	2.079	0.20	2.081	0.085
10.7	1.348	0.15	1.348	0.018	1.983	0.20	1.983	0.009
11.06	1.283	0.10	1.283	0.024	1.894	0.20	1.892	0.097
11.43	1.223	0.00	1.221	0.137	1.811	0.10	1.811	0.003
11.79	1.167	0.00	1.164	0.261	1.733	0.05	1.733	0.012
12.15	1.115	0.00	1.110	0.411	1.660	0.00	1.658	0.092
12.52	1.066	0.00	1.059	0.655	1.592	0.00	1.586	0.351
12.88	1.020	0.00	1.012	0.761	1.527	0.00	1.521	0.420
13.24	0.977	0.00	0.968	0.881	1.466	0.00	1.459	0.500
13.6	0.936	0.00	0.927	0.936	1.409	0.00	1.400	0.614
13.97	0.898	0.00	0.888	1.166	1.355	0.00	1.344	0.822
14.33	0.862	0.00	0.851	1.253	1.304	0.00	1.292	0.918
14.69	0.828	0.00	0.817	1.330	1.255	0.00	1.243	0.952
15.05	0.796	0.00	0.785	1.417	1.210	0.00	1.197	1.099

And finally, from the gathered information from Table 4.1, comes Figure 4.2. From Table 4.1 and Figure 4.2 it is possible to validate points already made in the previous paragraphs, for instance the fact that for lower order natural frequencies, the ideal value of the calibrated nonlocal parameter is higher than for higher order natural frequencies, as for ω_1, $e_0 = 0.70$, for ω_2, $e_0 = 0.6$ and for ω_4, $e_0 = 0.35$, for an aspect ratio of $\chi = 5.26$. Thus, it is possible to conclude that for higher order natural frequencies, the magnitude of the influence of the nonlocal parameter is reduced.

Regarding the critical value of the aspect ratio, it is now clear that this value is also higher for higher order natural frequencies. In fact, for the first natural frequency ω_1, the value of the critical aspect ratio is $\chi_{cr} = 9.98$, while for ω_2 it is $\chi_{cr} = 10.34$, for ω_3 the value is $\chi_{cr} = 11.43$ and finally for ω_4, $\chi_{cr} = 12.15$. Thus, even though the magnitude of the calibrated nonlocal parameter is higher for low number natural frequencies, the opposite effect happens when it comes to the permanence of influence of the nonlocal parameter in the natural frequency values, sustaining its relevance in longer carbon nanotubes for higher order natural frequencies, as its critical aspect ratio is also higher. Naturally, it can be identified a range of aspect ratio values in which the relevance and magnitude of the nonlocal parameter is similar for different natural frequencies ($\chi \in [7.5, 8.5]$), even though it is not clear the same range would be the same for chiralities that would lead to higher diameter values.

In an attempt to collect information on a carbon nanotube with a chirality that induces a higher diameter value, the same process applied in Table 4.1 is used regarding finite element analysis results from A. Sakhaee-Pour et al. [63]. The results are compiled in Figure 4.3.

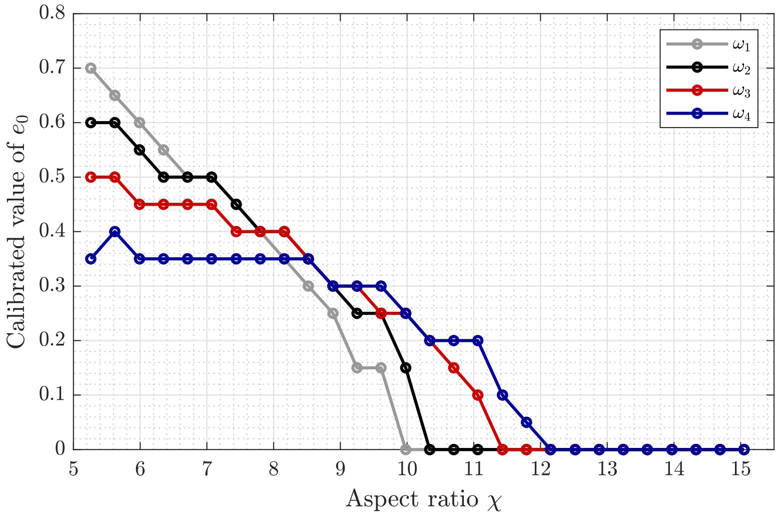

Figure 4.2: Calibration of e_0 for each natural frequency for clamped-clamped edges CNTs with $(r, s) = (5, 5)$ in comparison to MD results [7]

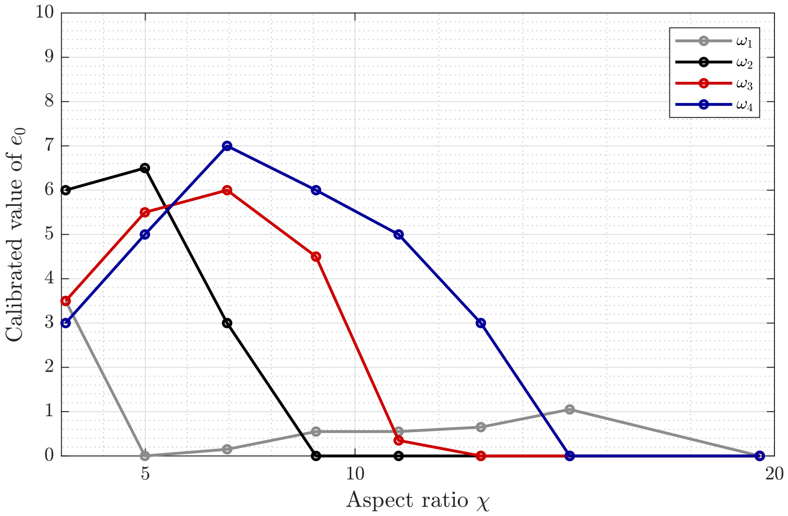

Figure 4.3: Calibration of e_0 for each natural frequency for clamped-clamped edges CNTs with $(r, s) = (12, 12)$ in comparison to FEA results [63]

From Figure 4.3 it possible to gauge and validate some of the previous conclusions. In fact, the behaviour of the plotted curves is similar in terms of tendence to the critical aspect ratio to the already described hypothesis, with the exception of ω_1 that after its tendency for the nonlocal parameter to be null, it has small variations before returning to the null value. Then, regarding the magnitude of the nonlocal parameter associated with each natural frequency's number, ω_4 reveals a considerable increase for $\chi = 6.95$. This fact along with the behaviour of the natural frequency values for the lower registered aspect ratio are most likely connected to the fact that the simulation comes from finite element analysis with beam elements and not molecular dynamics simulations, even though it is modelled so that each atom is a concentrated mass and their bonds are modelled by the beam elements. As already described in the previous chapter, for lower aspect ratios the results of FEA tend to not be in agreement with the present model, as for higher aspect ratios the values end up converging. Thus, not further conclusions may be taken from comparison to FEA results.

4.2.2 Double-walled carbon nanotube

Regarding the double-walled carbon nanotube, as mentioned on the previous chapter, only the fundamental frequency was analysed. Thus, the nonlocal parameter calibration process is simpler, as again an iterative method paced by 0.05 dimensionless units is selected, allowing for the determination of the value associated with the minimum relative difference in the end, for each value of aspect ratio/length of the nanotube.

Utilizing Ansari et al. [101] molecular dynamics values as a reference, it is firstly presented the comparison between the curves of the MD results of a clamped-clamped DWCNT and the calculated ones by the model developed in this dissertation, for different values of the nonlocal parameter e_0. The values in the abscissa axis come as aspect ratio instead of the length of the nanotube in nanometers, as presented in the last chapter, to maintain coherence with the values presented in the current chapter. Still, it is important to note that they are equivalent to the length values already documented in Table 3.13. Thus, the natural frequency values are presented in Figure 4.4.

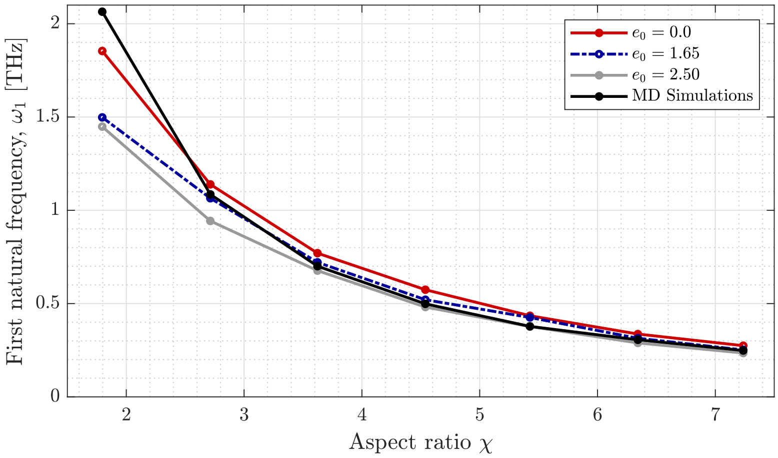

Figure 4.4: Comparison between the natural frequencies calculated by MD [101] and values from the present model for different nonlocal parameters, clamped-clamped edges DWCNT with $(r, s) = (5, 5); (10, 10)$

As may be observed from Figure 4.4, it is possible to observe that the MD results are well fitted inside the curves of the local model and the nonlocal model for $e_0 = 2.50$. In fact, the MD simulations values are always inferior to the nonlocal model except for the first value of aspect ratio. This may come as unexpected, even though the same behaviour where for very low values of aspect ratio the natural frequency previewed by MD is higher than for the shell model, in a work of Ansari et al. [12], for example. Still, the curves illustrate the common behaviour where as the aspect ratio increases, the natural frequency value tends to decrease, and the values regarding different values of the nonlocal parameter tend to be closer, as the nonlocal theory's relevance reduces, tending to the values of the local theory with the increase of dimensions of the nanotube in general.

Finally, a similar calibration to the one performed and presented in Table 4.1 is taken, for the DWCNT fundamental frequency case. For the sake of brevity, the table is not presented, as the values are exposed in Figure 4.5.

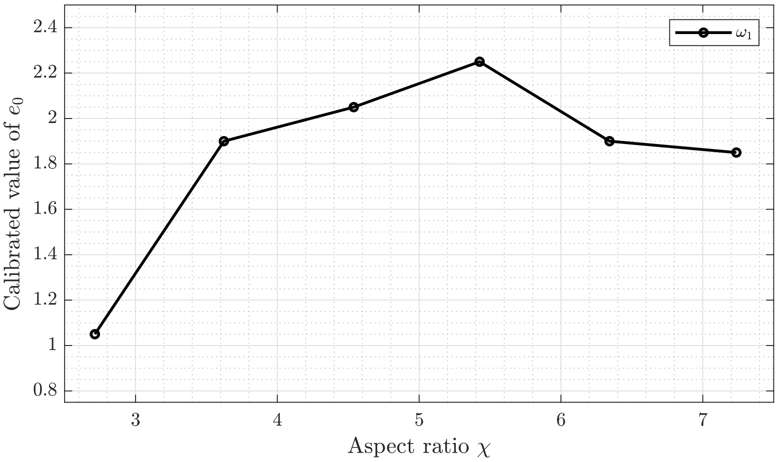

Figure 4.5: Calibration of e_0 for the fundamental natural frequency for clamped-clamped edges DWCNT with $(r, s) = (5, 5); (10, 10)$ in comparison to MD results [101]

Regarding Figure 4.5, it is evident that with the present results, a critical aspect ratio value was not achieved. In fact, it can be observed that with the exception of the first value (which is not referring to the same aspect ratio value as Figure 4.4, as its first χ yielded a higher MD result in comparison to the shell local model), the calibrated nonlocal parameter e_0 values are close. This may come from the fact that the range of the documented aspect ratio values is small, in comparison to the available used data for the SWCNT, for example, as for this case the maximum value of the aspect ratio is still inferior than the critical value for the SWCNT. Even though conclusions about the preponderance of the nonlocal theory on the DWCNT case along the aspect ratio spectrum may not be taken, it may be observed that for similar χ values, for a DWCNT the values of e_0 are higher than for a SWCNT. Utilizing wider data for length values, a more detailed study would be possible, even though it may be seen that from the last three values presented on Figure 4.5, a decrescent tendency for the value of e_0 is noticeable, while for said aspect ratio values the nonlocal parameter effect on the natural frequency is less significant.

4.3 Influence of e_0 on the frequency ratio

As discussed regarding Figure 4.1 about the more significant displacement of the curves plotted of a higher value of e_0 for higher order natural frequencies, the effect of the nonlocal parameter on the frequency ratio is now investigated. Therefore, for the same chirality conditions studied, where $(r, s) = (5, 5)$, and with the frequency ratio defined as $\frac{\omega_{nonlocal}}{\omega_{local}}$, or the ratio of the frequency given for a defined value of e_0 and a frequency given for $e_0 = 0$. This ratio is studied as a function of the nonlocal parameter, for different values of the aspect ratio, as is given in Figure 4.6.

Analysing Figure 4.6, it is important to note that the same scale on the y-axis is applied to all the four graphics. The first evident conclusion to take note is the fact that for the same natural frequency order, for instance ω_1, it is clear that for lower values of aspect ratio, the frequency ratio drop is higher than for higher values of aspect ratio. Naturally it is already known that for the same chirality, for an increasing value of the aspect ratio, a smaller value of the natural frequency is yielded, as well as for an increasing value of

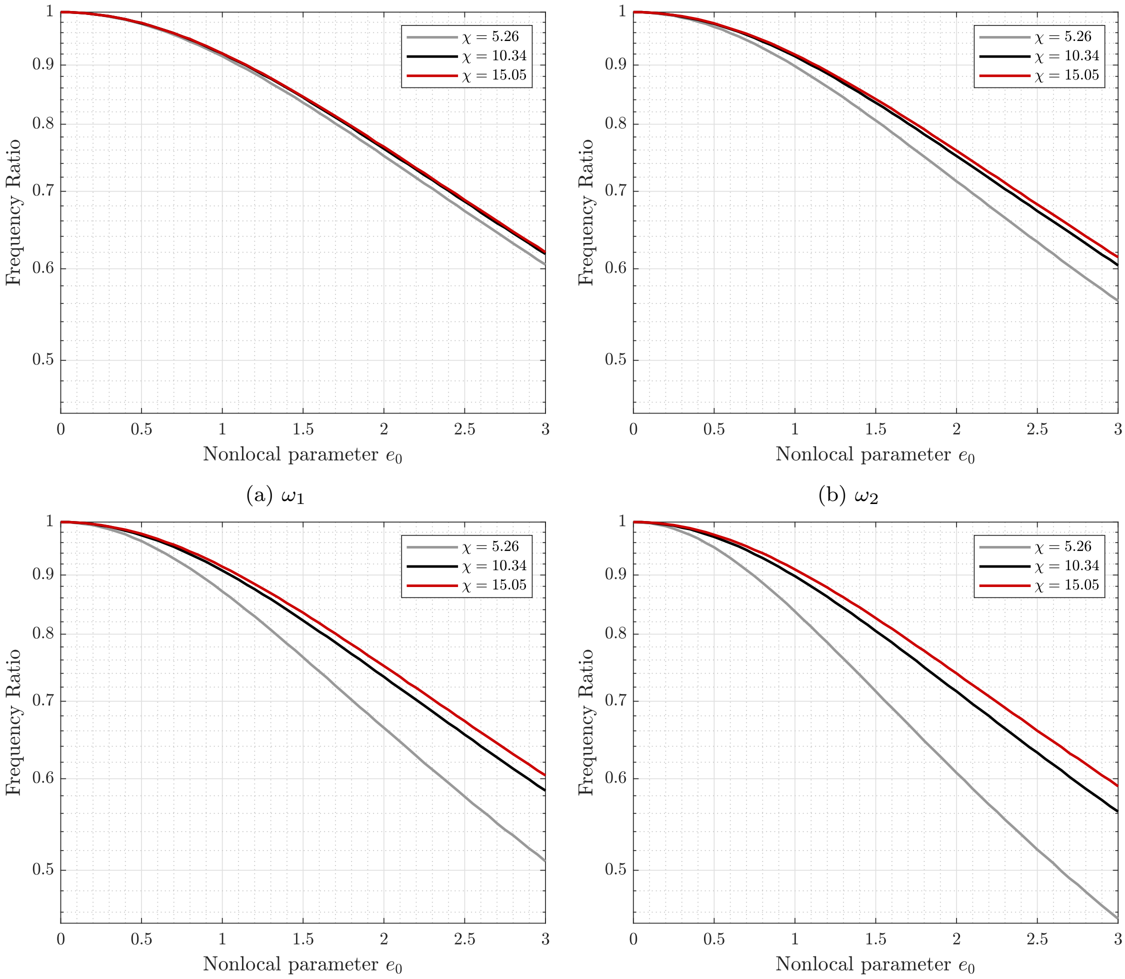

(a) ω_1

(b) ω_2

(c) ω_3

(d) ω_4

Figure 4.6: Frequency ratio as a function of the nonlocal parameter, for different values of aspect ratio, regarding the first four natural frequencies of a $(r, s) = (5, 5)$ clamped-clamped edges carbon nanotube

the nonlocal parameter, a smaller value of natural frequency is also calculated. With this plot it is concluded that in comparison to the local natural frequency value, a relatively lower value of nonlocal natural frequency is produced for lower aspect ratios.

Furthermore, when comparing the curves of the same aspect ratios for different natural frequency's numbers, it is concluded that the higher that number is, the more significant the decrease in frequency ratio is. For example, for an aspect ratio of $\chi = 15.05$ and $e_0 = 3$, for ω_1 the frequency ratio is 0.6202, while for ω_2 the frequency ratio is 0.6137, and for ω_3 and ω_4 the frequency ratio is 0.6039 and 0.5912 respectively.

On the same note, as the order of the natural frequency progresses, the gap between the curves of different aspect ratios is increased, meaning that for ω_4 the influence of lower aspect ratios for the same value of nonlocal parameter is higher, for example. Thus, the higher the order of the natural frequency, the more the nonlocal parameter becomes relevant on the whole range of aspect ratios, specially for lower values of aspect ratio, in comparison to the local values of the natural frequency. This is related to the fact that for higher order natural frequencies the wavenumber associated with its mode shape is higher, yielding for a greater influence of the nonlocal parameter.

The described behaviour needs to be evaluated for a different value of chirality, in order to study the effect of the diameter on the object of study. Therefore, for a chirality of $(r, s) = (20, 20)$ the same research on the influence of the nonlocal parameter is performed using the same values of aspect ratio, leading to Figure 4.7.

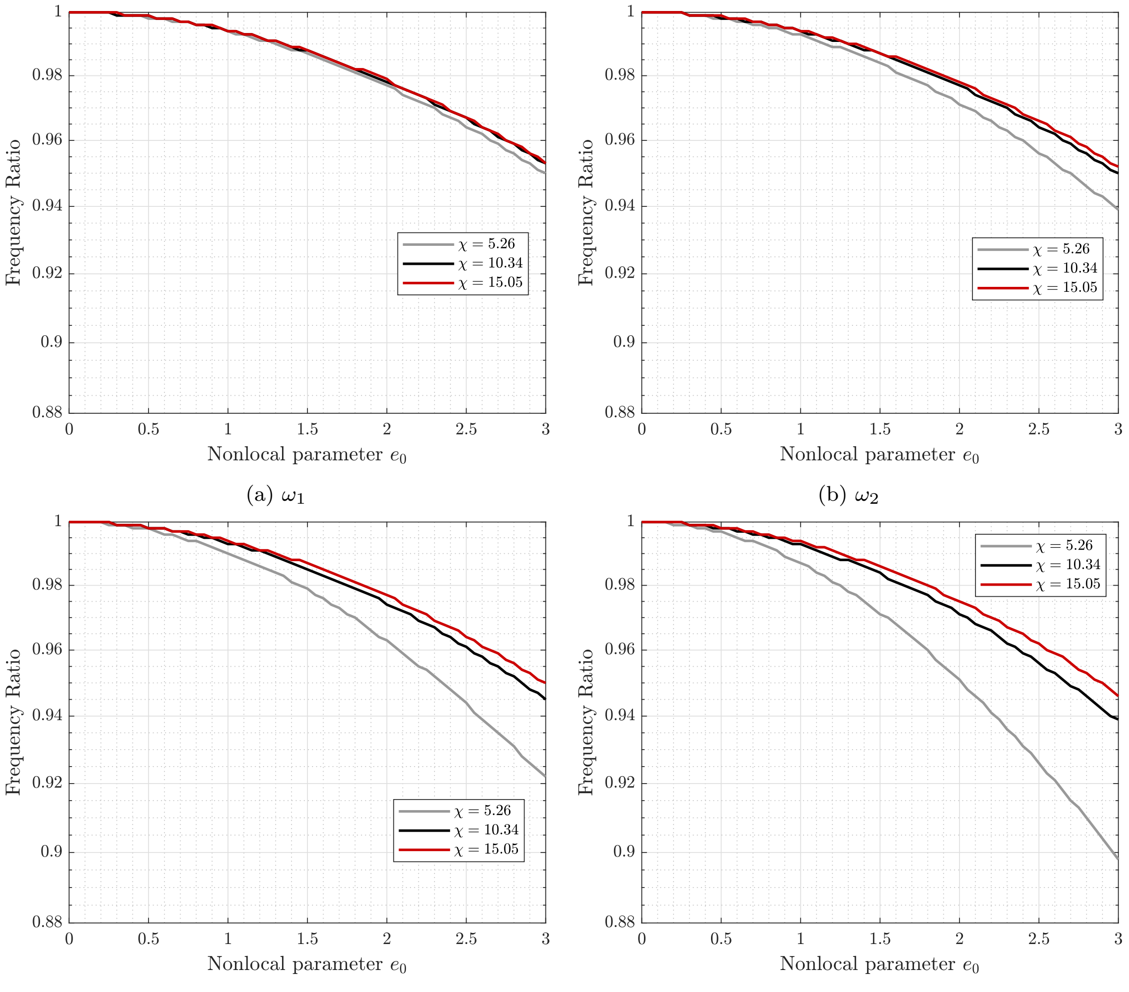

(a) ω_1

(b) ω_2

(c) ω_3

(d) ω_4

Figure 4.7: Frequency ratio as a function of the nonlocal parameter, for different values of aspect ratio, regarding the first four natural frequencies of a $(r, s) = (20, 20)$ clamped-clamped edges carbon nanotube

From Figure 4.7 the same behaviour described for a chirality of $(r, s) = (5, 5)$ is shown. It should be noted that the values of the y-axis scale are different, as higher values of frequency ratio are plotted. Thus, it is concluded that for higher diameter values, the same type of behaviour is produced while having a smaller relative influence, so that for higher order natural frequencies, the influence of the nonlocal parameter is increasingly relevant specifically for lower values of aspect ratios, but with a smaller order of magnitude when comparing the results coming from smaller diameters. This is in accordance to the fact that the nonlocal theory is in fact more relevant the smaller the size the object of study.

4.4 Influence of e_0 and circumferential mode number

In the present section, the influence of the circumferential mode number on the value of the natural frequencies, along with the effect of the nonlocal parameter e_0 is verified. One of the many characteristics that distinguishes the behaviour of mode shapes in shells and plates is the fact that for shells, the resulting consecutive natural frequencies and associated mode shapes are not necessarily linked to the ascending behaviour of natural frequencies with increasing values of axial and circumferential mode/wave numbers. This means that the first natural frequency, for example, may not be the natural frequency associated with $n = 1$ and $k = 1/4$ or $k = 1/2$, depending on the boundary conditions. In fact, swaps related to the circumferential mode numbers associated with each natural frequencies are more common than the latest, reason why it is studied in the current section.

The described phenomenon is clear for low aspect ratio carbon nanotubes, as for higher values of aspect ratio the natural frequencies naturally increase with the ascending value of the circumferential mode number n, with the growth having less expression the higher the value of the nonlocal parameter. Therefore, the study will be exemplified by carbon nanotubes with a relatively low value of aspect ratio.

In Figure 4.8 it is presented, for a carbon nanotube with chirality $(r, s) = (5, 5)$ and aspect ratio of $\chi = 2.5$, the values of natural frequencies as a function of the circumferential mode number n, for different values of the nonlocal parameter.

For the considered aspect ratio, it is clear that for the whole scenario of natural frequency's number, the value of the natural frequency for $n = 2$ is always inferior to the value for $n = 1$. It is important to note that independently from this phenomenon, the natural frequencies ω_1, ω_2, ω_3 and ω_4 nomenclature is still defined, and for a given value of n, their value is crescent with the order of the respective natural frequency. Still, it must be understood that when calculating the natural frequencies for a given value of $n > 2$ that uses all integer values until the selected one, the nomenclature that sorts ascending values of natural frequencies attributed with an integer number may or may not be associated with the $\omega_i, i = 1, 2, 3, 4$ used in these graphics, as this nomenclature is used not only to maintain coherence within the present chapter, but also to illustrate the behaviour and effect of the nonlocal parameter, as the natural frequencies are calculated using discrete values of n and not the entire sum of its values (for the sake of brevity and clarity), as equated in Equations (2.41).

It should also be noted that regarding the influence of the nonlocal parameter, a higher value of e_0 naturally yields lower values of natural frequencies in comparison to a null value - local theory - as already discussed and proved along this dissertation. Analysing this specific case, it it possible to conclude that the same value of the nonlocal parameter produces a smaller drop in the value of ω from $n = 1$ to $n = 2$ as the number of the natural frequency increases. The behaviour of the curves also appears to be more compact and with smaller value discrepancy for the whole range of values of n when comparing to the natural frequency given for $n = 1$, for an increasing value of e_0. Another relevant aspect consists of the fact that for certain values of e_0, for instance $e_0 = 2$ in this case, the behaviour of the curve may be altered, as for example for ω_3 the value of the natural frequency for $n = 3$ would be greater than the one for $n = 2$ from a local theory, becoming inferior to the value of $n = 2$ for this specific value of the nonlocal parameter.

Having illustrated and discussed the phenomenon of the swaps of natural frequencies regarding the value of n they are associated with, the same behaviour should be studied for a different chirality carbon nanotube, as for different and higher values of aspect ratios this phenomenon is not clear, and thus its relevancy is not enough to include on the present study. Thus, in Figure 4.9 the natural frequencies are presented as a function

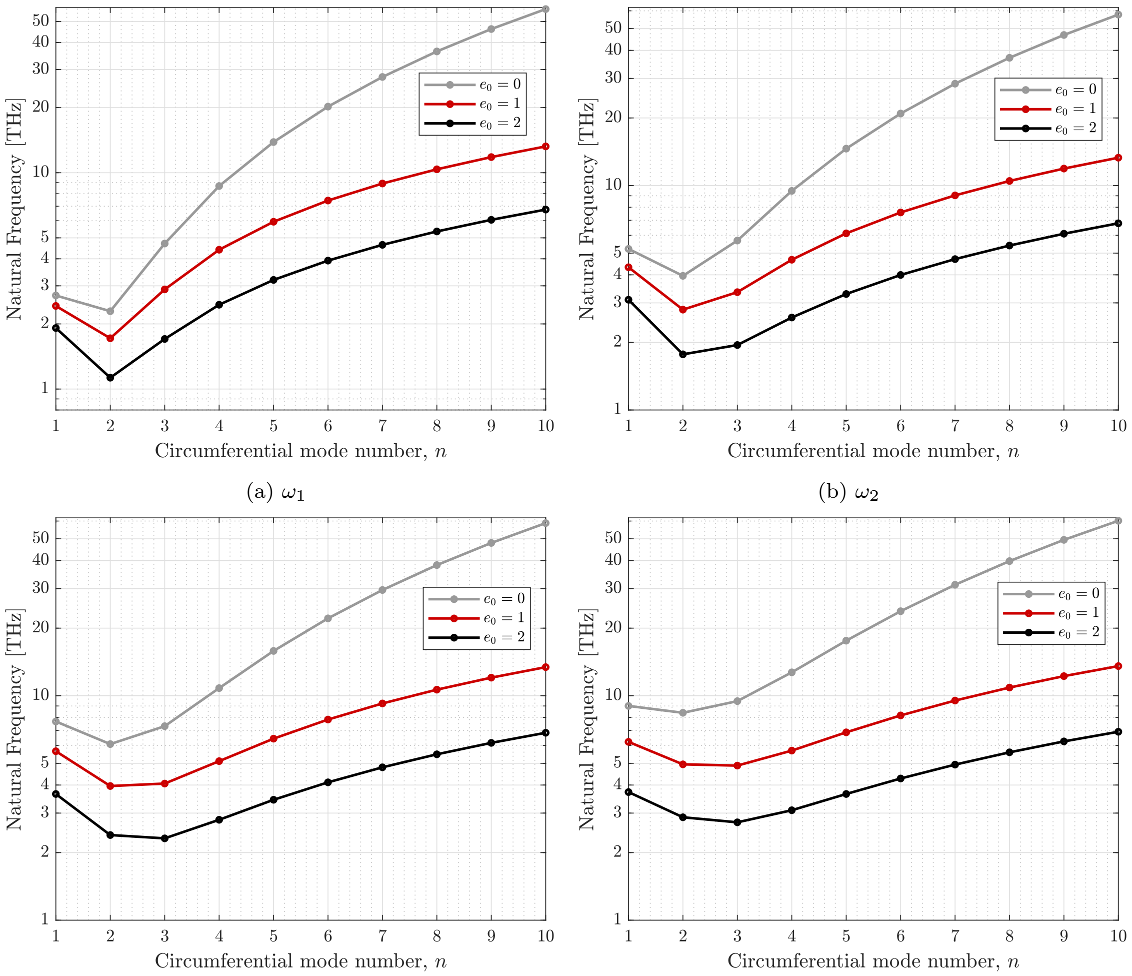

(a) ω_1 (b) ω_2

(c) ω_3 (d) ω_4

Figure 4.8: Natural frequencies (THz) as a function of the circumferential mode number n, for different values of e_0, for a CNT of $(r, s) = (5, 5)$ and $\chi = 2.5$ with clamped-clamped edges

of the circumferential mode number, for different values of the nonlocal parameter, for a chirality of $(r, s) = (20, 20)$ and the same aspect ratio of $\chi = 2.5$.

Analysing Figure 4.9, the first impression possible to register is that the already described phenomenon associated with the values of the circumferential mode shapes is not only relevant for a higher value of chirality and diameter, but also it is more noticeable and apparent for a higher diameter value, while the absolute values of the natural frequencies are significantly lower, being also closer for different values of e_0.

Comparing to Figure 4.8, it should be noted that the decrease in value of natural frequencies with n is more relevant the higher the number of the natural frequency is, as for ω_4 for example, the consecutive values of ω decrease from $n = 1$ until $n = 4$, having a slow but steady growth for the following values of n, while for ω_1 the value of the natural frequencies decreases until $n = 3$, having a significant growth from that value of n on. Naturally, for an increasing order of ω, the higher the natural frequencies are for the same value of n.

The nonlocal parameter e_0 appears to have the same influence as described previously, compacting the curve and smoothing the growth rates of the natural frequencies with the value of the circumferential mode number. It should also be noted that the influence of the nonlocal parameter regarding the gap between the local and nonlocal values of ω is

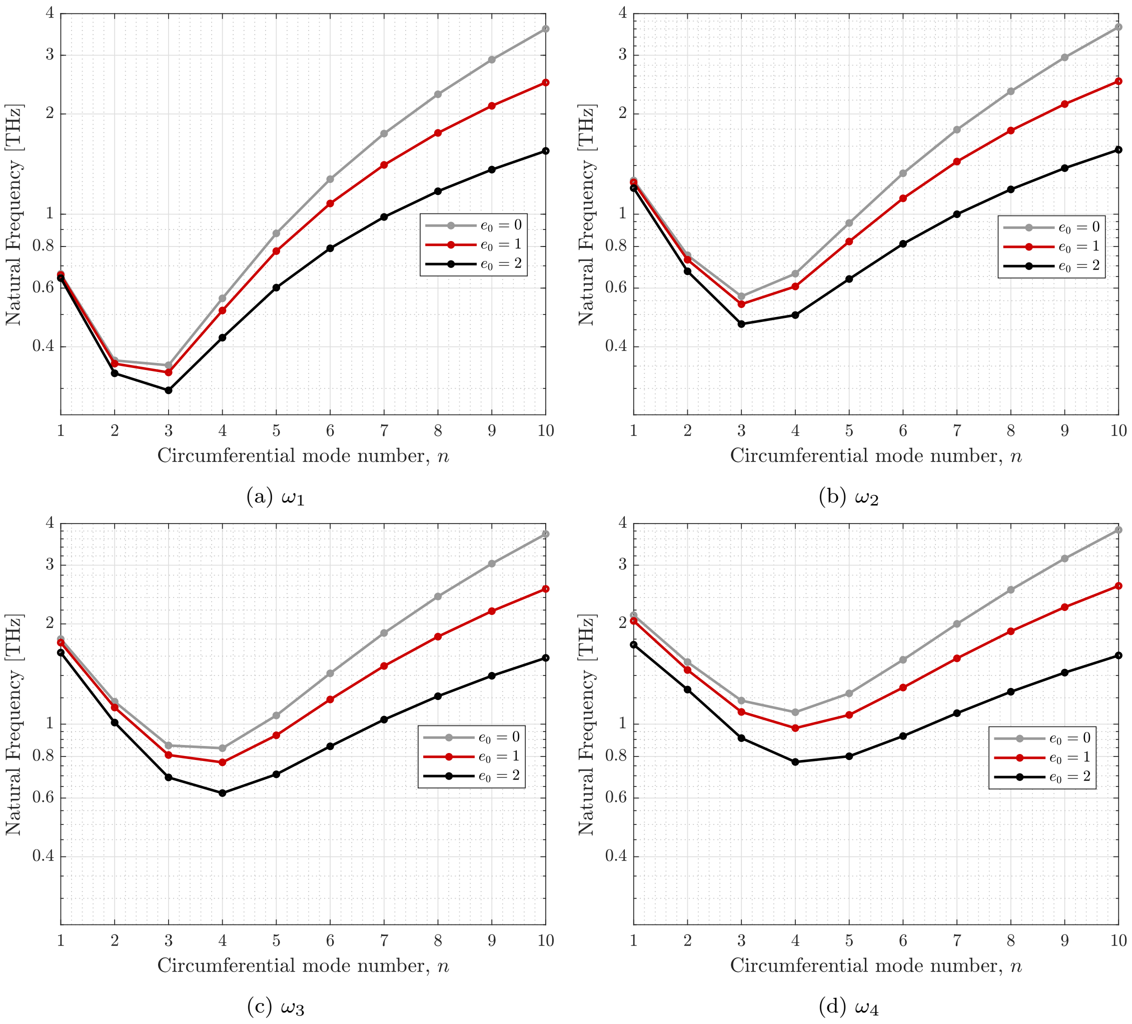

(a) ω_1 (b) ω_2 (c) ω_3 (d) ω_4

Figure 4.9: Natural frequencies (THz) as a function of the circumferential mode number n, for different values of e_0, for a CNT of $(r, s) = (20, 20)$ and $\chi = 2.5$ with clamped-clamped edges

more evident for higher order natural frequencies specifically for lower values of n, while being of more relevant influence for higher values of n across all orders of ω. It is also clear that the nonlocal parameter is of generic inferior relevance for a higher value of diameter - $(r, s) = (20, 20)$ - when comparing to the plots for an inferior value of diameter - $(r, s) = (5, 5)$ -, as should be concluded based on the difference of values in the scale of the y-axis used.

Lastly, the values plotted in Figure 4.9 should be used to point and clearly illustrate the visible swap of the predicted mode shapes association with a position in an organization of ascending values of natural frequencies. For a simulation with extended range of mode shapes, accounting for values of n from 1 to 10, for a local theory, all of the discrete values of the grey plots would be obtained, with mode shapes of higher values of n being associated with lower and less energetic values of natural frequencies, a phenomenon associated with low aspect ratios carbon nanotubes and shells in general [12].

4.5 Influence on the mode shapes

In the present section, the influence of the nonlocal parameter e_0 is studied regarding the influence on the mode shapes. First, the mode shapes will be studied for their behaviour along the x coordinate, as it is the axis that illustrates variations in shape and magnitude (which has no meaning, only exists if they are not normalized). The θ axis produces, for different values of n, a periodic repetition of behaviour in x or ξ represented along the said θ axis, and thus, the mode representations will not take place in θ but in x.

In Figure 4.10, the normalized mode shapes of a clamped-clamped CNT are plotted, so that the maximum values for the mode shapes are defined by the unit value.

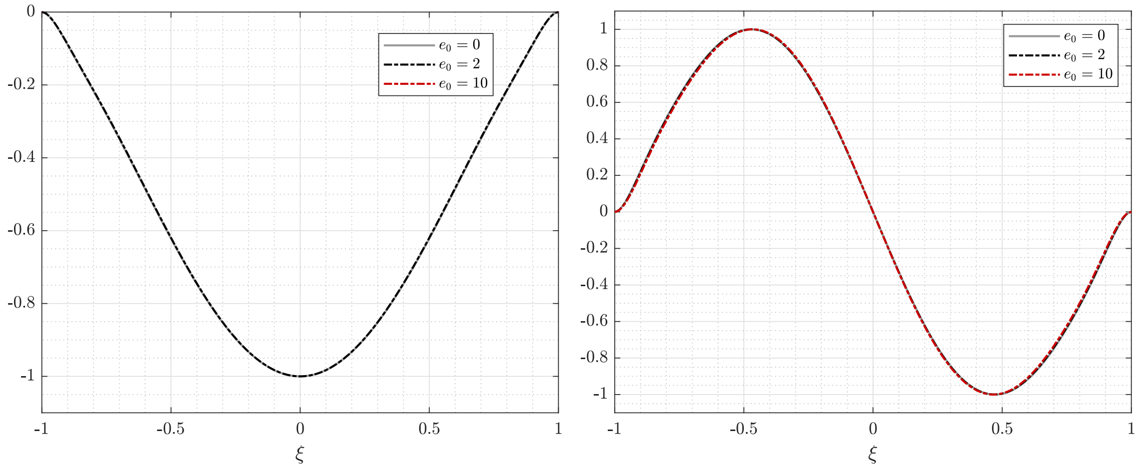

(a) First mode shape

(b) Second mode shape

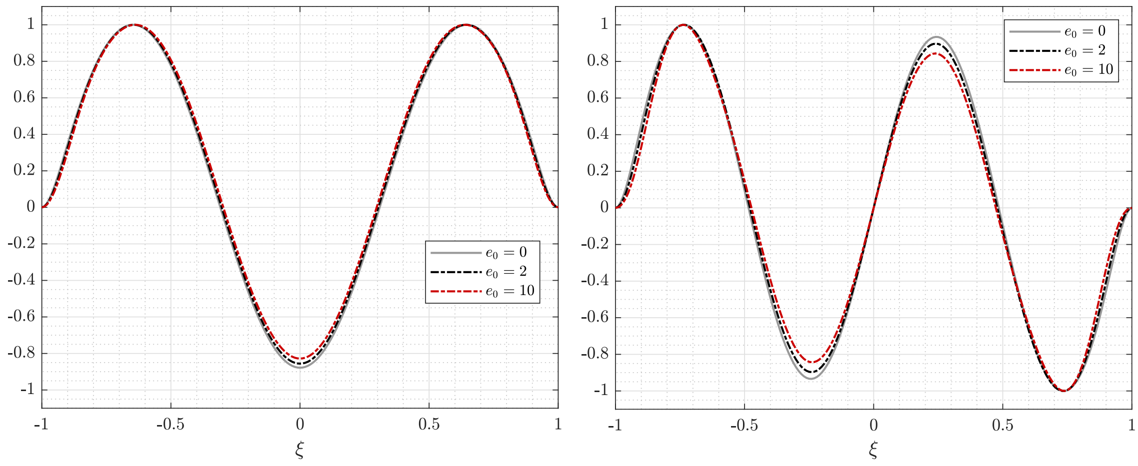

(c) Third mode shape

(d) Fourth mode shape

Figure 4.10: Nonlocal parameter effect on mode shapes in x of a clamped-clamped carbon nanotube, for $(r, s) = (5, 5)$, $\chi = 5.26$ and $n = 1$

As can be observed in Figure 4.10, the mode shapes are plotted for the local theory ($e_0 = 0$) and for two different values of the nonlocal parameter, $e_0 = 1$ and $e_0 = 10$. As mode shapes are associated with a given natural frequency, and as in this case the first mode shape corresponds to the first natural frequency and so on, the same magnitude of influence observed for the natural frequencies is expected for the corresponding mode shape. Thus, it can be observed that for the first mode shape, the influence of the nonlocal parameter is practically null. This influence increases with the increasing mode shape number, as it becomes more evident for the fourth mode shape, with the nonlocal parameter compacting the curve of the mode shape and decreasing the amplitude on specific curve peaks. The ξ coordinate for the peaks also tends to dislocate towards $\xi = 0$.

4.6 Conclusions

The purpose of the present chapter was to study the influence of the nonlocal parameter on the developed thin shell model.

First, the calibration of the nonlocal parameter e_0 was performed for different orders of natural frequencies - ω_1, ω_2, ω_3, ω_4 - for a defined range of aspect ratios of a clamped-clamped edges SWCNT. It was found that for a lower order natural frequency - ω_1 - the magnitude of the nonlocal parameter is superior than for higher order natural frequencies when adjusting to the selected literature data and using defined parameters as thickness and Young's modulus. It was also concluded that for higher order natural frequencies the nonlocal parameter maintains its relevancy along a wider range of aspect ratio, having superior critical aspect ratios. It should also be noted that a more significant apparent influence of e_0 was detected for higher order natural frequencies.

Regarding the DWCNT case, a similar study was performed targeting the fundamental frequency values. Even though the available data for aspect ratios was of a relatively low spectrum, it was verified the expected behaviour of the nonlocal theory values tending to the local ones for higher lengths of the nanotube. A critical aspect ratio value was not found, while it was possible to observe a decrescent tendency in the nonlocal parameter value for the higher aspect ratio values. The e_0 values were found to be relatively higher than the ones for SWCNT.

The relative influence of the nonlocal parameter on a SWCNT was evaluated by the frequency ratio behaviour, having been concluded the hypothesised point of the more significant influence for higher order natural frequencies. Thus, for a higher order natural frequency, not only the nonlocal parameter reveals itself more relevant (a smaller nonlocal parameter is required to achieve the same frequency ratio of inferior number natural frequencies), but it also has a more significant influence for lower values of aspect ratios. This influence fades as the chirality and diameter of the carbon nanotube increases, as naturally predicted.

The phenomenon of having smaller values of natural frequencies associated with higher values of circumferential mode numbers was evaluated for a SWCNT of the same conditions as the previous studies, being important to note that it is more relevant for considerably small aspect ratios. The nonlocal parameter not only reduces the value of the natural frequency for a given n as expected, but also highlights the described phenomenon, while also compacting the curves and behaviour of the natural frequency values attributed to each n. For superior diameters, the output values of ω are smaller in comparison to inferior diameters, still the phenomenon is clearer for the first case, while it was confirmed the already discussed increasing influence of the nonlocal parameter as the natural frequency number also increases.

Lastly, the influence of the nonlocal parameter in the mode shapes was studied. As expected, the nonlocal parameter is of significant influence for higher order mode shapes, as the same value of e_0 yields more significant displacements and changes in the mode shape behaviour.

Chapter 5

Study of a CNT with an attached mass

5.1 Introduction

In the present chapter, a continuation of the already developed model is formulated. As stated in the introductory chapter of the present dissertation, an already established and clear application for CNTs is mass detection, through several methods and for different areas. Thus, a continuum model for a SWCNT and DWCNT with an attached mass for a bridged shell (clamped-clamped) is developed and analysed. The option to devote a single chapter to this matter and not include it in the three main chapters comes from a clarity reason for the reader and for the global organization of this work, in order not to overextend the length of the chapters, and also to emphasize a significant study which has a relevant concrete application.

This chapter's structure starts with the mathematical formulation of the equations of motion, based on the SWCNT model already developed, with the application of the p-version finite element method featuring the Galerkin method to deduce the weak formulation of the problem and establish the finite element matrices. Then, the model is validated with the aid of MD simulations results and mode shapes are illustrated, after which a nonlocal parameter research is conducted and proposed, and finally, a comparison between SWCNT and DWCNT results is performed.

5.2 Mathematical Formulation

5.2.1 Equations of motion

As the SWCNT model was already developed in Chapter 2, the process will not be repeated and the established work will be used. Thus, from Equations (2.18), (2.19) and (2.20), by neglecting the rotary inertia, not considering external forces as the dynamic problem is being studied on a free regime, and including the mass terms relative to the attached mass, with a similar process to Leizerovich and Seregin [103], using Dirac delta to further define a concentrated mass on a single point of the domain, come the following equations of motion:

$$\begin{aligned}&\rho h \ddot{u}^0 + \frac{m_x}{R}\,\delta(x - x^p)\,\delta(\theta - \theta^p)\,\ddot{u}^0 \\ &\quad - \frac{\partial N_{xx}}{\partial x} - \frac{1}{R}\frac{\partial N_{x\theta}}{\partial \theta} + \frac{1}{2R^2}\frac{\partial M_{x\theta}}{\partial \theta} = 0\end{aligned} \tag{5.1}$$

$$\begin{aligned}&\rho h \ddot{v}^0 + \frac{m_x}{R}\,\delta(x-x^p)\,\delta(\theta-\theta^p)\,\ddot{v}^0\\&\qquad -\frac{1}{R}\frac{\partial N_{\theta\theta}}{\partial\theta} - \frac{\partial N_{x\theta}}{\partial x} - \frac{1}{R^2}\frac{\partial M_{\theta\theta}}{\partial\theta} - \frac{3}{2R}\frac{\partial M_{x\theta}}{\partial x} = 0\end{aligned} \tag{5.2}$$

$$\begin{aligned}&\rho h \ddot{w}^0 + \frac{m_x}{R}\,\delta(x-x^p)\,\delta(\theta-\theta^p)\,\ddot{w}^0\\&\qquad +\frac{N_{\theta\theta}}{R} - \frac{\partial^2 M_{xx}}{\partial x^2} - \frac{1}{R^2}\frac{\partial M_{\theta\theta}}{\partial\theta} - \frac{2}{R}\frac{\partial^2 M_{x\theta}}{\partial x\partial\theta} = 0\end{aligned} \tag{5.3}$$

where m_x is mass per unit length refering to the attached mass, with $\frac{m_x}{R}\,\delta(x-x^p)\,\delta(\theta-\theta^p)$ being employed to obtain M_{conc} after integration on dx and dθ domain, and ξ^p and θ^p are the coordinates for which the attached concentrated mass will be defined in the shell domain.

5.2.2 Application of Eringen's nonlocal elasticity theory

After including the nonlocal parameters from Eringen's nonlocal theory and expanding the stress components, from Equations (2.33), come the equations of motion with respect to the displacement components:

$$\begin{aligned}&\rho h\left(1-(e_0a)^2\nabla^2\right)\ddot{u}^0 + \frac{m_x}{R}\,\delta(x-x^p)\,\delta(\theta-\theta^p)\left(1-(e_0a)^2\nabla^2\right)\ddot{u}^0\\&\quad -\frac{Eh}{1-\nu^2}\left[\frac{\partial^2 u^0}{\partial x^2} + \frac{1-\nu}{2}\frac{1}{R^2}\frac{\partial^2 u^0}{\partial\theta^2} + \nu\,\frac{1}{R}\frac{\partial w^0}{\partial x} + \frac{1+\nu}{2}\frac{1}{R}\frac{\partial^2 v^0}{\partial x\partial\theta}\right]\\&\qquad -\frac{Eh^3}{24(1+\nu)R^3}\left[\frac{\partial^3 w^0}{\partial x\partial\theta^2} - \frac{3}{4}\frac{\partial^2 v^0}{\partial x\partial\theta} + \frac{1}{4R}\frac{\partial^2 u^0}{\partial\theta^2}\right] = 0\end{aligned} \tag{5.4}$$

$$\begin{aligned}&\rho h\left(1-(e_0a)^2\nabla^2\right)\ddot{v}^0 + \frac{m_x}{R}\,\delta(x-x^p)\,\delta(\theta-\theta^p)\left(1-(e_0a)^2\nabla^2\right)\ddot{v}^0\\&\quad -\frac{Eh}{1-\nu^2}\left[\frac{1}{R^2}\frac{\partial^2 v^0}{\partial\theta^2} + \frac{1}{R^2}\frac{\partial w^0}{\partial\theta} + \frac{1+\nu}{2}\frac{1}{R}\frac{\partial^2 u^0}{\partial x\partial\theta} + \frac{1-\nu}{2}\frac{\partial^2 v^0}{\partial x^2}\right]\\&\quad -\frac{Eh^3}{12(1-\nu^2)}\left[\frac{1}{R^4}\frac{\partial^2 v^0}{\partial\theta^2} - \frac{1}{R^4}\frac{\partial^3 w^0}{\partial\theta^3} - \frac{3-\nu}{2}\frac{1}{R^2}\frac{\partial^3 w^0}{\partial x^2\partial\theta}\right.\\&\qquad\qquad\left. + \frac{9(1-\nu)}{8R^2}\frac{\partial^2 v^0}{\partial x^2} - \frac{3(1-\nu)}{8R^3}\frac{\partial^2 u^0}{\partial x\partial\theta}\right] = 0\end{aligned} \tag{5.5}$$

$$\begin{aligned}&\rho h\left(1-(e_0a)^2\nabla^2\right)\ddot{w}^0 + \frac{m_x}{R}\,\delta(x-x^p)\,\delta(\theta-\theta^p)\left(1-(e_0a)^2\nabla^2\right)\ddot{w}^0\\&+\frac{Eh}{1-\nu^2}\left[\frac{1}{R^2}\frac{\partial v^0}{\partial\theta} + \frac{w^0}{R^2} + \nu\frac{1}{R}\frac{\partial u^0}{\partial x}\right] + \frac{Eh^3}{12(1-\nu^2)}\left[\frac{\partial^4 w^0}{\partial x^4} - \frac{3-\nu}{2R^2}\frac{\partial^3 v^0}{\partial x^2\partial\theta}\right.\\&\quad\left. + \frac{2}{R^2}\frac{\partial^4 w^0}{\partial x^2\partial\theta^2} - \frac{1}{R^4}\frac{\partial^3 v^0}{\partial\theta^3} + \frac{1}{R^4}\frac{\partial^4 w^0}{\partial\theta^4} + \frac{1-\nu}{2}\frac{1}{R^3}\frac{\partial^3 u^0}{\partial x\partial\theta^2}\right] = 0\end{aligned} \tag{5.6}$$

5.2.3 The p-version Finite Element Method

Discretization of displacement components

For the process of discretization of displacement components, the process is very similar, almost equal to the already described for SWCNTs, as the only terms that will be added is the concentrated mass terms. The shape functions employed are ones already described in Chapter 2, being employed 17 shape functions for the x coordinate and 7 shape functions of the θ coordinate, as with the addition of the concentrated mass, modes of vibration for a singular value of n should not be extracted, being strictly necessary to use the sum of integer values until the defined circumferential mode number. Thus, for the middle surface displacements may be described as a shape function combination matrix multiplied by the generalized displacements, as comes from already defined equations (2.44), (2.45) and (2.46).

Finite element matrices

Following an analogous procedure, the Galerkin method is applied and the following equations are presented:

$$\int_0^{2\pi}\int_0^{l} f_r^u(x)\, f_s^u(\theta)\, \mathcal{L}_u^{AM}(x,\theta,t)\,\mathrm{d}x\, R\,\mathrm{d}\theta \tag{5.7}$$

$$\int_0^{2\pi}\int_0^{l} f_r^v(x)\, f_s^v(\theta)\, \mathcal{L}_v^{AM}(x,\theta,t)\,\mathrm{d}x\, R\,\mathrm{d}\theta \tag{5.8}$$

$$\int_0^{2\pi}\int_0^{l} f_r^w(x)\, f_s^w(\theta)\, \mathcal{L}_w^{AM}(x,\theta,t)\,\mathrm{d}x\, R\,\mathrm{d}\theta \tag{5.9}$$

where $\mathcal{L}_u^{AM}(x,\theta,t)$, $\mathcal{L}_v^{AM}(x,\theta,t)$ and $\mathcal{L}_w^{AM}(x,\theta,t)$ are (5.4), (5.5) and (5.6), respectively.

These equations are now presented with the differential operator ∇ expanded, and with each differential term associated with the respective sum term resultant from the Galerkin method application, designated from $ter(115)$ to $ter(157)$, again resulting in the linear model algebraic terms.

For the equation of motion in u^0 comes:

$$\begin{aligned}
\mathcal{L}_u^{AM}(x,\theta,t) = \rho h \Bigg[\underbrace{\frac{\partial^2 u^0}{\partial t^2}}_{ter(1)} - (e_0\, a)^2 \Bigg[\underbrace{\frac{\partial^2}{\partial x^2}\left(\frac{\partial^2 u^0}{\partial t^2}\right)}_{ter(2)} + \underbrace{\frac{1}{R^2}\frac{\partial^2}{\partial \theta^2}\left(\frac{\partial^2 u^0}{\partial t^2}\right)}_{ter(3)} \Bigg] \Bigg] \\
+ \frac{m_x}{R}\, \delta(x-x^p)\, \delta(\theta-\theta^p) \Bigg[\underbrace{\frac{\partial^2 u^0}{\partial t^2}}_{ter(115)} - (e_0\, a)^2 \Bigg[\underbrace{\frac{\partial^2}{\partial x^2}\left(\frac{\partial^2 u^0}{\partial t^2}\right)}_{ter(116)} + \underbrace{\frac{1}{R^2}\frac{\partial^2}{\partial \theta^2}\left(\frac{\partial^2 u^0}{\partial t^2}\right)}_{ter(117)} \Bigg] \Bigg] \\
- \frac{Eh}{1-\nu^2} \Bigg[\underbrace{\frac{\partial^2 u^0}{\partial x^2}}_{ter(4)} + \underbrace{\frac{1-\nu}{2}\frac{1}{R^2}\frac{\partial^2 u^0}{\partial \theta^2}}_{ter(5)} + \nu \underbrace{\frac{1}{R}\frac{\partial w^0}{\partial x}}_{ter(6)} + \underbrace{\frac{1+\nu}{2}\frac{1}{R}\frac{\partial^2 v^0}{\partial x \partial \theta}}_{ter(7)} \Bigg] \\
- \frac{Eh^3}{24(1+\nu)R^3} \Bigg[\underbrace{\frac{\partial^3 w^0}{\partial x \partial \theta^2}}_{ter(8)} - \underbrace{\frac{3}{4}\frac{\partial^2 v^0}{\partial x \partial \theta}}_{ter(9)} + \underbrace{\frac{1}{4R}\frac{\partial^2 u^0}{\partial \theta^2}}_{ter(10)} \Bigg] = 0
\end{aligned} \tag{5.10}$$

For the equation of motion in v^0 comes:

$$
\begin{aligned}
\mathcal{L}_v^{AM}(x,\theta,t) = \rho h \Bigg[& \underbrace{\frac{\partial^2 v^0}{\partial t^2}}_{ter(11)} - (e_0\,a)^2 \Bigg[\underbrace{\frac{\partial^2}{\partial x^2}\left(\frac{\partial^2 v^0}{\partial t^2}\right)}_{ter(12)} + \underbrace{\frac{1}{R^2}\frac{\partial^2}{\partial \theta^2}\left(\frac{\partial^2 v^0}{\partial t^2}\right)}_{ter(13)} \Bigg] \Bigg] \\
+ \frac{m_x}{R}\,\delta(x-x^p)\,\delta(\theta-\theta^p) \Bigg[& \underbrace{\frac{\partial^2 v^0}{\partial t^2}}_{ter(118)} - (e_0\,a)^2 \Bigg[\underbrace{\frac{\partial^2}{\partial x^2}\left(\frac{\partial^2 v^0}{\partial t^2}\right)}_{ter(119)} + \underbrace{\frac{1}{R^2}\frac{\partial^2}{\partial \theta^2}\left(\frac{\partial^2 v^0}{\partial t^2}\right)}_{ter(120)} \Bigg] \Bigg] \\
- \frac{Eh}{1-\nu^2} \Bigg[& \underbrace{\frac{1}{R^2}\frac{\partial^2 v^0}{\partial \theta^2}}_{ter(14)} + \underbrace{\frac{1}{R^2}\frac{\partial w^0}{\partial \theta}}_{ter(15)} + \underbrace{\frac{1+\nu}{2}\frac{1}{R}\frac{\partial^2 u^0}{\partial x \partial \theta}}_{ter(16)} + \underbrace{\frac{1-\nu}{2}\frac{\partial^2 v^0}{\partial x^2}}_{ter(17)} \Bigg] \\
- \frac{Eh^3}{12(1-\nu^2)} \Bigg[& \underbrace{\frac{1}{R^4}\frac{\partial^2 v^0}{\partial \theta^2}}_{ter(18)} - \underbrace{\frac{1}{R^4}\frac{\partial^3 w^0}{\partial \theta^3}}_{ter(19)} - \underbrace{\frac{3-\nu}{2}\frac{1}{R^2}\frac{\partial^3 w^0}{\partial x^2 \partial \theta}}_{ter(20)} \\
& + \underbrace{\frac{9(1-\nu)}{8R^2}\frac{\partial^2 v^0}{\partial x^2}}_{ter(21)} - \underbrace{\frac{3(1-\nu)}{8R^3}\frac{\partial^2 u^0}{\partial x \partial \theta}}_{ter(22)} \Bigg] = 0
\end{aligned}
\tag{5.11}
$$

And finally, for the equation of motion in w^0 comes:

$$
\begin{aligned}
\mathcal{L}_w^{AM}(x,\theta,t) = \rho h \Bigg[& \underbrace{\frac{\partial^2 w^0}{\partial t^2}}_{ter(23)} - (e_0\,a)^2 \Bigg[\underbrace{\frac{\partial^2}{\partial x^2}\left(\frac{\partial^2 w^0}{\partial t^2}\right)}_{ter(24)} + \underbrace{\frac{1}{R^2}\frac{\partial^2}{\partial \theta^2}\left(\frac{\partial^2 w^0}{\partial t^2}\right)}_{ter(25)} \Bigg] \Bigg] \\
+ \frac{m_x}{R}\,\delta(x-x^p)\,\delta(\theta-\theta^p) \Bigg[& \underbrace{\frac{\partial^2 w^0}{\partial t^2}}_{ter(121)} - (e_0\,a)^2 \Bigg[\underbrace{\frac{\partial^2}{\partial x^2}\left(\frac{\partial^2 w^0}{\partial t^2}\right)}_{ter(122)} + \underbrace{\frac{1}{R^2}\frac{\partial^2}{\partial \theta^2}\left(\frac{\partial^2 w^0}{\partial t^2}\right)}_{ter(123)} \Bigg] \Bigg] \\
+ \frac{Eh}{1-\nu^2} \Bigg[& \underbrace{\frac{1}{R^2}\frac{\partial v^0}{\partial \theta}}_{ter(26)} + \underbrace{\frac{w^0}{R^2}}_{ter(27)} + \underbrace{\nu\frac{1}{R}\frac{\partial u^0}{\partial x}}_{ter(28)} \Bigg] + \frac{Eh^3}{12(1-\nu^2)} \Bigg[\underbrace{\frac{\partial^4 w^0}{\partial x^4}}_{ter(29)} - \underbrace{\frac{3-\nu}{2R^2}\frac{\partial^3 v^0}{\partial x^2 \partial \theta}}_{ter(30)} + \underbrace{\frac{2}{R^2}\frac{\partial^4 w^0}{\partial x^2 \partial \theta^2}}_{ter(31)} \\
& - \underbrace{\frac{1}{R^4}\frac{\partial^3 v^0}{\partial \theta^3}}_{ter(32)} + \underbrace{\frac{1}{R^4}\frac{\partial^4 w^0}{\partial \theta^4}}_{ter(33)} + \underbrace{\frac{1-\nu}{2}\frac{1}{R^3}\frac{\partial^3 u^0}{\partial x \partial \theta^2}}_{ter(34)} \Bigg] = 0
\end{aligned}
\tag{5.12}
$$

As may be seen, the resultant terms from the application of the Galerkin method are analogous to terms $ter(1) - ter(34)$, with the exception of the terms relative to the attached mass. Thus, for the sake of brevity, only the terms related to the attached mass will be expanded, from Equations (5.7), (5.8) and (5.9), as comes:

$$
\begin{aligned}
ter(115):& \int_0^{2\pi}\int_0^{l} \frac{m_x}{R} f^u_{ix}\, f^u_{i\theta} \cdot (f^u_{jx}\, f^u_{j\theta})\, \delta(x-x^p)\, \delta(\theta-\theta^p)\, \mathrm{d}x\, R\, \mathrm{d}\theta\; \ddot{q}^u_{ij}(t) \\
&= M_{conc}\; f^u_{i\theta}(\theta^p)\, f^u_{j\theta}(\theta^p)\; f^u_{i\xi}(\xi^p)\, f^u_{j\xi}(\xi^p)\; \ddot{q}^u_{ij}(t)
\end{aligned}
\tag{5.13}
$$

$$\begin{aligned}
&ter(116): -\frac{1}{R}(e_0\,a)^2\int_0^{2\pi}\int_0^{l} m_x f^u_{ix}\,f^u_{i\theta}\cdot\frac{\partial^2}{\partial x^2}\big(f^u_{jx}\,f^u_{j\theta}\big)\,\delta(x-x^p)\,\delta(\theta-\theta^p)\,\mathrm{d}x\,R\,\mathrm{d}\theta\;\ddot{q}^u_{ij}(t)\\
&\quad= M_{conc}\,(e_0\,a)^2\,\frac{4}{l^2}\;f^u_{i\theta}(\theta^p)\,f^u_{j\theta}(\theta^p)\;\frac{\mathrm{d}f^u_{i\xi}(\xi^p)}{\mathrm{d}\xi}\,\frac{\mathrm{d}f^u_{j\xi}(\xi^p)}{\mathrm{d}\xi}\;\ddot{q}^u_{ij}(t)
\end{aligned}\tag{5.14}$$

$$\begin{aligned}
&ter(117): -\frac{1}{R}(e_0\,a)^2\frac{1}{R^2}\int_0^{2\pi}\int_0^{l} m_x\,f^u_{ix}\,f^u_{i\theta}\cdot\frac{\partial^2}{\partial\theta^2}\big(f^u_{jx}\,f^u_{j\theta}\big)\,\delta(x-x^p)\,\delta(\theta-\theta^p)\,\mathrm{d}x\,R\,\mathrm{d}\theta\;\ddot{q}^u_{ij}(t)\\
&\quad= \frac{M_{conc}}{R^2}(e_0\,a)^2\,\frac{\mathrm{d}f^u_{i\theta}(\theta^p)}{\mathrm{d}\theta}\,\frac{\mathrm{d}f^u_{j\theta}(\theta^p)}{\mathrm{d}\theta}\;f^u_{i\xi}(\xi^p)\,f^u_{j\xi}(\xi^p)\;\ddot{q}^u_{ij}(t)
\end{aligned}\tag{5.15}$$

$$\begin{aligned}
&ter(118): \int_0^{2\pi}\int_0^{l}\frac{m_x}{R}f^v_{ix}\,f^v_{i\theta}\cdot(f^v_{jx}\,f^v_{j\theta})\,\delta(x-x^p)\,\delta(\theta-\theta^p)\,\mathrm{d}x\,R\,\mathrm{d}\theta\;\ddot{q}^v_{ij}(t)\\
&\quad= M_{conc}\;f^v_{i\theta}(\theta^p)\,f^v_{j\theta}(\theta^p)\;f^v_{i\xi}(\xi^p)\,f^v_{j\xi}(\xi^p)\;\ddot{q}^v_{ij}(t)
\end{aligned}\tag{5.16}$$

$$\begin{aligned}
&ter(119): -\frac{1}{R}(e_0\,a)^2\int_0^{2\pi}\int_0^{l} m_x f^v_{ix}\,f^v_{i\theta}\cdot\frac{\partial^2}{\partial x^2}\big(f^v_{jx}\,f^v_{j\theta}\big)\,\delta(x-x^p)\,\delta(\theta-\theta^p)\,\mathrm{d}x\,R\,\mathrm{d}\theta\;\ddot{q}^v_{ij}(t)\\
&\quad= M_{conc}\,(e_0\,a)^2\,\frac{4}{l^2}\;f^v_{i\theta}(\theta^p)\,f^v_{j\theta}(\theta^p)\;\frac{\mathrm{d}f^v_{i\xi}(\xi^p)}{\mathrm{d}\xi}\,\frac{\mathrm{d}f^v_{j\xi}(\xi^p)}{\mathrm{d}\xi}\;\ddot{q}^v_{ij}(t)
\end{aligned}\tag{5.17}$$

$$\begin{aligned}
&ter(120): -\frac{1}{R}(e_0\,a)^2\frac{1}{R^2}\int_0^{2\pi}\int_0^{l} m_x\,f^v_{ix}\,f^v_{i\theta}\cdot\frac{\partial^2}{\partial\theta^2}\big(f^v_{jx}\,f^v_{j\theta}\big)\,\delta(x-x^p)\,\delta(\theta-\theta^p)\,\mathrm{d}x\,R\,\mathrm{d}\theta\;\ddot{q}^v_{ij}(t)\\
&\quad= \frac{M_{conc}}{R^2}(e_0\,a)^2\,\frac{\mathrm{d}f^v_{i\theta}(\theta^p)}{\mathrm{d}\theta}\,\frac{\mathrm{d}f^v_{j\theta}(\theta^p)}{\mathrm{d}\theta}\;f^v_{i\xi}(\xi^p)\,f^v_{j\xi}(\xi^p)\;\ddot{q}^v_{ij}(t)
\end{aligned}\tag{5.18}$$

$$\begin{aligned}
&ter(121): \int_0^{2\pi}\int_0^{l}\frac{m_x}{R}f^w_{ix}\,f^w_{i\theta}\cdot(f^w_{jx}\,f^w_{j\theta})\,\delta(x-x^p)\,\delta(\theta-\theta^p)\,\mathrm{d}x\,R\,\mathrm{d}\theta\;\ddot{q}^w_{ij}(t)\\
&\quad= M_{conc}\;f^w_{i\theta}(\theta^p)\,f^w_{j\theta}(\theta^p)\;f^w_{i\xi}(\xi^p)\,f^w_{j\xi}(\xi^p)\;\ddot{q}^w_{ij}(t)
\end{aligned}\tag{5.19}$$

$$\begin{aligned}
&ter(122): -\frac{1}{R}(e_0\,a)^2\int_0^{2\pi}\int_0^{l} m_x f^w_{ix}\,f^w_{i\theta}\cdot\frac{\partial^2}{\partial x^2}\big(f^w_{jx}\,f^w_{j\theta}\big)\,\delta(x-x^p)\,\delta(\theta-\theta^p)\,\mathrm{d}x\,R\,\mathrm{d}\theta\;\ddot{q}^w_{ij}(t)\\
&\quad= M_{conc}\,(e_0\,a)^2\,\frac{4}{l^2}\;f^w_{i\theta}(\theta^p)\,f^w_{j\theta}(\theta^p)\;\frac{\mathrm{d}f^w_{i\xi}(\xi^p)}{\mathrm{d}\xi}\,\frac{\mathrm{d}f^w_{j\xi}(\xi^p)}{\mathrm{d}\xi}\;\ddot{q}^w_{ij}(t)
\end{aligned}\tag{5.20}$$

$$\begin{aligned}
&ter(123): -\frac{1}{R}(e_0\,a)^2\frac{1}{R^2}\int_0^{2\pi}\int_0^{l} m_x\,f^w_{ix}\,f^w_{i\theta}\cdot\frac{\partial^2}{\partial\theta^2}\big(f^w_{jx}\,f^w_{j\theta}\big)\,\delta(x-x^p)\,\delta(\theta-\theta^p)\,\mathrm{d}x\,R\,\mathrm{d}\theta\;\ddot{q}^w_{ij}(t)\\
&\quad= \frac{M_{conc}}{R^2}(e_0\,a)^2\,\frac{\mathrm{d}f^w_{i\theta}(\theta^p)}{\mathrm{d}\theta}\,\frac{\mathrm{d}f^w_{j\theta}(\theta^p)}{\mathrm{d}\theta}\;f^w_{i\xi}(\xi^p)\,f^w_{j\xi}(\xi^p)\;\ddot{q}^w_{ij}(t)
\end{aligned}\tag{5.21}$$

Finally, the complete model is expressed in the matrix form, with the general displacements still depending on the time variable, as comes:

$$\left(\begin{bmatrix} [M_{uu}^{AM}] & 0 & 0 \\ 0 & [M_{vv}^{AM}] & 0 \\ 0 & 0 & [M_{ww}^{AM}] \end{bmatrix} + \begin{bmatrix} [M_{uu}^{\mu,AM}] & 0 & 0 \\ 0 & [M_{vv}^{\mu,AM}] & 0 \\ 0 & 0 & [M_{ww}^{\mu,AM}] \end{bmatrix}\right) \begin{Bmatrix} \{\ddot{q}^u(t)\} \\ \{\ddot{q}^v(t)\} \\ \{\ddot{q}^w(t)\} \end{Bmatrix}$$
$$+ \begin{bmatrix} [K_{uu}^{AM}] & [K_{uv}^{AM}] & [K_{uw}^{AM}] \\ [K_{vu}^{AM}] & [K_{vv}^{AM}] & [K_{vw}^{AM}] \\ [K_{wu}^{AM}] & [K_{wv}^{AM}] & [K_{ww}^{AM}] \end{bmatrix} \begin{Bmatrix} \{q^u(t)\} \\ \{q^v(t)\} \\ \{q^w(t)\} \end{Bmatrix} = \begin{Bmatrix} 0 \\ 0 \\ 0 \end{Bmatrix} \tag{5.22}$$

where each one of the submatrixes are defined as:

- $[M_{uu}] \leftarrow ter(1) + ter(115)$
- $[M_{vv}] \leftarrow ter(11) + ter(118)$
- $[M_{ww}] \leftarrow ter(23) + ter(121)$
- $[M_{uu}^{\mu}] \leftarrow ter(2) + ter(3) + ter(116) + ter(117)$
- $[M_{vv}^{\mu}] \leftarrow ter(12) + ter(13) + ter(119) + ter(120)$
- $[M_{ww}^{\mu}] \leftarrow ter(24) + ter(25) + ter(122) + ter(123)$
- $[K_{uu}] \leftarrow ter(4) + ter(5) + ter(10)$
- $[K_{uv}] \leftarrow ter(7) + ter(9)$
- $[K_{uw}] \leftarrow ter(6) + ter(8)$
- $[K_{vu}] \leftarrow ter(16) + ter(22)$
- $[K_{vv}] \leftarrow ter(14) + ter(17) + ter(18) + ter(21)$
- $[K_{vw}] \leftarrow ter(15) + ter(19) + ter(20)$
- $[K_{wu}] \leftarrow ter(28) + ter(34)$
- $[K_{wv}] \leftarrow ter(26) + ter(30) + ter(32)$
- $[K_{ww}] \leftarrow ter(27) + ter(29) + ter(31) + ter(33)$

Regarding the implementation of the dynamic problem, the same dependence of the generalized displacements on an harmonic function is considered. Thus, Equations (2.90) and (2.91) are again applied, so that the harmonic function is dropped from every term, resulting in time-independent equations.

5.3 Validation

The developed model must be subjected to result testing from other authors referenced data. An approach regarding molecular dynamics simulation values will be taken here, as they represent reliable and accurate results and have been adopted many times for this dissertation. Thus, the work of Li and Chou [104] for a bridged SWCNT is used as means of comparison, where the concentrated mass is placed on the center of the clamped-clamped edges shell.

In Table 5.1 the results of the comparison are presented. The parameters used to describe the CNT material properties are the ones of Table 3.1, as the position of the attached mass is described by the coordinate values $\xi^p = 0$ and $\theta^p = 0$. A range of different values of the concentrated mass M_{conc} are tested, from 1×10^{-8} [fg] to 1 [fg] - femtograms = 10^{-15} grams. The value of the diameter of the nanotube is $d = 0.8$ [nm].

As may be concluded by observing Table 5.1, the values of the developed model are in close agreement to the values of the molecular dynamics simulations proposed in [104]. Across the three studied length values, the magnitude of the relative difference is roughly the same, with the exception of the higher concentrated mass values for the lowest length, which is understandable when accounting for the last chapters' conclusions. It is important to note that for $l = 6$ [nm], the natural frequency values from the local model are higher than the ones given by the MD results up until a defined attached mass value, while for $l = 8$ [nm] this critical mass value is higher than for the lower length value, and for $l = 10$ [nm] a critical value is not found, as the values from the local model are always higher than the results from literature. This naturally opens the possibility for an investigation of the nonlocal parameter on a model with an attached mass, while already establishing that the nonlocal elasticity theory may not be relevant for all concentrated mass values, depending on the nanotube's length. Regarding the lower mass value presented on the table, it is clear that the natural frequency values are converging to a stagnant value (before the logarithmically linear relation), which is due to the concentrated mass being so low that it does not influence the dynamic behaviour of the CNT and cannot be detected.

Table 5.1: Comparison between the fundamental natural frequency [GHz] of a clamped-clamped SWCNT with an attached mass in the middle of the nanotube and MD simulations

M_{conc} [fg]	Model	MD [104]	Diff. (%)
$l = 6$ [nm]			
1.00×10^{-8}	492.1	474.9	3.6
1.00×10^{-7}	487.7	474.8	2.7
1.00×10^{-6}	443.1	437.5	1.3
1.00×10^{-5}	235.1	248.2	5.3
1.00×10^{-4}	79.67	82.60	3.5
1.00×10^{-3}	25.37	27.86	9.0
1.00×10^{-2}	8.027	8.730	8.1
1.00×10^{-1}	2.538	2.868	11
1.00×10^{0}	0.8027	0.8923	10
$l = 8$ [nm]			
1.00×10^{-8}	300.3	291.3	3.1
1.00×10^{-7}	298.2	288.3	3.4
1.00×10^{-6}	278.7	274.9	1.4
1.00×10^{-5}	174.3	173.9	0.19
1.00×10^{-4}	63.22	64.58	2.1
1.00×10^{-3}	20.29	20.91	3.0
1.00×10^{-2}	6.425	6.774	5.2
1.00×10^{-1}	2.032	2.135	4.8
1.00×10^{0}	0.6426	0.6821	5.8
$l = 10$ [nm]			
1.00×10^{-8}	200.6	191.5	4.8
1.00×10^{-7}	199.5	191.4	4.2
1.00×10^{-6}	189.0	178.0	6.2
1.00×10^{-5}	128.9	120.1	7.3
1.00×10^{-4}	49.75	47.86	3.9
1.00×10^{-3}	16.10	15.67	2.8
1.00×10^{-2}	5.104	4.972	2.7
1.00×10^{-1}	1.614	1.569	2.9
1.00×10^{0}	0.5105	0.4915	3.9

5.4 Mode shapes

With the new developed SWCNT with an attached concentrated mass model, the mode shapes are expected to change. For the position where the mass is attached, higher relative displacements in comparison to the opposite position in the shell are expected, as the mass yields significant influence on the natural frequency values and mode shapes of the carbon nanotube. Therefore, the first four mode shapes are presented in Figure 5.1.

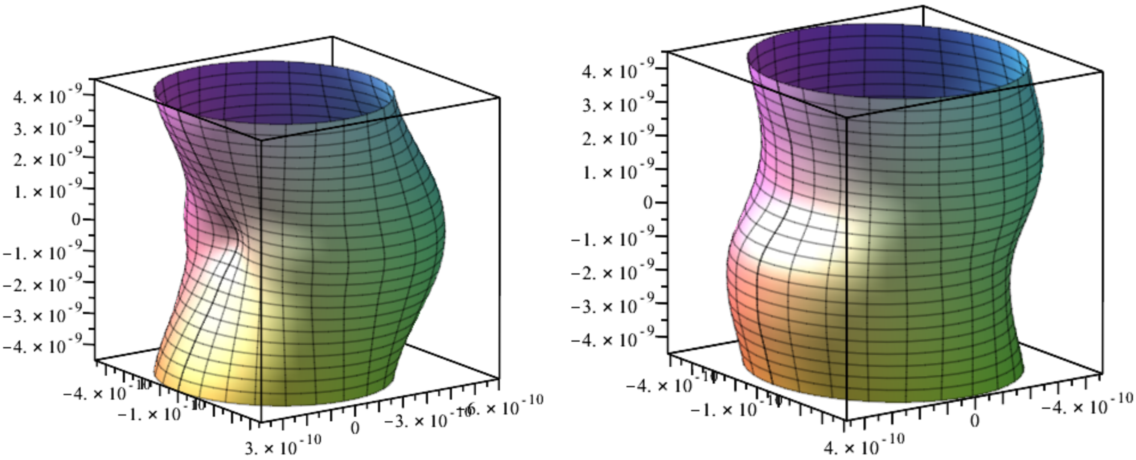

(a) $\omega_1 = 49.75$ GHz
(b) $\omega_2 = 324.8$ GHz

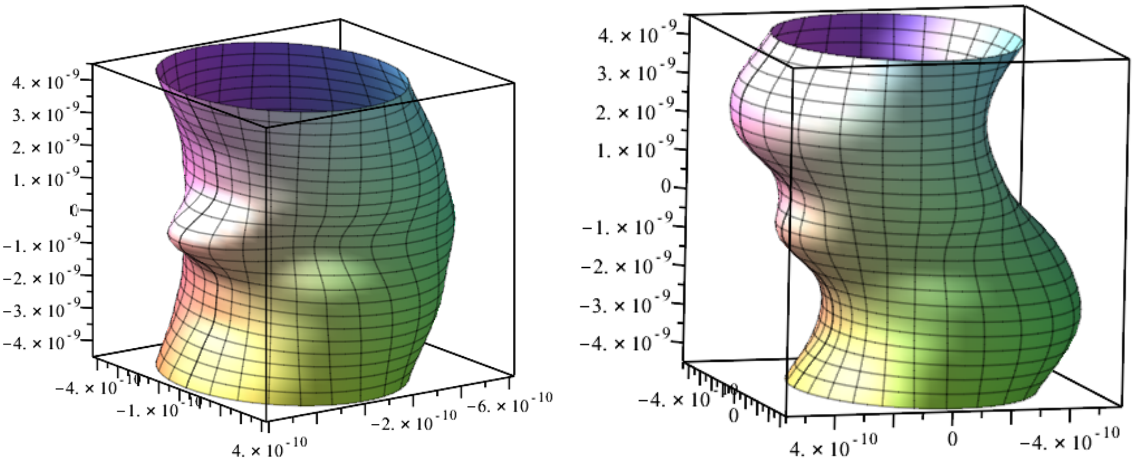

(c) $\omega_3 = 447,8$ GHz
(d) $\omega_4 = 680,9$ GHz

Figure 5.1: Mode shapes of a clamped-clamped edges SWCNT with an attached mass of 1.00×10^{-4} and $l = 10$ nm for $\xi^p = 0$ and $\theta^p = 0$

5.5 Nonlocal parameter influence

As stated in the last paragraph, a calibration of the nonlocal parameter is feasible. Thus, it is firstly presented a comparison between the curves of the natural frequencies given by the developed local and nonlocal model and by the MD simulations [104], in Figure 5.2.

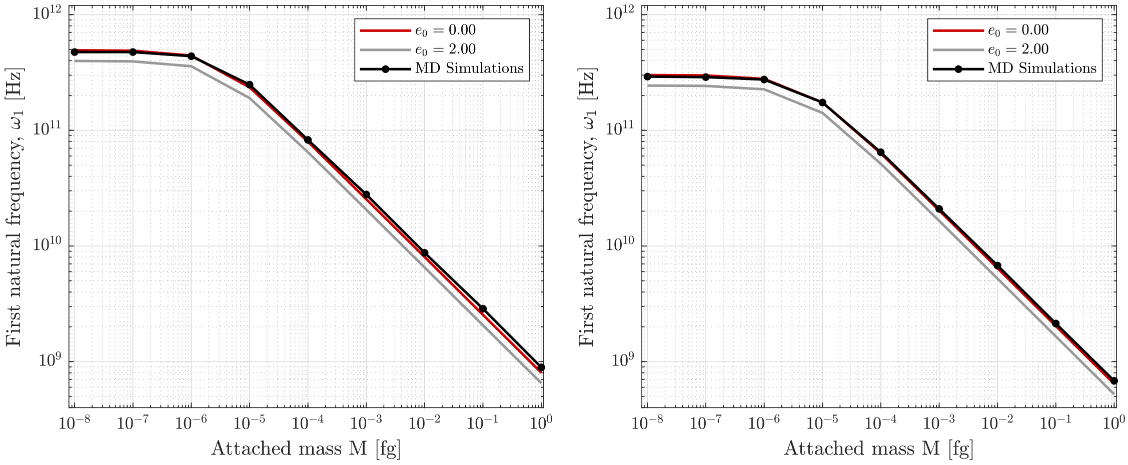

(a) $l = 6$ [nm]

(b) $l = 8$ [nm]

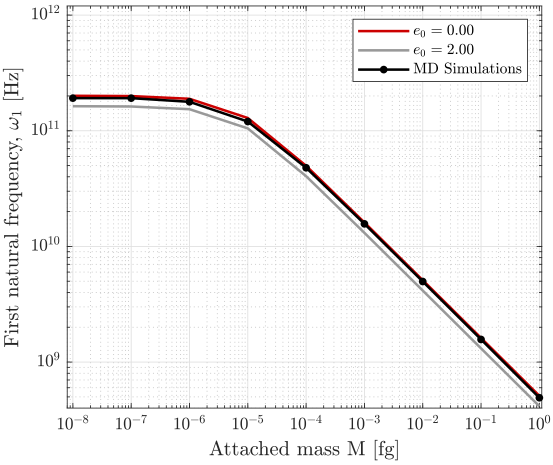

(c) $l = 10$ [nm]

Figure 5.2: Comparison between the fundamental natural frequencies (Hz) calculated by MD [104] and values from the present model for different nonlocal parameters, clamped-clamped edges SWCNT with $d = 0.8$ nm, for different values of attached concentrated mass

As may be observed in Figure 5.2, for lower values of attached mass, the values of the MD simulations are very close to the ones given by the local model. An important conclusion for this range is that for a nanotube of this diameter, for the different length values, a minimum concentrated mass value may be verified, below which the shift in the fundamental frequency values is not significant and may not be detected [104], being $M_{conc} = 1.00 \times 10^{-6}$ [fg]. As the attached concentrated mass value increases, a logarithmically linear relation between said value and the fundamental frequency is verified. It may be seen across the graphics for the three different length values that, as already stated, the local values are in very close agreement to the MD results, as the nonlocal values for an arbitrary parameter of $e_0 = 2.00$ is apparently more distant from the literature values. While for the lower concentrated mass values it is clear that the MD values are lower than the local model results across all length values, for the mass values that define the logarithmically linear relation, the MD yielded results become higher than the local model for lower l values, as already stated. Regarding the higher length value, it is also apparent that the MD values are in an intermediate position between the local and nonlocal models, while being closer to the local one. It may also be hypothesized that for the whole range of concentrated mass values, the difference or gap between the local and nonlocal theories remains relatively constant (attending that the scale is logarithmic).

In order to study the model regarding the nonlocal behaviour, and to investigate into the magnitude of the nonlocal parameter e_0 for the currently studied CNTs, a calibration of this parameter is carried out and presented in Figure 5.3.

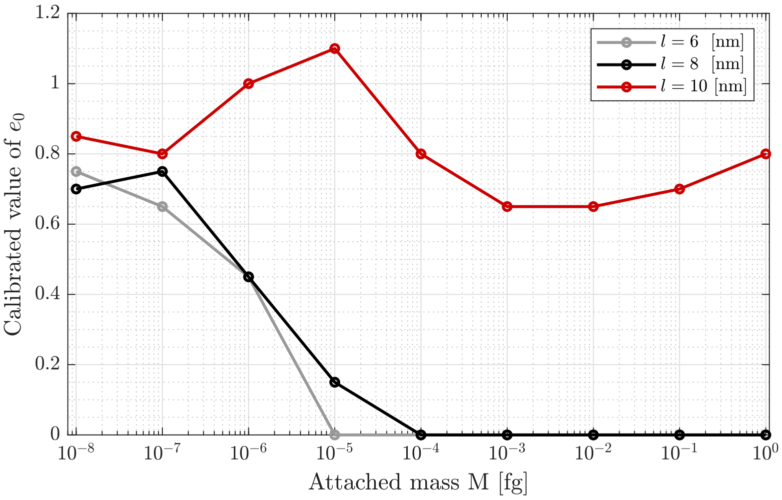

Figure 5.3: Calibration of e_0 for the fundamental natural frequency of clamped-clamped edges CNTs with $d = 0.8$ nm, for different values of an attached concentrated mass, in comparison to MD results [104]

Regarding Figure 5.3, several conclusions may be taken. Even though the length values and respective aspect ratio values ($\chi = 7.5$, $\chi = 10$ and $\chi = 12.5$) are relatively small, they are in within the same range studied in the examples of the current dissertation. It is clear that between all length values, for an attached mass of neglectable value, the nonlocal parameter value is close between the three cases and is also in the magnitude of the proposed nonlocal parameters in the last chapter, where free vibrations of CNTs with no attached masses are studied. In fact, as the diameter value is very similar to the one previously studied, and given the aspect ratio values, it is safe to assume a higher nonlocal parameter value for $l = 6$ [nm] and a lower nonlocal parameter for the highest length may be attributed, even though not represented in the considered figure, as for higher lengths the nonlocal parameter would be relevant for wider ranges of masses, which is in accordance with the represented situation.

As the concentrated mass increases, for the lowest and intermediate length value, the nonlocal parameter tends to a null value, as the natural frequency values calculated from the present model become inferior than the MD values, and thus the nonlocal theory becomes irrelevant. For $l = 6$ [nm] the critical mass value is in the order of magnitude of $M_{conc} = 1.00 \times 10^{-5}$ [fg], while for $l = 8$ [nm] the critical mass value is in the order of $M_{conc} = 1.00 \times 10^{-4}$ [fg], and for $l = 10$ [nm] no critical mass value is identified in the studied range (and is unknown if there is one), as the nonlocal parameter is more relevant for the higher length. Still regarding the length value of $l = 10$ [nm], is it possible to observe that across the mass values, the nonlocal parameter variation is relatively low. This leads to the hypothesis that for higher length values, the variation of e_0 becomes low enough that a single nonlocal parameter value may be adequate to the characteristics of said CNT, allowing for a more accurate and reliable model for mass detection. In an attempt to exemplify this type of study, the average nonlocal parameter from the calibrated results for $l = 10$ [nm] is taken, being $e_0 = 0.817$, and is plotted on Figure 5.4, for the top values of the concentrated mass, where the behaviour is logarithmically linear, being in great agreement with the MD results, as the highest relative difference value is of 1.4% for $M_{conc} = 1.00 \times 10^{-2}$ [fg].

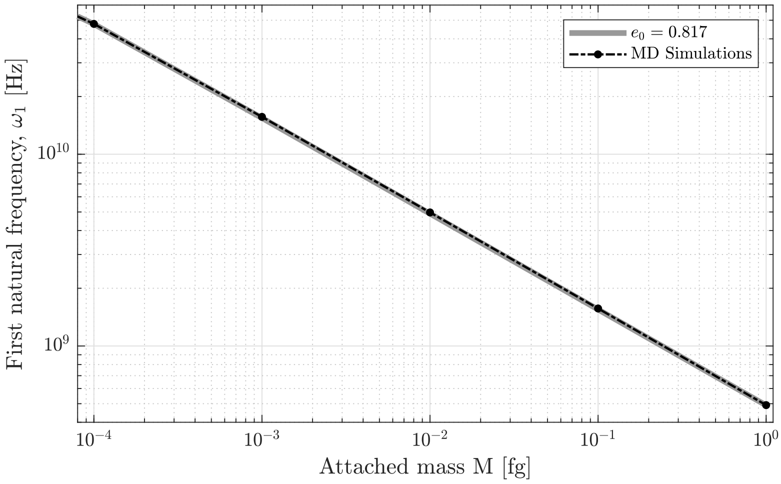

Figure 5.4: Comparison between the fundamental natural frequencies (Hz) calculated by MD [104] and the nonlocal model for $e_0 = 0.817$, clamped-clamped edges SWCNT with $d = 0.8$ nm, for different values of attached concentrated mass

5.6 Comparison between SWCNTs and DWCNTs with an attached mass

As a last study regarding the investigation of the applicability of different types of CNTs on mass detection, a comparison between the fundamental frequency results of SWCNTs and DWCNTs is performed. A formulation for DWCNTs with an attached mass is not detailed, as the process is analogous to an equivalent continuum model for a DWCNT, already formulated, and an attached mass on the outer tube, following the formulation presented in this chapter, still for an attached mass on coordinates $\xi^p = 0$ and $\theta^p = 0$.

For this analysis, a DWCNT of an outer tube of diameter $d_2 = 0.8$ [nm], equal to the dimensions of de SWCNT, is taken, with an inner tube of diameter $d_1 = 0.4$ [nm]. It is already known from Chapter 3 that for a DWCNT with the same length and outer diameter as a SWCNT, the fundamental frequency will be lower than the one for the considered DWCNT, and thus, the aim of this section is to investigate the influence of an attached mass on that natural frequency result. Considering the same values of length and attached mass, the fundamental frequency results are plotted on Figure 5.5.

As may be observed from Figure 5.5, the already stated property of the DWCNTs with equal outer diameter and length of a SWCNT having lower fundamental frequencies is confirmed for this case, considering no concentrated attached mass. As more considerable concentrated mass values are added to the nanotubes, it is clear that generally for DWCNTs the fundamental frequency decreases on a lower ratio when comparing to SWCNTs, presenting a behaviour which yields higher natural frequencies for DWCNTs after a critical concentrated mass value, being possible to note that this critical value is higher for higher length values.

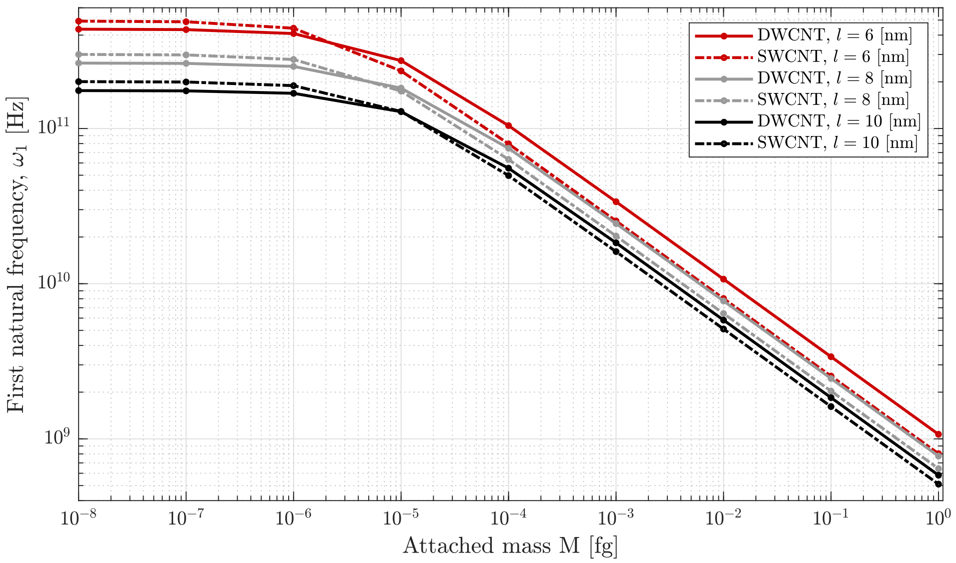

Figure 5.5: Comparison between the fundamental natural frequencies (Hz) for SWCNT with $d = 0.8$ nm and DWCNT with $d_2 = 0.8$ nm and $d_1 = 0.4$ nm, for clamped-clamped edges and for different values of attached concentrated mass

It should also be noted that for lower length values (see $l = 6$ [nm] for example), for the higher range of concentrated mass values, the SWCNTs fundamental frequency values display an apparent higher gap regarding the DWCNTs curve of fundamental frequencies. This gap tends to dissipate for higher length values.

In order to confirm the idea of the last paragraph and to evaluate the sensitivity of these two types of carbon nanotubes, the frequency ratios between the fundamental frequency of a determined concentrated mass value and the fundamental frequency of a regular carbon nanotube with no attached mass is plotted in Figure 5.6.

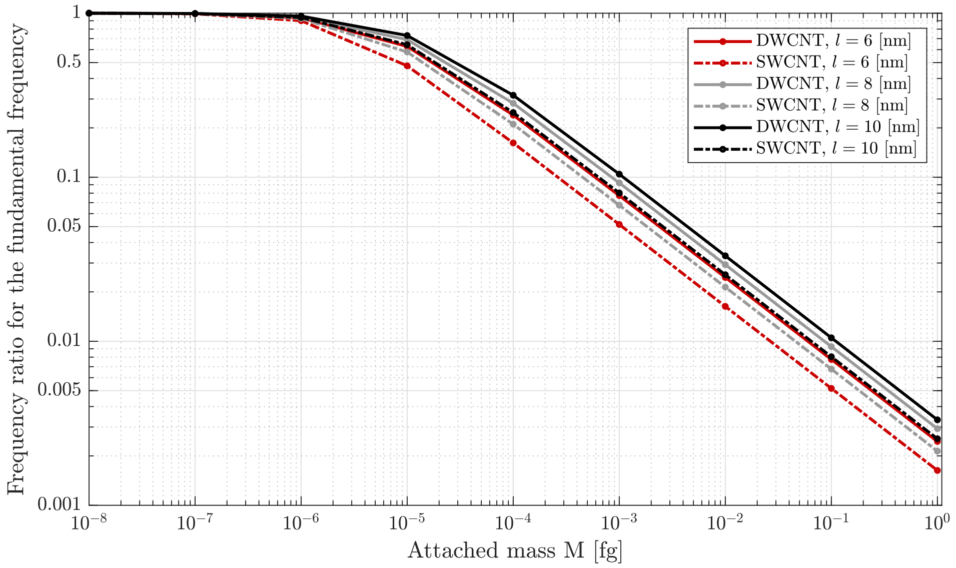

Figure 5.6: Comparison between the frequency ratios for SWCNT with $d = 0.8$ nm and DWCNT with $d_2 = 0.8$ nm and $d_1 = 0.4$ nm, for clamped-clamped edges and for different values of attached concentrated mass

Analysing Figure 5.6, it is confirmed that independently from the length value, as the concentrated mass value increases, the frequency ratio drop becomes more sharp (meaning of a lower value) for SWCNTs than for DWCNTs. Thus, the conclusion that SWCNTs are more suitable for mass detection, as their sensitivity is in fact higher, must be taken. Regarding the comparison between the frequency ratios among the SWCNTs of different lengths, it is possible to observe that a SWCNT with a lower length yields more significant shifts in the fundamental frequency, meaning the frequency ratio yields lower values. Therefore, the single-walled carbon nanotubes which yield higher fundamental frequency values (the ones of lower length) present a higher sensitivty and are optimal for usage in mass detection, within the present study variables, confirming what has been precognized in Chapter 1.

5.7 Conclusions

In this chapter, a complete model for a SWCNT with an attached concentrated mass was developed, from an already fully developed model that allowed to study the vibration of a SWCNT. From the established equations of motion, the attached concentrated mass terms were added, and with the incorporation of the Eringen's nonlocal elasticity theory, the model was implemented using the p-version finite element method, with the aid of the Galerkin method to obtain the finite element matrices.

The developed model was validated by comparison to molecular dynamics simulations results, from available literature, as the fundamental natural frequency values given by the model based on the Sanders-Koiter theory developed in this dissertation came in good agreement regarding the MD ones. In fact, for lower values of length the relative difference was higher than for higher length values from a specific concentrated mass value, while generally the relative difference was in the same order of magnitude for all lengths. The mode shapes regarding a SWCNT with an attached mass were also illustrated.

Then, a calibration and study of the influence of the nonlocal parameter in the preview of the natural frequency values given by different concentrated masses was performed. A value of a minimum concentrated mass proposed from the literature for the studied case was verified, as well as the logarithmically linear behaviour of the fundamental frequency values along the concentrated mass values. There were also critical attached mass values up to which the nonlocal theory is relevant, for lower aspect ratios, as this critical value would increase as the length of the nanotube would also increase, while the nonlocal parameter would be in the same order of magnitude as proposed in chapter 4. Regarding the higher studied length value, not only the nonlocal parameter relevance is more significant, the variation of the parameter across the whole range of concentrated masses would be lower, which may eventually need to an accurate singular e_0 value that for any mass value would accurately describe and predict the natural frequency behaviour. As there was not enough data of higher length values, study was performed for the only available case, yet representing a great topic for further investigation.

Lastly, a comparison between results of SWCNTs and DWCNTs was performed, having been concluded that SWCNTs generally display higher sensitivity to the attachment of concentrated masses than DWCNTs across different length values, while also confirming that the usage of lower length carbon nanotubes, which yield higher natural frequency values, also results in a significant increase in the sensitivity of the nanotube to attached masses.

Chapter 6

Conclusions

6.1 Summary

In the present dissertation an equivalent continuum model was developed for both SWCNT and DWCNT, in order to study the free linear undamped vibration response and, in particular, the modes of vibration. These models were based on Kirchhoff-Love assumptions for thin shells, after which the Sanders-Koiter thin shell theory was selected and developed. Eringen's nonlocal theory was then included, taking into account the small-scale nonlocal effects. Regarding the DWCNT model, the van der Waals forces were formulated and included in the interlayer stiffness. Then, the p-version finite element method was employed to discretize the displacement components and derive the equations of motion and resultant finite element matrices with the aid of the Galerkin method, ending with the transformation of the problem from time domain to frequency domain.

The developed models were tested and compared to existent referenced data from different authors, as the model convergence was verified in comparison to models from literature, and validation was carried out relatively to Raman spectrocopy, Molecular Dynamics simulations, and Finite Element Analysis data. Regarding the first case, convergence was in fact verified not only for the local model but also for the nonlocal model, for different input parameters and for different boundary conditions. As a distinct number of shape functions was found necessary for the convergence of each case, the maximum number of shape functions, $N = 25$ for x were used for Chapter 3 and Chapter 4. Regarding the second case, several vibration modes were tested for SWCNT for different parameters as chirality and diameter, aspect ratio and boundary conditions, as Radial Breathing modes and beam-like modes, along with higher order n modes both extensional and inextensional. Natural frequency results were found to be satisfactory as the relative differences revealed low values, specially for higher aspect ratios, when comparing to MD and FEA, for CC boundary conditions. FF boundary conditions were compared to a shell model and validated with close results. SS boundary conditions were compared to regular shell model values, as results were also in agreement to the analytical results and were found better than FEM results proposed by other authors. Finally, for DWCNTs, both CC and SS boundary conditions were tested and validated regarding MD results.

The natural frequency values from SWCNT and DWCNT values were then compared, as it was concluded that for a DWCNT with an outer tube of the same chirality as the SWCNT, the natural frequency for the first one would always be inferior than the one of a SWCNT. On the same note, the higher the chirality and diameter of the inner tube of the DWCNT, the higher the natural frequency values and the closer it would be to the SWCNT one, tending to its value. In fact, the stiffness increment is more preponderant than the inertia increment for an increasing value of the inner tube diameter for a DWCNT.

The mode shapes were then presented, regarding CC, SS and FF boundary conditions for a SWCNT, with the free-free serving as validation by comparison to the mode shapes from literature, and the rest coming as an illustration of the versatility of the implemented model, showcasing RBMs, beam-like modes, Rayleigh and Love modes, and modes for $n = 2$. Regarding the DWCNTs, in-phase and anti-phase modes were illustrated for both CC and SS boundary conditions, with the behaviour of the mode shapes coming as expected.

Further in the present dissertation, a study regarding the influence of the nonlocal parameter was carried out. It is important to note that the initial set of defining parameters of the CNTs as Young's modulus, Poisson's coefficient, thickness and density is of significant influence on the results the models produced. Even though a set of parameters is not established on the scientific community, many are proposed, from which one was adopted taking into account the frequency of usage and the quality of the results from other authors. Still, the results from the nonlocal theory are influenced by this decision, reason why the analysis must be meticulously evaluated.

Therefore, the study is started with the calibration of the nonlocal parameter for different order natural frequencies of a clamped-clamped SWCNT. Besides the common decrease in the natural frequency values with the increase of the aspect ratio, the relevance of the nonlocal parameter revealed itself higher for low values aspect ratio, as for higher aspect ratios the difference between the local and nonlocal theory would fade, being expected as the small-size effect becomes negligible with the increase in the structure's dimensions. It was also found that for higher order natural frequencies, the nonlocal parameter stays relevant for a wider range of aspect ratio, while also yielding lower nonlocal parameter values overall. For a DWCNT case, such conclusions were not able to be taken as the range of aspect ratio available values was relatively small, only being possible to observe a decreasing tendency in the nonlocal parameter for superior aspect ratio values considered.

Then, the relative influence of the nonlocal parameter was investigated regarding the frequency ratio, with the identification of a behaviour of more significant influence of the nonlocal parameter for higher order natural frequencies and for lower values of aspect ratio/length. This magnitude of relevancy would dissipate as the diameter of the nanotube would increase, as predicted.

Regarding the circumferential mode number paired with the nonlocal parameter influence, a phenomenon describing the association of smaller values of natural frequencies associated with higher values of circumferential mode numbers was evaluated for SWCNTs of CC boundary conditions, having been found that this behaviour is very relevant for low value aspect ratios, while the nonlocal parameter besides diminishing the natural frequency values, also highlights and magnifies the described behaviour. It is also important to note that this phenomenon is more significant not only for smaller diameter values, but also for higher order natural frequencies, meaning that for a list of ascending order natural frequency values, for bigger values, the association of natural frequencies with higher order circumferential mode numbers which may not be in an organized and ascending order will naturally occur. From a research standpoint, it reveals the importance of identifying the pair natural frequency-mode shape, specially for shells, for example when performing a similar study to the calibration of the nonlocal parameter already described in this dissertation.

With respect to the influence of the nonlocal parameter on the mode shapes, it has been found that the higher the parameter, the more significant and evident the nonlocal effect is, while also being clear that for higher order natural frequency values associated with higher order mode shapes, composed of an also higher wave numbers, the nonlocal effect was, as expected, more relevant, as the length of a single wave in the x direction diminishes, where the small-size effects are more pronounced. This influence was observed regarding the shape of the mode curve, as it was revealed more compact, while also describing lower values on local maximum points, in absolute terms.

Finally, a model for a SWCNT and an attached concentrated mass was developed from the established SWCNT model, including the Eringen's nonlocal elasticity theory, and implemented using the p-version finite element method. The results were then validated by comparison to available literature data. From here, the influence of the nonlocal parameter was investigated, as a calibration was performed for a wide range of concentrated mass values. The value of a minimum concentrated mass proposed in the literature for the studied conditions was verified, as well as the logarithmically linear behaviour of the fundamental frequencies as a function of the concentrated mass. Regarding different length values, for lower ones the nonlocal parameter relevance would cease up to a critical attached mass value that has been proposed for the studied conditions. This value would increase with the length value, until a point where no critical value was identified, and the nonlocal parameter variation would be significantly lower across the concentrated mass values, leading to the hypothesis that for certain lengths, a singular e_0 may be proposed to adequately and accurately describe the fundamental frequency results and consequently the mass value, in a mass detection device. A comparison between results of SWCNTs and DWCNTs was also performed, resulting in the conclusion that SWCNTs show a higher sensitivity to attached concentrated masses for different length values, and also that for lower length carbon nanotubes, the sensitivity also increases more significantly, with SWCNTs with these conditions being more suitable candidates for mass detection devices.

6.2 Future Work

Even though carbon nanotubes were discovered and synthesised almost three decades ago, research into this ramification of nanotechnology is still in a development stage, with the number of publications increasing in the past years. Thus, fields of research within this theme, both theoretical and experimental should be considered and invested on, as more in-depth scientific knowledge and great applications for CNTs are to be developed.

As a continuation from the work developed on this dissertation, it is apparent the development of a nonlinear model with inclusion of geometric nonlinearities. Starting with the simpler SWCNT case, the p-version finite element should be employed for a more complex, complete and accurate model regarding experimental results, also leading to the possibility of the study of nonlinear mode interaction.

A different topic plausible for investigation is forced vibration regime, which would be one step further regarding the considered dynamic problem, and should be solved with the aid of iterative processes. Within this possibility, the admission of an electrostatic force, which may be represented by a nonlinear behaviour, described in some applications in the introductory chapter, also reveals great interest.

Adapting the p-version finite element method versatility, a different but interesting topic of reasearch would be the study and analysis of carbon nanotubes framed on more than one (axial) axis, by either mechanical induced kinks (implying the usage of more than one element) or initial curvature along the nanotube (implying the admission of new terms on the initial formulation of the equations of motion).

With respect to the mass detection devices and concentrated attached mass study performed in this dissertation, a study regarding the calibration of a singular nonlocal parameter value (for high enough lengths of the nanotube), is highly cherished in order to accurately predict the fundamental frequency results and attached mass values, being of immediate and very relevant application.

Lastly, the study of the nonlocal parameter influence on a nonlinear theory, along with the investigation of different theories and their applicability on concrete cases, with a secondary aim to more precisely define a set of parameters that describe the mechanical behaviour of CNTs, represents a long-term yet rewarding and merit deserving research cause, which is believed to be on the verge of development.

References

[1] Sumio Iijima. Helical microtubules of graphitic carbon. *Nature*, 354(6348):56–58, 1991.

[2] Ronald F. Gibson, Emmanuel O. Ayorinde, and Yuan-Feng Wen. Vibrations of carbon nanotubes and their composites: A review. *Composites Science and Technology*, 67(1):1–28, 2007.

[3] A. K. Naik, M. S. Hanay, W. K. Hiebert, X. L. Feng, and M. L. Roukes. Towards single-molecule nanomechanical mass spectrometry. *Nature Nanotechnology*, 4(7):445–450, 2009.

[4] Zhidong Han and Alberto Fina. Thermal conductivity of carbon nanotubes and their polymer nanocomposites: A review. *Progress in Polymer Science*, 36(7):914–944, 2011.

[5] Merlin R. Weber WH. *Raman scattering in materials science*. Springer, New York, 2000.

[6] F. Khademolhosseini, A. S. Phani, A. Nojeh, and N. Rajapakse. Nonlocal continuum modeling and molecular dynamics simulation of torsional vibration of carbon nanotubes. *IEEE Transactions on Nanotechnology*, 11(1):34–43, 2012.

[7] W. H. Duan, C. M. Wang, and Y. Y. Zhang. Calibration of nonlocal scaling effect parameter for free vibration of carbon nanotubes by molecular dynamics. *Journal of Applied Physics*, 101(2):024305, 2007.

[8] R. Ansari, H. Rouhi, and S. Sahmani. Calibration of the analytical nonlocal shell model for vibrations of double-walled carbon nanotubes with arbitrary boundary conditions using molecular dynamics. *International Journal of Mechanical Sciences*, 53(9):786–792, 2011.

[9] Rumeng Liu and Lifeng Wang. Vibration of cantilevered double-walled carbon nanotubes predicted by timoshenko beam model and molecular dynamics. *International Journal of Computational Methods*, 12(04):1540017, 2015.

[10] K. V. Avramov. Nonlinear vibrations characteristics of single-walled carbon nanotubes by nonlocal elastic shell model. *International Journal of Non-Linear Mechanics*, 107:149–160, 2018.

[11] Matteo Strozzi, Leonid I. Manevitch, Francesco Pellicano, Valeri V. Smirnov, and Denis S. Shepelev. Low-frequency linear vibrations of single-walled carbon nanotubes: Analytical and numerical models. *Journal of Sound and Vibration*, 333(13):2936–2957, 2014.

[12] Reza Ansari, Hessam Rouhi, and Saeid Sahmani. Free vibration analysis of single- and double-walled carbon nanotubes based on nonlocal elastic shell models. *Journal of Vibration and Control*, 20(5):670–678, 2012.

[13] Matteo Strozzi, Valeri Smirnov, Massimo Milani, and Francesco Pellicano. Nonlinear vibrations and energy exchange of single-walled carbon nanotubes. circumferential flexural modes. *Journal of Sound and Vibration*, 381, 2016.

[14] M. S. Dresselhaus, G. Dresselhaus, and R. Saito. Physics of carbon nanotubes. *Carbon*, 33(7):883–891, 1995.

[15] Erik T. Thostenson, Zhifeng Ren, and Tsu-Wei Chou. Advances in the science and technology of carbon nanotubes and their composites: a review. *Composites Science and Technology*, 61(13):1899–1912, 2001.

[16] M. Dresselhaus G. Dresselhaus P. Eklund. *Science of Fullerenes and Carbon Nanotubes.* Academic Press, 1996.

[17] B. Q. Wei, R. Vajtai, and P. M. Ajayan. Reliability and current carrying capacity of carbon nanotubes. *Applied Physics Letters*, 79(8):1172–1174, 2001.

[18] Marco Buongiorno Nardelli and J. Bernholc. Mechanical deformations and coherent transport in carbon nanotubes. *Physical Review B*, 60(24):R16338–R16341, 1999.

[19] Chunyu Li and Tsu-Wei Chou. Theoretical studies on the charge-induced failure of single-walled carbon nanotubes. *Carbon*, 45(5):922–930, 2007.

[20] Chunyu Li, Erik T. Thostenson, and Tsu-Wei Chou. Sensors and actuators based on carbon nanotubes and their composites: A review. *Composites Science and Technology*, 68(6):1227–1249, 2008.

[21] Yufeng Guo and Wanlin Guo. Mechanical and electrostatic properties of carbon nanotubes under tensile loading and electric field. *Journal of Physics D: Applied Physics*, 36(7):805–811, 2003.

[22] B. I. Yakobson, C. J. Brabec, and J. Bernholc. Nanomechanics of carbon tubes: Instabilities beyond linear response. *Physical Review Letters*, 76(14):2511–2514, 1996.

[23] Jean-Paul Salvetat, G. Andrew D. Briggs, Jean-Marc Bonard, Revathi R. Bacsa, Andrzej J. Kulik, Thomas Stöckli, Nancy A. Burnham, and László Forró. Elastic and shear moduli of single-walled carbon nanotube ropes. *Physical Review Letters*, 82(5):944–947, 1999.

[24] C. Q. Ru. Effective bending stiffness of carbon nanotubes. *Physical Review B*, 62(15):9973–9976, 2000.

[25] Arthur W. Barnard, Mian Zhang, Gustavo S. Wiederhecker, Michal Lipson, and Paul L. McEuen. Real-time vibrations of a carbon nanotube. *Nature*, 566(7742):89–93, 2019.

[26] A. M. Rao, E. Richter, Shunji Bandow, Bruce Chase, P. C. Eklund, K. A. Williams, S. Fang, K. R. Subbaswamy, M. Menon, A. Thess, R. E. Smalley, G. Dresselhaus, and M. S. Dresselhaus. Diameter-selective raman scattering from vibrational modes in carbon nanotubes. *Science*, 275(5297):187–191, 1997.

[27] A. Jorio, M. A. Pimenta, A. G. Souza Filho, R. Saito, G. Dresselhaus, and M. S. Dresselhaus. Characterizing carbon nanotube samples with resonance raman scattering. *New Journal of Physics*, 5:139–139, 2003.

[28] Ernst Richter and K. R. Subbaswamy. Theory of size-dependent resonance raman scattering from carbon nanotubes. *Physical Review Letters*, 79(14):2738–2741, 1997.

[29] S. T. Purcell, P. Vincent, C. Journet, and Vu Thien Binh. Tuning of nanotube mechanical resonances by electric field pulling. *Physical Review Letters*, 89(27):276103, 2002.

[30] Yan-Gao Hu, K. M. Liew, Q. Wang, X. Q. He, and B. I. Yakobson. Nonlocal shell model for elastic wave propagation in single- and double-walled carbon nanotubes. *Journal of the Mechanics and Physics of Solids*, 56(12):3475–3485, 2008.

[31] A. Wadhawan, D. Garrett, and J. M. Perez. Nanoparticle-assisted microwave absorption by single-wall carbon nanotubes. *Applied Physics Letters*, 83(13):2683–2685, 2003.

[32] X. G. Liu, D. Y. Geng, H. Meng, P. J. Shang, and Z. D. Zhang. Microwave-absorption properties of zno-coated iron nanocapsules. *Applied Physics Letters*, 92(17):173117, 2008.

[33] Robert E. Tuzun, Donald W. Noid, Bobby G. Sumpter, and Ralph C. Merkle. Dynamics of fluid flow inside carbon nanotubes. *Nanotechnology*, 7(3):241–246, 1996.

[34] P. Soltani, M. M. Taherian, and A. Farshidianfar. Vibration and instability of a viscous-fluid-conveying single-walled carbon nanotube embedded in a visco-elastic medium. *Journal of Physics D: Applied Physics*, 43(42):425401, 2010.

[35] D. S. Bethune, C. H. Kiang, M. S. de Vries, G. Gorman, R. Savoy, J. Vazquez, and R. Beyers. Cobalt-catalysed growth of carbon nanotubes with single-atomic-layer walls. *Nature*, 363(6430):605–607, 1993.

[36] C. Journet, W. K. Maser, P. Bernier, A. Loiseau, M. Lamy de La Chapelle, S. Lefrant, P. Deniard, R. Lee, and J. E. Fischer. Large-scale production of single-walled carbon nanotubes by the electric-arc technique. *Nature*, 388:756, 1997.

[37] A. G. Rinzler, J. Liu, H. Dai, P. Nikolaev, C. B. Huffman, F. J. Rodríguez-Macías, P. J. Boul, A. H. Lu, D. Heymann, D. T. Colbert, R. S. Lee, J. E. Fischer, A. M. Rao, P. C. Eklund, and R. E. Smalley. Large-scale purification of single-wall carbon nanotubes: process, product, and characterization. *Applied Physics A*, 67(1):29–37, 1998.

[38] Pavel Nikolaev, Michael J. Bronikowski, R. Kelley Bradley, Frank Rohmund, Daniel T. Colbert, K. A. Smith, and Richard E. Smalley. Gas-phase catalytic growth of single-walled carbon nanotubes from carbon monoxide. *Chemical Physics Letters*, 313(1):91–97, 1999.

[39] Z. F. Ren, Z. P. Huang, D. Z. Wang, J. G. Wen, J. W. Xu, J. H. Wang, L. E. Calvet, J. Chen, J. F. Klemic, and M. A. Reed. Growth of a single freestanding multiwall carbon nanotube on each nanonickel dot. *Applied Physics Letters*, 75(8):1086–1088, 1999.

[40] Z. F. Ren, Z. P. Huang, J. W. Xu, J. H. Wang, P. Bush, M. P. Siegal, and P. N. Provencio. Synthesis of large arrays of well-aligned carbon nanotubes on glass. *Science*, 282(5391):1105–1107, 1998.

[41] Z. P. Huang, J. W. Xu, Z. F. Ren, J. H. Wang, M. P. Siegal, and P. N. Provencio. Growth of highly oriented carbon nanotubes by plasma-enhanced hot filament chemical vapor deposition. *Applied Physics Letters*, 73(26):3845–3847, 1998.

[42] Yahachi Saito, Keishi Nishikubo, Kenichiro Kawabata, and Takehisa Matsumoto. Carbon nanocapsules and single-layered nanotubes produced with platinum-group metals (ru, rh, pd, os, ir, pt) by arc discharge. *Journal of Applied Physics*, 80(5):3062–3067, 1996.

[43] Maohui Ge and Klaus Sattler. Bundles of carbon nanotubes generated by vapor-phase growth. *Applied Physics Letters*, 64(6):710–711, 1994.

[44] A. M. Fennimore, T. D. Yuzvinsky, Wei-Qiang Han, M. S. Fuhrer, J. Cumings, and A. Zettl. Rotational actuators based on carbon nanotubes. *Nature*, 424(6947):408–410, 2003.

[45] Kilho Eom, Harold S. Park, Dae Sung Yoon, and Taeyun Kwon. Nanomechanical resonators and their applications in biological/chemical detection: Nanomechanics principles. *Physics Reports*, 503(4):115–163, 2011.

[46] K. L. Ekinci, X. M. H. Huang, and M. L. Roukes. Ultrasensitive nanoelectromechanical mass detection. *Applied Physics Letters*, 84(22):4469–4471, 2004.

[47] Philip S. Waggoner and Harold G. Craighead. Micro- and nanomechanical sensors for environmental, chemical, and biological detection. *Lab on a Chip*, 7(10):1238–1255, 2007.

[48] B. Ilic, D. Czaplewski, M. Zalalutdinov, H. G. Craighead, P. Neuzil, C. Campagnolo, and C. Batt. Single cell detection with micromechanical oscillators. *Journal of Vacuum Science Technology B: Microelectronics and Nanometer Structures Processing, Measurement, and Phenomena*, 19(6):2825–2828, 2001.

[49] A. Gupta, D. Akin, and R. Bashir. Single virus particle mass detection using microresonators with nanoscale thickness. *Applied Physics Letters*, 84(11):1976–1978, 2004.

[50] Karen M. Goeders, Jonathan S. Colton, and Lawrence A. Bottomley. Microcantilevers: sensing chemical interactions via mechanical motion. *Chemical Reviews*, 108(2):522–542, 2008.

[51] Jeanne C. Stachowiak, Min Yue, Kenneth Castelino, Arup Chakraborty, and Arun Majumdar. Chemomechanics of surface stresses induced by dna hybridization. *Langmuir*, 22(1):263–268, 2006.

[52] Taeyun Kwon, Jinsung Park, Jaemoon Yang, Dae Sung Yoon, Sungsoo Na, Chang-Wan Kim, Jin-Suck Suh, Yong-Min Huh, Seungjoo Haam, and Kilho Eom. Nanomechanical in situ monitoring of proteolysis of peptide by cathepsin b. *PloS one*, 4(7):e6248–e6248, 2009.

[53] Jing Kong, Nathan R. Franklin, Chongwu Zhou, Michael G. Chapline, Shu Peng, Kyeongjae Cho, and Hongjie Dai. Nanotube molecular wires as chemical sensors. *Science*, 287(5453):622–625, 2000.

[54] Erich D. Steinle, David T. Mitchell, Marc Wirtz, Sang Bok Lee, Vaneica Y. Young, and Charles R. Martin. Ion channel mimetic micropore and nanotube membrane sensors. *Analytical Chemistry*, 74(10):2416–2422, 2002.

[55] Matthew Spletzer, Arvind Raman, Alexander Q. Wu, Xianfan Xu, and Ron Reifenberger. Ultrasensitive mass sensing using mode localization in coupled microcantilevers. *Applied Physics Letters*, 88(25):254102, 2006.

[56] Hongjie Dai, Jason H. Hafner, Andrew G. Rinzler, Daniel T. Colbert, and Richard E. Smalley. Nanotubes as nanoprobes in scanning probe microscopy. *Nature*, 384(6605):147–150, 1996.

[57] Philip Kim and Charles M. Lieber. Nanotube nanotweezers. *Science*, 286(5447):2148–2150, 1999.

[58] B. J. Landi, R. P. Raffaelle, M. J. Heben, J. L. Alleman, W. VanDerveer, and T. Gennett. Development and characterization of single wall carbon nanotube–nafion composite actuators. *Materials Science and Engineering: B*, 116(3):359–362, 2005.

[59] R. Haggenmueller, H. H. Gommans, A. G. Rinzler, J. E. Fischer, and K. I. Winey. Aligned single-wall carbon nanotubes in composites by melt processing methods. *Chemical Physics Letters*, 330(3):219–225, 2000.

[60] B. Arash and Q. Wang. A review on the application of nonlocal elastic models in modeling of carbon nanotubes and graphenes. *Computational Materials Science*, 51(1):303–313, 2012.

[61] B. Bodily and C. Sun. Structural and equivalent continuum properties of single-walled carbon nanotubes. *Int. J. of Materials and Product Technology*, 18:381–397, 2003.

[62] Matteo Strozzi, Valeri V. Smirnov, Leonid I. Manevitch, and Francesco Pellicano. Nonlinear vibrations and energy exchange of single-walled carbon nanotubes. radial breathing modes. *Composite Structures*, 184:613–632, 2018.

[63] A. Sakhaee-Pour, M. T. Ahmadian, and A. Vafai. Vibrational analysis of single-walled carbon nanotubes using beam element. *Thin-Walled Structures*, 47(6):646–652, 2009.

[64] A. Cemal Eringen. On differential equations of nonlocal elasticity and solutions of screw dislocation and surface waves. *Journal of Applied Physics*, 54(9):4703–4710, 1983.

[65] Ya-Xin Zhen and Bo Fang. Nonlinear vibration of fluid-conveying single-walled carbon nanotubes under harmonic excitation. *International Journal of Non-Linear Mechanics*, 76:48–55, 2015.

[66] Ender Cigeroglu and Hamed Samandari. Nonlinear free vibrations of curved double walled carbon nanotubes using differential quadrature method. *Physica E: Low-dimensional Systems and Nanostructures*, 64:95–105, 2014.

[67] Y. M. Fu, J. W. Hong, and X. Q. Wang. Analysis of nonlinear vibration for embedded carbon nanotubes. *Journal of Sound and Vibration*, 296(4):746–756, 2006.

[68] J. Yoon, C. Q. Ru, and A. Mioduchowski. Timoshenko-beam effects on transverse wave propagation in carbon nanotubes. *Composites Part B: Engineering*, 35(2):87–93, 2004.

[69] C. Y. Wang, C. Q. Ru, and A. Mioduchowski. Free vibration of multiwall carbon nanotubes. *Journal of Applied Physics*, 97(11):114323, 2005.

[70] W. Flügge. *Stresses in Shells.* Springer, Berlin, 1960.

[71] N. Silvestre, C. M. Wang, Y. Y. Zhang, and Y. Xiang. Sanders shell model for buckling of single-walled carbon nanotubes with small aspect ratio. *Composite Structures*, 93(7):1683–1691, 2011.

[72] Nuno Silvestre. On the accuracy of shell models for torsional buckling of carbon nanotubes. *European Journal of Mechanics - A/Solids*, 32:103–108, 2012.

[73] Tienchong Chang. A molecular based anisotropic shell model for single-walled carbon nanotubes. *Journal of the Mechanics and Physics of Solids*, 58(9):1422–1433, 2010.

[74] Tomás Rosas Coelho Chuaqui. *Linear and Non-Linear Vibrations of Single-Layer Graphene Sheets.* Master's degree dissertation, 2016.

[75] Q. Wang and V. K. Varadan. Application of nonlocal elastic shell theory in wave propagation analysis of carbon nanotubes. *Smart Materials and Structures*, 16(1):178–190, 2007.

[76] R. Ansari and S. Sahmani. Small scale effect on vibrational response of single-walled carbon nanotubes with different boundary conditions based on nonlocal beam models. *Communications in Nonlinear Science and Numerical Simulation*, 17(4):1965–1979, 2012.

[77] Marco Amabili. *Nonlinear vibrations and stability of shells and plates.* Cambrigde University Press, New York, 2008.

[78] Jaroslaw Meller. *Molecular Dynamics.* Nature Publishing Group, 2001.

[79] Dong Qian, Wagner, Gregory J , Wing Kam Liu, Min-Feng Yu, and Rodney S Ruoff. Mechanics of carbon nanotubes. *Applied Mechanics Reviews*, 55(6):495–533, 2002.

[80] H. Wan and F. Delale. A structural mechanics approach for predicting the mechanical properties of carbon nanotubes. *Meccanica*, 45(1):43–51, 2010.

[81] J. E. Jones and Sydney Chapman. On the determination of molecular fields.—i. from the variation of the viscosity of a gas with temperature. *Proceedings of the Royal Society of London. Series A, Containing Papers of a Mathematical and Physical Character*, 106(738):441–462, 1924.

[82] B. Faria, N. Silvestre, and J. N. Canongia Lopes. Tension–twisting dependent kinematics of chiral cnts. *Composites Science and Technology*, 74:211–220, 2013.

[83] Nuno Silvestre, Bruno Faria, and José N. Canongia Lopes. *11 - Atomistic Simulations of Carbon Nanotubes: Stiffness, Strength, and Toughness of Locally Buckled CNTs*, pages 259–290. Elsevier, 2018.

[84] Arthur W. Leissa. *Vibration of Shells.* NASA, Washington, United States, Washington, D.C., 1973.

[85] Theodor Krauthammer Eduard Ventsel. *Thin Plates and Shells: Theory: Analysis, and Applications.* New York, 2001.

[86] J. Lyell Sanders Jr. Nonlinear theories for thin shells. *Quarterly of Applied Mathematics, Vol. 21, No. 1*, pages pp. 21–36, 1963.

[87] Pedro Ribeiro and Olivier Thomas. Nonlinear modes of vibration and internal resonances in nonlocal beams. *Journal of Computational and Nonlinear Dynamics*, 12(3), 2017.

[88] N. S. Bardell. The application of symbolic computing to the hierarchical finite element method. *International Journal for Numerical Methods in Engineering*, 28(5):1181–1204, 1989.

[89] Wanmin Han, Maurice Petyt, and Kuo-Mo Hsiao. An investigation into geometrically nonlinear analysis of rectangular laminated plates using the hierarchical finite element method. *Finite Elements in Analysis and Design*, 18(1):273–288, 1994.

[90] P. Ribeiro. Hierarchical finite element analyses of geometrically non-linear vibration of beams and plane frames. *Journal of Sound and Vibration*, 246(2):225–244, 2001.

[91] Jack R. Vinson. *The Behaviour of Shells Composed of Isotropic and Composite Materials.* Kluwer Academic Publishers, Delaware, U.S.A., 1993.

[92] Leonard Meirovitch. *Computational methods in structural dynamics.* Springer Netherlands, 1980.

[93] X. Q. He, S. Kitipornchai, and K. M. Liew. Buckling analysis of multi-walled carbon nanotubes: a continuum model accounting for van der waals interaction. *Journal of the Mechanics and Physics of Solids*, 53(2):303–326, 2005.

[94] Stephen Timoshenko and James M. Gere. *Theory of elastic stability.* McGraw-Hill, New York, 1961.

[95] L. A. Girifalco and R. A. Lad. Energy of cohesion, compressibility, and the potential energy functions of the graphite system. *The Journal of Chemical Physics*, 25(4):693–697, 1956.

[96] Dresselhous G. Dresselhous M.S. Saito, R. Physical properties of carbon nanotubes. *Imperial College Press*, 1998.

[97] Francesco Pellicano. Vibrations of circular cylindrical shells: Theory and experiments. *Journal of Sound and Vibration*, 303(1):154–170, 2007.

[98] L. Meirovitch and H. Baruh. On the inclusion principle for the hierarchical finite element method. *International Journal for Numerical Methods in Engineering*, 19(2):281–291, 1983.

[99] A. Jorio, R. Saito, J. H. Hafner, C. M. Lieber, M. Hunter, T. McClure, G. Dresselhaus, and M. S. Dresselhaus. Structural (n,m) determination of isolated single-wall carbon nanotubes by resonant raman scattering. *Physical Review Letters*, 86(6):1118–1121, 2001.

[100] S. S. Gupta, F. G. Bosco, and R. C. Batra. Wall thickness and elastic moduli of single-walled carbon nanotubes from frequencies of axial, torsional and inextensional modes of vibration. *Computational Materials Science*, 47(4):1049–1059, 2010.

[101] R. Ansari, S. Ajori, and B. Arash. Vibrations of single- and double-walled carbon nanotubes with layerwise boundary conditions: A molecular dynamics study. *Current Applied Physics*, 12(3):707–711, 2012.

[102] Toshiaki Natsuki, Xiao-Wen Lei, Qing-Qing Ni, and Morinobu Endo. Free vibration characteristics of double-walled carbon nanotubes embedded in an elastic medium. *Physics Letters A*, 374(26):2670–2674, 2010.

[103] G. S. Leizerovich and S. V. Seregin. Free vibrations of circular cylindrical shells with a small added concentrated mass. *Journal of Applied Mechanics and Technical Physics*, 57(5):841–846, 2016.

[104] Chunyu Li and Tsu-Wei Chou. Mass detection using carbon nanotube-based nanomechanical resonators. *Applied Physics Letters*, 84(25):5246–5248, 2004.